

**DETERMINATION OF MATERIAL PROPERTIES FOR USE IN  
FEM SIMULATIONS OF MACHINING AND ROLLER BURNISHING**

**DISSERTATION**

Presented in Partial Fulfillment of the Requirements for  
the Degree of Doctor of Philosophy in the Graduate  
School of The Ohio State University

By

Partchapol Sartkulvanich, M.S.

\* \* \* \* \*

The Ohio State University  
2007

Dissertation Committee:  
Professor Taylan Altan, Adviser  
Professor Gary Kinzel  
Professor Jerald Brevick  
Professor Mark Walter

Approved by

---

Adviser  
Mechanical Engineering  
Graduate Program

© Copyright by  
Partchapol Sartkulvanich  
2007

## ABSTRACT

Abstract - In machining, Finite Element Method (FEM) simulation is used widely to analyze the effect of process conditions and tool edge design upon cutting variables. Thus, it is possible to investigate material machinability, process economics, and surface quality. One of the most crucial inputs in performing a reliable FEM simulation is the availability of material plastic properties. Special material testing methods are required to consider the high ranges of plastic strain, strain rate and temperature that occur in practical machining conditions (for strain rates up to  $10^6 \text{ s}^{-1}$  and temperatures up to  $10^3 \text{ }^\circ\text{C}$ ). Conventional material testing methods are not suitable.

Roller burnishing is a surface finishing process where a ceramic ball (3-12 mm in diameter) freely rolls on the machined surface under a high pressure and flattens the roughness peaks. The ball is hydrostatically supported and lubricated by the pressure fluid. The process improves surface finish, increases microhardness and induces compressive residual stresses on the surface. To implement FEM simulation of roller burnishing process, the flow stress properties of the machined surface layer must be known. Such surface layer properties could be significantly different from the substrate (bulk) material due to severe plastic deformation and possible phase transformation caused by prior machining operations. In this study, two approaches to determine the flow stress data are proposed.

a) The orthogonal slot milling tests to determine the flow stress at high strains, strain-rates and temperatures.

b) An inverse analysis in conjunction with the ball indentation test to determine the flow stress at the surface layer of a part but at low strain rates and room temperatures.

Furthermore, 2D and 3D FEM models were established by considering the flow stress properties obtained from the proposed procedures in order to analyze two problems: 1) effect of tool edge preparation and flank wear on burr formation in face milling of an aluminum alloy and 2) effect of roller burnishing parameters upon surface finish and residual stresses. Results from FEM simulations were compared and validated with the experimental data.

**Dedicated to my parents**

## ACKNOWLEDGMENTS

I would like to express my sincere gratitude to my adviser, Prof. Taylan Altan, for the opportunity to work at the Engineering Research Center for Net Shape Manufacturing (ERC/NSM) and his continuous guidance throughout the course of this thesis work. Without his thrust and patience, my research would not have been successful. My great appreciation extends to Prof. Gary Kinzel, Prof. Jerald Brevick and Prof. Mark Walter for serving as members of my dissertation committee and for providing valuable comments.

This work has been partially supported by the National Science Foundation (through the NSF Grant No. 9821020 and Grant No. 0323631) and General Motor Powertrain. This sponsorship is gratefully acknowledged.

Sincere thanks are extended to my colleagues in machining research group at the ERC/NSM, for their discussions and partial assistance in different parts of this research. Special thanks go to Dr. Yung-Chang Yen, Hakan Sahlan, Frank Koppka, Edward Morris, Francisco Jasso, Comron Moradi, Dr. Jörg Söhner, Ibrahim Al-Zkeri, and Zhongqiu Wang.

Finally, I want to thank my family, my girlfriend (Siripun) and friends (Yingyot, Cho, and Suwat) for their continued support and encouragement.

## VITA

June 28, 1975.....Born - Bangkok, Thailand

1996.....B.S. Mechanical Engineering,  
Chulalongkorn University, Bangkok,  
Thailand

1998.....M.S. Industrial Systems Engineering,  
The Ohio State University, Columbus, Ohio

1999 - 2006 .....Graduate Research Associate,  
Engineering Research Center for Net Shape  
Manufacturing (ERC/NSM),  
The Ohio State University, Columbus, Ohio

## PUBLICATIONS

### Papers Published in Peer Reviewed Journals

1. Sartkulvanich, P., Koppka, F., and Altan, T., 2004, "Determination of Flow Stress for Metal Cutting Simulation - A Progress Report", *Journal of Materials Processing Technology*, Volume 146, Issue 1, Pages 61-71
2. Sartkulvanich, P., Gocmen, A. and Altan, T., 2005, "Effects of Flow Stress and Friction Models in FE Simulation of Orthogonal Cutting - A Sensitivity Analysis", *Journal of Machining Science and Technology*, Vol. 9, Issue 1, Pages 1-26
3. Sartkulvanich, P., Soehner, J. and Altan, T., 2005, "Flow Stress Data for Finite Element Simulation in Metal Cutting - A progress report on MADAMS", *Journal of Machining Science and Technology*, Vol.9, Issue 2, Pages 271-288
4. Yen, Y.C., Sartkulvanich, P. and Altan, T., 2005, "Finite Element Modeling of Roller Burnishing Process", *CIRP Annals*, Vol. 54/1, Pages 237-240
5. Hamann, J.C., Meslin, F. and Sartkulvanich, P., 2002, "Criteria for the Quality Assessment of Constitutive Equations Dedicated to Cutting Models", *Journal of Machining Science and Technology*, Vol. 6, No. 3, Pages 331-351

### Papers Published in Conferences or Other Journals (not Peer Reviewed)

1. Sartkulvanich, P., Al-Zkeri, I., Yen, Y.C. and Altan, T., 2004, "Investigation of the effect of Tool Geometry upon Cutting Process Variables, Tool Wear and



Burr Formation using FE Simulation - A Progress Report", *NUMIFORM 2004* on June 2004, Columbus, Ohio, Pages 1347-1352

2. Altan, T., Sartkulvanich, P. and Al-Zkeri, 2006, "Status of FEM in Modeling of High Speed Cutting", *CIRP- High Performance Cutting Conference*, June 12-13, 2006, Vancouver, Canada

## **FIELDS OF STUDY**

**Major Field:** Mechanical Engineering

**Studies in:** Manufacturing Processes, Metal Cutting, Finite Element, Roller Burnishing

## TABLE OF CONTENTS

	Page
ABSTRACT .....	ii
ACKNOWLEDGMENTS .....	v
VITA .....	vi
PUBLICATIONS .....	vii
TABLE OF CONTENTS .....	ix
LIST OF FIGURES .....	xiv
LIST OF TABLES .....	xxi
LIST OF SYMBOLS .....	xxiii
GLOSSARY .....	xxv
CHAPTER 1 INTRODUCTION .....	1
CHAPTER 2 RESEARCH OBJECTIVES .....	5
CHAPTER 3 STATE-OF-THE-ART REVIEW .....	7
3.1. Mechanics of Metal Cutting .....	7
3.1.1. Chip Formation .....	9
3.1.2. Models of Orthogonal Cutting .....	11
3.2. Development and Applications of FEA in Simulation of Machining .....	14

3.3.	Determination of Flow Stress Material Properties for High Strain Rates .....	16
3.3.1.	Experimental Methods to Determine Flow Stress at High Strain Rates .....	17
3.3.2.	Constitutive Equations Used to Represent the Flow Stress for Machining .....	20
3.4.	Modeling of Burr Formation .....	25
3.5.	Inverse Analysis of Indentation Test.....	28
3.6.	Experimental Studies and Modeling of Roller Burnishing.....	31
 <b>CHAPTER 4 FLOW STRESS PROPERTIES FOR FEM SIMULATION OF MACHINING PROCESSES .....</b>		<b>38</b>
4.1.	Flow Stress Determination through Slot Milling Experiments .....	38
4.1.1.	Inverse Analysis of Oxley’s Machining Theory .....	42
4.1.2.	Experimental Tasks.....	44
4.1.2.1.	Slot Milling Experiments .....	44
4.1.2.2.	Quick-Stop Slot Milling Tests.....	52
4.1.3.	Computational Tasks.....	53
4.1.3.1.	Constitutive Models .....	54
4.1.3.2.	Minimization Scheme.....	57
4.1.4.	Determination of The Flow Stress Data for Selected Materials.....	59
4.1.4.1.	Experimental Results.....	59
4.1.4.2.	Sensitivity Analysis of Forces and Plastic Zones Thickness Ratios .....	60
4.1.4.3.	Discussion of Obtained Flow Stress Equations .....	69
4.1.4.4.	Validation of the Flow Stress Results.....	73
4.1.5.	Summary and Conclusions .....	82
4.2.	Effect of Flow Stress Parameters in FEM Simulation of Orthogonal Cutting - Sensitivity Analysis.....	83
4.2.1.	Sensitivity Analysis on One Cutting Condition.....	84
4.2.1.1.	Tool, Cutting Condition and Simulation Setup.....	84
4.2.1.2.	The Reference Flow Stress and Variations of Flow Stress Parameters .....	88

4.2.1.3.	Simulation Results for Sensitivity Analysis of One Cutting Condition .....	94
4.2.2.	Sensitivity Analysis for Different Cutting Conditions .....	96
4.2.2.1.	Additional Cutting Conditions and Variations of Flow Stress Parameter Sets.....	96
4.2.2.2.	Simulation Results .....	97
4.2.3.	Summary and Discussions on Sensitivity Analysis of Flow Stress in FEM Cutting Simulation .....	100
4.3.	MAterial DAtabase for Machining Simulation (MADAMS).....	103
4.3.1.	An Overview of MADAMS Program .....	104
4.3.2.	MADAMS Web Site and the Material Database .....	107
4.3.3.	Summary and Discussions .....	108
<b>CHAPTER 5 UTILIZATION OF THE FLOW STRESS DATA IN FEM MACHINING APPLICATION - A CASE STUDY: TOOL WEAR AND BURR FORMATION IN FACE MILLING OF AA356-T6 ALUMINUM ALLOY.....</b>		
<b>110</b>		
5.1.	Problems Description and Objectives .....	111
5.2.	Finite Element Modeling to Analyze Tool Wear and Burr Formation.....	111
5.2.1.	Material Properties and Friction Condition.....	112
5.2.2.	Process Simulation Procedure for Burr Formation in 2D Orthogonal Cutting .....	115
5.2.3.	The Effect of Tool Rake Angle and Flank Wear .....	117
5.2.4.	Performance of Variable Edge Honed Tool .....	117
5.2.4.1.	Analysis of Burr Formation .....	118
5.2.4.2.	Analysis of Tool Stress and Tool Temperature.....	120
5.2.5.	3D Face Milling Simulations .....	122
5.3.	Simulation Results and Discussions.....	125
5.3.1.	The Effects of Rake Angle and Flank Wear.....	125
5.3.2.	Performance of Variable Edge Honed Tool .....	128
5.3.3.	3D Simulation of Face Milling.....	131
5.4.	Conclusions.....	135

<b>CHAPTER 6 FLOW STRESS PROPERTIES FOR FEM SIMULATION OF ROLLER BURNISHING.....</b>	<b>140</b>
6.1. Finite Element Modeling of Indentation .....	141
6.1.1. Material Model .....	141
6.1.2. Finite Element Model .....	143
6.2. Evaluation of Indentation with a Conical Indenter .....	143
6.2.1. Representative Strain.....	147
6.2.2. Effect of Friction .....	148
6.3. Evaluation of Indentation with a Spherical Indenter .....	150
6.3.1. Effect of Strain-Hardening Exponent.....	150
6.3.2. Effect of Indentation Depth.....	151
6.3.3. Effect of Indentation Diameter.....	153
6.4. Comparison of Spherical and Conical Indenters.....	156
6.5. Development of Inverse Analysis to Determine the Flow Stress Property of Surface Layer .....	156
6.5.1. Proposed Inverse Analysis Methodology .....	158
6.5.2. Determination of the Flow Stress Property for Hard Turned Surface of AISI 52100 (60 HRC) .....	161
6.6. Conclusions.....	167
<b>CHAPTER 7 ANALYSIS OF SURFACE PROPERTIES FROM ROLLER BURNISHING SIMULATIONS AND COMPARISON WITH EXPERIMENTS .....</b>	<b>169</b>
7.1. Hard Turning and Hard Roller Burnishing Experiments.....	170
7.1.1. Specifications of Machine and Tools for Hard Turning and Hard Roller Burnishing Experiments .....	170
7.1.2. Experimental Procedures and Process Conditions .....	173
7.1.3. Experimental Measurements .....	176
7.2. FEM Modeling of Roller Burnishing.....	177

7.3.	Simulation Results and Discussions.....	186
7.3.1.	Data Extraction from FEM Roller Burnishing Simulation .....	186
7.3.2.	Effects of Burnishing Feed Rate .....	189
7.3.3.	Effects of Burnishing Pressure .....	195
7.3.4.	Effects of Ball Diameter .....	199
7.3.5.	Effect of Initial Residual Stresses Generated by Hard Turning ..	203
7.3.6.	Evaluation of 3D Roller Burnishing Simulation.....	206
7.4.	Summary and Conclusions.....	211
<b>CHAPTER 8 OVERALL CONCLUSIONS AND FUTURE WORK .....</b>		<b>214</b>
8.1.	Overall Conclusions.....	214
8.2.	Future Work.....	218
<b>REFERENCES .....</b>		<b>220</b>
<b>APPENDIX A - DOWNHILL SIMPLEX METHOD.....</b>		<b>234</b>
<b>APPENDIX B - UNIVERSAL HARDNESS.....</b>		<b>236</b>

## LIST OF FIGURES

<b>Figure</b>	<b>Page</b>
Figure 1.1: Major input parameters for FEM simulation of metal cutting .....	4
Figure 1.2: Roller burnishing with hydrostatic ball tool [Röttger, 2002] .....	4
Figure 3.1: Cutting principles in orthogonal cutting [König, 1996].....	9
Figure 3.2: Models of Orthogonal Cutting [Astakhov, 1997] .....	12
Figure 3.3: Parallel Sided Shear Zone Model [Oxley, 1989].....	14
Figure 3.4: Split Hopkinson's pressure bar, for impact compression tests [Shirakashi; 1983] .....	18
Figure 3.5: Tool motion and burr locations in face milling [Hashimura, 1999] .....	26
Figure 3.6: Schematic of burr formation mechanisms [Dornfeld, 2002] .....	26
Figure 3.7: Concept of flow stress determination using indentation test and FEM inverse analysis. ....	29
Figure 3.8: All true stress-true strain curves that have the same stress at a true plastic strain of 0.033 exhibit the same load-depth curve for the Berkovich indenter [Dao, 2001]. ....	30
Figure 3.9: Result of tangential residual stresses after hard turning and after hard roller burnishing using the cutting inserts with two different flank wear widths [Röttger, 2002].....	34
Figure 3.10: Simulation sequence for the 2-D FEM model of roller burnishing (left) and the predicted effective stress from FEM (right), in [Röttger, 2002] .....	35
Figure 4.1: Force predictions using three different flow stress equation obtained from flow stress determination approach in [Shatla, 1999] .....	40
Figure 4.2: Predictions of stress, strain, strain rate and temperature in primary and secondary shear zones, using three different flow stress equations in Figure 4-1. ....	41
Figure 4.3: Simplified flow chart of the methodology used to determine flow stress using the orthogonal slot milling test.....	43
Figure 4.4: Schematic of the orthogonal slot milling tests .....	45

Figure 4.5: Experimental setup of the slot milling process.....	47
Figure 4.6: Kistler dynamometer .....	47
Figure 4.7: Adapter plate .....	49
Figure 4.8: Plate sample for slot milling test.....	49
Figure 4.9: Cutting tool with negative rake angle.....	50
Figure 4.10: Cutting tool with positive rake angle.....	51
Figure 4.11: Schematic of quick stop milling experiments .....	53
Figure 4.12: Temperature factor versus temperature, for (a) Equation 4.4 and (b) Equation 4.5.....	56
Figure 4.13: Measurement of primary shear zone thickness .....	61
Figure 4.14: Measurement of secondary plastic zone thickness. ....	61
Figure 4.15: Change of force input data .....	64
Figure 4.16: Sensitivity analysis of force input on the obtained flow stress data.....	65
Figure 4.17: Sensitivity analysis of $R_p$ on the obtained flow stress data .....	66
Figure 4.18: Plots of Flow Stress Data at Different Inputs of $R_s$ .....	68
Figure 4.19: Comparison of the flow stress data for AISI 1045 steel between OXCUT predictions and Oxley's high speed compression data, [Oxley, 1989]: (a) at constant strain rate of $10,000 \text{ s}^{-1}$ ; (b) at constant temperature of $300 \text{ }^\circ\text{C}$ and (c) at constrain strain rate of $10,000 \text{ s}^{-1}$ .....	70
Figure 4.20: The flow stress data for AISI P20 steel obtained from OXCUT predictions: (a) stress-strain curves at constant strain rate of $10,000 \text{ s}^{-1}$ ; (b) stress-strain curves at constant temperature of $300 \text{ }^\circ\text{C}$ and (c) stress-temperature curves at constrain strain rate of $10,000 \text{ s}^{-1}$ .....	71
Figure 4.21: The flow stress data for AISI H13 steel obtained from OXCUT predictions: (a) stress-strain curves at constant strain rate of $10,000 \text{ s}^{-1}$ ; (b) stress-strain curves at constant temperature of $300 \text{ }^\circ\text{C}$ and (c) stress-temperature curves at constrain strain rate of $10,000 \text{ s}^{-1}$ .....	72
Figure 4.25: Comparison of experimental measurements in [Ivester, 2000], FEM-DEFORM predictions and OXCUT predictions for orthogonal turning tests on AISI 1045 steel .....	78
Figure 4.26: Comparison of experimental measurements in [Yen, 2000], FEM-DEFORM predictions and OXCUT predictions for orthogonal turning tests on AISI P20 steel.....	78
Figure 4.27: (a) location of temperature measurement is at 1.6 mm away from the major cutting edge [Müller, 2004]; (b) Comparison of chip surface temperature from FEM cutting simulations and measurement, for turning of AISI 1045 from [Müller, 2004].....	80



Figure 4.28: Verification for the uniqueness of the flow stress solution obtained from the proposed inverse analysis and slot milling tests. ....	81
Figure 4.29: Thermal properties of the workpiece material (AISI 1045) and uncoated tungsten carbide, from [ASM, 1990] and [Obikawa, 1995]; (a) Thermal conductivity and (b) heat capacity. ....	86
Figure 4.30: Workpiece and tool geometry used in the simulations for the sensitivity analysis of flow stress and friction .....	87
Figure 4.31: Reference flow stress equation compared with different flow stress data of AISI 1045 steel from the literature [Oxley, 1989; Maekawa, 1998 and Treppman, 2001]: a) stress-strain curves at strain rate of $200 \text{ s}^{-1}$ and temperature of $300 \text{ }^{\circ}\text{C}$ , and b) stress-temperature curves at strain rate of $400 \text{ s}^{-1}$ and strain of 0.3. ....	90
Figure 4.32: Variations of flow stress parameters over temperatures, according to Table 4.9 .....	92
Figure 4.33: Stress-strain rate curves of AISI 1045 steel from Hopkinson's bar tests at the strain of 0.1 and different temperatures [Treppman, 2001]. Lines represent a constitutive equation determined to fit the experimental flow stress data .....	93
Figure 4.34: Example of material data information provided in the MADAMS .....	109
Figure 5.1: Comparison of cutting force, thrust force and chip thickness from slot milling experiment and the predictions from FEM simulation with DEFORM-2D®, for orthogonal cutting of AA356-T6 alloy at $V_c = 200 \text{ m/min}$ and $f = 0.05 \text{ mm/rev}$ .....	114
Figure 5.2: Mesh density of tool and workpiece objects in FEM simulation of 2D orthogonal cutting.....	116
Figure 5.3: Simulation steps for chip formation and following burr formation.....	116
Figure 5.4: (a) Uniform edge honed tool and (b) variable edge honed tool.....	119
Figure 5.5: Tool-workpiece contact in face milling operation.....	119
Figure 5.6: Selected section planes along tool corner and the corresponding uncut chip thicknesses.....	121
Figure 5.7: Mesh definitions of tool and workpiece objects in 3D face milling simulation.....	124
Figure 5.8: (a) Flank wear on the actual tool and (b) a 3D solid model of a worn insert.....	124
Figure 5.9: Strain rate distribution in exit burrs for neutral tool at sharp (Left) and worn-out conditions (Right). ....	126
Figure 5.10: Comparison of the burr profiles from cutting with a neutral tool (with 0 degree rake angle) for sharp and worn-out conditions.....	126

Figure 5.11: Comparisons of burr area in relation to flank wear width (VB) between the tools with 0 degree and +20 degree rake angles.....	127
Figure 5.12: Distributions of effective stresses for cutting with neutral (0° rake angle) and hi-shear (+20° rake angle) tools .....	127
Figure 5.13: Comparison of the burr area when cutting using the tool with the edge radius of 25.4 μm and 4.2 μm. ....	129
Figure 5.14: Distributions of effective stresses and the maximum tool stress value from the 2D orthogonal cutting simulations of section A'-A', with uniform and variable edge honed tools.....	129
Figure 5.15: Maximum tool effective stresses for different tool orthogonal plane sections.....	130
Figure 5.16: Maximum tool temperatures for different tool orthogonal plane sections.....	131
Figure 5.17: (a) Burr locations observed from 3D milling simulation and (b) chip flow angle prediction.....	132
Figure 5.18: Strain distribution of the machined workpiece and possible fracture region .....	133
Figure 5.19: Section planes defined for burr investigation: a horizontal plane on the machined surface (Left) and a vertical plane normal to the machined surface (Right) .....	133
Figure 5.20: Comparison of the burr profiles from 2D simulation at section A-A and the size view of the vertical plane section from 3D face milling simulation.....	134
Figure 5.21: Comparison of burr geometries from the top view from (1) simulation with the sharp tool, (2) simulation of the worn tool and (3) milling experiments .....	136
Figure 5.22: Comparison of burr geometries from the side view, from (1) simulation with the sharp tool, (2) simulation with the worn tool and (3) milling experiments.....	137
Figure 5.23: Burr obtained from face milling experiment and the definition of burr geometries .....	138
Figure 5.24: Comparison of the burr profiles from the 2D simulations in cutting with a neutral tool at worn-out condition between the first cutting pass and the second cutting pass .....	138
Figure 6.1: True stress-true strain behavior of hardening material.....	142
Figure 6.2: Finite element model for ball indentation and boundary conditions in DEFORM-2D. ....	144

Figure 6.3:	Comparison of simulation results with the results provided in [Dao, 2001], for conical indentation ( $70.3^\circ$ ) on an aluminum sample. Flow stress parameters are $\sigma_y = 278.5$ MPa and $n = 0.088$ ).....	144
Figure 6.4:	Schematic of indentation with a conical indenter .....	145
Figure 6.5:	Normalized load-depth curve to demonstrate the effect of tip radius on the degree of the curvature (DEFORM 2D simulation results: $\sigma_y = 2000$ MPa, $n = 0.1$ ). .....	146
Figure 6.6:	The predicted load-depth curves from a conical indenter with a half-angle of $70.3^\circ$ (Berkovich indenter), using three flow stress equations with a representative strain of 0.033.....	149
Figure 6.7:	The flow stresses used in the simulations in Figure 6.6 showing the representative strain of 0.033.....	149
Figure 6.8:	The effect of friction on the load-depth curve in simulation of a conical indentation is negligible.....	150
Figure 6.9:	Sensitivity analysis results for spherical indentation at different strain-hardening exponents.....	152
Figure 6.10:	Normalized curves from the sensitivity analysis of spherical indentation ( $h_{max}/D=0.167$ , $\sigma_y = 300$ MPa). .....	152
Figure 6.11:	Normalized curves from the sensitivity analysis of spherical indentation, for $h_{max}/D = 0.1$ ( $h_{max} = 0.15$ mm, $D = 1.5$ mm) .....	154
Figure 6.12:	Normalized curves from the sensitivity analysis of spherical indentation, for $h_{max}/D = 0.033$ ( $h_{max} = 0.05$ mm, $D = 1.5$ mm) .....	154
Figure 6.13:	Comparison of the normalized load-depth curves from two different sized spherical indenters, for (a) Dia. = 1.5 mm and (b) Dia. = 1.0 mm. ....	155
Figure 6.14:	Yield strain contours from conical indentation at four different indentation depths, normalized with respect to the contact radius ( $r_c$ ) .....	157
Figure 6.15:	Yield strain contours from spherical indentation (with an indenter diameter of 1.5 mm) at four different indentation depths, normalized with respect to the contact radius ( $r_c$ ).....	157
Figure 6.16:	Flow chart of the developed inverse analysis procedure to determine the flow stress properties of the material surface layer from spherical indentation test. ....	159
Figure 6.17:	(a) Minimization of the sum-squared errors of the load-depth curve, assuming $n = 0$ , and (b) a plot of local minimum SSEs over different strain-hardening exponents.....	160
Figure 6.18:	Schematic of a cylindrical AISI 52100 sample .....	162

Figure 6.19: Automated Ball Indentation (ABI) machine, at Advanced Technology Corp., Oak Ridge, TN, used in indentation test on an AISI 52100 (60 HRC) sample.....	162
Figure 6.20: Experimental load-depth curves obtained from indentation tests on (a) hard turned surfaces, (b) roller burnished surfaces and (c) cross-section surfaces of an AISI 52100 cylindrical sample, as defined in Figure 6.18, using a 0.762 mm ball indenter (measurements conducted by Advanced Technology Corp., Oak Ridge, TN) .....	163
Figure 6.21: Comparison of the flow stress data of the hard-turned AISI 52100 surfaces obtained from FEM inverse analysis and analytical solution derived by [Haggag, 1993].....	166
Figure 6.22: Comparison of the flow stress data for AISI 52100 (60 HRC), obtained from indentation test and compression test.....	166
Figure 6.23: Comparison of the flow stress results for the three different surfaces of an AISI 52100 steel sample (as shown in Figure 6.20). .....	167
Figure 7.1: Hydraulic unit consists of pump, tank and electric control panel .....	172
Figure 7.2: Hydrostatic roller burnishing tool, Ecoroll-HG6.....	172
Figure 7.3: Sequences of hard turning and hard roller burnishing experiments.....	175
Figure 7.4: Contact angle between a burnishing tool and a workpiece sample. ....	175
Figure 7.5: (a) Roller burnishing process; (b) schematics of burnishing motion on the plane W [Yen, 2004] .....	180
Figure 7.6: Simulation sequence for 2-D FEM modeling of roller burnishing .....	181
Figure 7.7: Setups of the 2D roller burnishing simulation.....	181
Figure 7.8: Meshes of the ball tool and the workpiece in the 3D roller burnishing simulation .....	184
Figure 7.9: Burnishing force vs. depth curve, obtained from 3D roller burnishing simulations.....	184
Figure 7.10: Effect of friction factor on normal and rolling forces (in Z and Y directions).....	185
Figure 7.11: Surface nodes of initial hard turned and burnished surfaces obtained from a 2D simulation (a burnishing condition uses $P_b = 40$ MPa and $f_b = 0.05$ mm/rev) .....	188
Figure 7.12: Surface nodal points for extraction of residual stress data from 2D simulation ( $P_b = 40$ MPa and $f_b = 0.05$ mm/rev.) .....	188
Figure 7.13: Tangential and axial residual stress distributions of the hard turned and the burnished surfaces (from simulation and experiment), for $P_b = 40$ MPa and $f_b = 0.05$ mm/rev. ....	190

Figure 7.14: Effects of burnishing feed rate (for the same burnishing pressure of 40 MPa) on mean roughness and roughness depth .....	191
Figure 7.15: Effects of burnishing feed rate (for the same burnishing pressure of 40 MPa) on tangential and axial residual stress distributions along the depth (distance from surface) .....	194
Figure 7.16: Effects of burnishing pressure (for the same burnishing feed rate of 0.05 mm/rev) on mean roughness and roughness depth .....	196
Figure 7.17: Effects of burnishing pressure (for the same burnishing feed rate of 0.05 mm/rev) on tangential and axial residual stress distributions along the depth (distance from surface) .....	198
Figure 7.18: Burnishing force vs. penetration depth curves, obtained from 3D FEM burnishing simulation for 3 mm and 12 mm ball tools. ....	200
Figure 7.19: The effects of ball diameter on (a) roughness depth ( $R_z$ ) and (b) mean roughness ( $R_a$ ) from FEM simulations.....	200
Figure 7.20: The effects of ball diameter on the roughness profiles from FEM simulations .....	201
Figure 7.21: The effects of ball diameter of surface residual stress after burnishing in (a) tangential and (b) axial directions. ....	202
Figure 7.22: Residual stress of hard turned surface, assigned in the workpiece mesh model of 2D roller burnishing simulation: a) tangential residual stress and b) axial residual stress.....	204
Figure 7.23: Effects of initial residual stresses from hard turning in the predicted residual stresses in 2D roller burnishing simulation, for $P_b = 32$ MPa, $f_b = 0.05$ mm/rev .....	205
Figure 7.24: Points (point P1 to P100 along the depth) tracked for residual stress data from 3D simulation and comparison of the mesh size between surface and solid body .....	207
Figure 7.25: Comparison of surface residual stresses from 2D simulation, 3D simulation and the experiment, for $P_b = 40$ MPa, $f_b = 0.05$ mm/rev .....	209
Figure 7.26: Residual stress distributions from 3D roller burnishing simulation, after the 1st, 3rd and 5th rolling paths .....	210
Figure A.1: Schematic of downhill simplex minimization.....	235

## LIST OF TABLES

<b>Table</b>	<b>Page</b>
Table 3.1: Summary of various experimental studies on the effect of burnishing process parameters .....	32
Table 3.2: Comparison of roller burnishing simulation settings between Röttger’s original model [Röttger, 2002] and the refined model proposed in [Yen, 2004].....	36
Table 4.1: Experimental matrix for demonstrating the developed flow stress determination procedure with slot milling tests .....	59
Table 4.2: Experimental input data needed for OXCUT .....	62
Table 4.3: Sensitivity of force data on the flow stress equations obtained from slot milling tests, for P20 steel. ....	64
Table 4.4: Flow stress parameters obtained using different primary plastic zone thickness ratios, $R_p$ .....	65
Table 4.5: Flow stress parameters obtained using different secondary plastic zone thickness ratios, $R_s$ .....	67
Table 4.6: Flow stress equations of AISI 1045, P20 and H13 steels obtained from slot milling tests .....	69
Table 4.7: A cutting condition used in orthogonal cutting experiments of AISI 1045, in [Kalhori, 2000] .....	85
Table 4.8: Basic mechanical properties of the AISI 1045 workpiece and uncoated tungsten carbide tool.....	85
Table 4.9: Flow stress parameter sets for the preliminary analysis of flow stress on one cutting condition .....	91
Table 4.10: Simulation results for the preliminary analysis of flow stress on one cutting condition .....	94
Table 4.11: Flow stress parameter sets for the analysis of flow stress on different cutting conditions.....	96
Table 4.12: Selected flow stress parameter sets for an analysis on the effect of strain rate hardening ( $m$ ).....	98

Table 4.13:	Simulation results for the analysis of flow stress on different cutting conditions .....	98
Table 4.14:	Summary of the sensitivity analysis of the flow stress parameters .....	101
Table 4.15:	Active research groups on the area of material modeling for high strain rates .....	106
Table 5.1:	Physical and thermal properties of the workpiece and the cutting tool materials [GESA, 2003; Matweb, 1996].....	114
Table 5.2:	Simulation matrix for the study on the effects of tool rake angles and flank wear .....	117
Table 6.1:	The flow stress parameters of the hard-turned surface of AISI 52100 (60 HRC), obtained from the FEM inverse analysis and spherical indentation tests .....	165
Table 7.1:	Specifications of the machine and the cutting tools for hard turning experiments.....	171
Table 7.2:	Specifications of hydraulic pump, tools and coolant used in hard roller burnishing experiments.....	171
Table 7.3:	Process conditions for hard turning and hard roller burnishing tests .....	174
Table 7.4:	Conditions used in the X-ray measurement of residual stresses .....	177
Table 7.5:	Setup in the 3D FEM roller burnishing model.....	183
Table B.1:	Summary of angle and area data for the four most commonly used indenter geometries, where $\alpha_t$ is the total included angle, $\alpha$ is the angle between the two opposing faces of the pyramid, $A_r$ is the real (or 'developed') contact area and $A_p$ is the project contact area.....	237

## LIST OF SYMBOLS

Symbol	Units	Description
$R_a$	(mm or $\mu\text{m}$ )	Algorithmic surface roughness
$R_z$	(mm or $\mu\text{m}$ )	Peak-to valley surface roughness
$VB$	(mm)	Average flank wear
$V_c, v_c$	(m/min)	Cutting surface velocity
$V_b, v_b$	(m/min)	Burnishing surface speed
$V_s, v_s$	(m/min)	Relative sliding speed at contact interface
$f, f_c$	(mm/rev)	Cutting feed rate
$f_b$	(mm/rev)	Burnishing feed rate
$t_u$	(mm)	Undeformed or uncut chip thickness
$t_c$	(mm)	Average cut chip thickness
$d_c$	(mm)	Depth of cut (DOC)
$r_e$	(mm)	Cutting edge radius
$T$	( $^{\circ}\text{C}$ )	Process temperature
$t$	(second)	Process time (cutting time)
$\sigma_Y, \bar{\sigma}_Y$	(MPa)	Yield strength of the material
$\bar{\sigma}$	(MPa)	Effective stress or material flow stress
$\bar{\epsilon}, \bar{\epsilon}_p, \bar{\epsilon}_e$	(-)	Total effective strain, effective plastic strain, and effective elastic strain
$\bar{\dot{\epsilon}}$	(1/sec)	Effective strain rate



<b>Symbol</b>	<b>Units</b>	<b>Description</b>
$\alpha$	(deg)	Tool normal rake angle
$\gamma$	(deg)	Tool relief or clearance angle
$\kappa$	(deg)	Side cutting edge angle (SCEA) or lead angle

## GLOSSARY

<i>Cutting Parameters</i>	Cutting speed, feed rate, and depth of cut.
<i>Burnishing Parameters</i>	Burnishing pressure (or force), burnishing speed, feed rate, and ball diameter.
<i>Burr Formation</i>	Undesirable protrusions of workpiece material beyond the edge of the workpiece, generated by machining.
<i>Edge Preparation</i>	Modification of the cutting edge geometry by honing or chamfering or a combination of both in order to enhance the edge strength.
<i>SHPB</i>	Split Hopkinson Pressure Bar. Experimental technique used for testing material at impact loading and/or at high deformation rate.
<i>WC</i>	Cemented tungsten carbide. WC is the most common material for cutting tools

## CHAPTER 1

### INTRODUCTION

In conventional and high-speed machining, the interactions between the cutting tool and the workpiece are extremely important and complex. To understand these interactions, techniques of Finite Element Method (FEM) simulation for metal flow have been implemented widely to establish the effect of process conditions (feed rate, depth of cut, cutting speed) and tool edge preparations upon cutting forces, tool temperatures and stresses, and chip formation. Such information is essential to the assessment of material machinability, tool edge design, tool material selection, process economics, and surface quality of the machined surface. Figure 1.1 provides an overview of overall input parameters for FEM cutting simulation. One of the most crucial inputs in performing a reliable FEM simulation of high speed machining processes is the availability of material plastic properties under actual machining conditions, i.e. flow stress as a function of strain, strain rate and temperature. More importantly, special material testing methods are required to reflect the considerably high ranges of plastic strain, strain rate and temperature that occur in practical high speed machining conditions.

To be useful in metal cutting simulation, flow stress data must be obtained at high strain rates (up to  $10^6 \text{ s}^{-1}$ ), temperatures (up to  $1000 \text{ }^\circ\text{C}$ ) and strains (up to 4). The experimental methods commonly used to determine flow stress data are

Split Hopkinson's Pressure Bar (SHPB) test and orthogonal cutting test. SHPB technique may provide the material data through the direct measurement over an entire range of controlled parameters, whereas the practical orthogonal cutting method involves analytical and empirical calculations based on the experimental observations (e.g. cutting force, chip thickness). However, the controlled ranges of strain, strain rate and temperature in the SHPB test are significantly lower than those experienced in actual machining process. Typical ranges of SHPB test are approximately  $2,000 \text{ s}^{-1}$  for strain rate limit and 1.5 for strain limit. Furthermore, the SHPB test requires a special test apparatus and it is rather costly to carry out. As a result, the approach to estimate flow stress data by the orthogonal slot milling test is investigated and aimed to provide reliable material data for use in FEM cutting simulation.

The proposed method needs to be able to provide reliable flow stress properties that can be used in FEM cutting simulation for analysis of a practical machining problem. One recent industrial problem concerns burr formation due to edge deterioration when milling cylinder block and head surfaces, made of cast Aluminum Alloy AA 356-T6. The investigation of this problem was needed to develop the recommendations for increasing tool life and reducing burrs. For this case study, FEM modeling of burr formation in face milling is established while experiments are conducted in order to evaluate/compare the tool performance, and to analyze burr formation based on different tool edge/flank wear geometries.

In machining of hard materials such as hardened steels or titanium alloys, issue on tool wear is of major concern. Increase in tool wear affects a change in the tool edge geometries. Machining hard metals with worn tools tends to produce a poor surface finish as well as generate tensile residual stress on the surface, which potentially shortens fatigue life and lowers performance of the

functional surface. Therefore, it is practical to employ a surface enhancement operation that provides necessary surface modifications (i.e. improving surface finish and converting tensile residual stress to compressive). Roller burnishing would be best suited since it can be readily installed in the same CNC machine setting as that used for machining. Figure 1.2 illustrates a typical roller burnishing operation with a hydrostatic ball tool. It is characterized by a single pass of a smooth free-rolling ball (3-12 mm in ball diameter) under a high pressure to flatten the roughness peaks. The ball is supported and lubricated by the pressure fluid. The burnishing tool can be continuously fed, similar to machining, so that a small surface deformation progresses over the entire workpiece surface.

Most research on roller burnishing has focused on experimental studies and used simplified analytical approaches. A well-established FEM simulation model of roller burnishing with reliable material flow stress property of the surface layer may help to understand the process mechanics and recommend the optimal burnishing conditions for favorable surface qualities.

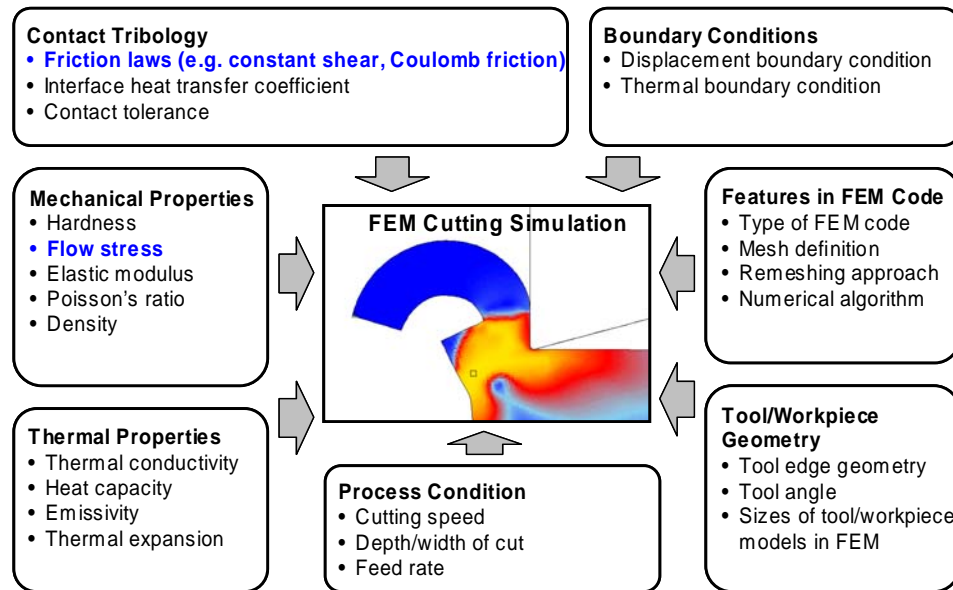


Figure 1.1: Major input parameters for FEM simulation of metal cutting

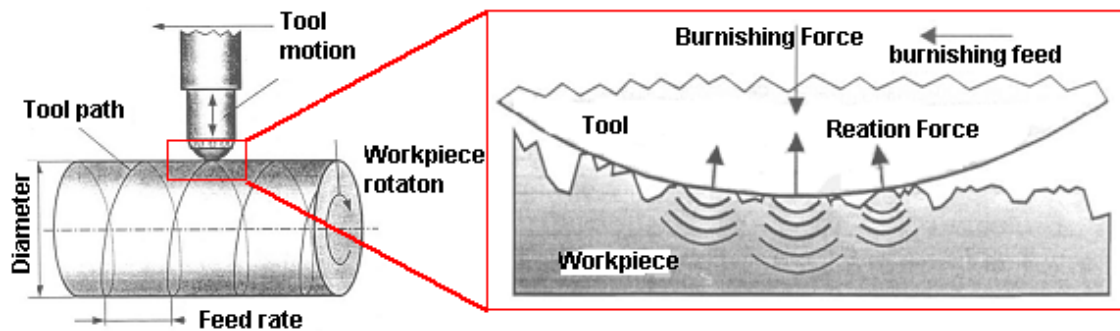


Figure 1.2: Roller burnishing with hydrostatic ball tool [Röttger, 2002]

## CHAPTER 2

### RESEARCH OBJECTIVES

FEM simulations of metal forming processes are highly influenced by material flow stress properties. In machining, special material testing methods are required to reflect the considerably high ranges of plastic strains, strain rates and temperatures. For roller burnishing, the properties of the surface layer could be significantly different from the substrate (bulk) material due to severe plastic deformation from prior machining operations. Thus, the overall objective of the proposed research is to determine the material properties of the finishing processes considered (machining and roller burnishing) and be able to employ the developed procedures in the analyses of practical applications.

In particular, the specific objectives of the proposed research are to:

- develop a method to determine the flow stress data that can be used for FEM simulations of machining and roller burnishing processes.
- demonstrate the use of this flow stress data in FEM simulation of machining process.
- establish a material database that can be useful for those who implement FEM for machining.

- analyze the effect of burnishing process parameters and recommend the process parameters for obtaining the desirable surface quality (i.e. required surface roughness and compressive residual stress)



## CHAPTER 3

### STATE-OF-THE-ART REVIEW

#### 3.1. Mechanics of Metal Cutting

Most practical cutting operations, such as turning and milling, involve two or more cutting edges inclined at various angles to the cutting direction. The basic mechanism of cutting can be explained by analyzing cutting with a single edge. The simplest cutting operation is known as orthogonal cutting, in which the cutting edge is perpendicular to the cutting velocity. In turning, orthogonal cutting can be achieved by turning a disk where the cutting edge is set parallel to the rotation axis of the workpiece. The feed is leading to the center of the disk. With the progress of the tool the cutting speed decreases and has to be adjusted by increasing the rotation speed. Another experimental setup for orthogonal cutting can be accomplished by turning tubes. Here the cutting speed varies over the cutting edge. By using a tube with a large diameter and a small wall thickness, this variation can be minimized. In milling, orthogonal cutting can be achieved by setting all tool axial angles to be zero while cutting a plate sample. During orthogonal milling, the cutting speed is held constant while the uncut chip thickness varies over the tool rotation. The width of cut ( $w$ ) is given by the plate thickness. More details of slot milling test will be presented in Section 4.1.2.1.

Usually orthogonal cutting model implies plane strain condition, which means there is no flow of work material in the direction parallel to the cutting edge. Thus, the cutting process can be treated as two-dimensional. Plane strain assumption is satisfied if the width of cut ( $w$ ) is more than or equal to 10 times the uncut chip thickness ( $t_u$ ) [Oxley, 1989].

In Figure 3.1, the schematic flow of a material with elastic-plastic characteristics in orthogonal cutting is shown. During material removal by the wedge-shaped tool, the metal undergoes a very large plastic deformation. The uncut material starts deforming when it reaches the primary deformation zone (the area ahead of the tool tip). High shear and compressive stresses in this zone will stretch the material grains and form them into a new shape. The stresses and the deformation will be maximized in the middle of the shear zone, and will decrease again after passing the shear zone. The new deformed material is now called the chip, which slides up the tool face. Due to high normal stresses and friction, the chip velocity in a narrow zone, close to the tool rake face is small. This velocity gradient causes a secondary deformation zone where the near parallel flow lines of the chip structure take an asymptotic form. High temperatures develop mostly in this secondary deformation zone. The contact between the flank face of the tool and the workpiece creates a third deformation zone that mainly influences the structure of the machined surface but has no effect on the chip formation.

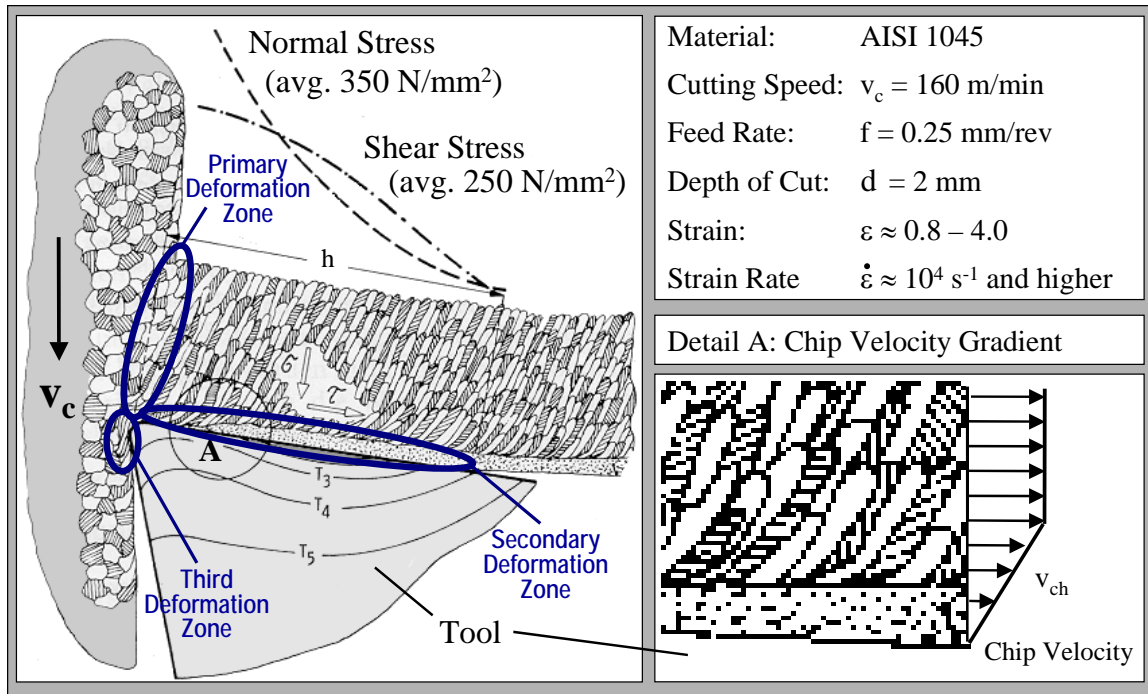


Figure 3.1: Cutting principles in orthogonal cutting [König, 1996]

### 3.1.1. Chip Formation

During the cutting process, a part of work material is removed. The result of this formation is the chip. The type of chip produced in this operation depends on the properties of the workpiece and the cutting conditions. Researchers in metal cutting classified the different types of chip forms. Methods of classification can be divided into two groups. The first group considers the chip appearance and its flow shapes that are used in practice, where the main goal is to obtain short breaking chips that can be better handled during the cutting process. A detailed description of this type of chip classification is given by [Jawahir, 1993].

The second group classified the cut chip by its inner structure or its formation process. Contrary to the first classification, there is no standardized description of the chip structure in the literature. Different researchers use their own definition, which may be similar but different in basic definition. For example, Vyas [Vyas, 1999] classified the chips into two groups: steady state continuous chips and cyclic chips. The cyclic group was sub-categorized into discontinuous chips, wavy chips, chips produced with a built-up edge and saw tooth chips.

Another approach was introduced in [Komanduri, 1981] and was complemented in [Sutter, 1997]. In this case, the chips were classified by geometrical appearance. Four levels of classification were introduced. The first level divided the chips into continuous and discontinuous structure. The second level was referring only to the continuous chip, which was sub-categorized later into smooth, wavy and segmented chips. Regularity was the third level and the appearance of adiabatic shear bands represented the fourth level.

The continuous chip formation happens when the chip formation occurs without fracture. This is usually the case that the material has very large formability. Oxley [Oxley, 1989] referred the continuous chip as a continuous steady state chip formation with a smooth chip surface and no segmentations.

A discontinuous chip formation occurs when material flow depends on elastic material properties, such as cast iron or tungsten carbide. The formability of the material is very low and fracture occurs before complete chip formation takes place.

The wavy chip structure may be caused by vibrations during cutting process. Vibrations lead to a variation of the uncut chip thickness, which leads to a variation in chip thickness. A cyclic change of chip velocity along the tool rake

face can also cause a wavy chip. The chip surface of a wavy chip is hilly but no sharp edges are formed [Vyas, 1999].

In segmented (or serrated) chip, the chip surface is characterized by sharp edges (or saw tooth shape) of the chip, formed during cutting. The frequency and the size of segmentations depend on cutting conditions and the workpiece properties. In most cases, segmentations occur along with shear bands. Two models are described in literature to explain the shear bands. First, the adiabatic shear theory describes that shear bands is caused by catastrophic thermoplastic instability. During deformation, localized stress concentrations are formed. When the strain-rate is relatively high, adiabatic heating of the localized areas causes a localized softening, which is followed by increasing local strain until an instantaneous shearing occurs [Jawahir, 1993]. The second explanation is given by fracture theory. In this theory, the shearing occurs after micro cracks are formed, running from the workpiece surface to the tool tip, [Vyas, 1999]. If the shear velocity and temperature is high enough in these areas, the material will also undergo adiabatic shear bands.

### **3.1.2. *Models of Orthogonal Cutting***

Many models of chip formation have been introduced by different researchers. Figure 3.2 represents some of the common models of orthogonal cutting.

The simplest and most widely known model of orthogonal cutting was developed by Ernst and Merchant, [Ernst, 1941]. The chip formation was considered as shearing in a very narrow zone, called the shear plane. This shear plane was found between the tool tip and the workpiece surface, and its location was defined by the shear angle,  $\phi$ . This shear plane is assumed to be in the

direction of maximum shear stress and shear strain rate. The model of Ernst and Merchant is only valid for continuous chip formation.

Based on the minimum energy analysis by Ernst and Merchant, it is assumed that the maximum shear stress occurs in the shear plane and the chip thickness can be estimated by minimizing cutting force with respect to shear angle. The solution of the shear angle can be obtained as

$$\phi = \frac{\pi}{4} + \frac{\alpha}{2} - \frac{\beta}{2}, \quad \text{Equation 3.1}$$

where  $\phi$  = Shear angle (radian)

$\alpha$  = Rake angle (radian)

$\beta$  = Friction angle (radian)

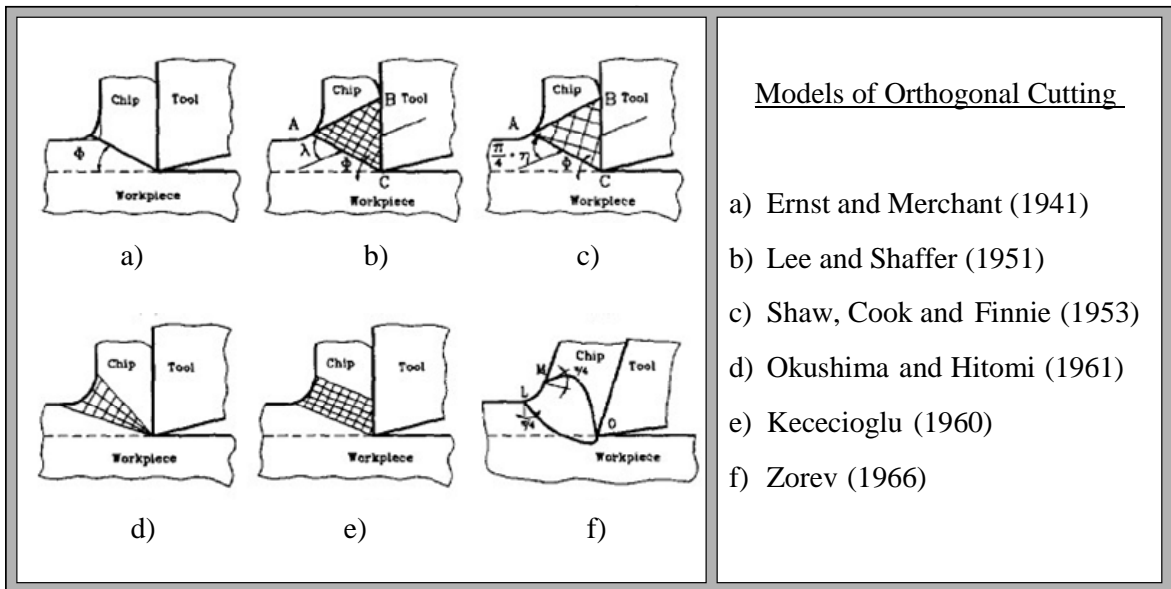


Figure 3.2: Models of Orthogonal Cutting [Astakhov, 1997]

Lee and Shaffer, [Lee, 1951], added the slip line theory to Ernst and Merchant's model, which provides the solution for  $\phi$  as

$$\phi = \frac{\pi}{4} + \alpha - \beta, \quad \text{Equation 3.2}$$

Okushima and Hitomi [Okushima, 1961] assumed that shearing takes place within a particular triangular flow region rather than along a single shear plane. Kececioglu's approach was similar to Merchant's model but assumed the primary and secondary deformation zones within parallel-sided boundaries. He assumed a uniform stress distribution in these deformation zones, [Kececioglu, 1960].

The above-mentioned models only reflect a particular aspect of metal cutting practice. These models cannot consider the variations of cutting conditions and cannot represent the influence of workpiece material.

Oxley [Oxley, 1989] introduced the relation of strain rate and strain into the determination of the shear angle by using the slip line and parallel-sided shear zone theory. The strain rate is empirically modeled as a function of the velocity of material flow in shear plane direction and the length of the shear plane.

Oxley's theory enables the influence of the flow stress of the workpiece material to calculate the cutting force and thrust force. Oxley modeled two plastic zones; primary zone and secondary zone, by assuming that metal is plastically deformed between two parallel planes, as shown in Figure 3.3. Thus, two constant plastic zone thicknesses are defined. The flow stress is considered in both plastic regions to calculate the average stresses, and consequently the cutting force and thrust force.

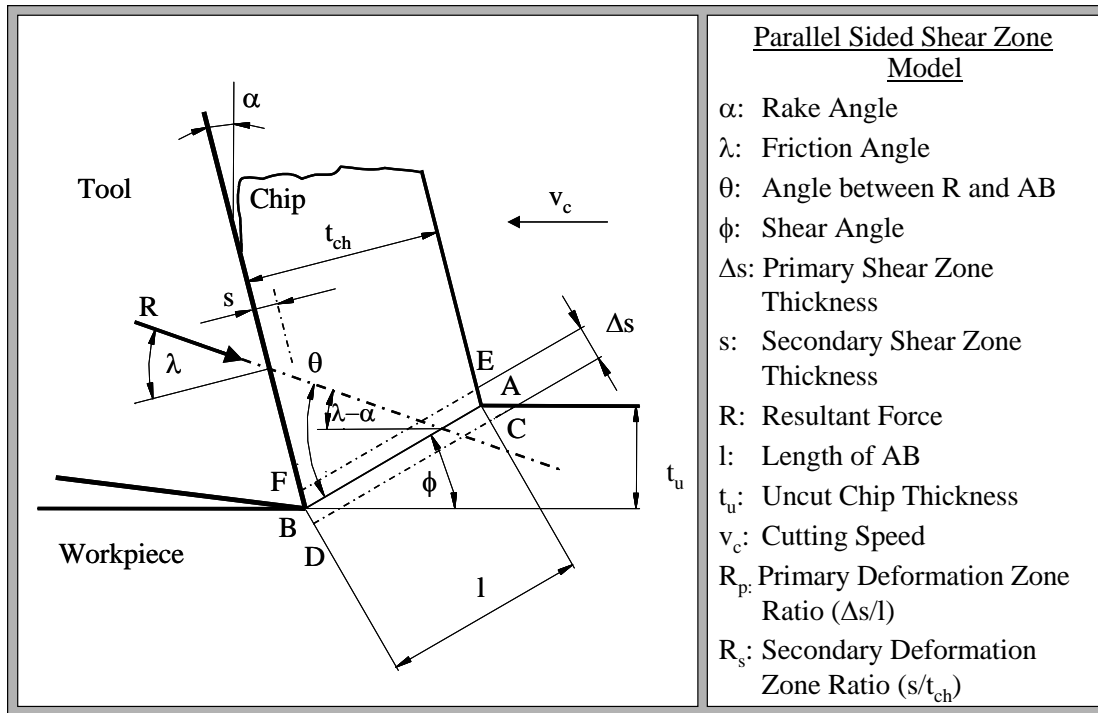


Figure 3.3: Parallel Sided Shear Zone Model [Oxley, 1989]

### 3.2. Development and Applications of FEA in Simulation of Machining

Finite Element Analysis (FEA) technique was first introduced in 1960s and has been widely used to analyze the design of tools and forming processes. Based on the success of FEM simulations for bulk forming processes, many researchers developed their own FEM codes to analyze metal cutting processes during the early 1980s [Usui, 1982; Iwata, 1984; Stenkowski, 1985]. Usui and Shirakashi [Usui, 1982] assumed a rigid sharp tool and elasto-plastic workpiece, and defined a node separation criterion based on the geometry of the element approaching the cutting edge. Iwata et al. [Iwata, 1984] established a rigid-plastic cutting model and used a ductile fracture criterion for node separation. However, the effects of temperature were excluded. Stenkowski et al.



[Strenkowski, 1985] used an implicit code “NIKE-2D®” and assumed fracture strain criterion to determine the separation of the predefined plane near the tool cutting edge. All of these early FEM models for metal cutting assumed perfectly sharp tool.

In the 1990s, automatic remeshing methods were developed to allow FEM cutting models to consider the tool edge geometry [Sekhon, 1993; Marusich, 1995; Ceretti, 1996]. These remeshing methods use fairly similar procedures, which start by detecting mesh distortion, dividing the contact boundary, adding up suitable internal nodes and then interpolating stress and strain data for the new mesh. Marusich [Marusich, 1995] developed a FEM cutting model using six-node quadratic triangular elements, based on dynamic Lagrangian formulation. His model was later transformed into an explicit FEM code called “Third Wave AdvantEdge™” [thirdwavesys.com]. Ceretti [Ceretti, 1996] used an early version of a commercial implicit FEM code “DEFORM-2D™” [deform.com]. This code uses four-node quadrilateral elements and is based on static Lagrangian formulation. Today, both DEFORM-2D™ and Third Wave AdvantEdge™ codes are commonly used by researchers and industry. Their simulation results are widely discussed in the literature. A number of researchers pointed out that after repetitive remeshing the errors may accumulate in the Lagrangian approach. Some researchers proposed the cutting models using Arbitrary Lagrangian-Eulerian (ALE) formulation to simulate steady state cutting [Jyot, 1998; Movahhedy, 2000].

Applications of FEM models for machining can be divided into six groups: 1) tool edge design, 2) tool wear, 3) tool coating, 4) chip flow, 5) burr formation and 6) residual stress and surface integrity.

Tool design can be improved by prediction of tool stresses and tool temperature. A study of tool edge design using FEM in [Shatla, 1999] shows that

tool edge radius has a small effect on cutting forces but influences chip flow direction, tool stresses and surface finish. Modeling of tool wear has been studied only recently using FEM by incorporating tool wear data from experiments [Yen, 2002]. Modeling tool wear using FEM has advantages over conventional statistical approach because it requires less experimental effort and it provides useful information such as normal tool stress and tool temperature. These variables can approximately determine how cutting parameters affect tool life and tool performance. However, FEM simulation cannot provide exact geometric prediction of tool wear at this moment.

A vast majority of cutting tools and inserts today are coated in order to increase the tool life. Several experimental studies have analyzed the effects of coatings with respect to their thermal barrier and low friction properties. Few recent attempts have been studied using FEM modeling [Yen, 2003].

Several studies have been conducted using FEM for modeling serrated chip, chip curling, chip breakage, and the 3D chip flow [Usui, 1982; Ceretti, 1996, Ng, 2002]. Modeling burr formation using FEM was initiated by Dornfeld and his associates [Park, 2000]. However, this initial work was limited by the assumption of a sharp tool and a need of element-separation criterion. The predictions of residual stresses and surface integrity are significant to access the fatigue life and the performance of machined components. A number of researchers have attempted to use FEM simulation to predict and obtain desirable residual stresses due to machining [Liu, 2000; Ramesh, 2002].

### **3.3. Determination of Flow Stress Material Properties for High Strain Rates**

A literature review of this section will cover the available experimental methods to determine flow stress property at high strain rates and the common

constitutive equations that are used to represent the flow stress data at high strain rates.

### ***3.3.1. Experimental Methods to Determine Flow Stress at High Strain Rates***

The material property for metal cutting has been obtained mainly using five methods: (1) high-speed compression tests, (2) Split Hopkinson's Pressure Bar (SHPB) tests, (3) practical machining tests, (4) integration of conventional tests at low strain rates and machining tests, and (5) inverse analysis using FEA technique.

In high-speed compression tests [Oyane, 1967; Oxley, 1989], a compressed air pushes a punch to compress a specimen at a very high speed. The test specimen can be preheated in the furnace before the tests for obtaining material flow stress at elevated temperatures. However, maximum strain rate for this test is limited to about  $450 \text{ s}^{-1}$ . The heating rate in high-speed compression test is much slower than that in machining process and thus potentially causes anneal softening and/or age hardening of the sample. However, no such effects have been observed in practical machining [Shirakashi, 1983].

Split Hopkinson's Pressure Bar (SHPB) technique was introduced in the early 20th century and has been further developed to study material behavior (i.e. deformation, mechanical properties and fracture) at high deformation rates [Hopkinson, 1905; Kolsky, 1949]. Later the SHPB test was adopted to determine the flow stress properties for machining processes [Shirakashi, 1983, Maekawa, 1983], as shown in Figure 3.4. Compared with high-speed compression tests, SHPB technique provides higher punch speed by the use of high-pressure air gun and faster heating rate by an induction coil. With these improvements,

anneal softening and age hardening can be prevented, and the flow stress data at high strain rates up to  $2,000 \text{ s}^{-1}$  can be obtained [Shirakashi, 1983]. Other applications of SHPB technique are performing high speed tension and torsion tests instead of compression tests. The procedures of tension and torsion tests are described in [Johnson, 1985] and [Eleiche, 1983] respectively. The strain and strain rate ranges in tension tests are typically lower than those obtainable in compression tests. Strains are up to 0.5 and strain rates are up to  $500 \text{ s}^{-1}$ . For torsion tests, the strain can be higher than 1, and strain rate can go up to more than  $5000 \text{ s}^{-1}$ . By modifying the sample geometry and testing in shearing mode, it is possible to achieve strain rates up to  $10^4 \text{ s}^{-1}$  [Treppman, 2001; El-Magd, 1999].

However, strain-rate values obtained from SHPB tests are still lower than those reached in high speed machining (up to  $10^6 \text{ s}^{-1}$ ). Moreover, SHPB tests can be costly and take considerable effort to obtain the data that are applicable in a wide range of strains and strain rates.

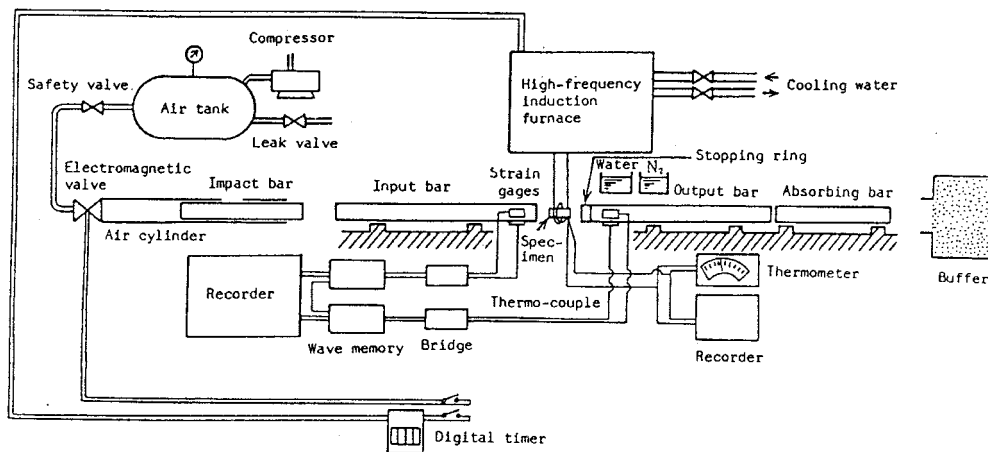


Figure 3.4: Split Hopkinson's pressure bar, for impact compression tests [Shirakashi; 1983]

Various research groups have proposed to use machining tests to determine the flow stress data. Attempts were made to approximate the stress, strain, strain rate and temperature conditions that truly exist in machining. Analytical and/or empirical models were used to convert experimental data (i.e. cutting forces, thrust forces and chip geometry) into average stresses, strains, strain rates and temperatures of the plastic deformation zone in cutting, [Mathew, 1993; Lei, 1999; Kopac, 2001]. Shatla [Shatla, 2001] introduced the inverse mapping method to indirectly determine the flow stress data by using Oxley's machining theory [Oxley, 1989] and a minimization algorithm. Concept of his method is to minimize the error between the experimental forces (cutting and thrust forces) and the predicted forces from iterated flow stress parameters. Shatla's procedure requires relatively little experimental effort, but is not able to generate a unique solution in all investigated cases. This method needs more computational robustness that can provide a unique solution.

In determining the flow stress data by machining tests, the reliability of the obtained flow stress data depends on the analytical models and assumptions employed to determine average stress and strain data in cutting. At the present, machining tests can provide only approximate flow stress data for hard metals that generate serrated chip formation since all available theoretical models still assume a continuous (non-serrated) chip.

Extrapolation of data from the tests conducted at various strain rate ranges have been suggested by some researchers [Treppman, 2001; Guo, 2002; Stevenson, 1997; Meyer, 1984]. The flow stress data obtained at low and high strain rates were fitted and represented by one or several flow stress equations. Thus, these obtained equations could be used to represent the flow stress for a wide range of strain rates. For example, tensile tests were conducted in a servo-hydraulic press to obtain the flow stress at the strain rates of  $10^{-5}$  to  $1 \text{ s}^{-1}$ ,

combined with the data from impact pendulum tests for the strain rates of 1 to  $10^2 \text{ s}^{-1}$  [Meyer, 1984].

Inverse engineering method using FEA technique has been performed together with orthogonal turning tests to obtain the flow stress data [Kumar, 1997; Özel, 2000]. Kumar [Kumar, 1997] used the estimated flow stress data as input for FEM simulation of orthogonal cutting and modified the flow stress data until the predicted cutting forces agreed with experimental forces. The instantaneous flow stress data for each iteration was intuitionally selected by considering the difference between predicted force and experimental force. When the calculated and measured forces matched, the flow stress data is obtained. After Kumar, Özel [Özel, 2000] attempted to improve the flow stress determination method by changing both the flow stress data and the parameters used in the friction model until the predicted cutting force and thrust force were equal to those obtained from orthogonal turning experiments. This method, however, showed limit success due to non-unique solution of the problem and the fact that the flow stress solution is dependent on the FEM code.

### *3.3.2. Constitutive Equations Used to Represent the Flow Stress for Machining*

Different constitutive equations (or flow stress equations) have been employed to represent the flow stress data of materials. For metal cutting, such equations generally derive true stress as a function of true strain, strain rate and temperature. Constitutive equations, most commonly used for material modeling in machining, are discussed below.

### Power Law Equation

$$\sigma = C \varepsilon^n \dot{\varepsilon}^m, \quad \text{Equation 3.3}$$

where  $\sigma$  = True stress,  $C$  = Strength coefficient  
 $\varepsilon$  = True strain,  $n$  = Strain hardening  
 $\dot{\varepsilon}$  = Strain rate,  $m$  = Strain rate hardening

The coefficients  $C$ ,  $n$  and  $m$  are considered as functions of temperatures. For the tested data at high strain rates, a power law equation can have a reference strain rate ( $\dot{\varepsilon}_0$ ) as a denominator of the strain rate term. A reference strain rate can be selected according to testing strain rate of particular experiments (e.g.  $\dot{\varepsilon}_0 = 1000 \text{ s}^{-1}$  for SHPB tests [Shirakashi, 1983]). The power law equation has been commonly employed for representing the flow stress of various materials (e.g. steels and titanium alloys) from quasi-static and room temperature (from conventional tensile and compression tests) up to the data at high strain rates and high temperatures (from SHPB tests).

### Johnson & Cook's Equation

$$\sigma = (A + B \varepsilon^n) (1 + C \ln \dot{\varepsilon}) (1 - T^{*m}), \quad \text{Equation 3.4}$$

where  $T^* = (T - T_{room}) / (T_{melt} - T_{room})$

$A$ ,  $B$ ,  $C$ ,  $n$  and  $m$  are constants

Johnson and Cook [Johnson, 1983] established a constitutive equation, Equation 3.4, in a simple form. This equation consists of five constant coefficients, for representing material behavior at high deformation rate. The equation has been widely employed for both ferrous and nonferrous materials, and mostly for fitting the flow stress data from SHPB tests. No elastic range is considered since plastic deformation generally dominates in forming at high

deformation rate. While this equation is relatively simple, it may be valid only within certain ranges of strain rates and temperatures.

### Zerilli & Armstrong's Equation

$$\sigma = C_0 + C_1 \exp(-C_3 T + C_4 T \ln \dot{\epsilon}) + C_5 \epsilon^n, \quad \text{for BCC material} \quad \text{Equation 3.5}$$

$$\sigma = C_0 + C_2 \epsilon^{1/2} \exp(-C_3 T + C_4 T \ln \dot{\epsilon}), \quad \text{for FCC material} \quad \text{Equation 3.6}$$

where  $C_1, C_2, C_3, C_4$  and  $C_5$  are constants

$T$  = absolute temperature,

Zerilli and Armstrong [Zerilli, 1987] established a dislocation-mechanics-based constitutive equation. They distinguished two equations based on types of crystal structures of the materials. For body-centered cubic (BCC) material, strain hardening is modeled independently from temperature and strain rate influence. For face-centered cubic (FCC) material, the effects of thermal softening and strain-rate hardening on the flow stress increase with increasing strain hardening. This model was shown to represent well the flow stress data of Armco iron, Copper and Aluminum [Zerilli, 1987].

### Macgregor's Equation

$$\begin{aligned} T_{\text{mod}} &= T(1 - \nu \ln(\dot{\epsilon}/\dot{\epsilon}_0)) \\ \sigma &= C(T_{\text{mod}}) \epsilon^{n(T_{\text{mod}})} \end{aligned} \quad \text{Equation 3.7}$$

where  $T_{\text{mod}}$  = Velocity modified temperature

$\nu$  = Constant strain rate factor

$\dot{\epsilon}_0$  = Reference Strain rate

$n$  = Strain hardening in a function of  $T_{\text{mod}}$



Macgregor [Macgregor, 1946] correlated the effects of strain rate and temperature in one term, called velocity-modified temperature ( $T_{mod}$ ). This term represents the inverse effects of temperature and strain rate upon the flow stress, due to the fact that flow stress decreases with increasing temperature and decreasing strain rate. Strength coefficient and strain hardening in a power law equation are modeled as functions of this velocity-modified temperature. Macgregor's equation has been applied for low to medium carbon steels [Oxley, 1989] and Al-alloys [Kristyanto, 2002]. Functions of velocity-modified temperatures can be exponential or polynomial.

### Marusich's Equation

$$\begin{aligned} \left(1 + \frac{\dot{\varepsilon}^p}{\dot{\varepsilon}_0^p}\right) &= \left(\frac{\bar{\sigma}}{g(\varepsilon^p)}\right)^{m_1}, \quad \text{if } \dot{\varepsilon}^p \leq \dot{\varepsilon}_t \\ \left(1 + \frac{\dot{\varepsilon}^p}{\dot{\varepsilon}_0^p}\right) \left(1 + \frac{\dot{\varepsilon}_t}{\dot{\varepsilon}_0^p}\right)^{m_2/m_1-1} &= \left(\frac{\bar{\sigma}}{g(\varepsilon^p)}\right)^{m_1}, \quad \text{if } \dot{\varepsilon}^p > \dot{\varepsilon}_t \end{aligned} \quad \text{Equation 3.8}$$

$$g(\varepsilon^p) = [1 - \alpha(T - T_0)]\sigma_0 \left(1 + \frac{\varepsilon^p}{\varepsilon_0^p}\right)^{1/n}$$

where $\bar{\sigma}$ = the effective stress	$m_1$ = low strain rate exponent
$g$ = flow stress at static strain rate	$m_2$ = high strain rate exponent
$\dot{\varepsilon}_0^p$ = a reference plastic strain rate	$\alpha$ = softening coefficient
$\dot{\varepsilon}_t$ = the threshold strain rate	$T$ = current temperature
$\varepsilon_0^p$ = a reference plastic strain	$T_0$ = a reference temperature
$\varepsilon^p$ = plastic strain	$\sigma_0$ = the yield stress at $T_0$
$n$ = strain hardening exponent	

Marusich [Marusich, 1995] defined strain rate hardening in a piecewise function in order to take account of flow stress at low and high strain rate ranges

while maintaining continuity of the flow stress. The linear relation expressing the effect of temperature can be replaced with a polynomial relation for obtaining more reliable data. Values of the flow stress parameters can be determined by hot compression tests for the strain and temperature factors. Inverse approximation from the simulation results may be used for determining strain rate hardening factors. The equation has been used for various metals (e.g. steels, cast iron, Al-alloys and Ti-alloys).

Other than five constitutive equations presented above, different equations used for different testing ranges can be integrated for representing flow stress data for a wide range of strain rates and temperatures. Treppman [Treppman, 2001] modeled a piecewise constitutive equation of AISI 1045 steel by representing the data in three states of deformation; (1) a power law equation for low strain rates and temperatures, (2) another power law equation with different coefficients for intermediate ranges of strain rates and temperatures, and (3) a Swift-linear damping equation for high strain rates. These equations fully represent the flow stress of one material. Considerable experimental efforts and calculations were necessary to obtain the numerous coefficients for the equations.

So far, establishing constitutive equations is still mostly based on curve fitting of the experimental stress-strain data and not on physical and chemical first principles. Modifications on materials such as the effects of inclusions and heat treatment require a whole new set of experiments to obtain the flow stress properties. In addition, during machining the material properties of machined surface can be altered due to accumulated strain by repeated cutting passes and phase transformation where the surface is repeatedly heated and cooled in a short time. Future research in material modeling for machining will need to consider these issues.

### 3.4. Modeling of Burr Formation

Burrs are undesirable protrusions of workpiece material beyond the edge of the workpiece. Burr formation during machining is a very significant industrial problem since it reduces the dimensional accuracy and increases the final product cost through the cost of deburring. There are numerous studies that classify burr formation mechanisms and types of burrs generated during machining. Gillespie [Gillespie, 1976] suggested four types of burrs, namely; Poisson, rollover, tear, and cut-off burrs. The Poisson burr is formed when material is bulged plastically in the direction perpendicular to the direction that it is compressed. The rollover burr is a chip that is bent at the edge of the workpiece rather than sheared (hence cut off) at the end of a cut. The tear burr is the result of material tearing loose from the workpiece. The less important cut-off burr is the result of workpiece separating from the raw material before material separation is complete. In face milling, burrs are formed in three-dimensions and can be classified according to the directions of cutting edge (i.e. major cutting edge, minor cutting edge, corner) and the burr locations, as presented in [Nakayama, 1987; Hashimura, 1999]. Based on where they occur, burrs can be defined as entrance burr, top burr, side burr and exit burr, as shown in Figure 3.5.

Step-by-step schematic of burr formation mechanisms for ductile and brittle materials is given in [Dornfeld, 2002] and shown in Figure 3.6. In the pre-initiation and the initiation stages, the elastic and then the plastic deformation zones move toward the workpiece edge. At the pivoting stage, a large deformation occurs at the pivoting point on the workpiece edge, and a negative shear zone develops, triggering the burr development.

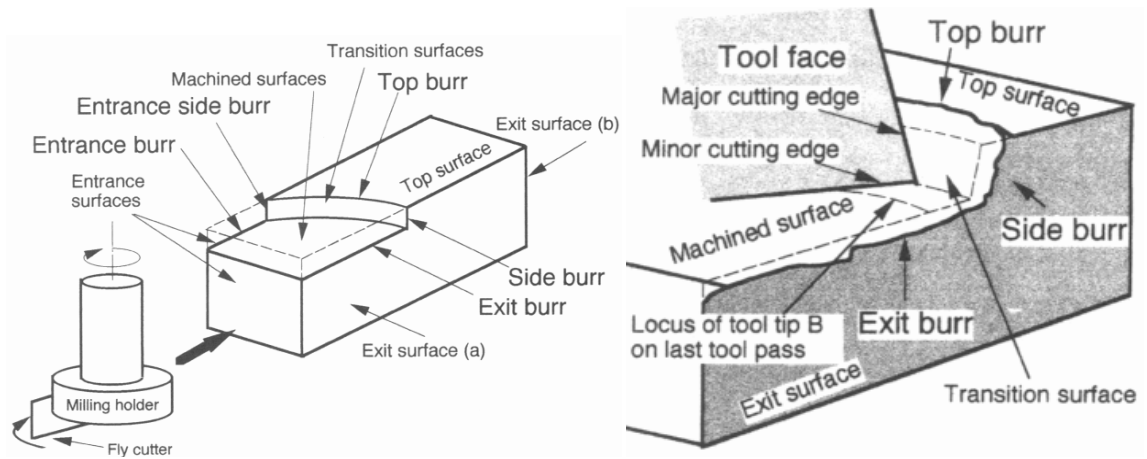


Figure 3.5: Tool motion and burr locations in face milling [Hashimura, 1999]

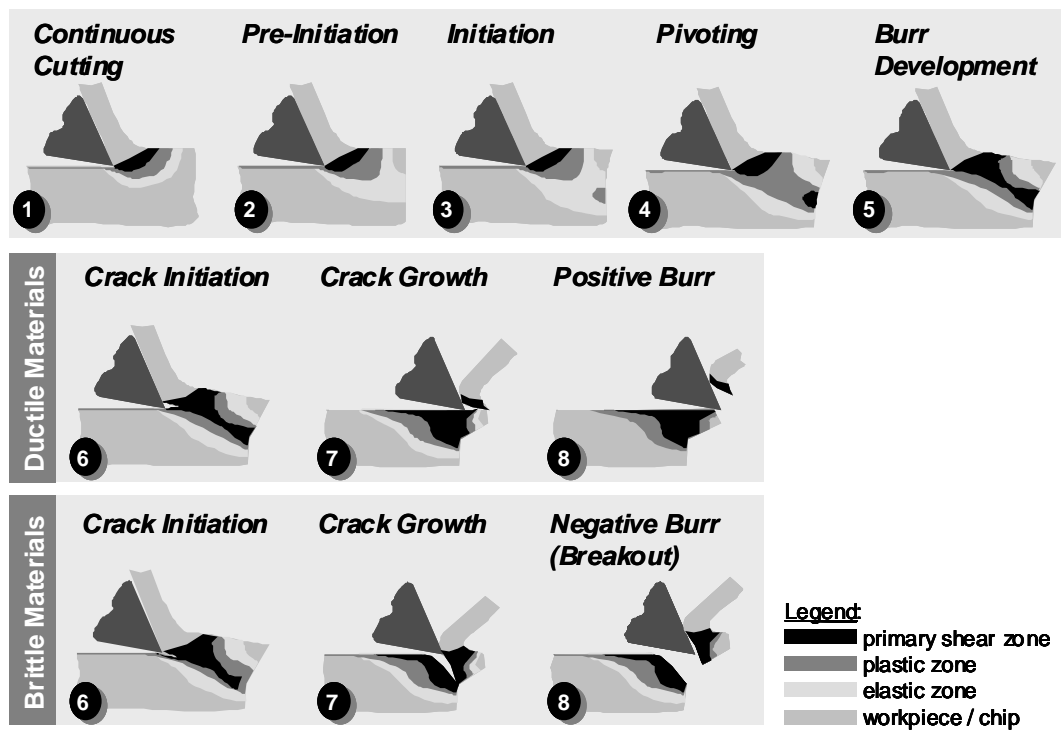


Figure 3.6: Schematic of burr formation mechanisms [Dornfeld, 2002]

In ductile materials, the crack develops and separates along the cutting line, forming a burr, whereas in brittle materials, the crack develops and separates along the negative shear zone, creating a breakout.

Cutting conditions, tool edge geometries, and cutter tool paths play a large role in burr formation. The results of an experimental study in shoulder face milling showed that a very low depth of cut (less than 0.6 mm) and a tool exit angle of about 90 degree could provide large exit burrs [Olvera, 1996]. The higher the feed rate, the larger were the exit burrs. In addition, neutral to slightly positive axial and radial rake angles were found to reduce burr formation. In [Hashimura, 1999], the exit and the side burrs on transition surfaces of a workpiece were analyzed for the effects of in-plane exit angle and tool radial rake angle. It was concluded that the exit order of the tool edges was a significant factor in determining the burr size and locations. Observations in practical milling operations indicate that burrs in face milling are influenced by tool wear and tool edge sharpness. As tool wear increases, the edge becomes dull and burr formation increases.

Modeling of burr formation using analytical models and FEM was studied extensively by Dornfeld and his associates. In [Ko, 1996], an analytical model for a material exhibiting fracture during burr formation was proposed by considering the fracture strain, obtained from McClintock's ductile fracture criterion. The predictions were found to be more accurate for less ductile materials (i.e. Al 6061-T6 and Al 2024-T4) while rollover burr in more ductile materials (i.e. copper and aluminum) could not be predicted. Burr formation and fracture models for 3D oblique cutting were proposed in [Ko, 1996a].

Park [Park, 2000; Park, 2000a] established an FEM model to simulate 2D orthogonal cutting to predict burr formation. The FEM code "ABAQUS/Explicit" was used. Tool and workpiece were assumed respectively as rigid and plastic

while the flow stress was a function of strain and temperature. During the simulation, several displacement constraints and values of ductile fracture criterion were arbitrarily assigned in order to produce a realistic burr geometry. In [Park, 2000a], a series of 2D FEM simulations were conducted to understand the influences of exit angle, rake angle and backup material on burr/breakout formation. A 3D FEM model of drilling was also established to understand burr formation and to prove that the use of backup material could reduce burrs, [Dornfeld, 1999]. However, this early FEM model was limited by the assumption of a sharp tool. Recent developments in FEM commercial codes with remeshing capability can now overcome this limiting assumption.

### **3.5. Inverse Analysis of Indentation Test**

An extensive literature review on inverse analysis of indentation test was provided by Morris [Morris, 2005]. A brief review of the past research relevant to the proposed studied is given in the following paragraphs.

In indentation test, an indenter, usually having conical or spherical shapes, approaches to contact with a sample surface and is gradually pushed to penetrated into the surface until reaching a certain depth or a certain applied load. Subsequently, the indenter unloads from the workpiece and returns to its original position. Indentation load ( $P$ ) as a function of penetration depth ( $h$ ) is usually measured during loading and unloading. Figure 3.7 shows a schematic of indentation testing, a stress-strain relationship of elastic-plastic material and a typical indentation load-depth ( $P-h$ ) curve.

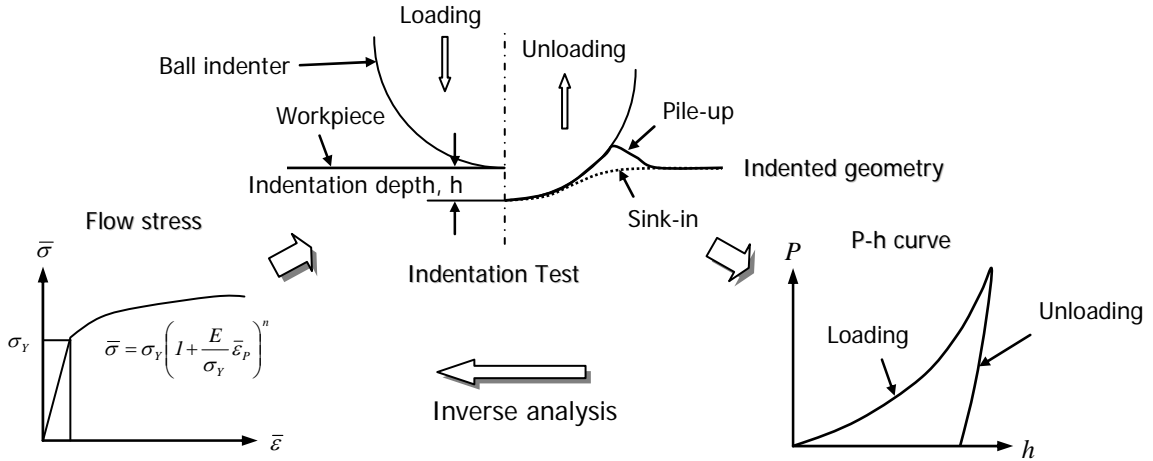


Figure 3.7: Concept of flow stress determination using indentation test and FEM inverse analysis.

Herbert [Herbert, 2001], Haggag [Haggag, 1993], Dao [Dao, 2001], and Chollacoop [Chollacoop, 2003] utilized the loading portion of indentation load-depth curve in order to determine the flow stress data of workpiece materials.

In [Dao, 2001], forward and inverse analyses were established using the conical indenter (also known as Berkovich's indenter) and the pyramidal indenter (also known as Vickers' indenter). From dimensional calculations and FEM simulations, analytical expressions were derived to relate indentation data to elastic-plastic properties, including Young's modulus, yield stress and strain hardening exponent of the flow stress equation. The results showed that the determined flow stress parameters were very sensitive to the variation of the experimental data. Further, it was found that representative plastic strains of conical and pyramid indenters could be identified while the loading curvature was responded independently to the strain-hardening exponent ( $n$ ). The estimated representative strains are 3.3% and 5.7% for conical and pyramidal

indenters, respectively. Figure 3.8 shows the representative strain of 3.3%, indicating that different flow stress curves that have the same true stress at the strain of 3.3% could predict the same load-depth curve of conical indentation. Thus, the inverse analysis using conical and pyramidal indenters raises the question of non-unique solution.

Later, Chollacoop and Dao [Chollacoop, 2003] further developed a methodology using dual indenters that have different tip apex angles. The representative strain was constructed as a function of tip angle. Comprehensive sensitivity analyses showed improvement of the result in dual indenters over single indenter. Experimental verification of the dual indenters were carried out using a 60° half-angle cone tip and a standard Berkovich indenter tip (with a 70.3° half-angle cone tip) for AA 6061-T6511 and AA 7075-T651 aluminum alloys.

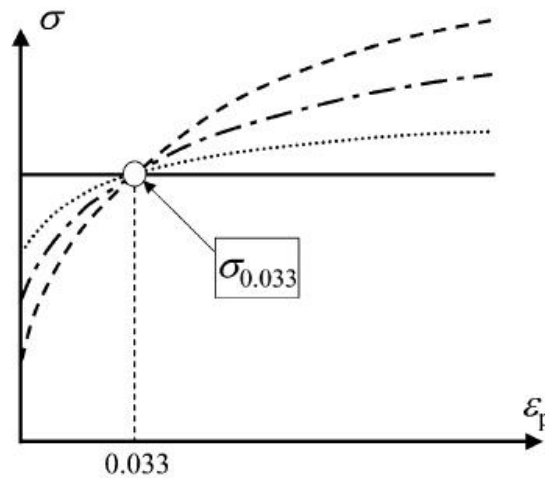


Figure 3.8: All true stress-true strain curves that have the same stress at a true plastic strain of 0.033 exhibit the same load-depth curve for the Berkovich indenter [Dao, 2001].



Meanwhile, the comprehensive work done on spherical indentation (also known as ball indentation) was presented in [Haggag, 1993]. The flow stress was determined by iteratively solving a series of equations derived analytically from plasticity and elasticity theories. The relationship between true plastic strain and the ratio of plastic indentation diameter to ball indenter diameter, " $d/D$ ", was defined. The data were fit by regression analysis to the power law flow stress ( $\sigma = K\varepsilon^n$ ) to obtain the values for the strength coefficient ( $K$ ) and the strain-hardening exponent ( $n$ ).

### **3.6. Experimental Studies and Modeling of Roller Burnishing**

Key research groups contributing to roller burnishing research include the WZL/RWTH, Aachen, Germany [Klocke, 1998; Röttger, 2002], Ecoroll Company [Ecoroll, 2001], TU Magdeburg [Emmer, 1992], Lambda Research [Prevéy, 2003], PMMC/University of Toledo [Luca, 2002], Menoufia University, Egypt [El-Axir, 2003], Jordan University of Science and Technology [Hassan, 1996; 1999; 2000].

Experimental studies from [Prevéy, 2000; 2000a; 2000b; 2001; 2003] showed that parts finished by roller burnishing process had longer fatigue life compared to conventional shot peening, for IN 718, Ti-6Al-4V, stainless steels and Aluminum 7075-T6. Similar observations were made for nonferrous materials [Hassan, 1996; 2000]. In [Klocke, 1998; Röttger, 2002], experiments on 100Cr6 (or AISI 52100) bearing steel showed that roller burnishing not only improved the surface roughness but also converted tensile residual stresses previously produced by hard turning into compressive residual stresses.

The process parameters of roller burnishing include 1) burnishing speed ( $V_b$ ), 2) burnishing feed rate ( $f_b$ ), 3) applied fluid pressure ( $P_b$ ) or normal force ( $F_b$ )

and 4) ball diameter ( $d_b$ ). Table 3.1 summarizes some of the experimental research conducted on the effects of roller burnishing parameters.

<b>Author</b>	<b>Parameters studied</b>	<b>Material / Condition</b>	<b>Tool</b>
[Bouزيد, 2004]	Feed ( $f_b$ ), force ( $F_b$ )	AISI 1042 steel (soft)	Spring-loaded
[El-Axir, 2000]	Speed ( $V_b$ ), force ( $F_b$ ), feed ( $f_b$ ), number of tool passes ( $n$ )	St-37 steel (soft)	Spring-loaded
[El-Khabeery, 2001]	Speed ( $V_b$ ), number of tool passes ( $n$ )	Aluminum 6061-T6 (soft & flat surface)	Spring-loaded
[Hassan, 1998]	Force ( $F_b$ ), number of tool passes ( $n$ )	Brass (soft)	Spring-loaded
[Hassan, 1996]	Speed ( $V_b$ ), force ( $F_b$ ), feed ( $f_b$ ), number of tool passes ( $n$ ), ball diameter ( $d_b$ )	Non ferrous metals (soft)	Spring-loaded
[Klocke, 1998]	Feed ( $f_b$ ), speed ( $V_b$ ), pressure ( $P_b$ )	100Cr6 (AISI 52100) Steel (Hardened)	Hydrostatic
[Luca, 2005]	Pressure ( $P_b$ ), feed ( $f_b$ )	Steel (Hardened)	Hydrostatic
[Némat, 2000]	Number of tool passes ( $n$ ), feed ( $f_b$ ), force ( $F_b$ ), burnishing speed ( $V_b$ )	Mild Steel and Aluminum (soft)	Spring-loaded
[Röttger, 2002]	Ball diameter ( $d_b$ ), pressure ( $P_b$ ), feed ( $f_b$ ), speed ( $V_b$ )	100Cr6 (AISI 52100) Steel (Hardened)	Hydrostatic

Table 3.1: Summary of various experimental studies on the effect of burnishing process parameters

In [Röttger, 2002; Klocke, 1998], 100Cr6 bearing steels (AISI 52100) were initially heat-treated for three different hardness levels (56, 59 & 62 HRC), hard-turned using CBN tools with different amount of flank wear and then roller burnished using a hydrostatic ball tool with different burnishing conditions. The following findings were drawn from Röttger's experimental study:

- Roller burnishing can reduce surface roughness considerably. The improvement of surface roughness is defined as  $VR_z$ , and is given below

$$VR_z = \frac{R_{z,ht} - R_{z,b}}{R_{z,ht}} \times 100\% \quad \text{Equation 3.9}$$

where  $VR_z$  = the percentage improvement of surface roughness

$R_{z,ht}$  = the average surface roughness depth after hard turning

$R_{z,b}$  = the average surface roughness depth after roller burnishing

$VR_z$  decreases with increasing initial surface microhardness and decreasing burnishing pressure. Larger tool diameters increase  $VR_z$ . The  $VR_z$  value tends to increase with increasing initial surface roughness from hard turning.

- Changes in burnishing speed over a wide range from 50 to 450 m/min result in the same surface roughness improvement. Beyond this range, the surface improvement was reduced due to dynamic effect of the machine tool. The effect of burnishing feed rate on surface improvement remains unchanged until a critical feed rate is exceeded.
- Roller burnishing increases the microhardness/strength of the surface. Burnishing pressures higher than 20 MPa provide an increase in surface hardness. In addition, lower initial hardness gains a higher

percentage increase of hardness after roller burnishing. An increase in ball diameter causes a small increase in the hardness but strong influence on the penetration depth.

- Compressive residual stresses in the surface layer generated by roller burnishing are insensitive to the initial state of residual stresses by hard turning, as shown in Figure 3.9. Although the initial stress behaviors are very different, due to the progression of tool wear, the resulting residual stress profiles after roller burnishing are nearly identical.
- Increases in burnishing pressure and ball diameter increase the magnitude of the maximum compressive residual stress and the depth of penetration. Increasing workpiece hardness however did not significantly change the stress behavior after roller burnishing.

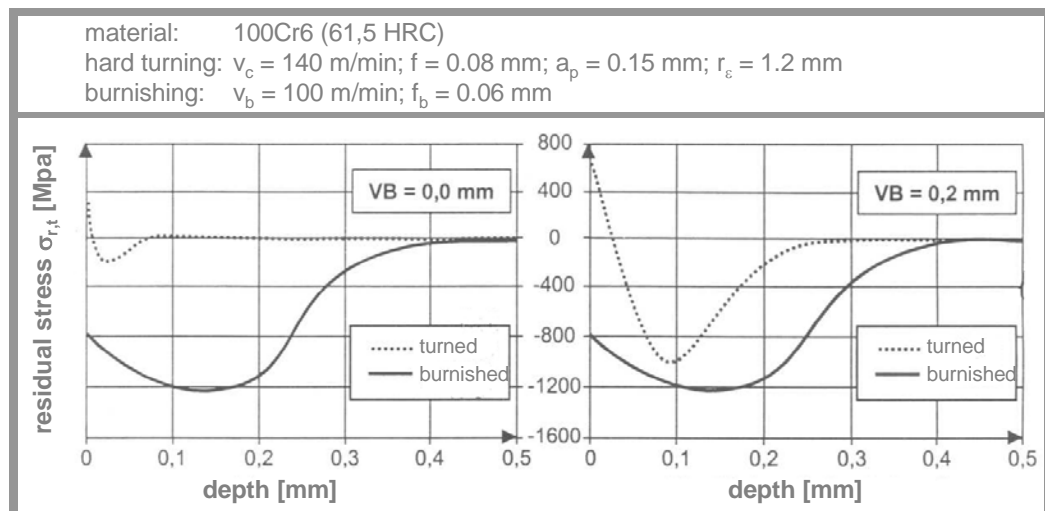


Figure 3.9: Result of tangential residual stresses after hard turning and after hard roller burnishing using the cutting inserts with two different flank wear widths [Röttger, 2002]

At Menoufia University (Egypt) and Jordan University, several studies on the effects of process parameters were conducted but with a spring-loaded burnishing tool [El-Axir, 2000; El-Khabeery, 2001; Hassan, 1996; 2000]. Due to a spring mechanism, burnishing force was controlled by tool positioning. The number of tool passes was considered. Additional findings to Röttger's study were that the surface finish was degraded at very low feed and at more than 3 tool passes, due to repeated plastic deformation and surface fatigue.

Röttger [Röttger, 2002] developed a 2D FEM model of roller burnishing using DEFORM-2D™. In Röttger's model, the ball (rigid, 6mm diameter) pressed down the workpiece surface (elasto-plastic) until the normal load reached the burnishing force that was obtained from the corresponding experiment. Subsequently, the ball was lifted up from the surface and shifted horizontally by a distance of burnishing feed. This process was then repeated for four cycles. The detailed sequence and predicted stress are shown in Figure 3.10.

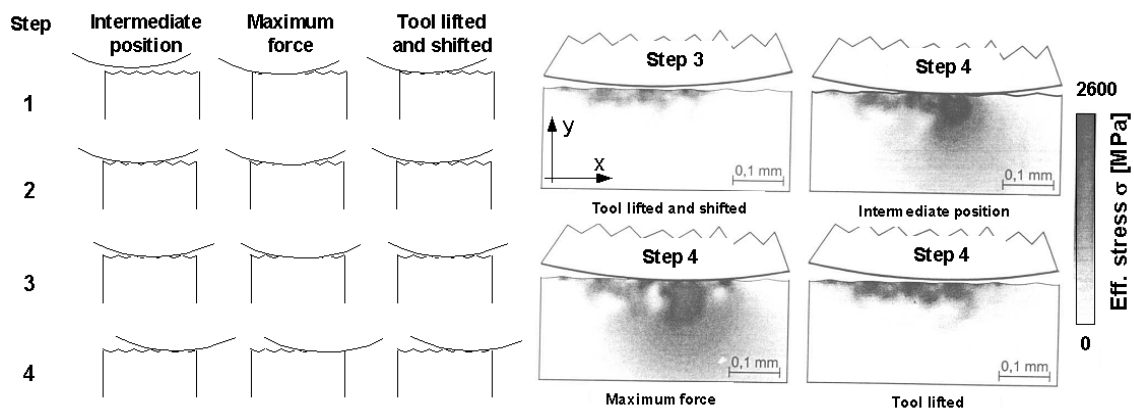


Figure 3.10: Simulation sequence for the 2-D FEM model of roller burnishing (left) and the predicted effective stress from FEM (right), in [Röttger, 2002]

Röttger model was later improved by Yen [Yen, 2004]. Major modifications include increase of simulation cycles, ball movement by displacement control, simulation time step corresponding to burnishing speed, validation of different bulk material models and an analysis for the effects of surface property variations (i.e. pre-strain and initial residual stress), as shown in Table 3.2.

	<b>Röttger's Model (2002)</b>	<b>Yen's Model (2004)</b>
# simulation cycles / length	4 cycles / 0.18 mm	> 6-10 cycles / 0.6 mm
Control method for tool movement	Force control	Force control / Displacement control
Duration of one cycle	2 seconds	~ 0.0003 second
Shape of loading curve	Linear	Second-order polynomial
Workpiece dimensions	1.95mm × 2.3mm	2mm × 4 mm
Bulk material model for the workpiece	[Röttger, 2002]	[Röttger, 2002] [Poulachon, 2001] & [ATP, 2002]-corrected
Variation of surface layer properties (initial strain)	Not considered (homogeneous)	Evaluated (heterogeneous)
Residual stress by cutting	Not considered	Evaluated
# elements between two roughness peaks	12 – 14	15 - 17
Surface geometry (p-p width, p-v height)	(0.18mm, 0.011mm)	(0.18mm, 0.011mm)
FEM code used	DEFORM-2D™ (v7.0)	DEFORM-2D™ (v7.2)

Table 3.2: Comparison of roller burnishing simulation settings between Röttger's original model [Röttger, 2002] and the refined model proposed in [Yen, 2004]

In addition to 2-D model, a complete 3-D FEM model for roller burnishing was also developed using DEFORM 3D™. In this model, the ball

translates toward the workpiece at the burnishing speed without rotation. The penetration depth was iteratively adjusted to maintain and match the burnishing force. Predicted results of the proposed 2-D and 3-D models were compared with the experimental results from [Röttger, 2002]. However, both Röttger's and Yen's models considered bulk flow stress property of the workpiece from compression tests in stead of the surface property. Therefore, the procedure to determine the flow stress property of the hard turned surface is important to develop a more reliable FEM simulation of roller burnishing.

## CHAPTER 4

### FLOW STRESS PROPERTIES FOR FEM SIMULATION OF MACHINING PROCESSES

This chapter describes a) the development of the procedures to determine flow stress through slot milling experiments, b) a sensitivity analysis on the effect of flow stress parameters in FEM simulation of orthogonal cutting, and c) the establishment of MAterial DAtabase for Machining Simulations (MADAMS).

#### **4.1. Flow Stress Determination through Slot Milling Experiments**

The inverse analysis of Oxley's mechanistic model [Oxley, 1989] and slot milling experimentation were developed in order to determine the material flow stress properties at machining conditions. The present method consists of minimizing the error between the predicted forces and chip flow with measured experimental data by adjusting the parameters of the flow stress equation. The procedure represents an approximation that can be applied in industry and used in FEM simulations of machining. The developed approach is an enhancement of previous work by Shatla [Shatla, 1999]. The major improvements to Shatla's approach include a) the measurement of plastic zone thickness ratios in both primary and secondary zones, b) the use a quick stop mechanism, c) expansion of the test conditions, d) modification of the constitutive equations and e)



modification of minimization function. The present approach provides increasing computational robustness and eliminates the non-unique solution problem encountered in Shatla's approach.

Non-unique solution in Shatla's approach can be explained in Figure 4.1. As three different sets of initial guesses of the flow stress parameters were tried out using the same experimental forces, three different flow stress equations were obtained in Figure 4.1. All three obtained flow stress equations were different but could predict the same cutting and thrust forces ( $F_c$  and  $F_t$ ) in slot milling. This problem was further investigated through the average stress/strain calculated in the plastic deformation zones. As can be seen in Figure 4.2, all stress, strain and temperature are the same for three different flow stress inputs except the strain rate in primary and secondary shear zones. This finding indicates that non-uniqueness can be solved by estimation of the strain rate. In cutting, strain rate can be determined from the flow velocity in shearing direction and the plastic zone thickness of the deformation zone. Since the flow velocity is known from the given cutting speed and theoretical calculation of the shear angle, only plastic zone thickness is required in the methodology to obtain a unique solution.

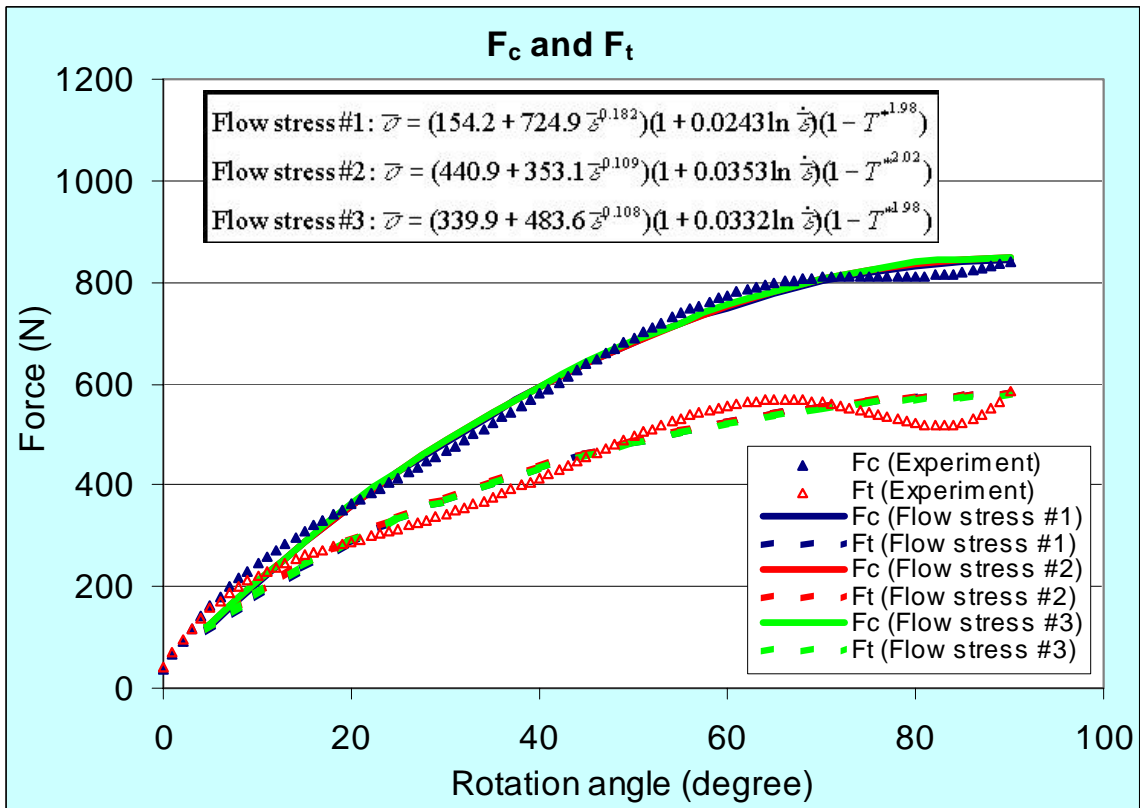


Figure 4.1: Force predictions using three different flow stress equation obtained from flow stress determination approach in [Shatla, 1999]

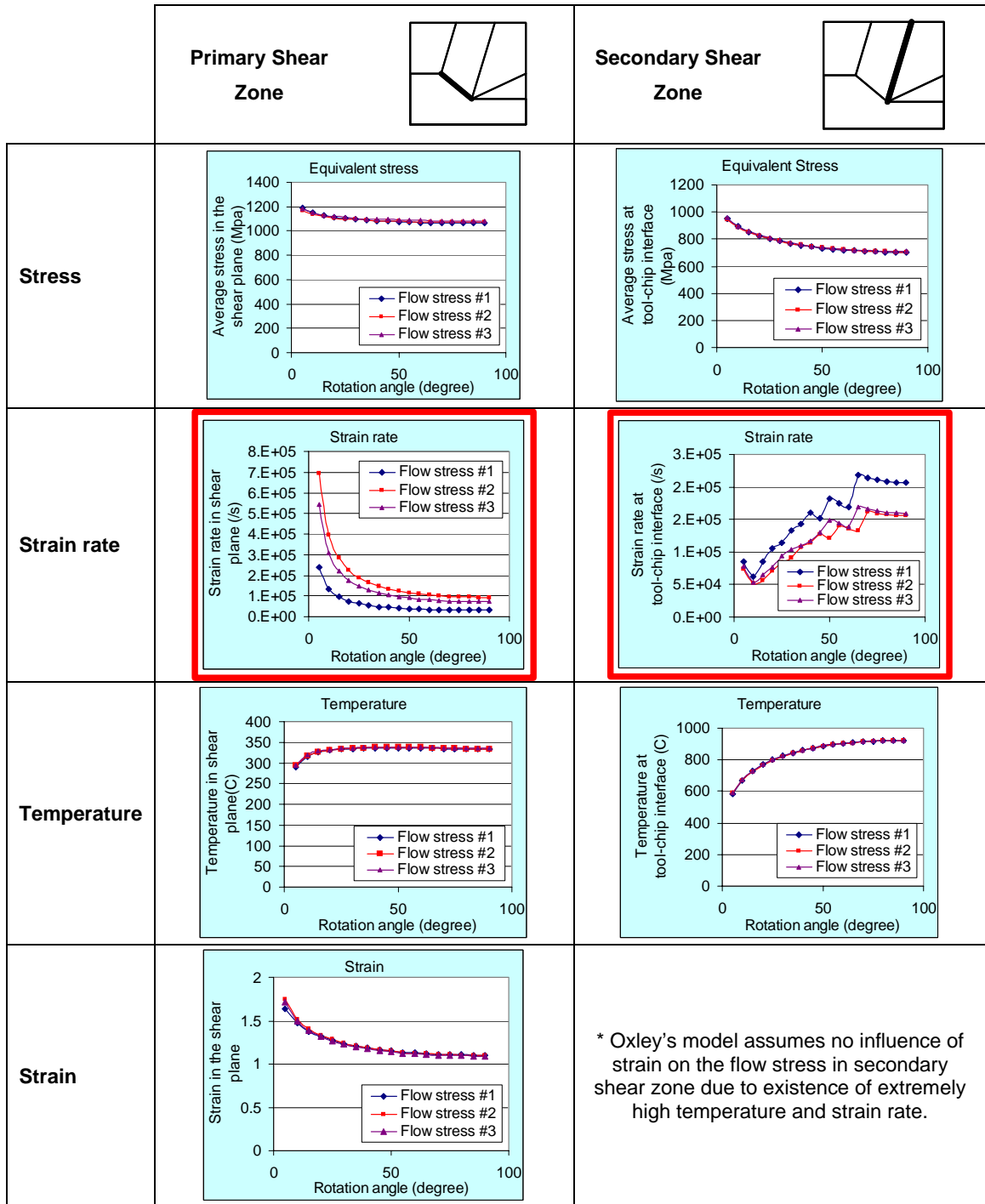


Figure 4.2: Predictions of stress, strain, strain rate and temperature in primary and secondary shear zones, using three different flow stress equations in Figure 4-1.

#### 4.1.1. *Inverse Analysis of Oxley's Machining Theory*

The present procedure consists of experimental and computational tasks. Experimental tasks deliver the actual measurements from orthogonal slot milling tests, which are used as input information for the program, called OXCUT. The program employs Oxley's machining theory to predict force, average temperature and other machining variables. The experimental data and the predictions are compared to determine the error. A minimization scheme iterates and reduces the error by automatically adjusting the flow stress parameters. The program stops when the total error is within a certain predefined tolerance. Figure 4.3 shows schematically the procedure used to determine the flow stress data.

The approach presented here has a number of limitations. These limitations come from the assumptions made in Oxley's theory [Oxley, 1989] as well as from experimental measurements. They are listed below.

- Tool edge is assumed to be sharp (very small edge radius).
- Chip formation is of continuous type (no serrations).
- The width of cut must be more than 10 times of the feed rate to satisfy the plane strain condition.
- No built-up-edge (BUE) appears on the tool.
- Tool wear must be extremely small (new edge of insert is used for each cutting test).
- Vibrations in the milling operation do not affect force data acquisition
- No chip breakage
- No excessive material along the side of the chip

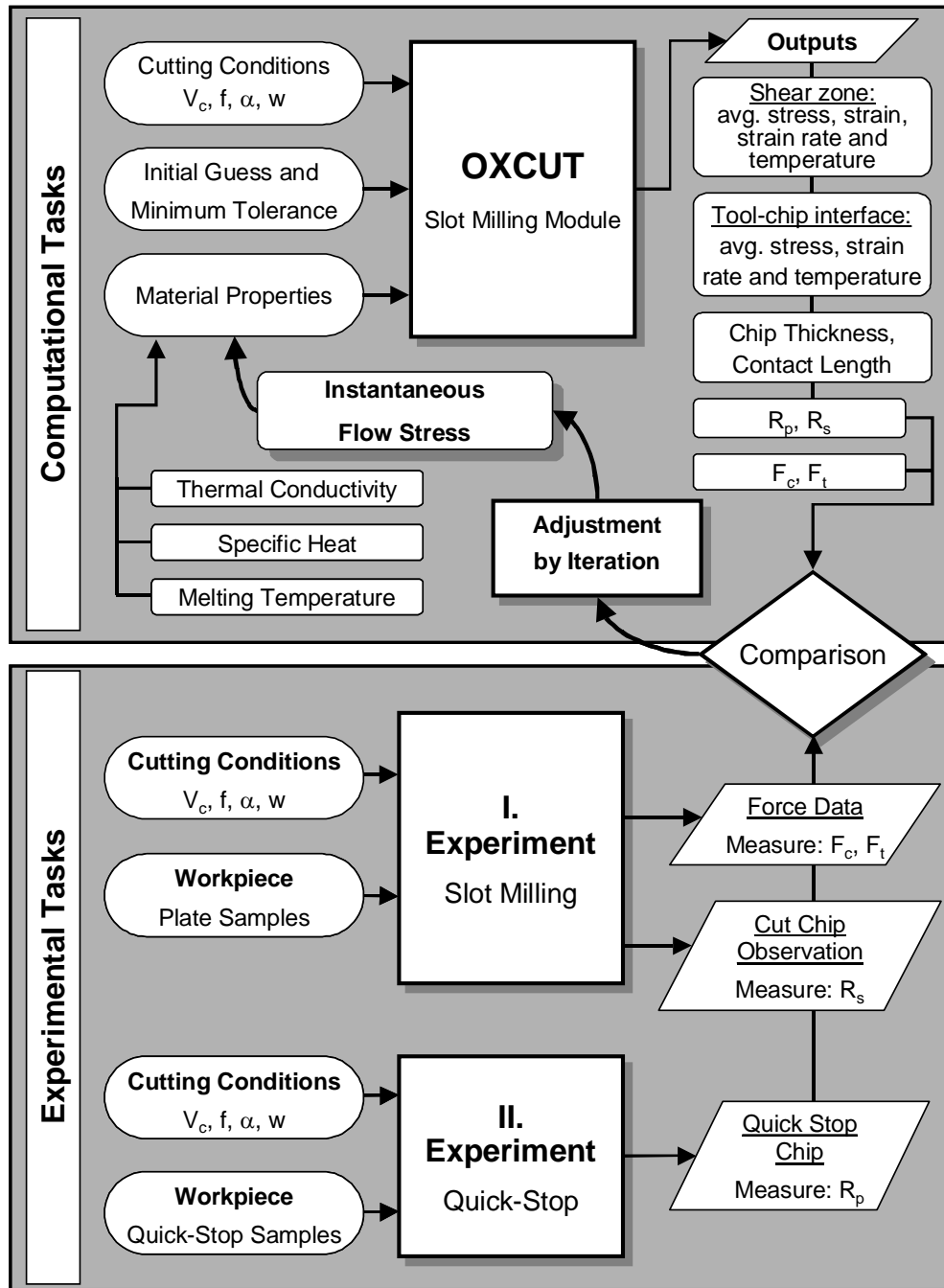


Figure 4.3: Simplified flow chart of the methodology used to determine flow stress using the orthogonal slot milling test.

#### 4.1.2. *Experimental Tasks*

Experimental work can be divided into 2 subtasks: 1) Slot milling tests and 2) Quick-stop slot milling tests. Both experimental subtasks can be conducted on the same CNC milling center and are described below.

##### 4.1.2.1. *Slot Milling Experiments*

The slot milling test is illustrated in Figure 4.4. The process represents orthogonal cutting with variation in uncut chip thicknesses. In slot milling, orthogonal cutting assumption can be satisfied by setting the axial rake angle and the lead angle of the milling tool close to zero and preparing the thickness of the plate sample smaller than the length of tool major cutting edge. During milling, workpiece touches the tool only along the major cutting edge. The uncut chip thickness in orthogonal slot milling process varies over the tool rotation angle ( $\theta_r$ ) and can be calculated from the feed rate ( $f_z$ ). A good approximation of the effective uncut chip thickness is given in Equation 4.1.

$$t_u = f_z \sin \theta_r \quad \text{Equation 4.1}$$

where  $t_u$  = Uncut chip thickness (mm)

$f_z$  = Feed rate in slot milling (mm/tooth)

$\theta_r$  = Tool rotation angle (degree)

From slot milling tests, force measurements are performed using the Kistler 9257A dynamometer to acquire force data in X and Y directions, as shown in Figure 4.4. These forces are later converted to cutting force ( $F_c$ ) and thrust force ( $F_t$ ) contours over incremental tool rotation angles, using Equation 4.2.

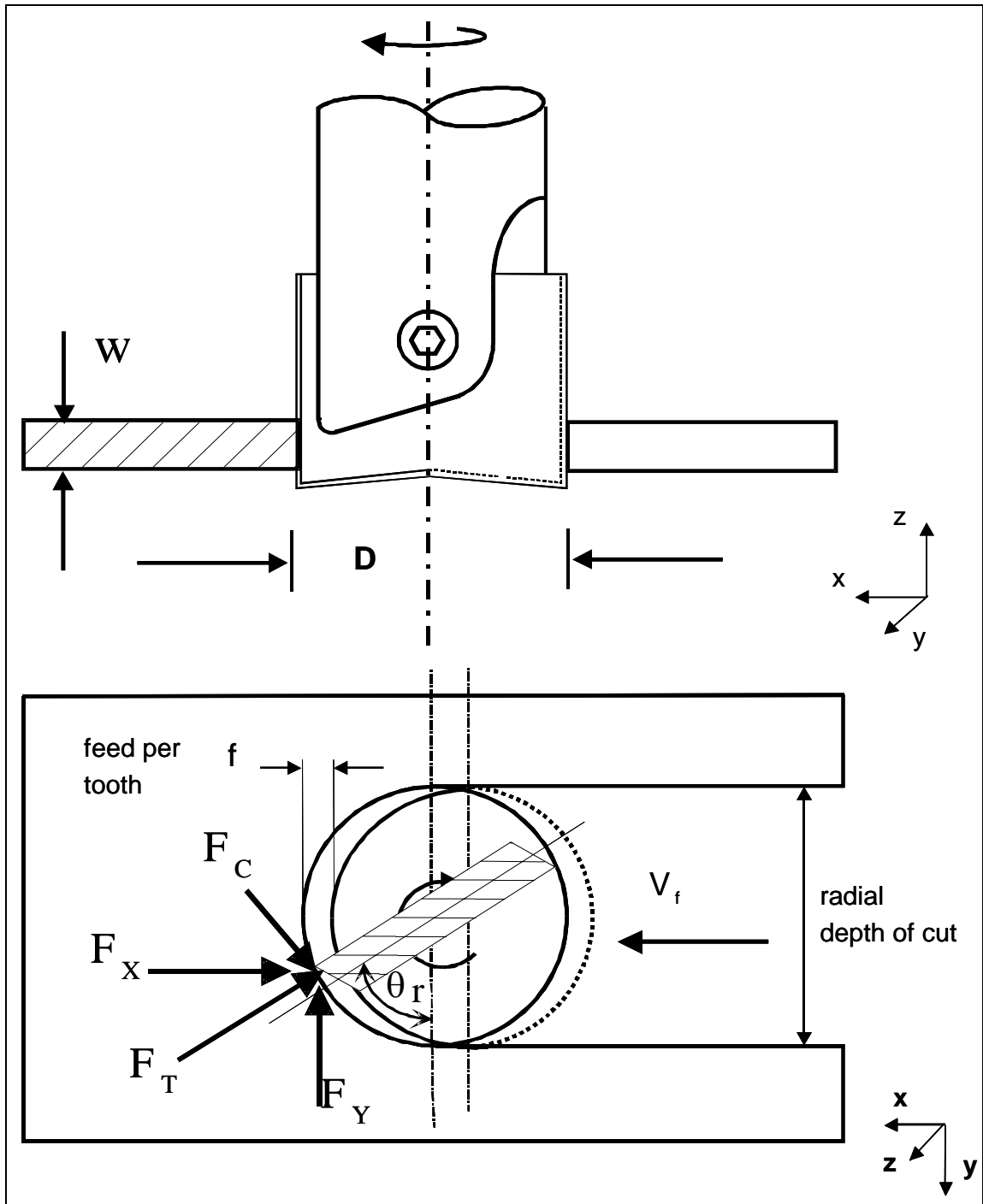


Figure 4.4: Schematic of the orthogonal slot milling tests

$$\begin{aligned}
 F_c &= F_x \cos \theta_r + F_y \sin \theta_r \\
 F_t &= F_x \sin \theta_r - F_y \cos \theta_r
 \end{aligned}
 \tag{Equation 4.2}$$

where

- $F_x$  = Force in x-direction (N)
- $F_y$  = Force in y-direction (N)
- $F_c$  = Cutting force (N)
- $F_t$  = Thrust force (N)
- $\theta_r$  = Tool rotation angle (degree)

The experimental setup used for force measurements in slot milling tests is shown in Figure 4.5. The dynamometer (#1) is attached with four clamps to the tombstone of the CNC high speed milling center. The adapter (#2) is screwed to the dynamometer and used for holding the workpiece (#3). The workpiece is fixed with six screws to the adapter plate. The coaxial cables for transmission of the electrical signals from the dynamometer to the data acquisition system are displayed in the left side of the picture.

The following paragraphs describe the major components of the experimental setup.

A dynamometer “Kistler type 9257A” (#1 in Figure 4.5 and Figure 4.6) mainly consists of four three-component force sensors fitted under high preload between a base plate and a top plate. Each sensor contains three pairs of quartz plates, one sensitive to pressure in the Z direction and the other two responding to shear in the X and Y directions respectively. This dynamometer was mounted to the tombstone. Three co-axial cables were connect to the charge amplifier (Kistler type 5001) of the force platform and then a connector block (National Instruments, BNC-2110) and finally attached to a PC data acquisition system (National Instruments, Labview 5.1.1).



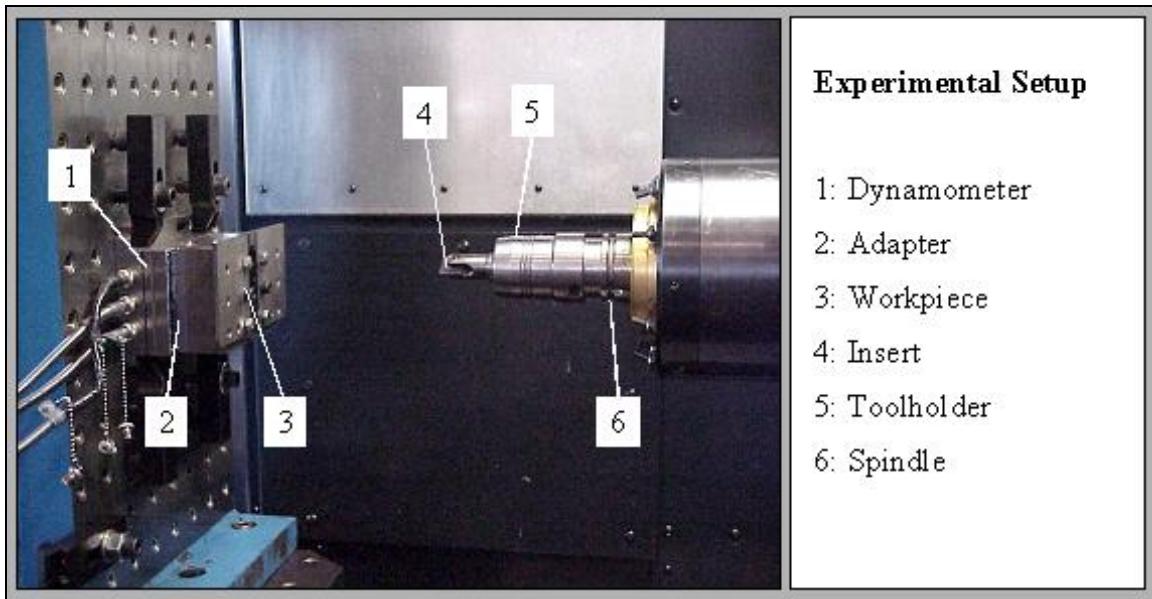


Figure 4.5: Experimental setup of the slot milling process

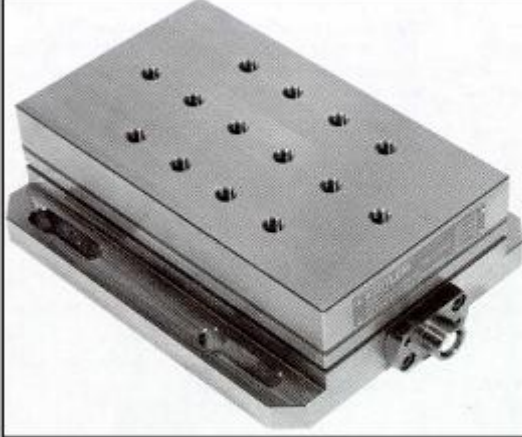
<b>Dynamometer:</b>	
	<b>Measuring Range:</b> $F_x$ : 0...5000 N $F_y$ : 0...5000 N $F_z$ : 0...10000 N
	<b>Sensitivity:</b> $F_x$ : -7.84 pC/N $F_y$ : -7.91 pC/N $F_z$ : -3.74 pC/N
	<b>Linearity:</b> $F_x, F_y, F_z$ : $\leq \pm 0.3\%$ FSO
	<b>Hysteresis:</b> $\leq 0.5\%$ FSO
	<b>Cross Talk:</b> $\leq \pm 0.2\%$
<b>Type:</b> Kistler Type 9257A <b>Serial Number:</b> 95368	<b>Natural Frequency:</b> $f_0(x,y) \approx 2.3$ kHz

Figure 4.6: Kistler dynamometer

The adapter plate (#2 in Figure 4.5 and Figure 4.7) acts as a buffer to protect the dynamometer from being damaged by the cutting tool. It consists of a metal block with a slot and several holes. The slot allows shifting the cutting tool in Z direction so that a sharp and unworn cutting edge can be used for the next experiment.

The workpiece (#3 in Figure 4.5 and Figure 4.8) is a rectangular plate, 100 x 100 mm. Six holes are drilled into the plate for attaching to the adapter with screws. Part of the plate, which is used for the slot milling experiments, should have a thickness of at least 10 times the feed rate. The thickness is chosen based on type of workpiece material, from 1 to 3 mm.

Cutting tool in this context refer to an assembly of tool insert and tool holder (respectively #4 and #5 in Figure 4.5). Two different cutting tools were used. The first tool, manufactured by DAPRA Corp., had a negative rake angle of  $-9.06^\circ$ , Figure 4.9. Here, the insert placed into the tool holder allows cutting with two cutting edges. The diameter of the tool is 25.4 mm. The lead angle and the axial rake angle are set to zero. The second tool, provided by Ingersoll-Cutting Tools, had a positive rake angle of  $2.8^\circ$ , Figure 4.10. Only one cutting edge is in use during the cutting process. This tool also has a diameter of 25.4 mm. The lead angle is set to zero. The axial rake angle of the tool is positive with  $4.42^\circ$  and therefore a near orthogonal cut is achieved. Tool insert material was chosen to be either uncoated cemented carbide (WC) or WC insert with TiAlN-coating, depending on workpiece material. If high tool wear was observed, an insert with TiAlN-coating was used.

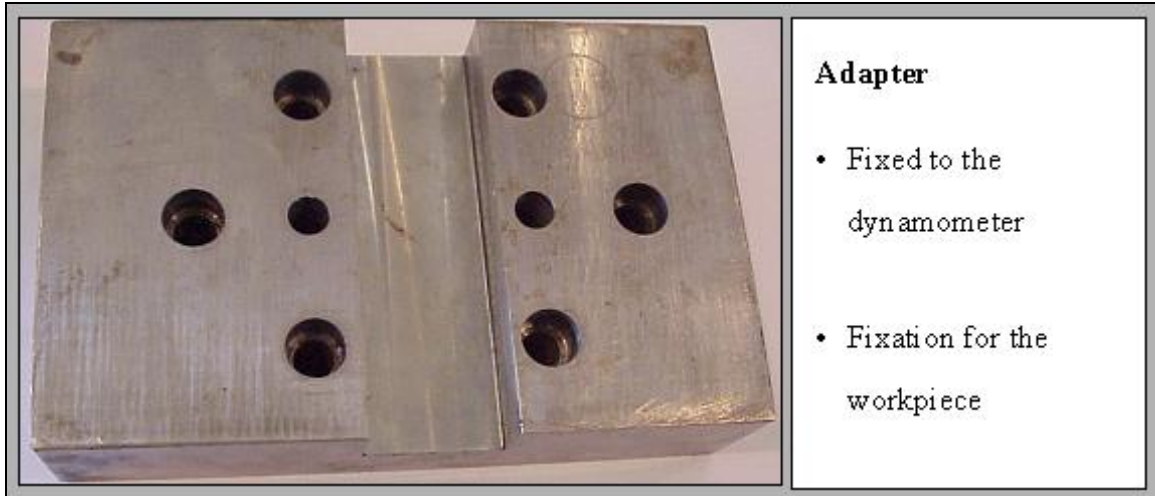


Figure 4.7: Adapter plate

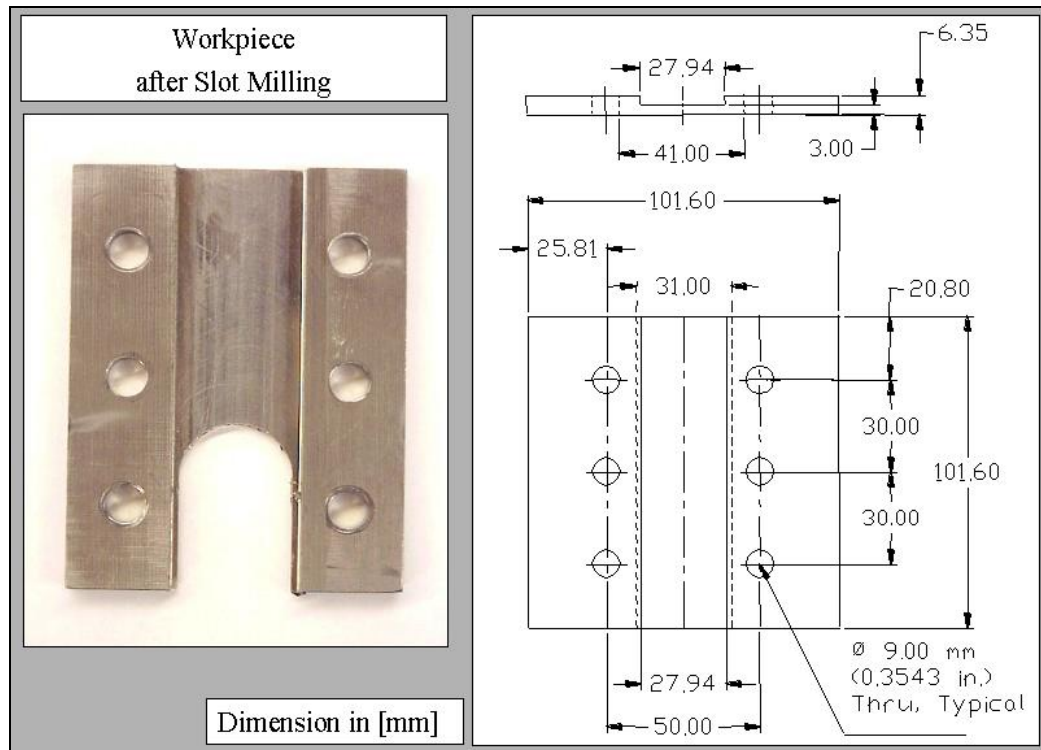


Figure 4.8: Plate sample for slot milling test

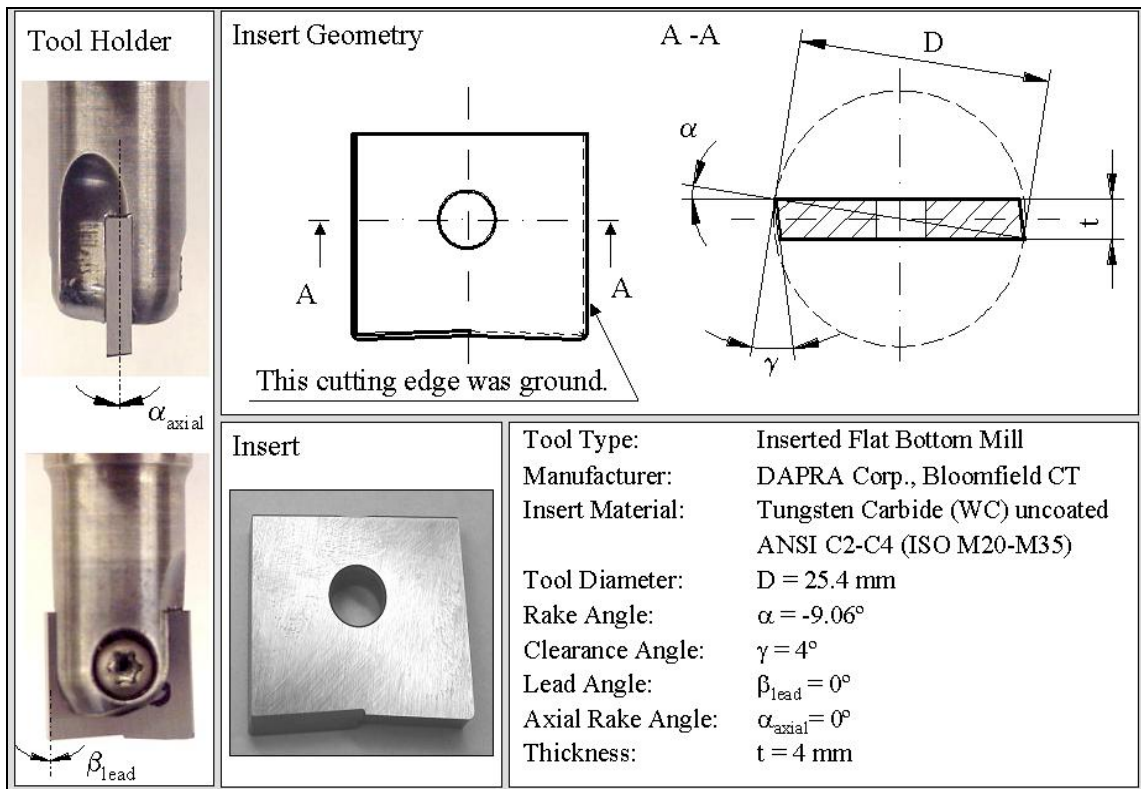


Figure 4.9: Cutting tool with negative rake angle

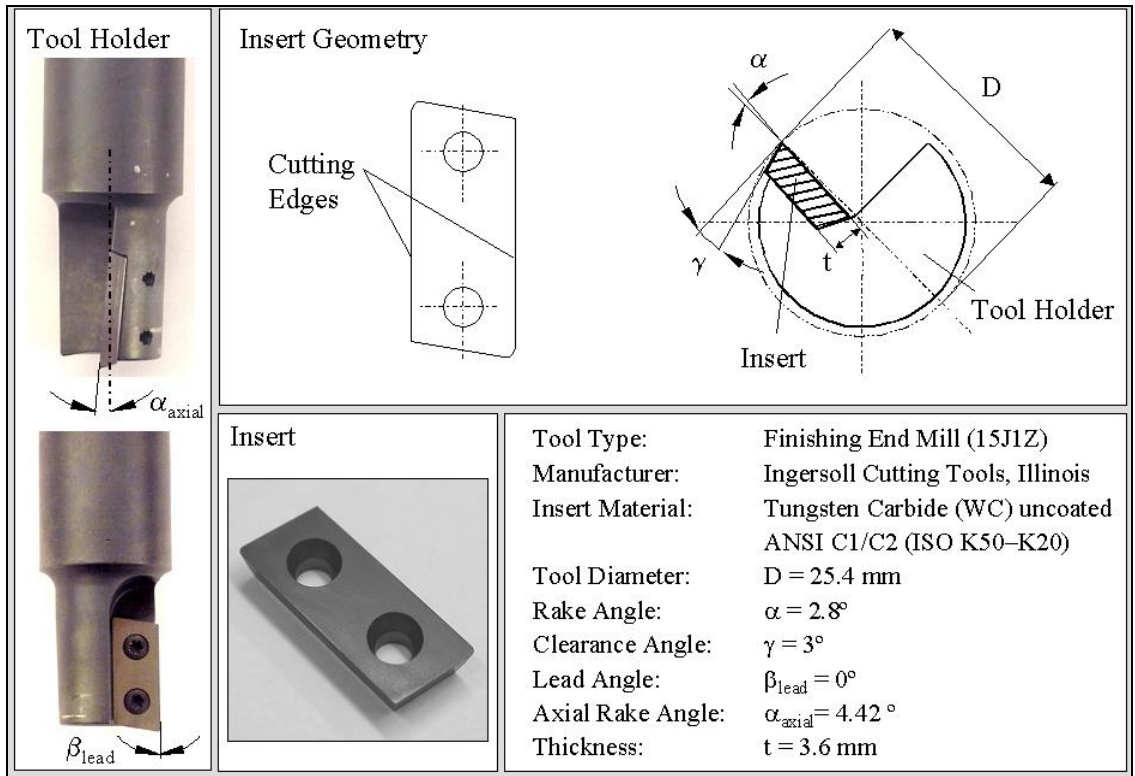


Figure 4.10: Cutting tool with positive rake angle.

In addition to force measurements, the cut chips from slot milling are collected and processed through metallographic preparation. The chips are observed with a high-magnification optical microscope to measure the deformed plastic zone thicknesses in the secondary shear zone and the cut chip thicknesses. The ratios of the deformed plastic zone thickness to the cut chip thickness ( $R_s$ ) are calculated for use as inputs for OXCUT. Thus, the slot milling experiments deliver three important inputs for the OXCUT, which are the cutting force ( $F_c$ ), the thrust force ( $F_t$ ) and secondary plastic shear zone thickness ratio ( $R_s$ ).

#### 4.1.2.2. *Quick-Stop Slot Milling Tests*

Quick-stop slot milling tests are conducted using special designed quick-stop plate samples (Figure 4.11). The tool motion allows the chip to accelerate and break itself. The quick-stop plate is designed with a series of notches along the sample edges that are prepared by electro discharged machining. This geometry allows the chip root to break instantly when the area above the circular notch is decreased by the tool feed and cannot withstand the cutting force that will push the chip root to break. Thus, the chip root can be obtained for the same cutting conditions as slot milling experiments. The collected samples are metallographically prepared for the measurement of the chip deformation and the deformed plastic zone geometry. Alternatively, this measurement can be approximated from the cut chip, as presented in [Lei, 1999]. The ratio of the average deformed plastic zone thickness in primary zone to the length of the shear plane ( $R_p$ ) is calculated and used as an input for OXCUT.

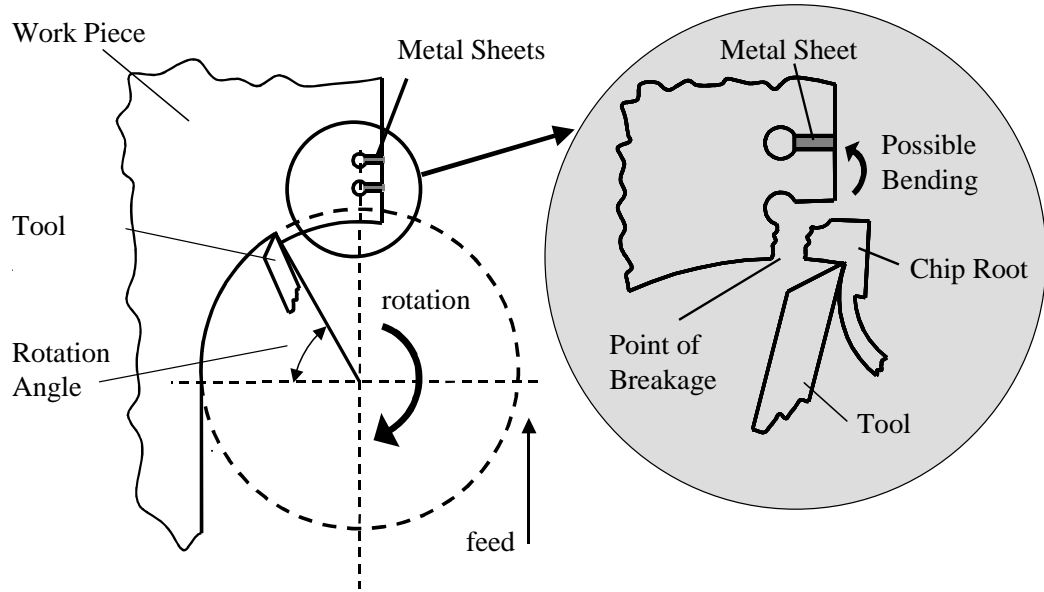


Figure 4.11: Schematic of quick stop milling experiments

#### 4.1.3. Computational Tasks

In the computational task, four experimental parameters ( $F_c$ ,  $F_t$ ,  $R_p$ ,  $R_s$ ) and basic material properties (i.e. thermal conductivity, specific heat and melting temperature of the workpiece) are used as inputs to OXCUT. Initial guesses of the flow stress parameters and a minimum tolerance are selected and inputted as required by the minimization algorithm. As can be seen in Figure 4.3, the procedure starts by using the initial flow stress parameters in OXCUT to calculate for forces ( $F_c$  and  $F_t$ ) and plastic zone thickness ratios ( $R_p$  and  $R_s$ ). These predictions are compared with the experiments. Then the flow stress parameters are modified for the next iteration, until a minimum total error between the predictions and the measurements is reached. The flow stress parameters determined at this stage are considered to be the solution. The obtained flow stress equation is then inputted into FEM simulations of orthogonal cutting for

validation. The flow stress equations and the minimization scheme used in this procedure are discussed in Section 4.1.3.1 and 4.1.3.2.

#### 4.1.3.1. Constitutive Models

The flow stress equations used for flow stress determination are modified from Johnson & Cook's [Johnson, 1983] equations (Equation 4.3). Equation 4.4 is the first modified J-C equation which takes the blue brittleness effect in carbon steel into account. The second modified J-C equation, Equation 4.5, is used for materials that do not exhibit blue brittleness.

$$\sigma = (A + B\varepsilon^n) \left( 1 + C \ln \left( \frac{\dot{\varepsilon}}{\dot{\varepsilon}_0} \right) \right) \left( 1 - \left( \frac{T - T_{room}}{T_{melt} - T_{room}} \right)^m \right) \quad \text{Equation 4.3}$$

$$\sigma = (B\varepsilon^n) \left( 1 + C \ln \left( \frac{\dot{\varepsilon}}{\dot{\varepsilon}_0} \right) \right) \left( \left( \frac{T_{melt} - T}{T_{melt} - T_{room}} \right) + ae^{-0.00005(T-700)^2} \right) \quad \text{Equation 4.4}$$

$$\sigma = (B\varepsilon^n) \left( 1 + C \ln \left( \frac{\dot{\varepsilon}}{\dot{\varepsilon}_0} \right) \right) \left( 1 - \left( \frac{T - T_{room}}{T_{melt} - T_{room}} \right)^m \right) \quad \text{Equation 4.5}$$

- where  $\sigma$  = Stress (MPa)  
 $\varepsilon$  = Strain  
 $\dot{\varepsilon}$  = Strain rate (s<sup>-1</sup>)  
 $\dot{\varepsilon}_0$  = Reference strain rate (s<sup>-1</sup>)  
 $T$  = Uncut chip thickness (°C)  
 $A, B, C, n, a, m$  = Material flow stress parameters

The use of these constitutive equations reduces the problem of non-uniqueness from the previous constitute model that has seven parameters, given in [Shatla, 1999]. Both modified J-C models are assumed to have no effect of



coupling (or the influence of the interaction between strain, strain rate and temperature) and also no effect of strain history.

The first term of modified J-C equations which represents strain hardening behavior of the material includes the parameters “ $B$ ” and “ $n$ ”, namely strength coefficient and strain hardening exponent. The initial stress parameter “ $A$ ” is disregarded since no initial stress was used for modeling plastic property of the workpiece in Oxley’s machining theory. The small number of parameters is preferred for reducing computational time and promoting computational robustness. The second term which represents the effect of strain rate is assumed to be similar to that of Johnson & Cook’s model with a reference strain rate of  $1,000 \text{ s}^{-1}$ . The third term is the temperature factor defined differently for different materials. As can be seen in Figure 4.12 (a), the temperature factor used in Equation 4.4 is able to take account of the blue brittleness effect that is always present in low carbon steel. For other materials, the temperature factor is represented as an exponential of a term that includes the melting point, similar to Johnson & Cook’s equation, as shown in Figure 4.12 (b).

Four parameters are to be iterated to determine the flow stress data of the workpiece materials. For demonstration, three specific materials were selected for testing the developed procedure. These include AISI 1045 carbon steel, AISI P20 mold steel and AISI H13 tool steel. Parameters “ $B$ ”, “ $C$ ”, “ $n$ ”, and “ $a$ ” of Equation 4.4 are to be determined for AISI 1045 steel while the parameters “ $B$ ”, “ $C$ ”, “ $n$ ” and “ $m$ ” of Equation 4.5 are used for AISI P20 and AISI H13 steels.

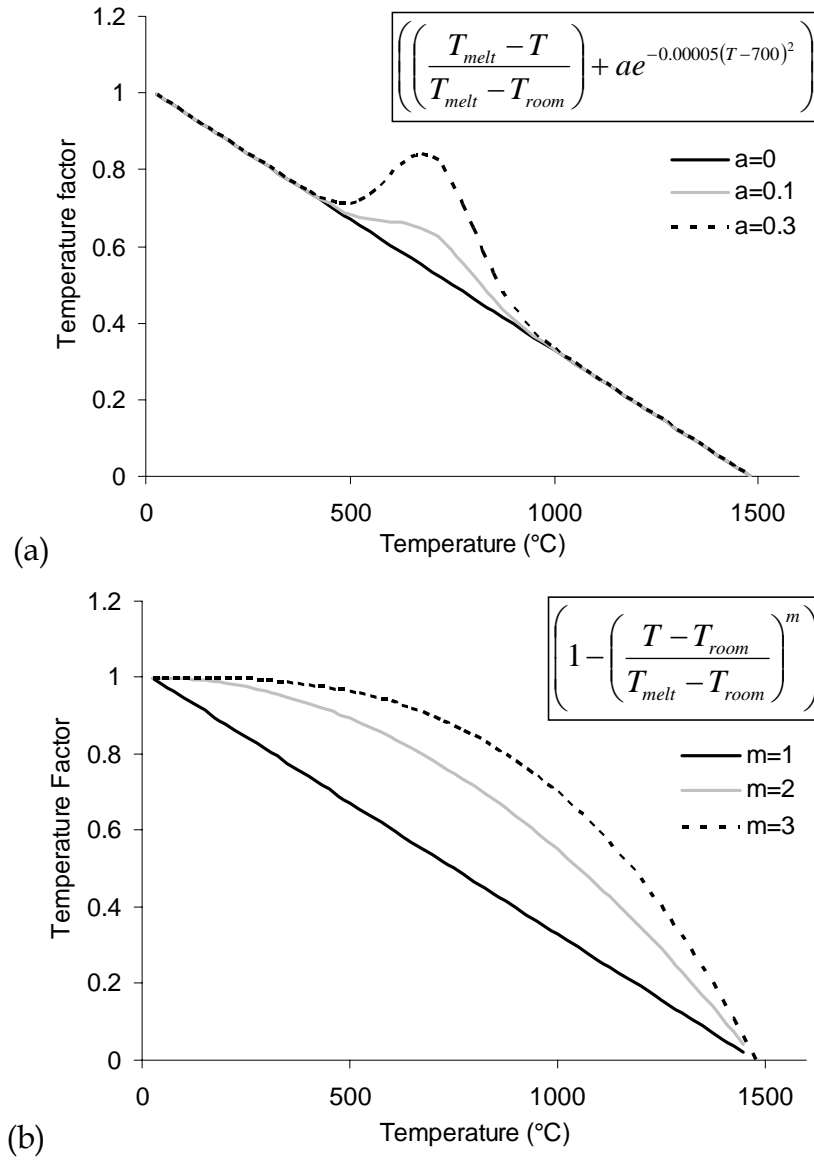


Figure 4.12: Temperature factor versus temperature, for (a) Equation 4.4 and (b) Equation 4.5

#### 4.1.3.2. Minimization Scheme

The criteria used in matching the predictions and the measurements are (a) the total of the least mean square error between predicted forces and measured forces at each rotation angle, and (b) the weighed error of plastic zone thickness ratios at the 90th degree of the tool rotation angle between experiments and predictions. The error function is summarized in Equation 4.6. In the present procedure, the experimental data are selected from four cutting conditions ( $i = 4$ ). From Equation 4.6, “ $f$ ” function refers to a lengthy nonlinear function representing Oxley’s theory with arbitrary flow stress parameter inputs ( $B, C, n$  and  $a$  (or  $m$ )) for the prediction of forces, deformation, etc. The weighed constant for the error of plastic zone thickness ratios are set as 1000 for  $W_1$  and 2000 for  $W_2$  since they adjust the amount of the errors of the plastic zone thickness ratios, namely  $R_p$  and  $R_s$ , to be approximately in the same levels as the error of forces. In addition, these values reduce the computational time and the number of iterations.

Minimize :

$$\sum_i \left( \text{RMS Error of forces} + \text{Error of } R_p \text{ and } R_s \right)_i = f(B, C, n, a \text{ or } m)$$

$$\sum_i \left( \frac{\sqrt{\sum_{\theta} \left\{ \left( F_{c,\text{exp}}(\theta) - F_{c,\text{OX CUT}}(\theta) \right)^2 + \left( F_{t,\text{exp}}(\theta) - F_{t,\text{OX CUT}}(\theta) \right)^2 \right\}}}{\text{the number of collected force data}} + \left( W_1 \left| R_{p,\text{exp}}\left(\frac{\pi}{2}\right) - R_{p,\text{OX CUT}}\left(\frac{\pi}{2}\right) \right| + W_2 \left| R_{s,\text{exp}}\left(\frac{\pi}{2}\right) - R_{s,\text{OX CUT}}\left(\frac{\pi}{2}\right) \right| \right) \right)_i \quad \text{Equation 4.6}$$

Where  $i$  = Number of cutting conditions  
 $\theta$  = Tool rotation angle (degree)  
 $F_{c,\text{exp}}$  = Experimental cutting force (N)  
 $F_{c,\text{OX CUT}}$  = Predicted cutting force from OXCUT (N)

- $F_{t,exp}$  = Experimental thrust force (N)  
 $F_{t,OXCUT}$  = Predicted thrust force from OXCUT (N)  
 $R_{p,exp}$  = Experimental ratio of deformed plastic thickness to the length of the shear plane  
 $R_{p,OXCUT}$  = Predicted ratio of deformed plastic thickness to the length of the shear plane from OXCUT  
 $R_{s,exp}$  = Experimental ratio of deformed plastic thickness to the cut chip thickness  
 $R_{s,OXCUT}$  = Predicted ratio of deformed plastic thickness to the cut chip thickness from OXCUT  
 $W_1$  = Weighed constant for the error of  $R_p$   
 $W_2$  = Weighed constant for the error of  $R_s$

Downhill simplex, a minimization method for a multidimensional problem, is employed to minimize the error between predictions and measurements by tuning the flow stress parameters and iterating until the error reaches a minimum. Required inputs for Downhill simplex method are the initial guesses and minimum tolerances. Initial guesses were selected by considering the data available from the literature, such as the flow stress parameters from SHPB tests or from conventional compression tests. Minimum tolerance, or a fractional range from highest to lowest, was set to 0.001 by default. Description of Downhill simplex method is addressed in [Press, 1992] and briefly presented in APPENDIX B. After running “OXCUT” and obtaining final flow stress parameters, it is suggested to change the initial guess to the parameters obtained from the last run and rerun the program again until the final flow stress parameters show no difference in their values and the same error is obtained.

#### 4.1.4. Determination of The Flow Stress Data for Selected Materials

The established procedure was tested on three different steels; AISI 1045, AISI P20 and AISI H13. First, a series of slot milling tests were conducted and four conditions that give continuous chip formation with no tool wear and no build up edge were selected. The selected materials and cutting conditions addressed in Table 4.1 satisfy all the mentioned criteria.

Material	AISI1045	AISI P20	AISI H13
Tool radial rake angle (°)	-9.06, 2.8	-9.06, 2.8	-9.06, 2.8
Cutting speed (m/min)	200, 300	200, 300	50, 100
Feed rate (mm/tooth)	0.1	0.1	0.1
Width of cut (mm)	3	3	3

Table 4.1: Experimental matrix for demonstrating the developed flow stress determination procedure with slot milling tests

##### 4.1.4.1. Experimental Results

In all tests, lower dynamic forces (i.e. less vibration due to dynamic impact) were observed beyond the 90<sup>th</sup> degree of tool rotation angle. Thus, cutting forces and thrust forces at the 90<sup>th</sup>, 110<sup>th</sup>, 130<sup>th</sup>, 150<sup>th</sup> degrees for any cutting conditions are selected for OXCUT inputs.

The method used in measuring the plastic zone thickness for the primary zone is similar to the method used in [Lei, 1999]. As shown in Figure 4.13, upper and lower boundary lines are drawn to locate the deformed plastic zone. The measurement of the primary shear zone thickness ( $\Delta s$ ) is taken at approximately the middle of the shear plane. The primary shear zone thickness is then divided

by the length of the shear plane ( $l$ ) to obtain the primary plastic zone thickness ratio ( $R_p$ ).

Since different uncut chip thicknesses vary over the tool rotation angles, the measurement in the secondary shear zone is taken at the middle of the cut chip (equivalent to chip formation at the 90<sup>th</sup> degree rotation angle). The secondary shear zone thickness is measured by taking the average of maximum and minimum plastic zone thicknesses ( $s_{max}$  and  $s_{min}$ ), as shown in Figure 4.14. The zone thickness is indicated from the point where the slope of the flow line changes and the separation of tool-sticking zone can be noticed. The minimum and maximum chip thicknesses ( $t_{ch,max}$  and  $t_{ch,min}$ ) are also measured and averaged. Thus, the ratio of an average secondary plastic zone thickness to an average of cut chip thickness ( $R_s$ ) is calculated and used as input to OXCUT.

Table 4.2 summarizes experimental inputs required for OXCUT. All cutting conditions have the same width of cut of 3 mm. These experimental data along with the basic material properties of three materials obtained from different sources, i.e. [ASM, 1990], [Matweb, 1996] and [Oxley, 1989], were inputted into OXCUT to determine for the flow stress equations.

#### 4.1.4.2. *Sensitivity Analysis of Forces and Plastic Zones Thickness Ratios*

The sensitivity analysis of experimental inputs was conducted to study the effects of changes (e.g. experimental errors) in the input data on the determination of the flow stress equation. This sensitivity analysis was tested on P20 steel. Forces ( $F_c$  and  $F_t$ ) and plastic zone ratios ( $R_p$  and  $R_s$ ) were changed systematically to observe the influence on the obtained flow stress parameters.

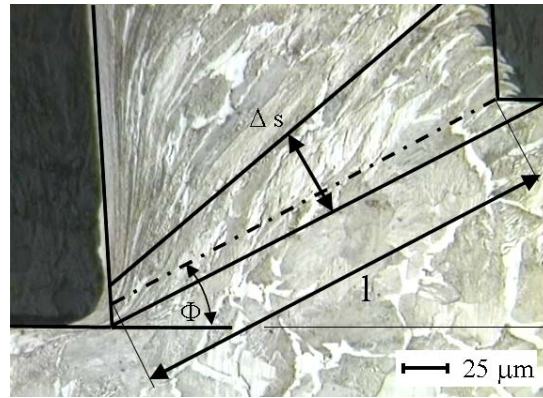


Figure 4.13: Measurement of primary shear zone thickness

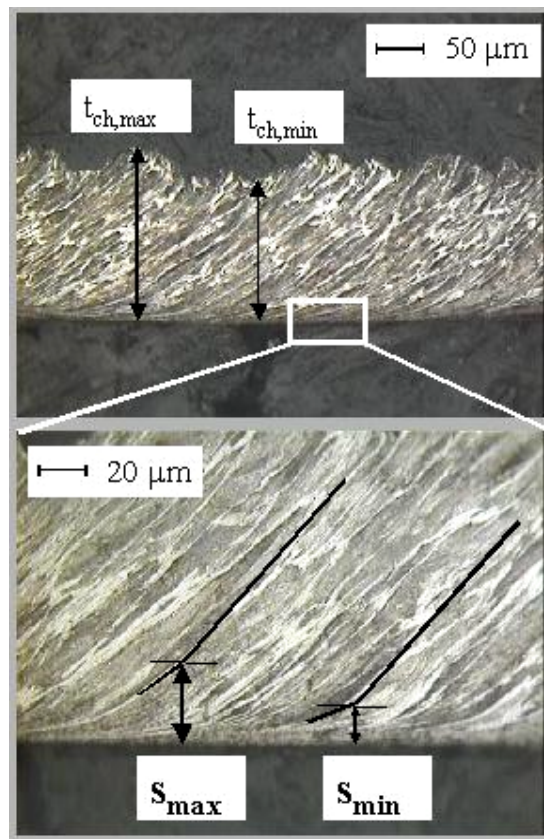


Figure 4.14: Measurement of secondary plastic zone thickness.

Material Type	Cutting condition [Rake (°), Speed (m/min), Feed rate (mm/tooth)]	Force data at the different tool rotation angle (N)				$R_p$	$R_s$	
		$F_c/F_t$	90°	110°	130°			150°
AISI 1045	[-9.06, 200, 0.1]	$F_c$	832	789	659	462	0.23	0.140
		$F_t$	601	577	500	374		
	[-9.06, 300, 0.1]	$F_c$	833	786	647	440	0.17	0.167
		$F_t$	534	509	432	312		
	[+2.8, 200, 0.1]	$F_c$	776	729	607	427	0.28	0.086
		$F_t$	477	457	403	314		
	[+2.8, 300, 0.1]	$F_c$	752	708	583	400	0.31	0.070
		$F_t$	398	384	337	259		
AISI P20	[-9.06, 200, 0.1]	$F_c$	829	793	674	488	0.23	0.088
		$F_t$	611	608	554	444		
	[-9.06, 300, 0.1]	$F_c$	790	756	641	462	0.21	0.079
		$F_t$	543	535	483	385		
	[+2.8, 200, 0.1]	$F_c$	766	732	629	465	0.38	0.083
		$F_t$	469	462	440	384		
	[+2.8, 300, 0.1]	$F_c$	783	747	630	449	0.30	0.130
		$F_t$	490	479	438	359		
AISI H13	[-9.06, 50, 0.1]	$F_c$	1109	1056	914	692	0.22	0.094
		$F_t$	955	936	844	671		
	[-9.06, 100, 0.1]	$F_c$	951	912	779	568	0.21	0.125
		$F_t$	677	681	632	519		
	[+2.8, 50, 0.1]	$F_c$	973	944	828	634	0.21	0.075
		$F_t$	806	815	770	655		
	[+2.8, 100, 0.1]	$F_c$	831	795	685	511	0.32	0.100
		$F_t$	517	521	504	446		

Table 4.2: Experimental input data needed for OXCUT

#### Sensitivity of Force Input Data ( $F_c$ , $F_t$ )

The analysis on force input data was conducted by using two cutting conditions of slot milling experiments on P20 steel. In fact, deviation of forces may result from tool wear and vibration. In this analysis, the cutting forces and the thrust forces at the 90<sup>th</sup> degree rotation angle are assumed to increase in multiples of 5% and those forces of other tool rotation angles are assumed to be parabolically proportional to the force data at the 90<sup>th</sup> degree. Percent increase of



thrust forces was also assumed to be approximately equal to the percent increase of cutting force, as shown Figure 4.15. Five series of force data were inputted into OXCUT to determine the parameters of the flow stress equation, Equation 4.5.

The obtained flow stress equations from different force data is shown in Table 4.3 and Figure 4.16. The flow stress data determined from different forces show slightly different for the parameter ' $C$ ' and ' $n$ '. However, parameters ' $B$ ' and ' $m$ ' appear to increase with increasing force data. The study, in Figure 4.16, also showed that 5% change of the force data can cause 10% deviation of the obtained flow stress data at the strain of 2.

#### Sensitivity of Plastic Zone Input Data ( $R_p, R_s$ )

The influence of plastic zone thickness ratios was investigated since the error from the plastic zone thickness measurement is inevitable. Sensitivity analysis of primary zone thickness ratio ( $R_p$ ) was conducted on P20 steel. The sensitivity of flow stress due to the variation of plastic zone thickness ratios from the reference value, in multiples of 20%, was analyzed. This sensitivity study considers the effect of plastic zone thickness in primary zone and secondary zone independently. In other words, one ratio is changed to see the effect while the other ratio is fixed.

The obtained flow stress equations from different primary deformation zone thickness ratios are shown in Table 4.4 and Figure 4.17. The results show an increase of 60% in the primary plastic zone thickness ratio ( $R_p$ ) causes only 10% change in the flow stress data (at the strain of 2 and temperature of 300 °C).

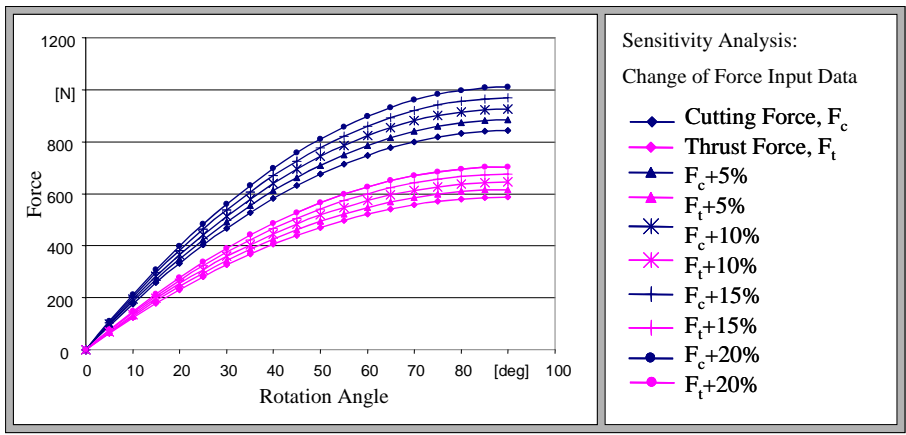


Figure 4.15: Change of force input data

	<b>B</b>		<b>C</b>		<b>n</b>		<b>m</b>	
	Value	%error	Value	%error	Value	%error	Value	%error
Exp. Forces	872.85	-	0.076	-	0.202	-	1.830	-
+5%	913.41	4.65	0.077	1.33	0.200	-0.64	2.033	11.04
+10%	949.64	8.80	0.077	1.22	0.200	-0.89	2.303	25.81
+15%	981.23	12.42	0.078	2.73	0.201	-0.53	2.549	39.25
+20%	1012.3	15.98	0.079	3.65	0.202	0.28	2.932	60.19

Table 4.3: Sensitivity of force data on the flow stress equations obtained from slot milling tests, for P20 steel.

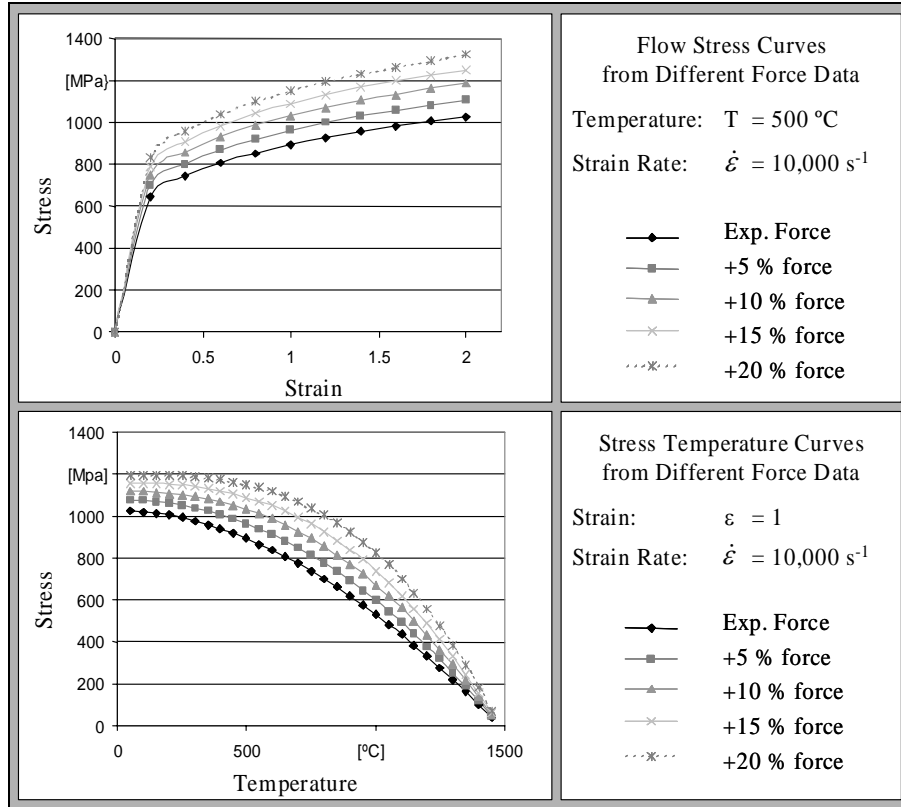


Figure 4.16: Sensitivity analysis of force input on the obtained flow stress data

Test No.	Assume $R_p=0.2$	Assume $R_s=0.05$	$B$	$C$	$n$	$m$
1	0.20, +0%	0.05, +0%	739.8	0.082	0.153	2.239
2	0.24, +20%	0.05, +0%	746.9	0.084	0.185	2.171
3	0.28, +40%	0.05, +0%	741.6	0.083	0.213	2.201
4	0.32, +60%	0.05, +0%	759.1	0.089	0.243	2.114

Table 4.4: Flow stress parameters obtained using different primary plastic zone thickness ratios,  $R_p$

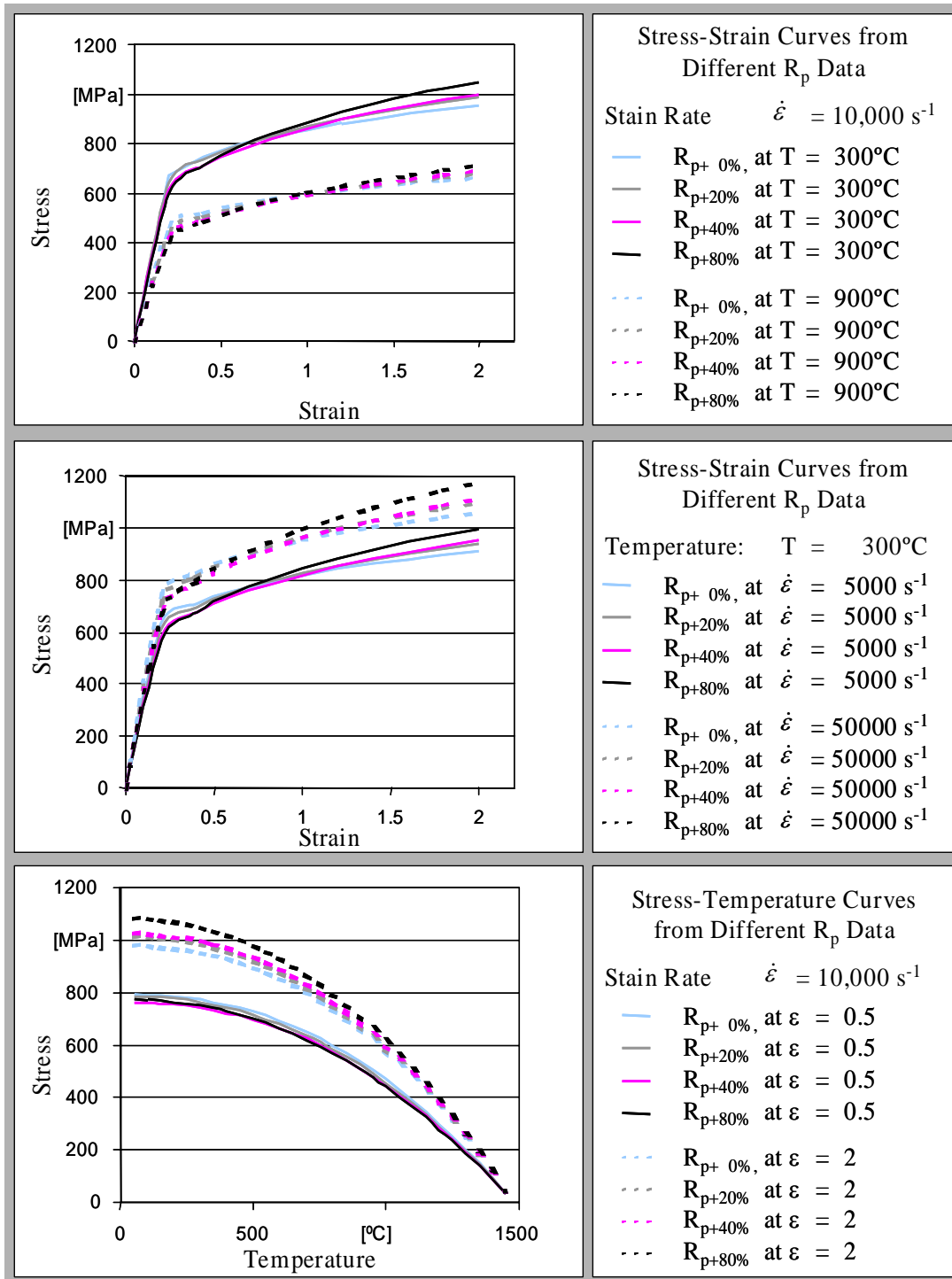


Figure 4.17: Sensitivity analysis of  $R_p$  on the obtained flow stress data

For the secondary zone thickness ratio  $R_s$ , Table 4.5 and Figure 4.18 shows that the changes of secondary deformation zone thickness ratios slightly influence the obtained flow stress data. Parameters “B” and “C” are affected by the change of  $R_s$ . The maximum error of 12% was observed at room temperature and the strain of 2, when  $R_s$  increases 80%.

Test No.	Assume $R_p = 0.2$	Assume $R_s = 0.05$	<i>B</i>	<i>C</i>	<i>n</i>	<i>m</i>
1	0.20, +0%	0.05, +0%	739.8	0.082	0.153	2.239
2	0.20, +0%	0.06, +20%	716.2	0.093	0.153	2.235
3	0.20, +0%	0.07, +40%	688.5	0.096	0.153	2.260
4	0.20, +0%	0.08, +60%	663.6	0.096	0.155	2.310
5	0.20, +0%	0.09, +80%	656.2	0.096	0.155	2.391

Table 4.5: Flow stress parameters obtained using different secondary plastic zone thickness ratios,  $R_s$

Results from the sensitivity analysis demonstrated that the accuracy of the flow stress determination is affected by (a) force measurements (influenced by tool wear and vibrations) and (b) measurements of the plastic zone thicknesses. However, force measurements affect the results much more significantly than the measurement of plastic zone thicknesses.

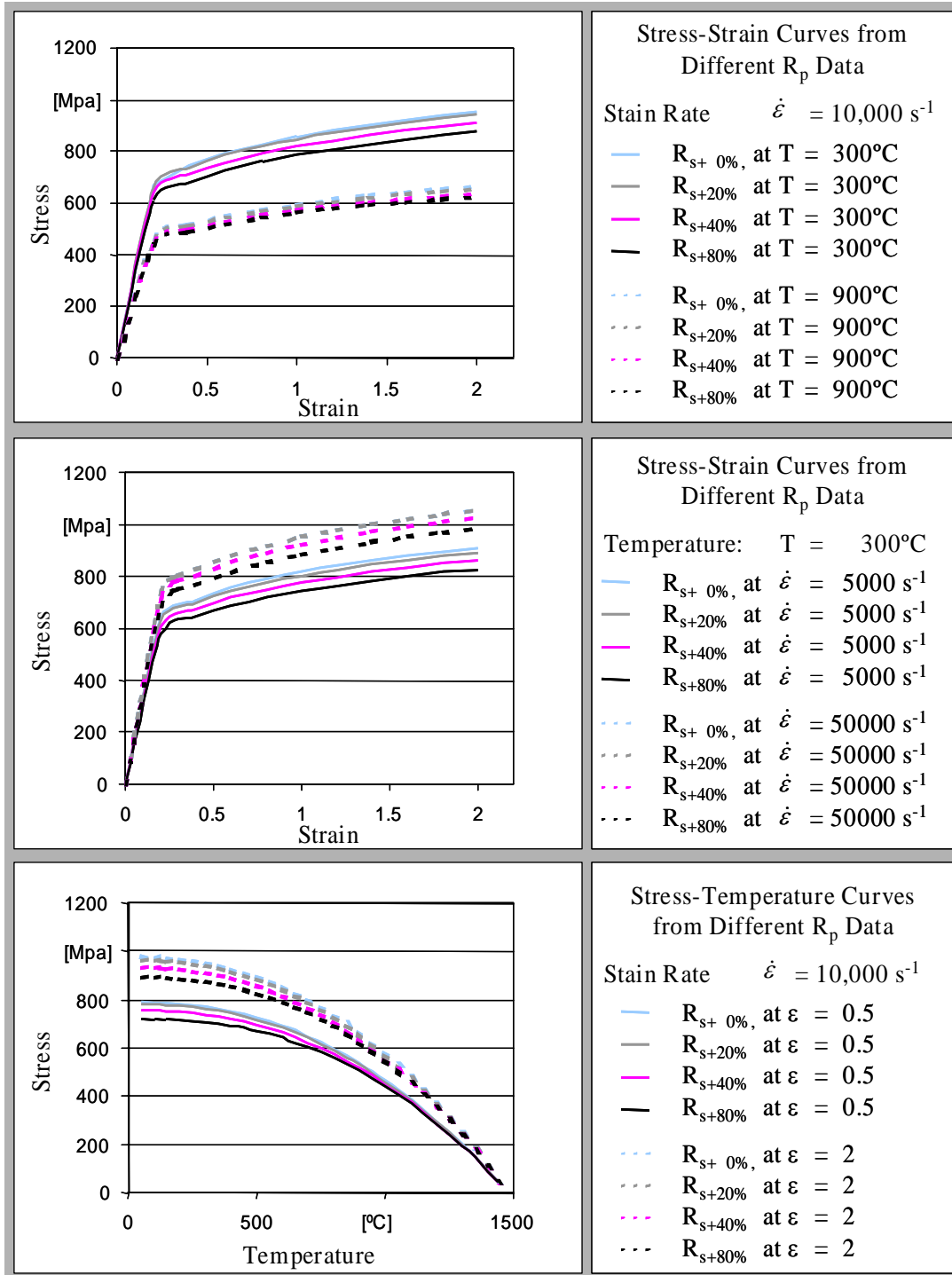


Figure 4.18: Plots of Flow Stress Data at Different Inputs of  $R_s$

#### 4.1.4.3. Discussion of Obtained Flow Stress Equations

Experimental data shown in Table 4.2 along with the physical and thermal properties of the workpiece material were inputted into OXCUT to calculate for the flow stress equation. Computational time for obtaining flow stress data for one material was approximately five hours (on PC 600 MHz Processor). The obtained flow stress equations and their applicable range of three selected steels are shown in Table 4.6. The comparison of flow stress of AISI 1045 steel obtained by this procedure and by high speed compression tests shows an acceptable agreement, as show in Figure 4.19. Flow stress curves of AISI P20 and AISI H13 are shown in Figure 4.20 and Figure 4.21. Applicable ranges of the obtained flow stress equations are within actual conditions that exist in machining processes. However, the ranges of the applicable strains are limited and the equation does not represent fully the flow stress properties at low temperatures without extrapolation.

Material Type	Flow Stress Equation	Flow Stress Parameters					Applicable Ranges		
		$B$ (MPa)	$C$	$n$	$a$	$m$	$\epsilon$	$\dot{\epsilon}$ (s <sup>-1</sup> )	$T$ (°C)
AISI 1045	Equation 4.4	996	0.097	0.168	0.275	-	[0.7, 1.4]	[26000, 680000]	[240, 900]
AISI P20	Equation 4.5	645	0.094	0.195	-	2.6	[0.9, 1.4]	[7300, 110000]	[240, 940]
AISI H13	Equation 4.5	982	0.023	0.18	-	2.7	[0.9, 1.7]	[1800, 36000]	[260, 890]

Table 4.6: Flow stress equations of AISI 1045, P20 and H13 steels obtained from slot milling tests

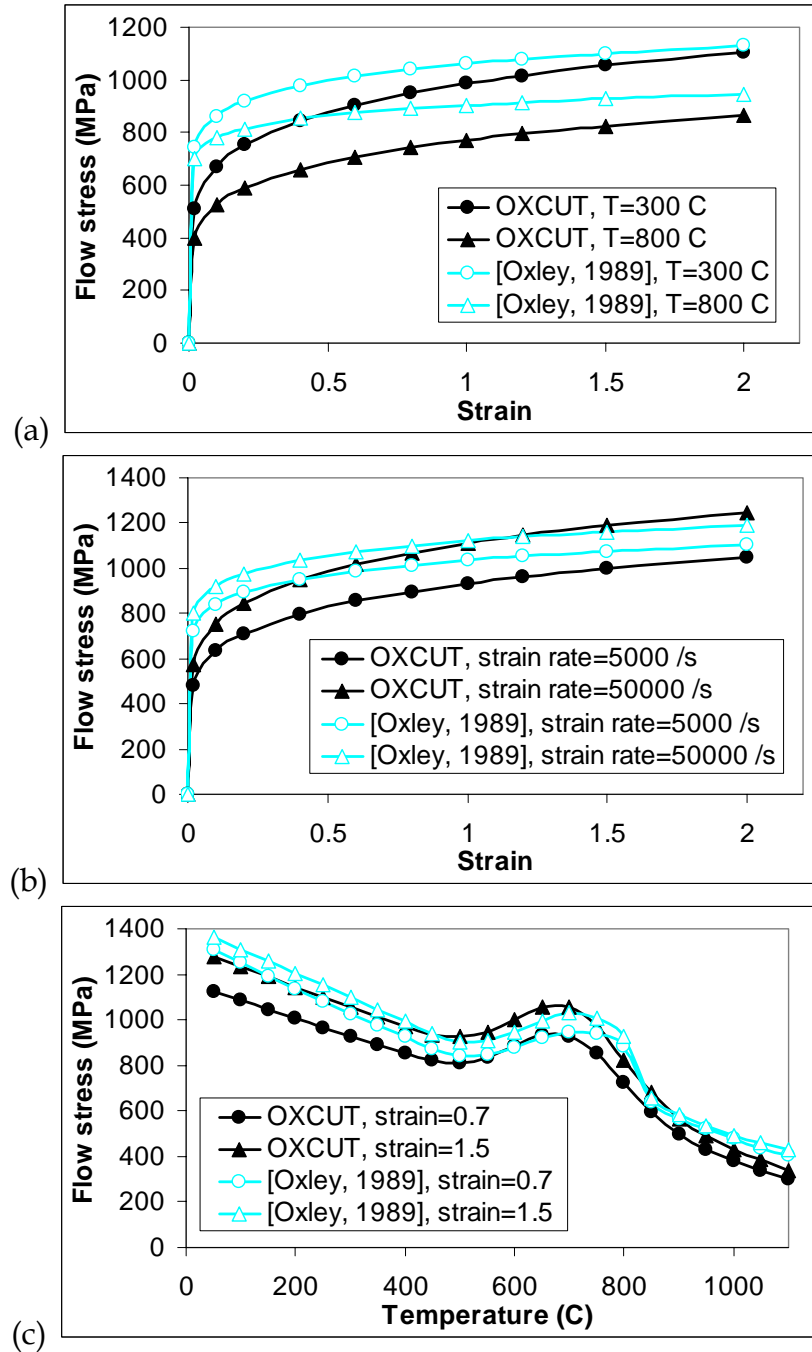


Figure 4.19: Comparison of the flow stress data for AISI 1045 steel between OXCUT predictions and Oxley's high speed compression data, [Oxley, 1989]: (a) at constant strain rate of  $10,000 \text{ s}^{-1}$ ; (b) at constant temperature of  $300 \text{ }^\circ\text{C}$  and (c) at constant strain rate of  $10,000 \text{ s}^{-1}$



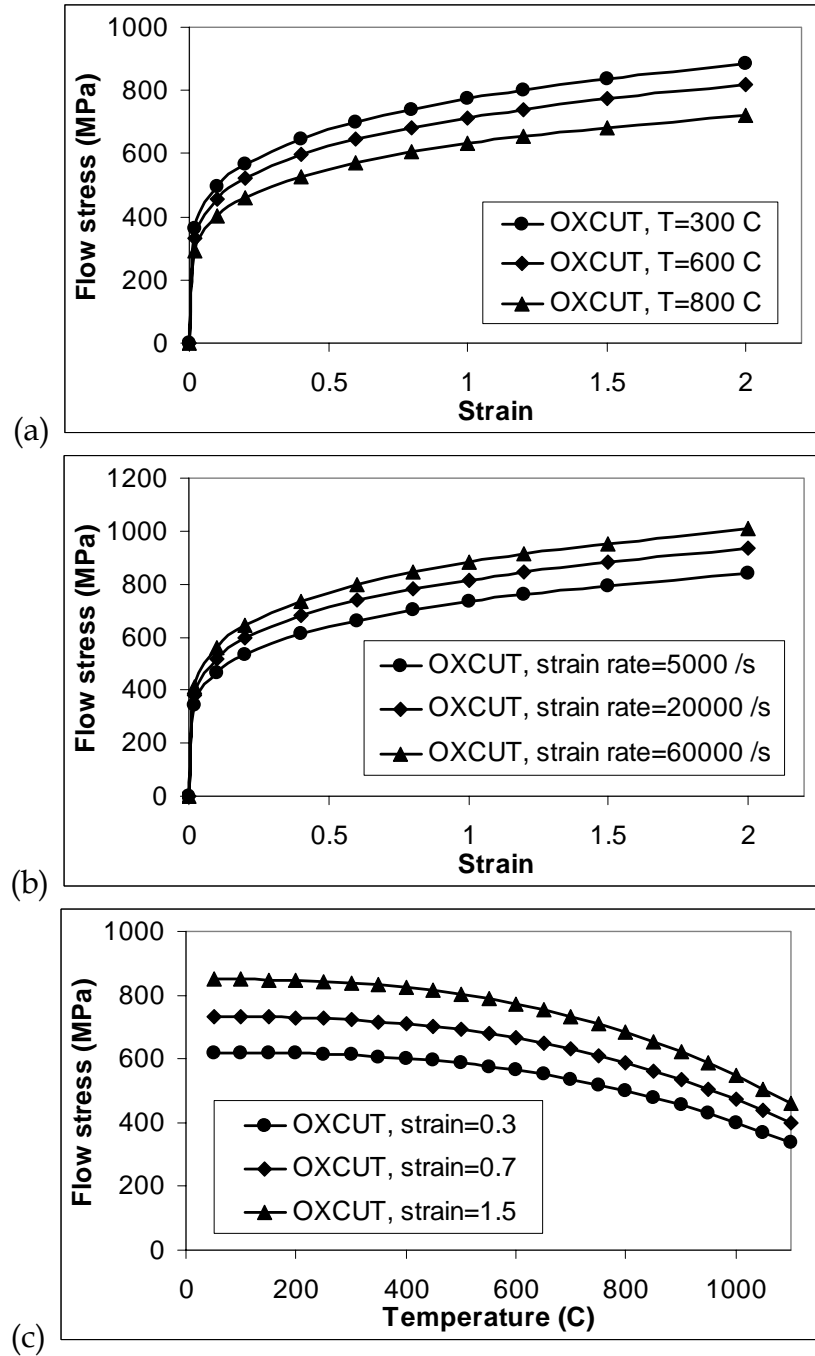


Figure 4.20: The flow stress data for AISI P20 steel obtained from OXCUT predictions: (a) stress-strain curves at constant strain rate of 10,000 s<sup>-1</sup>; (b) stress-strain curves at constant temperature of 300 °C and (c) stress-temperature curves at constant strain rate of 10,000 s<sup>-1</sup>

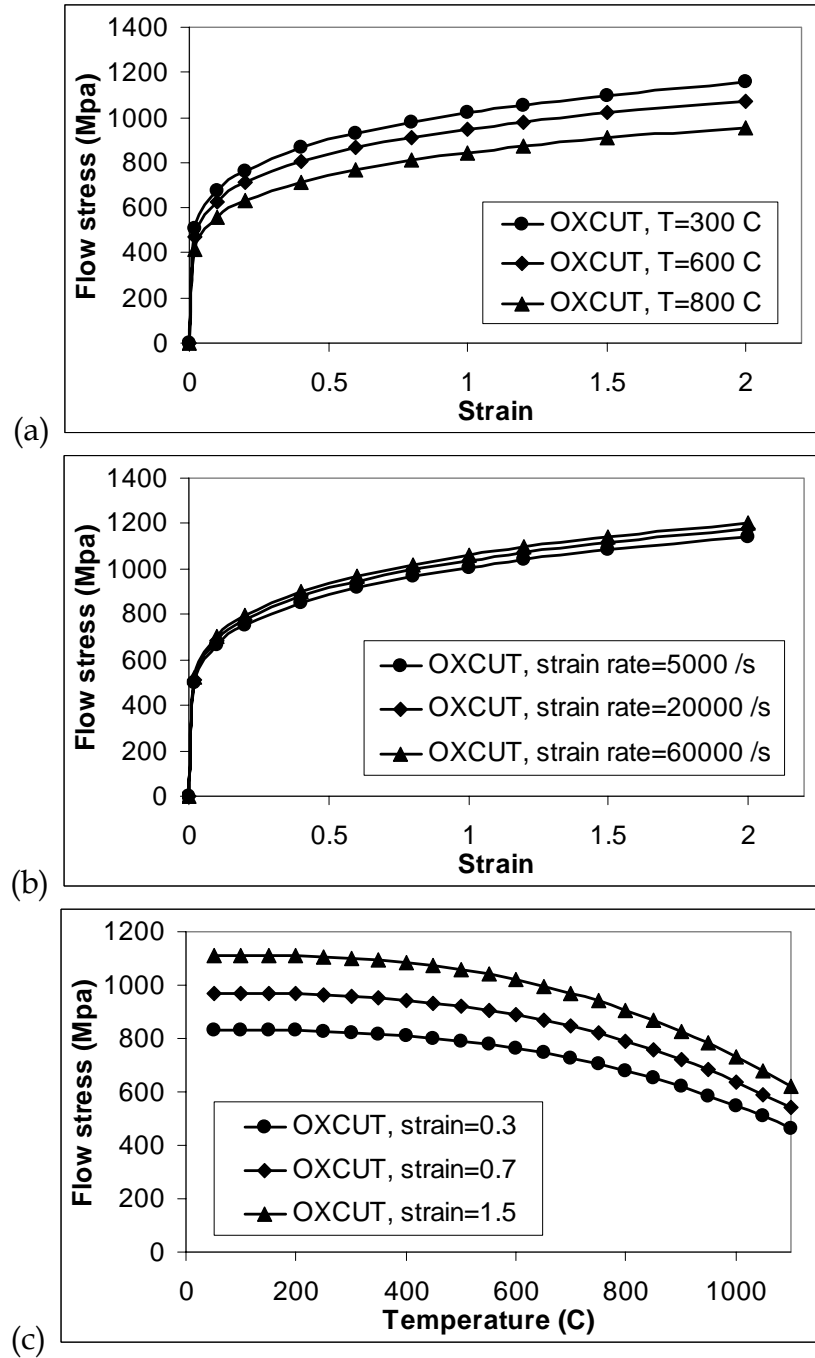


Figure 4.21: The flow stress data for AISI H13 steel obtained from OXCUT predictions: (a) stress-strain curves at constant strain rate of 10,000 s<sup>-1</sup>; (b) stress-strain curves at constant temperature of 300 °C and (c) stress-temperature curves at constant strain rate of 10,000 s<sup>-1</sup>

#### 4.1.4.4. Validation of the Flow Stress Results

The validation of the obtained flow stress data was conducted by using the obtained flow stress on two applications; 1) OXCUT force prediction module and 2) FEM simulations of orthogonal cutting. In addition, robustness of the developed procedure was tested by assuring that the unique flow stress solution could be obtained.

From the force prediction using OXCUT (see Figure 4.22 to Figure 4.24), the predicted forces for negative rake tool are well matched with experimental forces for all three materials. For milling with positive rake tool on AISI 1045 and AISI P20 steels, predicted forces are within acceptable range of accuracy for practical purpose, approximately within 20 %.

For additional validation, flow stress data obtained from the developed procedure were used in the FEM code, "DEFORM-2D™", to simulate orthogonal cutting process. For turning of AISI 1045, comparison was made between FEM simulation results and experimental data from [Ivester, 2000]. A tool insert was uncoated tungsten carbide (WC) with a tool rake angle of  $-7^\circ$ . The feed rate and the width of cut used in the experiment were 0.15 mm/rev and 1.6 mm, respectively. Thermal properties of the workpiece (e.g. thermal conductivity, specific heat) required for FEM simulation were similar to those used for OXCUT inputs. The simulations assumed shear friction ( $\tau = m_f k_{chip}$ ; where  $\tau$  is shear frictional stress,  $m_f$  is shear friction factor and  $k_{chip}$  is shear flow stress of the workpiece) with friction factor ( $m_f$ ) of 0.5 along the tool-chip contact on the rake face, tool edge radius and the tool flank face.

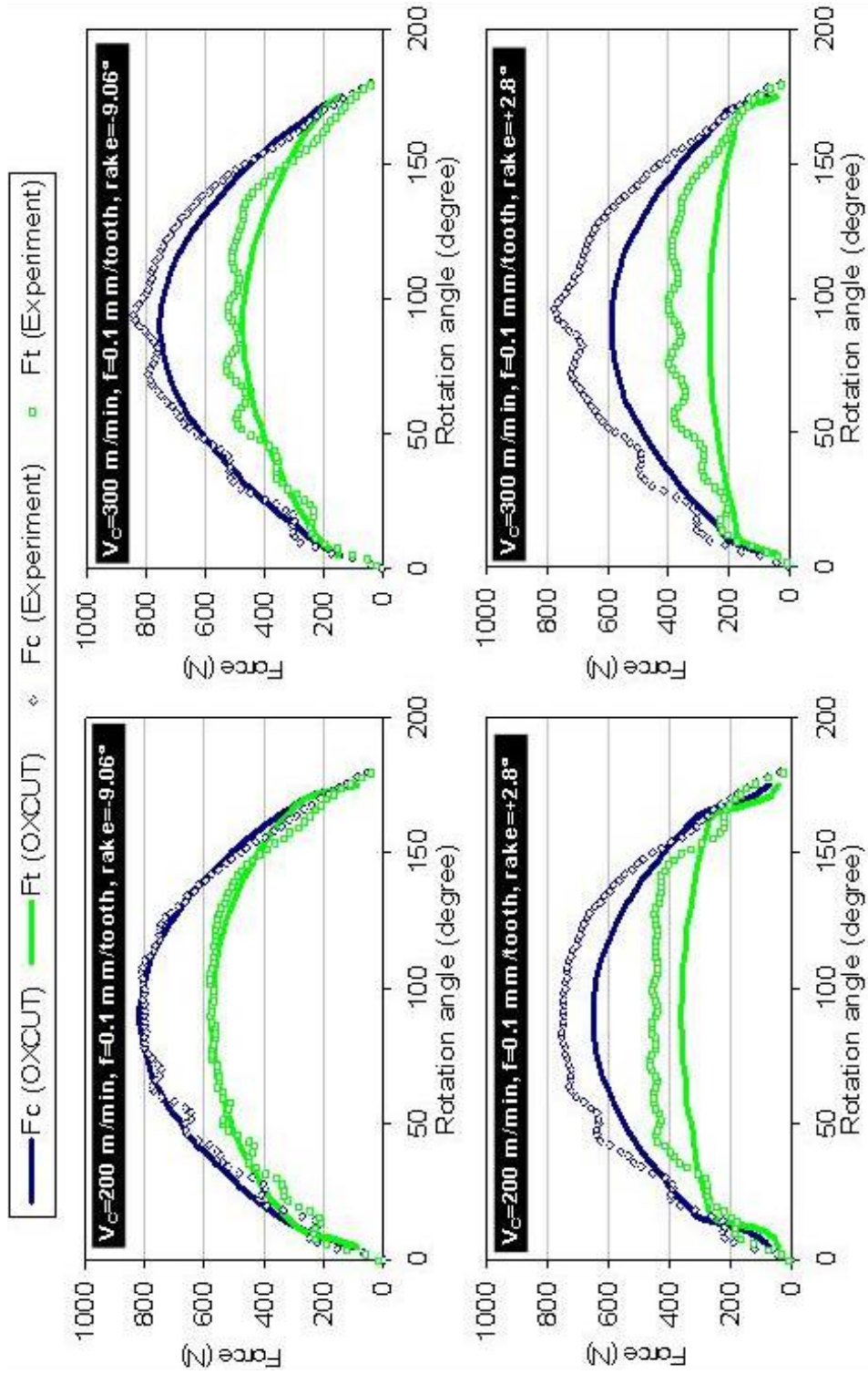


Figure 4.22: Force prediction for AISI 1045

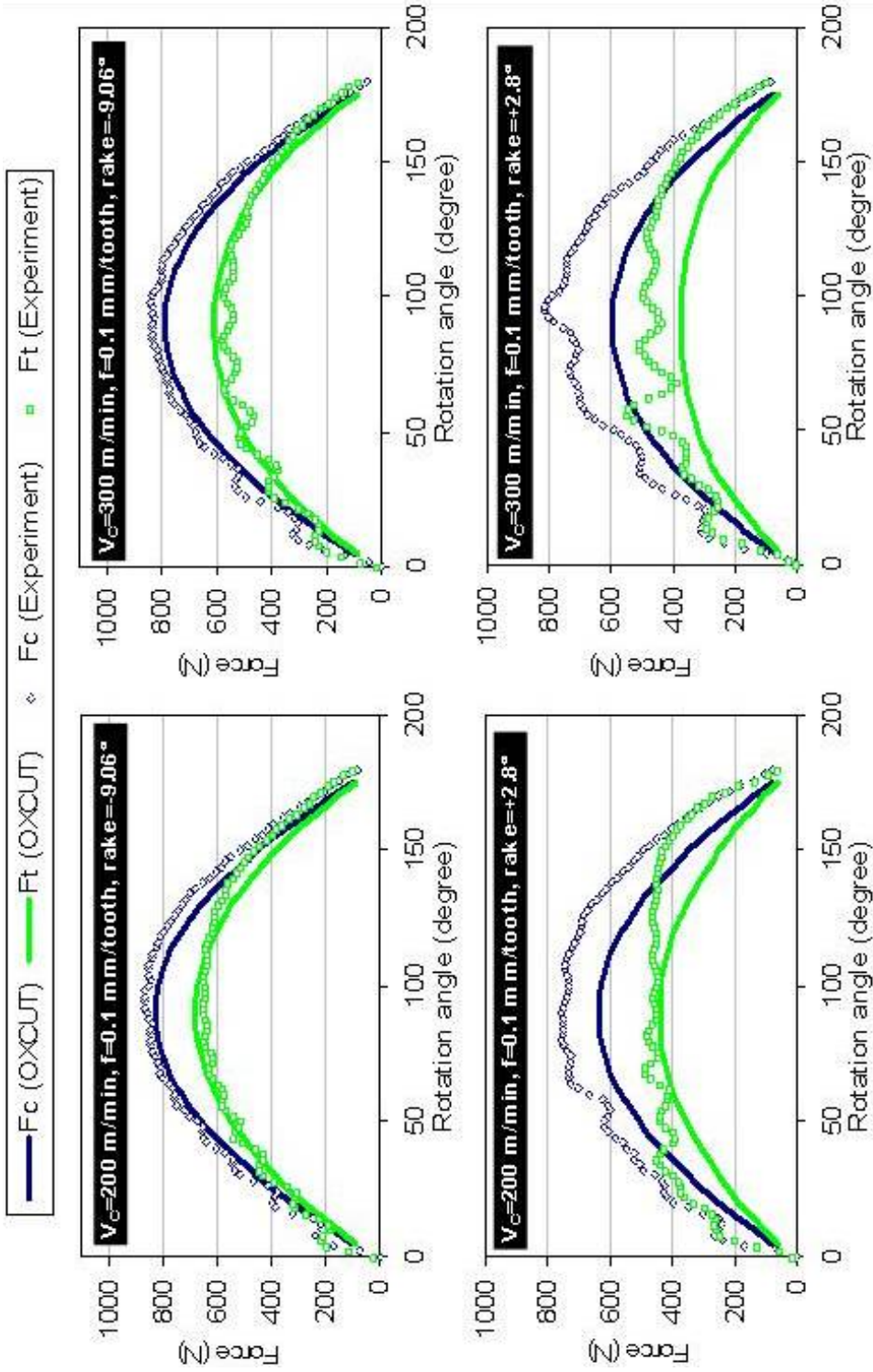


Figure 4.23: Force prediction for AISI P20

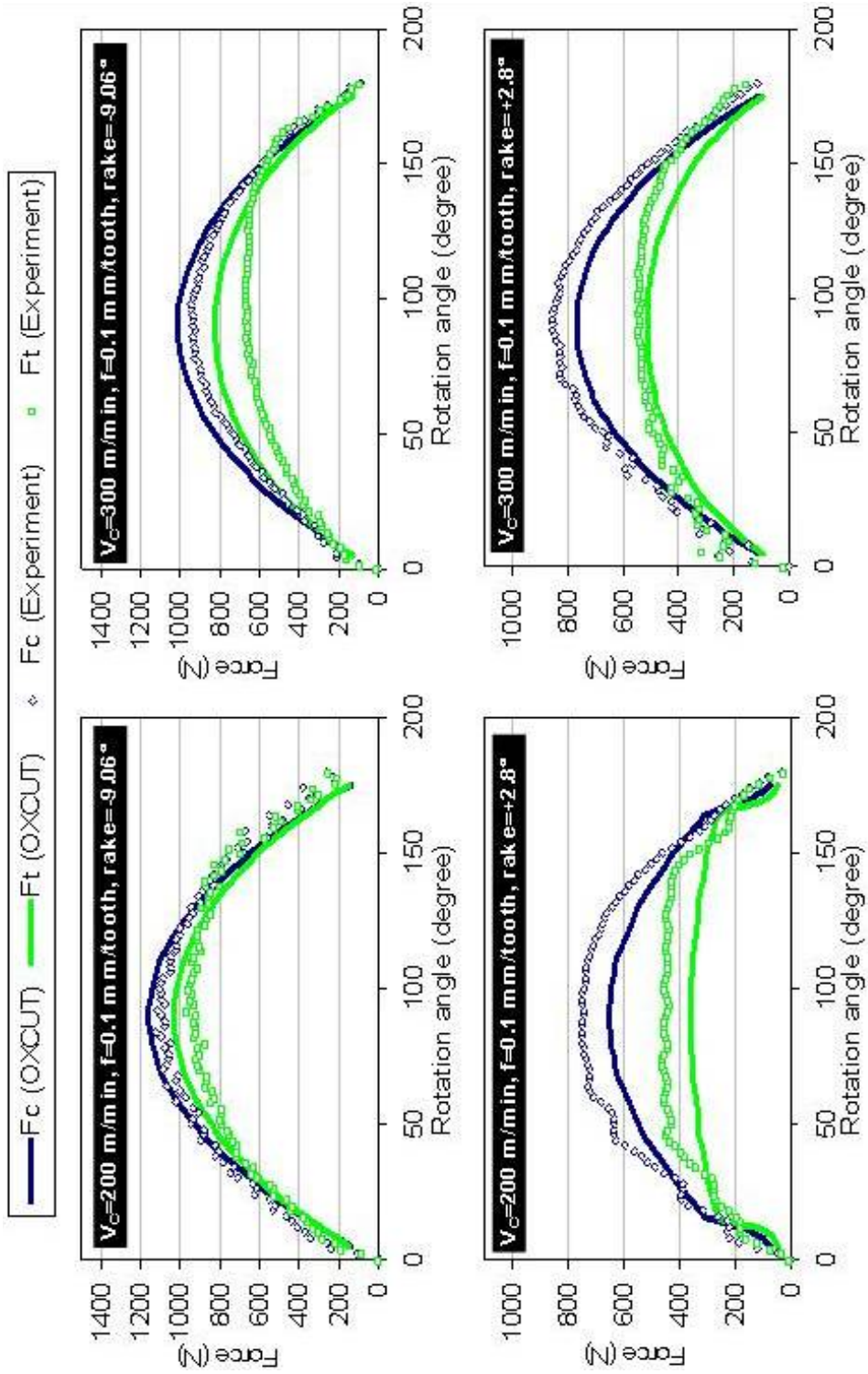


Figure 4.24: Force prediction for AISI H13

In [Chandrasekeran, 1965; Childs, 1989], experimental investigation of tool stresses using the split tool technique estimated the friction factor ( $m_f$ ) of 0.5 to 0.9 for various tool-workpiece contacts and temperature. In addition, it was found that there is only a small sliding region (which is described by Coulomb's friction,  $\tau = \mu\sigma_n$ ; where  $\tau$  is shear frictional stress,  $\mu$  is friction coefficient and  $\sigma_n$  is normal stress) on the tool rake face [Chandrasekeran, 1965; Childs, 1989]. This assumed friction condition was applied on the tool/chip contact.

Comparisons between experimental results, FEM predictions and OXCUT predictions for turning of AISI 1045 steel are shown in Figure 4.25. The predicted cutting forces from FEM simulation show 18% higher than the experimental forces while the predicted thrust forces is approximately 37% lower than that of the experiment. The chip thicknesses from FEM simulations, OXCUT predictions and experiments are in good agreement.

For orthogonal turning on P20, the flow stress data of P20 obtained from the developed procedure (in Table 4.6) was used in FEM cutting simulation. Comparisons were made with experiment results from [Yen, 2000]. A cutting tool was uncoated WC with a rake angle of  $-7^\circ$ . Tests were conducted at the speed of 200, 300 m/min, the feed rate of 0.1 mm and the width of cut of 2 mm. At tool chip contact, shear friction factor ( $m_f$ ) of 0.6 was assumed in the simulation. The comparison of the results is shown in Figure 4.26. Predicted cutting forces from FEM and OXCUT show good agreement with those from experiments, within 6% error. Nevertheless, the thrust force and the chip thickness from FEM simulations showed some difference to experimental measurements.

The error of FEM predictions might be caused by the difference of material batch used in slot milling tests conducted at Ohio State University and orthogonal turning tests from the literature. Those samples can be differentiated

by their chemical composition, heat treatment condition and surface hardness. In addition, the friction law used for tool-chip interface and the extrapolated flow stress properties at low temperature may contribute to errors.

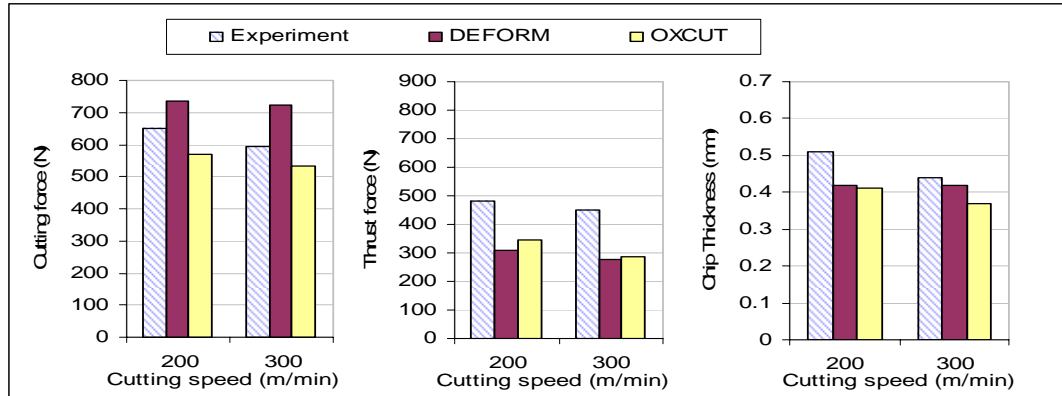


Figure 4.25: Comparison of experimental measurements in [Ivester, 2000], FEM-DEFORM predictions and OXCUT predictions for orthogonal turning tests on AISI 1045 steel

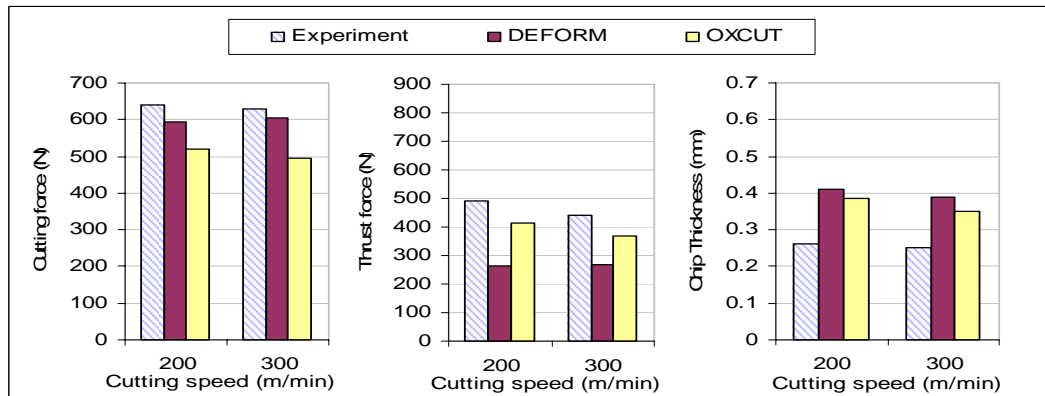


Figure 4.26: Comparison of experimental measurements in [Yen, 2000], FEM-DEFORM predictions and OXCUT predictions for orthogonal turning tests on AISI P20 steel



The flow stress data of AISI 1045, obtained from slot milling tests were used in FEM simulations of orthogonal cutting to validate temperature predictions. Tool geometries and cutting conditions used in the simulation follow those used in orthogonal turning experiments by Müller [Müller, 2004]. The author performed temperature measurements at the surface of the chip during turning by using a fiber-optic two-color pyrometer attaching to the cutting insert at the distance of 1.6 mm away from the major cutting edge, as shown in Figure 4.27(a). FEM simulations were conducted using the same settings as those previously used for force validation. After uniform chip was observed in the simulation, temperature data of the element node, at which location was corresponding to the location of temperature measurement, are extracted and averaged. Figure 4.27(b) shows the comparison of chip temperatures from FEM simulations and measurements. The temperature predictions are in good agreement with the temperature measurements. As commonly known in machining fundamentals, both FEM and experiments show that the chip temperature increases with increasing cutting speed.

The developed inverse analysis procedure and slot milling tests was tested for the uniqueness of the obtained flow stress solution. With the same experimental forces and plastic zone thickness ratios from slot milling tests on AISI P20 steel, three different initial guess sets were used as inputs to determine the flow stress parameters. The flow stress parameters obtained from different sets of initial guesses were compared to evaluate for the uniqueness of the solution. As shown in Figure 4.28, although different values of initial guesses were used, the total error and the values of all flow stress parameters conversed almost to the same final solution after several iterations.

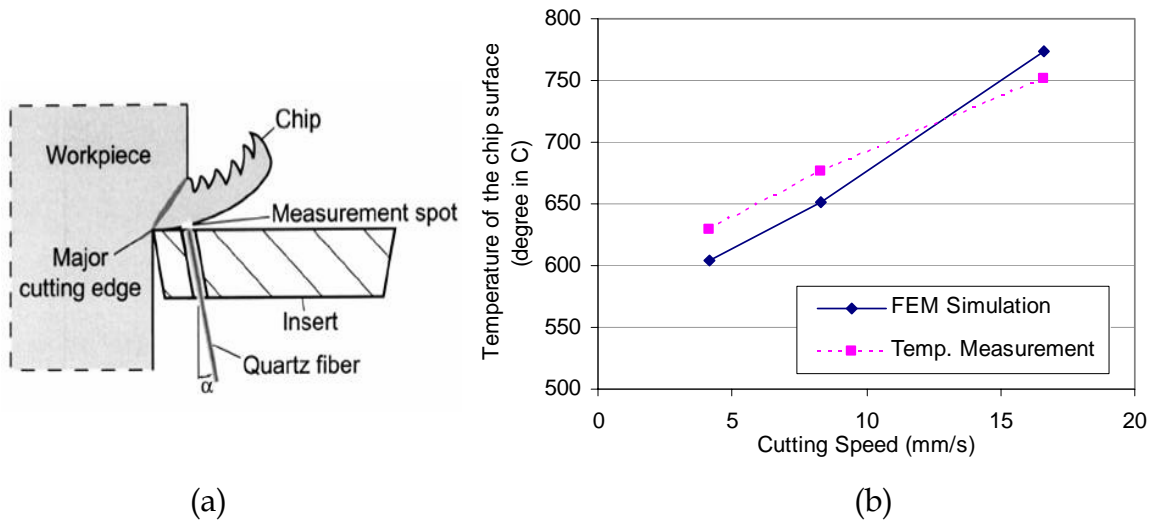


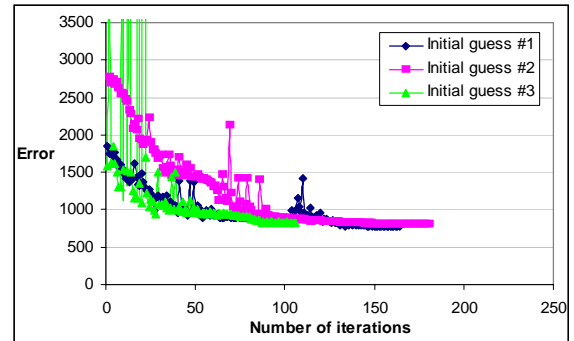
Figure 4.27: (a) location of temperature measurement is at 1.6 mm away from the major cutting edge [Müller, 2004]; (b) Comparison of chip surface temperature from FEM cutting simulations and measurement, for turning of AISI 1045 from [Müller, 2004].

**Initial guesses used for verification of solution uniqueness**

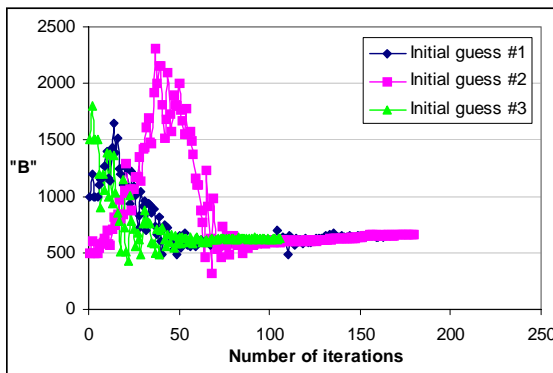
Initial guess #1:  $B = 1000$ ,  $C = 0.05$ ,  $n = 0.1$ ,  $m = 1$

Initial guess #2:  $B = 500$ ,  $C = 0.02$ ,  $n = 0.08$ ,  $m = 0.6$

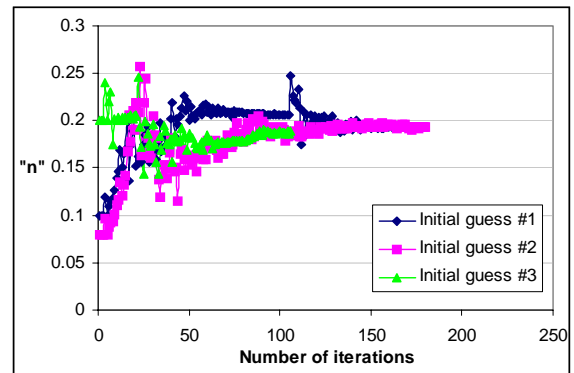
Initial guess #3:  $B = 1500$ ,  $C = 0.08$ ,  $n = 0.2$ ,  $m = 1.5$



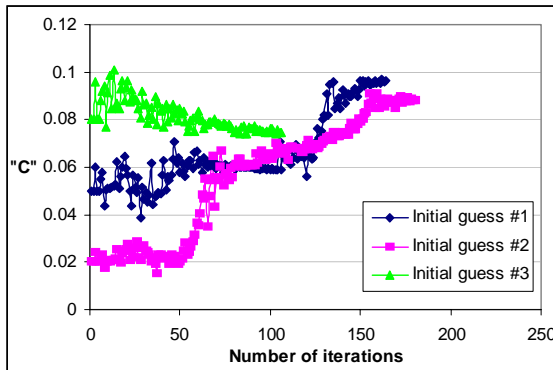
(a) Total error vs. Number of iteration



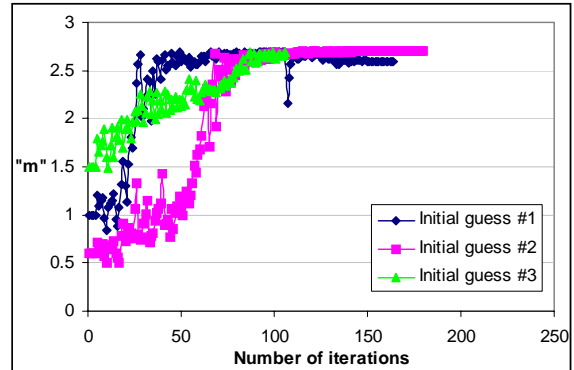
(b) Parameter "B" vs. Number of iteration



(c) Parameter "n" vs. Number of iteration



(d) Parameter "C" vs. Number of iteration



(e) Parameter "m" vs. Number of iteration

Figure 4.28: Verification for the uniqueness of the flow stress solution obtained from the proposed inverse analysis and slot milling tests.

#### 4.1.5. *Summary and Conclusions*

The computer program OXCUT that is based on Oxley's machining theory was developed and applied to determine the flow stress data for three selected materials; namely AISI 1045, P20 and H13. For each workpiece material, cutting force and thrust force contours were obtained from orthogonal slot milling experiments and used as input data for OXCUT. As additional input information for OXCUT, the primary and secondary plastic zone thickness ratios were obtained by examining the chip roots and the cut chips, respectively. To obtain chip roots for selected cutting conditions, a quick stop mechanism on the plate sample was designed.

The flow stress data of AISI 1045 steel obtained from the present procedure are in a good agreement with the data obtained from high speed compression tests. The force predictions using OXCUT program are in good agreement with experimental results except for the cases of cutting with a positive rake tool. The difference between the cutting forces predicted by FEM simulation of orthogonal turning and those obtained from experiments is within 18% for turning with AISI 1045 and P20 steels. The thrust forces from FEM simulations, however, are in average 40% lower than those from experiments.

Error of the thrust forces from FEM simulation can be contributed by several factors; a) assumed friction used for tool-chip contact, b) the material properties at low temperature and low strain rate are not valid and extrapolated from slot milling tests, and c) the effect of elastic tool deflection and d) the fact that typical experimental force measurement consider also the tool force that presses the workpiece in which the FEM cutting model does not consider.

The developed methodology has been applied to determine the flow stress properties for several materials, for both ferrous and non-ferrous types. These

materials are AISI 1045, P20 tool steel, H13 mold steel, AISI 1018, AISI 1080, AISI 8219, AA 356-T6 aluminum alloy, SS 348 stainless steel, copper alloys, Inconel 718 and Ti-17 alloy.

Further research on the flow stress determination for machining may include:

- Incorporating the flow stress at different testing ranges and different testing methods. For example, the flow stress data for a wide testing range can be obtained from conventional compression tests for low strain rates, SHPB tests for mid strain rates and machining tests for high strain rates.
- Implementing inverse analysis with FEM cutting simulation. This may reduce the errors that are caused by a number of assumptions made in the analytical approach.

#### **4.2. Effect of Flow Stress Parameters in FEM Simulation of Orthogonal Cutting - Sensitivity Analysis**

A study on different types of constitutive equations (e.g. power law and Johnson & Cook's equations [Johnson, 1983]) for machining analysis was presented in [Hamann, 2002], [Childs, 2003] and [Arrazola, 2003]. Hamann [Hamann, 2002] conducted FEM simulations using constitutive equations from three different sources. His results showed significant differences in cutting ratio and maximum tool temperature due to differences in the relations of the flow stress to the temperature. Childs [Childs, 2003] used a broad range of material models and an FEM software, Third Wave AdvantEdge™ [thirdwavesys.com], for predicting shear angle, friction angle, and normal contact stress. Results of

Childs' study suggested that the use of classical analysis could provide a framework to understand and to evaluate the results obtained from FEM simulations, i.e. calculation of shear angle and energy consumption. Recent results of an extensive analysis on cutting simulation were presented in [Arrozola, 2003]. Arrozola used ABAQUS™ Explicit version 6.1 [hks.com] and Johnson & Cook's flow stress equation [Johnson, 1983]. Sensitivity analyses were conducted to study the effects of mesh definition, thermal conductivity, specific heat, values of the parameters in a flow stress equation, coefficient of friction and contact thermal properties. Results were also compared with cutting simulations using Third Wave AdvantEdge™ software.

In this study, the FEM commercial software "DEFORM-2D™" was used to simulate orthogonal cutting. In the preliminary analysis, ten different flow stress parameter sets were used to simulate one cutting condition. However, the results from the FEM simulation of one condition did not clearly indicate the influence of all flow stress parameters. Therefore, twelve additional simulations with different cutting conditions were conducted. The predicted results (cutting force, thrust force, chip thickness, shear angle, tool/chip contact length and maximum temperature at tool/workpiece interface) were compared.

#### **4.2.1. Sensitivity Analysis on One Cutting Condition**

##### *4.2.1.1. Tool, Cutting Condition and Simulation Setup*

A reference cutting condition used in [Kalhori, 2000] was selected due to availability of the experimental forces and chip geometries from orthogonal turning tests on AISI 1045. This plain carbon steel is commonly used in the industry and the flow stress data of AISI 1045 is available from a number of publications. These data could be used as basis for this study. In [Kalhori, 2000],

orthogonal cutting tests were conducted using an uncoated tungsten carbide tool with rake angle of +6 degrees. Table 4.7 summarizes tool geometry and cutting condition used.

Physical and thermal material properties of the tool and the workpiece were obtained from the literature [ASM, 1990; Obikawa, 1995]. Other simulation inputs (i.e. mesh definition, sizes of the tool and the workpiece in FEM model) were selected such that the simulated results would not be sensitive to these inputs. For example, approximately 30 percent change in element size or numbers of elements would not cause significant difference in the simulation results. Physical and thermal properties of AISI 1045 and uncoated tungsten carbide, used in this study, are summarized in Table 4.8 and Figure 4.29.

<b>Cutting Parameter [Unit]</b>	<b>Magnitudes</b>
Cutting velocity, $V_c$ , [m/min]	198
Feed rate, $f$ [mm/rev]	0.25
Rake angle, $\alpha$ [degree]	6
Clearance angle, $\gamma$ [degree]	6
Edge radius, $r$ [ $\mu\text{m}$ ]	50

Table 4.7: A cutting condition used in orthogonal cutting experiments of AISI 1045, in [Kalhori, 2000]

	<b>Workpiece: AISI 1045</b>	<b>Tool: Uncoated Tungsten Carbide</b>
Material Behavior	Plastic	Rigid
Young's Modulus, $E$ [MPa]	205,000	558,000
Poisson's ratio, $\nu$	0.30	0.22
Material density, $\rho$ [ $\text{Kg/m}^3$ ]	7850	11900
Emissivity, $\gamma_c$	0.75	-

Table 4.8: Basic mechanical properties of the AISI 1045 workpiece and uncoated tungsten carbide tool

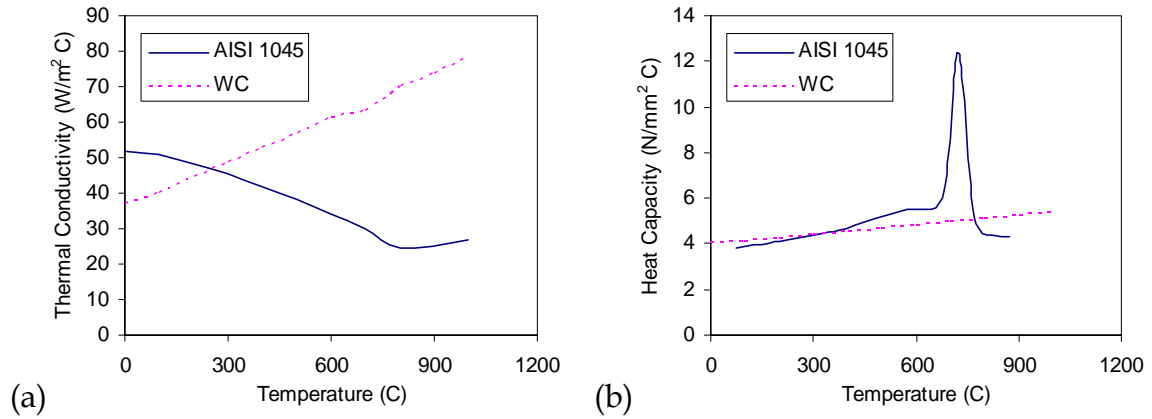


Figure 4.29: Thermal properties of the workpiece material (AISI 1045) and uncoated tungsten carbide, from [ASM, 1990] and [Obikawa, 1995]; (a) Thermal conductivity and (b) heat capacity.

Friction condition along the tool-chip interface was assumed according to the shear friction law with the friction factor ( $m_f$ ) of 0.6 because high normal pressure is present along the tool-chip contact area and the friction factor of 0.6 was recommended from previous simulation work on low carbon steel [Jain, 2001]. Experimental investigation of tool stresses using the split tool technique estimated the friction factor ( $m_f$ ) of 0.5 to 0.9 for various tool-workpiece contacts and found that only a small sliding region (which is described by Coulomb's friction) on the tool rake face existed [Chandrasekeran, 1965; Childs, 1989]. This assumed friction condition was applied on the tool/chip contact on the rake face, tool edge radius and the tool flank face.

Figure 4.30 shows the workpiece and tool geometry at the initial position. The sizes of the workpiece and the tool in simulation model need to be large enough so that the predicted results are not sensitive to the displacement boundary conditions. Mesh density was defined such that sufficient numbers of



elements (at least three elements) fit along the tool edge radius to avoid inaccuracy from remeshing after element distortion. Displacement and thermal boundary conditions of the tool and the workpiece are defined in Figure 4.30 (where  $V$  = velocity,  $T$  = temperature,  $V_c$  = cutting velocity and  $RT$  = room temperature).

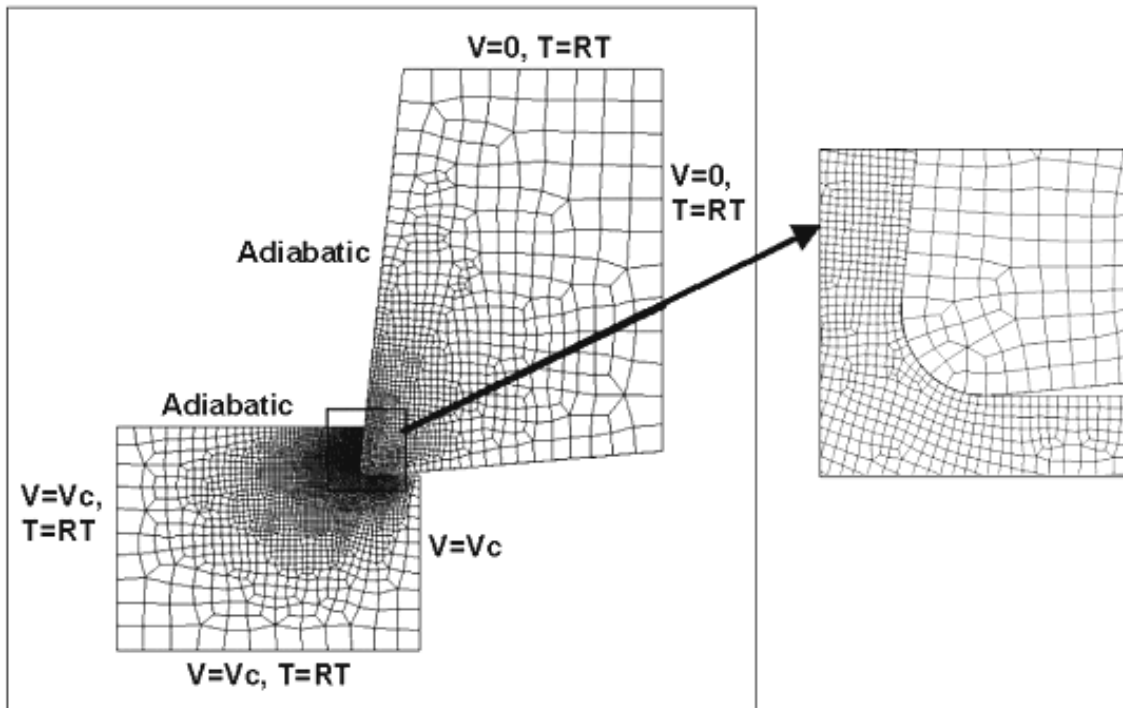


Figure 4.30: Workpiece and tool geometry used in the simulations for the sensitivity analysis of flow stress and friction

#### 4.2.1.2. *The Reference Flow Stress and Variations of Flow Stress Parameters*

A complete sensitivity analysis of Johnson & Cook flow stress equation was conducted and presented in [Arrozola 2003]. Arrozola's results showed strong relation with temperature factor in the flow stress equation. It was suggested that Johnson & Cook's equation may not sufficiently explain the relation of temperature to the flow stress. The use of Power law equation could provide more variety in modeling temperature influence. Thus, for the sensitivity analysis of the flow stress in this study, a Power law (Equation 4.7) is used to represent plastic behavior of the workpiece because it is commonly used to represent the flow stress data in a broad testing range. Temperature effects were coupled with the flow stress parameters (i.e. strength coefficient, strain hardening and strain rate hardening) for better representing the flow stress behavior. A simplified equation that decouples the temperature effect (e.g. Johnson & Cook's equation) may not capture all aspects of the flow stress properties such as the reduction of strain hardening over increasing temperature.

$$\sigma = C(T)\varepsilon^{n(T)}\left(\frac{\dot{\varepsilon}}{1000}\right)^{m(T)} \quad \text{Equation 4.7}$$

where  $\sigma$  = Flow stress or true stress (MPa)

$T$  = Temperature (°C)

$C(T)$  = Strength coefficient (MPa), in function of temperature

$\varepsilon$  = Strain

$\dot{\varepsilon}$  = Strain rate (s<sup>-1</sup>)

$n(T)$  = Strain hardening in function of temperature

$m(T)$  = Strain rate hardening in function of temperature

A reference flow stress equation was selected such that the data approximately matched the flow stress data obtained from the literature within various testing conditions, as shown in Figure 4.31. Flow stress data of AISI 1045 steel obtained from different sources were consistent except for the maximum difference of 39% at the blue-brittleness temperature of 550 °C, for the strain of 0.3 and the strain rate of 400 s<sup>-1</sup> (see Figure 4.31 (b)). Linear relations of the temperatures were assumed for all flow stress parameters (i.e.  $C(T)$ ,  $n(T)$ ,  $m(T)$ ) to simplify the sensitivity analysis and to minimize the number of simulations.

The reference flow stress equation has the parameters  $C(T) = 1400(0.95 - 0.00065T)$ ,  $n(T) = 0.2(0.95 - 0.00065T)$  and  $m = 0.03$ . The reference flow stress curves are shown in Figure 4.31. Due to high temperature, strain and strain rate in metal cutting, the flow stress data was assumed to be applicable in wide ranges of conditions, for

strain:	$0 \leq \varepsilon \leq 5$
strain rate:	$0.1 \leq \dot{\varepsilon} \leq 1,000,000 \text{ s}^{-1}$
temperature:	$20 \leq T \leq 1,200 \text{ } ^\circ\text{C}$

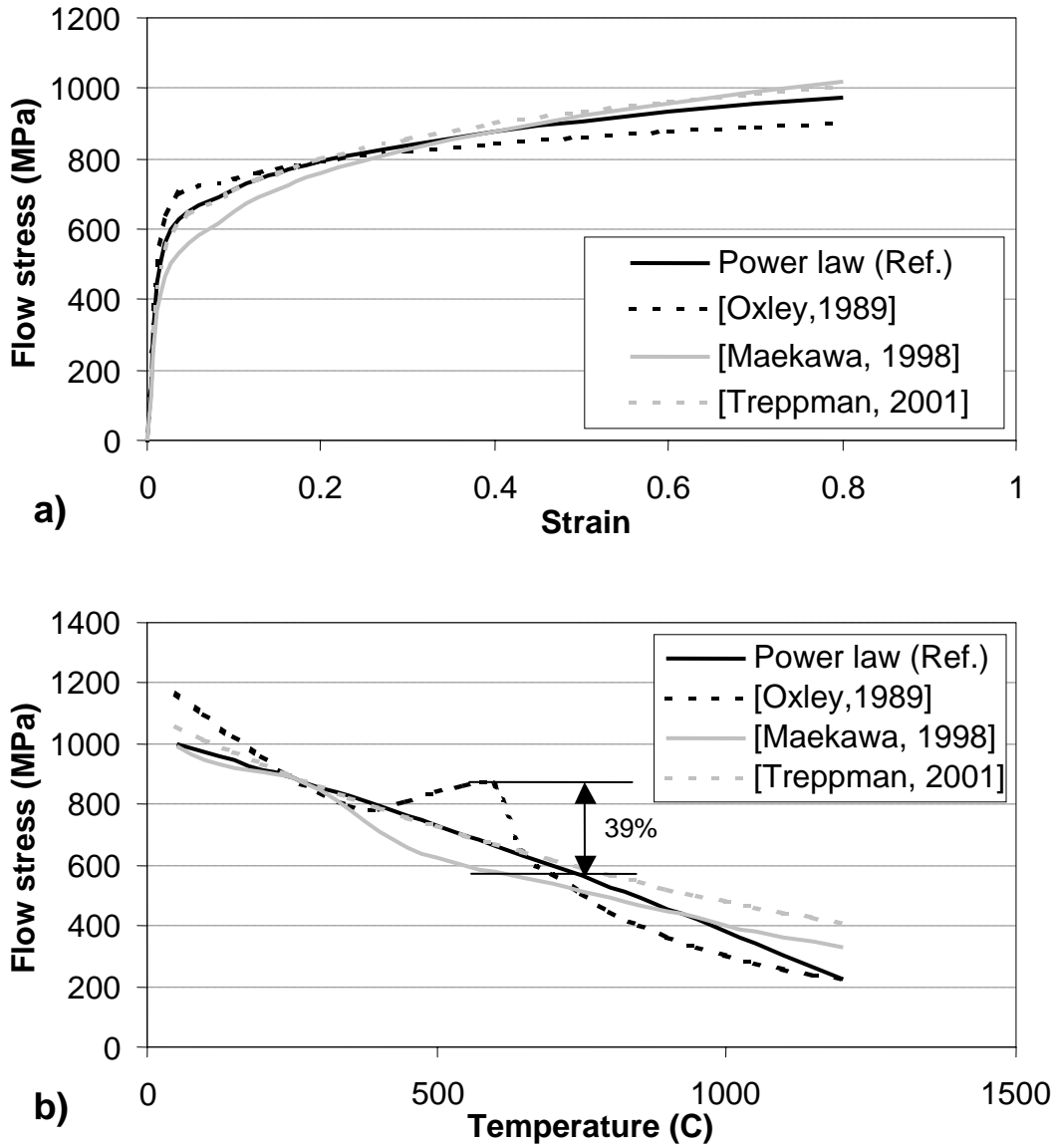


Figure 4.31: Reference flow stress equation compared with different flow stress data of AISI 1045 steel from the literature [Oxley, 1989; Maekawa, 1998 and Treppman, 2001]: a) stress-strain curves at strain rate of  $200 \text{ s}^{-1}$  and temperature of  $300 \text{ }^\circ\text{C}$ , and b) stress-temperature curves at strain rate of  $400 \text{ s}^{-1}$  and strain of 0.3.

Table 4.9 illustrates the variations of the flow stress parameter sets for the preliminary FEM simulations (#1 to #10) used to conduct the sensitivity analysis for one cutting condition. Simulation #1 uses the reference flow stress equation. Compared to the reference flow stress, the flow stress used in simulation #2 has a larger drop of the strength coefficient,  $C(T)$ , with increasing temperature. Simulation #3 uses the flow stress that has a smaller drop of the strength coefficient,  $C(T)$ , with increasing temperature. Simulation #4 uses the flow stress that has a higher magnitude of the strength coefficient,  $C(T)$ , but the same slope as the reference flow stress, as shown in Figure 4.32(a) (curves #1 and #4). The flow stress for simulation #5 has a larger reduction of the strain hardening coefficient,  $n(T)$ , with increasing temperature. The flow stress for simulation #6 has a smaller reduction of  $n(T)$  with increasing temperature than the reference flow stress, as shown in Figure 4.32(b).

Run No.	Flow Stress Parameter		
	$C(T)$	$n(T)$	$m(T)$
#1 (ref.)	1400(0.95-0.00065T)	0.2(0.95-0.00065T)	0.03
#2	1400(1.1-0.0009T)	0.2(0.95-0.00065T)	0.03
#3	1400(0.8-0.0004T)	0.2(0.95-0.00065T)	0.03
#4	1400(1.086-0.00065T)	0.2(0.95-0.00065T)	0.03
#5	1400(0.95-0.00065T)	0.2(1.1-0.0009T)	0.03
#6	1400(0.95-0.00065T)	0.2(0.8-0.0004T)	0.03
#7	1400(0.95-0.00065T)	0.2(0.95-0.00065T)	0.06
#8	1400(0.95-0.00065T)	0.2(0.95-0.00065T)	0.03+0.00002T
#9	1400(0.95-0.00065T)	0.2(0.95-0.00065T)	0.03+0.00004T
#10	1400(0.95-0.00065T)	0.2(0.95-0.00065T)	0.03 when $\dot{\epsilon} \leq 1000 \text{ s}^{-1}$ 0.07 when $\dot{\epsilon} > 1000 \text{ s}^{-1}$

Table 4.9: Flow stress parameter sets for the preliminary analysis of flow stress on one cutting condition

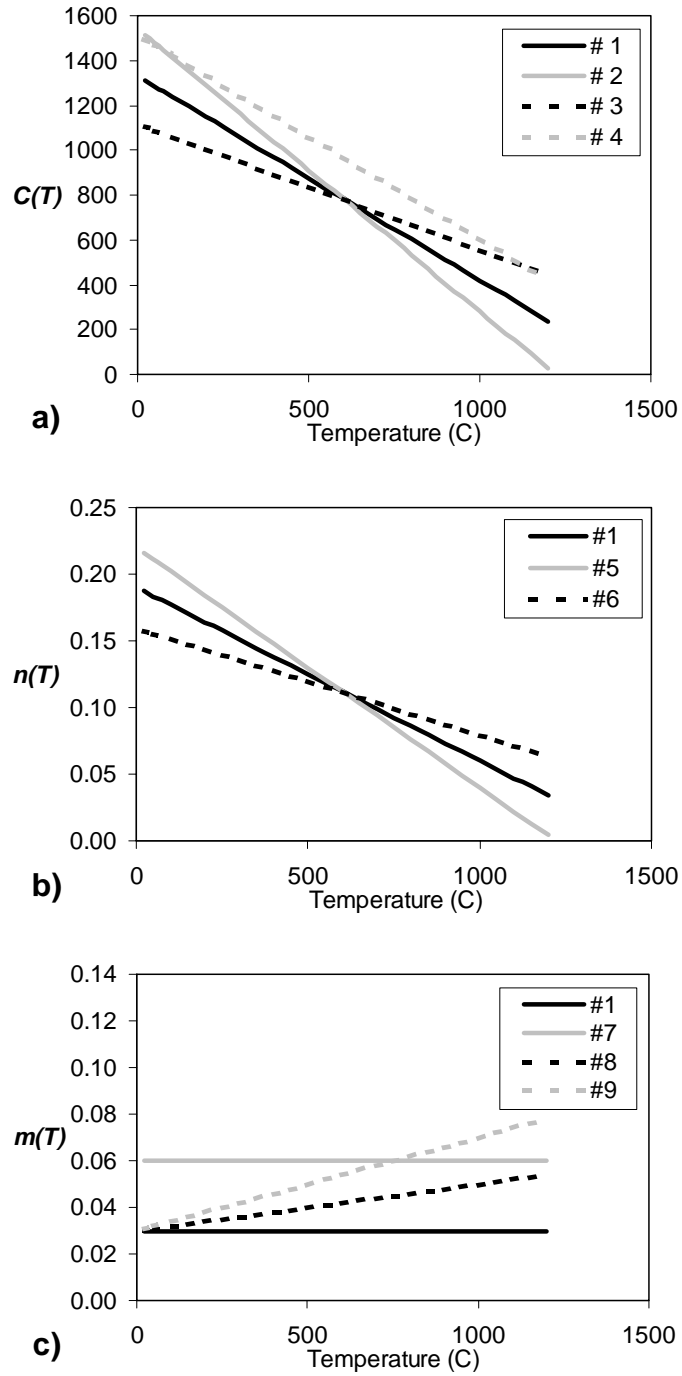


Figure 4.32: Variations of flow stress parameters over temperatures, according to Table 4.9

In Figure 4.32(c), the flow stress for simulation #7 has a higher constant strain rate hardening than that of the reference. The flow stress data for simulations #8 and #9 have a smaller and a larger increment of  $m(T)$  with increasing temperature. In fact, an increase of strain rate hardening with increasing temperature can be observed in hot compression tests in most metals. Flow stress input for simulation #10 has two strain rate hardenings coefficients,  $m=0.03$  for low strain rate range and  $m=0.07$  for high strain rate range. Increase in strain rate hardening at high strain rate was normally observed in SHPB tests, as shown in Figure 4.33 [Treppman, 2001].

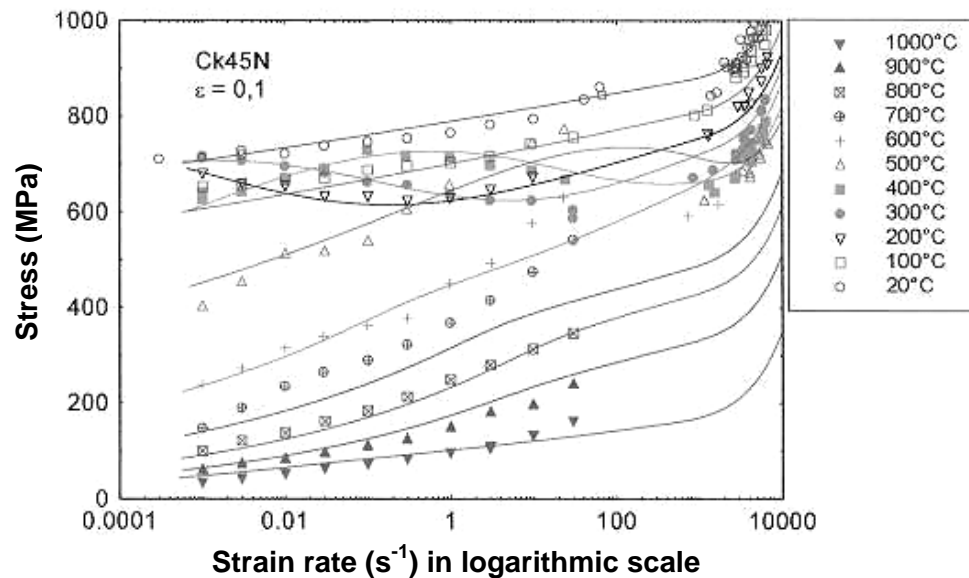


Figure 4.33: Stress-strain rate curves of AISI 1045 steel from Hopkinson's bar tests at the strain of 0.1 and different temperatures [Treppman, 2001]. Lines represent a constitutive equation determined to fit the experimental flow stress data

#### 4.2.1.3. Simulation Results for Sensitivity Analysis of One Cutting Condition

Each flow stress parameter of the power law equation was changed in its magnitude and its variation with temperature. Table 4.10 shows the results of the simulations #1 to #10.

Simulation Results						
Run No.	Cutting Force [N]	Thrust Force [N]	Chip Thickness [mm]	Shear Angle [°]	Contact Length [mm]	Max. Tool Temperature [°C]
#1 (ref.)	1681	433	0.52	28.8	0.45	771
#2	1710	424	0.47	30.3	0.41	780
#3	1680	461	0.62	24.7	0.49	751
#4	1932	499	0.53	28.0	0.44	869
#5	1701	430	0.55	27.2	0.45	770
#6	1657	436	0.51	28.9	0.43	772
#7	1763	445	0.51	26.3	0.44	804
#8	1708	438	0.55	27.8	0.44	793
#9	1710	424	0.47	30.5	0.41	807
#10	1797	450	0.49	29.4	0.44	837

Table 4.10: Simulation results for the preliminary analysis of flow stress on one cutting condition

For the effect of the parameter  $C(T)$ , the results from the simulations #1, #2, #3 and #4 (see Table 4.9 and Figure 4.32(a)) were compared. 10% decrease in chip thickness was observed for simulation #2 (large drop of  $C(T)$  over temperature) while 20% increase in chip thickness was observed for simulation #3 (small drop of  $C(T)$  over temperature). Shear angle was inversely proportional to the chip thickness and was independent of the flow stress input. The tool/chip



contact length had a direct relation with the chip thickness. Simulation #4 (with higher  $C(T)$  magnitude but same variation with temperature as that of reference data) yielded 15% increase in both cutting force and thrust force, though there was almost no difference in chip thickness. Results indicated that variation of  $C(T)$  over temperature influences chip thickness. The larger is the reduction of  $C(T)$  over increasing temperature, the thinner is the chip and the shorter is the contact length. Cutting force and thrust force are not much affected by the variation of  $C(T)$  with increasing temperature but by the magnitude of  $C(T)$ .

To study the sensitivity of the parameter  $n(T)$ , results from the simulations #1, #5 and #6 (see Table 4.9 and Figure 4.32(b)) were compared. These three simulations had different variations of the strain hardening exponents over the temperatures. From Table 4.10, different variations of  $n(T)$  over temperature did not show significant difference in all simulation outputs (approximately within  $\pm 5\%$  difference compared with the results from the reference simulation). Therefore, the effect of temperature upon strain hardening is considered insignificant and can be assumed to be approximately constant. Additional simulations were later conducted using constant strain hardening and different tool rake angles, as will be addressed in the next section.

For the sensitivity study of the parameter  $m(T)$ , results from the simulations #1, #7, #8, #9 and #10 were compared. Insignificant differences of all results (within  $\pm 8\%$  change of cutting force, thrust force, chip thickness and contact length) were observed although there is considerable difference in strain rate hardening, and its relations with temperature and with strain rate. Similar to strain hardening, strain rate hardening coefficient can be assumed as constant. Results of additional simulations with different speeds and feed rates will be discussed in the next section, Section 4.2.2.

#### 4.2.2. Sensitivity Analysis for Different Cutting Conditions

The analysis of one cutting condition did not sufficiently showed the effects of the flow stress parameters  $n(T)$  and  $m(T)$ . Thus, additional cutting simulations were conducted. Different cutting conditions and flow stress parameters are listed in Table 4.11.

Run No.	Flow Stress Parameter			Cutting Condition		
	$C(T)$	$n(T)$	$m$	Rake Angle $\alpha$ [deg]	Cutting Speed $V_c$ [m/min]	Feed Rate $f$ [mm/rev]
#11	1400(0.95-0.00065T)	0.1	0.03	6	198	0.25
#12	1400(0.95-0.00065T)	0.2	0.03	6	198	0.25
#13	1400(0.95-0.00065T)	0.1	0.03	-5	198	0.25
#14	1400(0.95-0.00065T)	0.2	0.03	-5	198	0.25
#15	1400(0.95-0.00065T)	0.2(0.95-0.00065T)	0.03	6	500	0.25
#16	1400(0.95-0.00065T)	0.2(0.95-0.00065T)	0.03	6	500	0.125
#17	1400(0.95-0.00065T)	0.2(0.95-0.00065T)	0.06	6	500	0.25
#18	1400(0.95-0.00065T)	0.2(0.95-0.00065T)	0.06	6	500	0.125
#19	1400(0.95-0.00065T)	0.2(0.95-0.00065T)	0.1	6	198	0.25
#20	1400(0.95-0.00065T)	0.2(0.95-0.00065T)	0.1	6	500	0.25
#21	1400(0.95-0.00065T)	0.2(0.95-0.00065T)	0.1	6	500	0.125

Table 4.11: Flow stress parameter sets for the analysis of flow stress on different cutting conditions

##### 4.2.2.1. Additional Cutting Conditions and Variations of Flow Stress Parameter Sets

The analysis on one cutting condition showed that strain hardening coefficient could be assumed to be constant. Simulations #11 and #12 use  $n=0.1$  and  $n=0.2$ , respectively. These two simulations have the same cutting conditions

and use the same tool rake angle as that of the reference (with 6 degree positive rake angle). Simulations #13 and #14 use constant  $n=0.1$  and  $n=0.2$ , but using a tool with negative rake angle of -5 degree. Different rake angles provide different magnitudes of strains in cutting, where a larger negative rake angle indicates more plastic strain produced in primary shear zone.

Simulations at higher strain rate conditions (higher cutting speed and feed rate) were also added in order to observe the effect of strain rate hardening. Simulations used for analysis of strain rate effect are indicated as the simulations #1, #7, and #15 to #21, as shown in Table 4.11. Three cutting conditions were simulated: (a)  $V_c=198$  m/min with  $f=0.25$  mm/rev., (b)  $V_c=500$  m/min with  $f=0.25$  mm/rev. and (c)  $V_c=500$  m/min with  $f=0.125$  mm/rev., respectively, from low to high strain rate conditions. Summary of flow stress parameter inputs and cutting conditions relevant to levels of strain rates is shown in Table 4.12.

#### 4.2.2.2. *Simulation Results*

Results of simulations #11 to #21 are shown in Table 4.13. For the effect of the strain hardening, simulations #11 to #14 are considered. Results show that strain hardening influences the chip thickness, the contact length and the force. For positive rake tool, 100% increase in strain hardening ( $n$  value) provides 11% increase in cutting force, 7% increase in thrust force and 19% increase in chip thickness. For negative rake tool, 100% increase in  $n$  value has more influence on the simulation results, where it yielded 27% increase in cutting force, 23% increase in thrust force and 31% increase in chip thickness. The larger influence of  $n$  value when using a negative rake tool can be explained by the larger deformation (high strain) in the primary shear zone. In the flow stress model, the difference in strain hardening causes more difference in the flow stress at the higher strain condition, comparing to the lower strain that exists when cutting with a positive rake tool.

Run No.	Flow Stress Parameter			Cutting Condition		Strain Rate Level [ $\propto V_c/f$ ]
	$C(T)$	$n(T)$	$m$	Cutting Speed, $V_c$ [m/min]	Feed Rate, $f$ [mm/rev]	
#1(Ref.)	1400(0.95-0.00065T)	0.2(0.95-0.00065T)	0.03	198	0.25	Low
#15	1400(0.95-0.00065T)	0.2(0.95-0.00065T)	0.03	500	0.25	Midium
#16	1400(0.95-0.00065T)	0.2(0.95-0.00065T)	0.03	500	0.125	High
#7	1400(0.95-0.00065T)	0.2(0.95-0.00065T)	0.06	198	0.25	Low
#17	1400(0.95-0.00065T)	0.2(0.95-0.00065T)	0.06	500	0.25	Midium
#18	1400(0.95-0.00065T)	0.2(0.95-0.00065T)	0.06	500	0.125	High
#19	1400(0.95-0.00065T)	0.2(0.95-0.00065T)	0.10	198	0.25	Low
#20	1400(0.95-0.00065T)	0.2(0.95-0.00065T)	0.10	500	0.25	Midium
#21	1400(0.95-0.00065T)	0.2(0.95-0.00065T)	0.10	500	0.125	High

Table 4.12: Selected flow stress parameter sets for an analysis on the effect of strain rate hardening ( $m$ )

Run No.	Simulation Results					
	Cutting Force [N]	Thrust Force [N]	Chip Thickness [mm]	Shear Angle [°]	Contact Length [mm]	Max. Tool Temperature [°C]
#11	1840	511	0.48	31.2	0.40	876
#12	2045	546	0.57	25.9	0.46	907
#13	2195	936	0.54	25.5	0.50	885
#14	2608	1148	0.71	21.6	0.62	901
#15	1654	384	0.51	28.7	0.43	946
#16	963	347	0.29	27.7	0.24	851
#17	1765	396	0.50	30.1	0.41	997
#18	1053	373	0.26	29.2	0.23	906
#19	1888	459	0.48	30.0	0.43	850
#20	1933	418	0.47	31.0	0.41	1059
#21	1165	408	0.26	31.0	0.23	983

Table 4.13: Simulation results for the analysis of flow stress on different cutting conditions

The simulation results also indicated that for  $n=0.1$ , an increase of 13% in chip thickness was observed when switching from positive to negative rake tools. For  $n=0.2$ , the chip thickness increased by 25%. Differences in cutting forces between positive and negative rake tools were 19% for  $n=0.1$  but 27% for  $n=0.2$ . These observations indicate that it is possible to estimate the value of strain hardening from the simulations of cutting with two different tool rake angles.

Table 4.12 presents the simulations considered for studying the effect of strain rate hardening ( $m$  value). The results of three different  $m$  values for three different strain rate conditions are shown in Table 4.10 (for simulations #1 and #7) and Table 4.13 (for simulations #15 to 21). No significant differences in chip thickness, contact length and shear angle were found for the simulations with different  $m$  values for one cutting condition. Differences in cutting forces between  $m=0.03$  and  $m=0.1$  were observed at different cutting conditions. Difference in cutting forces between  $m=0.03$  and  $m=0.1$  were 12% for low-strain-rate condition (from the simulations #1 and #19), 17% for mid-strain-rate condition (from the simulations #15 and #20) and 21% for high-strain-rate condition (from the simulations #16 and #21). Thus, the effect of  $m$  values on the cutting force was noticeable when cutting at high speed and low feed rate. Thrust forces also showed similar effects. Experimental observations mostly show that the cutting force decreases as the cutting speed increases. This was observed from the predicted cutting forces of the simulations #1 and #15 (see Table 4.10 and Table 4.13), cutting force slightly decreased from 1681 to 1654 N as the cutting speed increased from 198 to 500 m/min.

#### 4.2.3. *Summary and Discussions on Sensitivity Analysis of Flow Stress in FEM Cutting Simulation*

Flow stress parameters influence mainly the chip thickness, the cutting force and the thrust force, as summarized in Table 4.14. However, the shear angle and the tool/chip contact length are directly proportional to the chip thickness for all simulations, regardless of the differences in the flow stress parameters.

Cutting and thrust forces obtained from the simulations are directly proportional to the magnitude of  $C(T)$ . This is due to the fact that the level of  $C(T)$  parameter represents the work required to form the chip but does not influence the geometry of the deformed workpiece. The reduction of  $C(T)$  with increasing temperature shows an inverse relation with chip thickness. The larger reduction of  $C(T)$  with increasing temperature implies a higher flow stress at low temperature and a lower flow stress at high temperature (previously shown in Figure 4.32 (a)). Higher flow stress at low temperature allows the chip to form with more difficulty at the beginning of cutting and thus causes a thinner chip. On the contrary, the chip was thicker for a smaller reduction of  $C(T)$  with increasing temperature.

Effects of the variations of the strain hardening  $n(T)$  with increasing temperature showed insignificant differences (approximately  $\pm 5\%$ ) in all simulation results (i.e. cutting force, thrust force, chip thickness, contact length). Thus, the effect of temperature upon strain hardening can be neglected. Increasing the magnitude of strain hardening shows significant increase in cutting force, chip thickness but slight increase in thrust force. The strain hardening has a large effect on cutting force when using a negative rake tool. The reasons are that a high strain exists when cutting with a negative rake tool and that strain hardening causes a high flow stress at a high strain.

Flow Stress Parameter	Changes in Flow Stress Parameter	Effects on Simulation Results	
<b><math>C(T)</math></b>	Magnitude	Higher (+18%) 15% increase in cutting force and thrust force however insignificant change in chip thickness.	
	Variation over the temperature	Smaller drop over temperature	20% increase in chip thickness but insignificant changes in cutting force and thrust force
		Larger drop over temperature	10% decrease in chip thickness but insignificant changes in cutting force and thrust force
<b><math>n(T)</math></b>	Magnitude (Constant)	Higher (+100%) on positive rake tool	18% increase in chip thickness, 11% increase in cutting force and 7% increase in thrust force
		Higher (+100%) on negative rake tool	31% increase in chip thickness, 24% increase in cutting force and 19% increase in thrust force
	Variation over temperature	Smaller drop over temperature	Less than $\pm 5\%$ change in all simulation results
		Larger drop over temperature	Less than $\pm 5\%$ change in all simulation results
<b><math>m(T)</math></b>	Magnitude (Constant)	Higher (+100%)	Less than $\pm 5\%$ change in all simulation results
		Higher (+233%)	12% increase in cutting force, 6% increase in thrust force and 8% decrease in chip thickness
		Higher (+233%) but at high cutting speed and low feed rate	21% increase in cutting force, 17% increase in thrust force and 10% decrease in chip thickness
	Variation over temperature	Small increase over temperature	Within $\pm 6\%$ changes in all simulation results
		Large increase over temperature	Within $\pm 8\%$ changes in all simulation results
Sudden increase at high strain rate	Higher m-value at $\dot{\epsilon} > 1000 \text{ s}^{-1}$	Within $\pm 7\%$ changes in all simulation results	

Table 4.14: Summary of the sensitivity analysis of the flow stress parameters

The effects of temperature and strain rate on strain rate hardening did not show significant differences (about  $\pm 8\%$ ) in all simulation results (i.e. cutting force, thrust force, chip thickness, contact length). The effect of constant  $m$  value

did not show significant effect since 100% increase in  $m$  value gave only  $\pm 5\%$  change in all cutting simulation results.

The reason that  $m$  value shows small effect in simulation results is mainly due to the fact that strain rate dependence is small in most metals. For most materials,  $m$  values fall in the range of 0.01 to 0.1 while  $n$  values are between 0.1 to 0.5. In cutting, although high cutting speed may generate very high strain rate in the deformation zone, the effect of strain and temperature are still dominant. High strain up to 10 can exist for the workpiece along the tool/chip interface and near the tool edge. Temperature can rise up to 1000 °C due to heat generated from friction, which tends to be higher at high cutting speed.

The effect of strain rate can be significant at extremely high cutting speed and low feed rate. As can be seen in Table 4.13, at reference cutting condition ( $V_c=198$  m/min and  $f=0.25$  mm/rev), 12% increase in cutting force and 6% increase in thrust force were observed when  $m$  increases from 0.03 to 0.1. Meanwhile, at higher speed and lower feed ( $V_c=500$  m/min and  $f=0.125$  mm/rev), 21% and 17% increases in cutting force and thrust force were observed for the same increment of  $m$ . This effect is due to considerably higher strain rate condition when using a higher cutting speed and a lower feed rate. Thus it causes higher flow stress and cutting force.

Simulations showed some independent relations between the flow stress and the predicted machining results, as summarized below.

- The tool/chip contact length is directly proportional to the predicted cut chip thickness rather than to the flow stress parameters.
- The thrust force is always much less sensitive to the flow stress parameters than the cutting force.



- The predicted thrust forces at the reference cutting condition are always lower than experimental force (755 N), by approximately 30% to 45%. A similar discrepancy was observed in [Bil, 2004], although the authors used three different FEM packages and various values of friction parameters. Disagreement of the thrust forces may be due to the difference between the FEM model and actual turning operation. Force measurement in orthogonal turning considers not only the thrust force from chip formation but also the force that presses the tool upon the workpiece in feed direction. Most 2D FEM cutting models, however, simulate a “shaving operation” and disregard this force. This issue needs to be addressed in future research.

#### **4.3. MAterial DAtabase for Machining Simulation (MADAMS)**

Although, there are a vast number of material properties at high strain rates and temperatures available from the literature and those data publicly available from different researchers, there is still no attempt of putting these data together to benefit researchers and engineers who are working in FEM modeling of machining.

As part of research contribution on the field of material flow stress properties for machining, mainly discussed in this section, MAterial DAtabase for Machining Simulation (MADAMS) was established. This database is a collection of the material property information, which is crucial for FEM simulations of machining processes.

To date, material data have been collected from 1) a literature review and 2) the information provided by German researchers who participated in the DFG-High Speed Cutting project [Toenshoff, 1999]. An overview of MADAMS

program (i.e. the objectives, the activities and the on-line electronic database) is given below.

#### *4.3.1. An Overview of MADAMS Program*

Two major objectives of MADAMS program are to a) create and document a database for the material flow stress data for use in FEM simulation of machining processes and b) promote collaboration among researchers interested in modeling of machining. To accomplish these objectives, a number of tasks have been conducted.

- Conduct a literature review to collect the material flow stress data at high strain rates (above  $500 \text{ s}^{-1}$ ).
- Create and distribute a questionnaire to researchers in areas of machining and material property determination.
- Review the completed questionnaires and contributed papers.
- Build an electronic database file (a MADAMS ACCESS file) to compile the material data provided.
- Prepare progress reports summarizing the material information.
- Create an Internet website to continue obtaining additional material data, updating the database and distributing an access to the on-line material database to any researchers, interested in this study.

Provided they were available, data for various materials, stored in the database, consist of:

- Material name
- Chemical composition (in either %weight or %volume)

- Heat treatment condition of the workpiece sample, used in the tests
- Hardness of workpiece surface (at room temperature)
- Tensile and yield strength (from tensile tests at room temperature)
- Percentage of elongation (from tensile tests at room temperature)
- Percentage reduction in cross section area (from tensile test)
- Flow stress at room temperature (stress-strain curves or flow stress equation of material at room temperature)
- Flow stress at high strain rate (in form of diagrams or constitutive equations), together with the information of the testing machine used, and applicable ranges of strain, strain rate and temperature.

Some information on tested materials may be absent if this data was not provided by the contributors. In addition, thermal properties of the workpiece (e.g. thermal conductivity, heat capacity), which are also necessary for FEM simulations, are not included into MADAMS. Thermal properties, in general, can be found in various metal handbooks [ASM, 1990] and [ASM, 1991].

Currently, the material information are obtained from three main sources, namely:

- A review of literature [Sartkulvanich, 2001]
- Questionnaires completed by the researchers who contributed to the DFG-High Speed Cutting project [Sartkulvanich, 2001a]
- Slot milling tests, conducted at the ERC/NSM [Sartkulvanich, 2004]

A number of research groups who are working on determining the material properties at high strain rates can be summarized in Table 4.15. Results by most of these researchers are published and given in the reference column of

the table. This list however represents only the contributors of the material data in MADAMS database.

<b>Research Leader</b>	<b>Institute /Country</b>	<b>Testing Methods</b>	<b>Materials</b>	<b>References</b>
Altan	ERC/NSM at Ohio State U., USA	Machining tests	Steels, Al alloys	[Shatla, 1999; Shatla, 2001; Sartkulvanich, 2004]
Armstrong	U. of Maryland, USA	SHPB and Explosive tests	Al alloys	[Zerilli, 1987]
Bless	U. of Dayton, USA	SHPB tests	Steels, Al alloys, Ni alloys, W alloys	[Rosenberg, 1986]
Dautzenberg	Eindhoven U. of Tech., Netherlands	Machining and SHPB tests	Steels, Al alloys	[Dautzenberg, 1981]
El-magd	RWTH Aachen, Germany	SHPB tests	Steels, Al alloys, Ti alloys	[Trepman, 2001; El-Magd, 1999]
Elbestawi	McMaster U., Canada	SHPB and Machining tests	Steels	[Becze, 2001]
Gilat	Ohio State U., USA	SHPB tests	Steels, Al alloys	[Gilat, 1994; Gilat, 1994a]
Gray	Los Alamos Nat. Lab., USA	SHPB tests	Ni alloys, Ti, Mo alloys	[Sizek, 1993; Gray, 1997; Chen, 1997]
Lee	National Cheng Kung U., Taiwan	SHPB tests	Steels, Ti alloys, W alloys, Al alloys	[Lee, 1998; Lee, 1998a; Lee, 2000]
Shin	Purdue U., USA	Machining tests	Steels	[Lei, 1999]
Liang	Georgia Tech., USA	SHPB and Machining tests	Hardened steels	[Ramesh, 2002; Huang, 2002]
Liu	Purdue U., USA	Tensile and Machining tests	Hardened steels	[Liu, 2000; Guo, 2002]

**Continued →**

Table 4.15: Active research groups on the area of material modeling for high strain rates

Table 4.15 continued

<b>Research Leader</b>	<b>Institute /Country</b>	<b>Testing Methods</b>	<b>Materials</b>	<b>References</b>
Maekawa	Ibaraki U., Japan	SHPB tests	Steels, Ti alloys	[Shirakashi, 1983; Maekawa, 1983; Maekawa, 1991; Maekawa, 1993; Maekawa, 1996; Childs, 1990; Childs, 1997]
Mathew	U. of New South Wales, Australia	Machining tests	Steels, Al alloys	[Mathew, 1993; Kristyanto, 2002]
Meslin	LMM Nantes, France	SHPB tests	Steels, Ti alloys	[Hamann, 2002]
Meyer	Tech. U. Chemnitz, Germany	Impact pendulum, Fly wheel and SHPB tests	Steel, Al alloys, Ti alloys, W alloys	[Meyer, 1984; Meyer, 2000]
Meyers	U. of Cal. at San Diego, USA	SHPB tests	Al alloys	[Xu, 2001]
Nemat-Nasser	CEAM U. of CA. at San Diego, USA	SHPB tests	Ta alloys	[Nemat-Nasser, 1997]
Poulachon	LaBoMap ENSAM, France	SHPB tests	Hardened steels	[Poulachon, 2001]
Schulze	U. Karlsruhe (TH), Germany	SHPB tests	Steels	[Schulze, 2000]
Shirakashi	Tokyo Denki U., Japan	SHPB tests	Steels, Ti alloys	[Shirakashi, 1983; Maekawa, 1983; Maekawa, 1993; Usui, 1984]
Stevenson	GM R&D Center, USA	Static compression and Machining tests	Steels	[Stevenson, 1997]

#### 4.3.2. *MADAMS Web Site and the Material Database*

The web site of MADAMS was established in order to provide user-friendly access and to provide an update of MADAMS (e.g. new materials, new activity, etc.). The web site is located at

<http://nsm.eng.ohio-state.edu/madams/index.html>

The MADAMS web site contains four main pages: 1) introduction page, 2) material data submission page and 3) access to the database page. User name and password are required for access to the material database. More detailed aspects of MADAMS and procedure to obtain the password are described on the web site.

The first introduction page describes the general aspects of MADAMS database, and current announcements for new materials and updates.

The second page contains a questionnaire for uploading new material information. Purpose of this page is to encourage researchers (both (a) visitors who have already used MADAMS and (b) those who are first time visitors) to submit their contact information and material properties to MADAMS administrator. Uploaded information will be verified and transferred into the database.

The third page contains the link to access MADAMS database. Username and password are required to gain access to the database. Procedure and regulation to obtain the password are also described in this third page. Once, the user is able to enter to on-line the database, he/she can select the material name and view the material property information, as shown in Figure 4.34.

#### **4.3.3. *Summary and Discussions***

MADAMS or (MAterial DAtabase for Machining Simulation) program is established to collect mainly the material flow stress properties for FEM machining simulation in a database. General information and the current status of MADAMS can be found at its web site, at

<http://nsm.eng.ohio-state.edu/madams/index.html>

The web site as well as the material database has been updated periodically for the new material data. This established program provides very useful information for the researchers who are interested and facilitates collaboration for obtaining additional material property data for machining research.

The screenshot shows a web browser window displaying the MADAMS Material Database for Machining Simulations. The page features a header with the Ohio State University logo and the title "Material Database for Machining Simulations (MADAMS)". Below the header are navigation links: "Select Material", "Show Publication", and "Menu".

The main content area displays material data for AISI 1045, organized into several tables:

Material	Composition	Heat Treatment	Note to Heat Treatment	Hardness
AISI 1045		Annealed		93 HRB

Tensile Strength	Yield Strength	Elongation	Reduction in Area	Flow Stress at RT
655 MPa	515 MPa			

Constitutive Equation	Note to Constitutive Equation	Source of Constitutive Equation	Diagram	Thermal Condition
<a href="#">Click for Equation</a>			<a href="#">Click for Diagram</a>	

Testing Machine	Limits of the Machine	Notes Regarding Limits
Slot milling experiments		Strain = 0.74 to 1.35 Strain rate = 26,222-684,114 /s Temperature = 244 to 902 °C

Note: The equations and diagrams open in MS Word format in a new window

Figure 4.34: Example of material data information provided in the MADAMS

## CHAPTER 5

### UTILIZATION OF THE FLOW STRESS DATA IN FEM MACHINING APPLICATION - A CASE STUDY: TOOL WEAR AND BURR FORMATION IN FACE MILLING OF AA356-T6 ALUMINUM ALLOY

The procedure to determine the flow stress properties developed in section 4.1 was used to obtain the material data of the workpiece for an analysis of this specific problem, namely burr formation and tool stress analysis.

Burrs are undesirable material protrusions beyond the edge of the workpiece, leftover during machining or shearing processes. Burr formation is a critical issue because it reduces the dimensional accuracy and the surface integrity of the machined components. Furthermore, deburring that is necessary before assembly may significantly increase the product cost. Various parameters in the cutting operation can influence the burr formation. Among these, tool wear and edge sharpness of the cutting insert are most important. As tool wear increases and the tool edge becomes dull, the burr is enlarged. Numerous cutting tool designs are tried out to optimize the cutting tool geometry in order to minimize burr formation and increase tool life. However, trial and error experimentation requires considerable effort, investment and time. Therefore, FEM simulation is useful because it can provide fundamental insight into the burr formation mechanics, e.g. directions of metal flow and distributions of stress/strain/temperature. Such information can lead to evaluation of cutting



performance and improvements of tool edge design, for a given tool and workpiece material combination.

### **5.1. Problems Description and Objectives**

A case study in actual face milling of cast cylinder block and cylinder head surfaces, those are made of Aluminum Alloy AA356-T6 was conducted. A very hard material “Polycrystalline Diamond (PCD)” was used for the tool inserts. As part of this study, a new tool edge preparation method that allows manufacturing of variable edge hone radii around tool corner radius of the cutting insert [Conicity, 1999] was evaluated. This new method is claimed to provide higher tool-life than conventional uniform edge honed tool. Thus, the overall research objectives of this study were to 1) demonstrate how the FEM cutting simulation can be used to analyze burr formation based on different tool geometries considered (i.e. tool rake angle, flank wear and tool edge preparation), and 2) provide recommendations of tool geometries that reduce burr formation in face milling.

### **5.2. Finite Element Modeling to Analyze Tool Wear and Burr Formation**

Four aspects of the FEM modeling were considered for this case study: 1) flow stress of the workpiece material and friction, 2) the effects of tool rake angle and tool flank wear, 3) the cutting performance of the variable edge honed tool and 4) 3D face milling simulations. A typical cutting condition, used in actual face milling operation, was used for all simulations. This condition has the cutting speed of 1437 m/min, the feed of 0.25 mm/rev and the width of 2.5 mm.

Commercial FEM packages “DEFORM-2D™” and “DEFORM-3D™” were used for FEM modeling of orthogonal cutting and practical face milling, respectively.

### 5.2.1. Material Properties and Friction Condition

Flow stress data of the workpiece must be obtained at or close to machining conditions (strain rates up to  $10^6 \text{ s}^{-1}$ , temperatures up to  $10^3 \text{ °C}$ ). In this study, the flow stress data of AA356-T6 workpiece were determined using slot milling and quick stop milling tests, as well as a numerical routines based on Oxley’s machining theory [Oxley, 1989]. This procedure was explained in details in Section 4.1. The obtained flow stress equation for AA356-T6 workpiece is given in Equation 5.1.

$$\bar{\sigma} = 477\bar{\varepsilon}^{0.144} \left( 1 + 0.0067 \ln \left( \frac{\dot{\bar{\varepsilon}}}{1000} \right) \right) \left( 1 - \left( \frac{T - 20}{585 - 20} \right)^{1.62} \right) \quad \text{Equation 5.1}$$

$$\text{for } 0.7 \leq \bar{\varepsilon} \leq 1.2$$

$$20,000 \leq \dot{\bar{\varepsilon}} \leq 500,000 \text{ s}^{-1}$$

$$50 \leq T \leq 350 \text{ °C}$$

Where  $\bar{\sigma}$  = Flow stress or true stress (MPa)

$T$  = Temperature (°C)

$\bar{\varepsilon}$  = Strain

$\dot{\bar{\varepsilon}}$  = Strain rate ( $\text{s}^{-1}$ )

Constant shear friction ( $\tau = m_f k_{chip}$ ; where  $\tau$ ,  $m_f$  and  $k_{chip}$  are shear frictional stress, friction factor and shear stress of the chip, respectively) with friction factor ( $m_f$ ) of 0.6 was assumed in the simulation. According to split tool experiments, presented in [Childs, 2000], friction factors can be in the range from 0.5 to 0.95 for

various tool-workpiece contacts and temperatures. The obtained flow stress equation of AA356-T6 and assumed friction condition were used in FEM simulation of orthogonal cutting for validation. The simulation was conducted for one of the cutting conditions used during slot milling tests, which had the cutting speed of 200 m/min, the uncut chip thickness of 0.05 mm/rev and the width of cut of 3 mm. The FEM package “DEFORM-2D™”, which was based on an updated Lagrangian formulation, was used. As shown in Figure 5.1, cutting force, thrust force and chip thickness from the simulation were compared with experimental forces from slot milling tests at the 90<sup>th</sup> degree of the tool rotation angle (where the corresponding effective uncut chip thickness is maximum at 0.05 mm). The cutting force and chip thickness from FEM simulation reasonably agreed with the results obtained from the experiments but the predicted thrust force was 40% lower than the experimental force.

A similar discrepancy in thrust force prediction was observed in section 4.2 and in [Bil, 2004], although different flow stress data and three different FEM packages were used. Disagreement of the thrust forces may be due to several factors, which were already discussed in Section 4.2.3. Nevertheless, based on an agreement of cutting force and chip thickness, in this study the flow stress given in Equation 5.1 and the assumed friction factor ( $m_f = 0.6$ ) were used for all 2D and 3D simulations for the analysis of burr formation and tool wear. Tool material is PCD. Physical and thermal properties for the tool and the workpiece are given in Table 5.1.

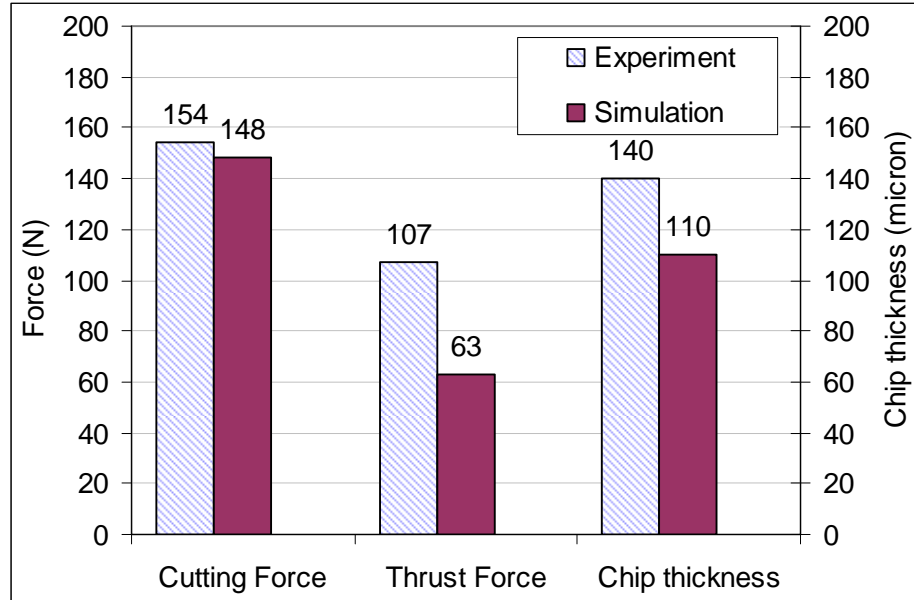


Figure 5.1: Comparison of cutting force, thrust force and chip thickness from slot milling experiment and the predictions from FEM simulation with DEFORM-2D®, for orthogonal cutting of AA356-T6 alloy at  $V_c = 200$  m/min and  $f = 0.05$  mm/rev..

	Workpiece (AA356-T6)	Tool (PCD)
Material Behavior	Plastic	Rigid
Young's Modulus, $E$ [MPa]	72,400	1,100,000
Poisson's ratio, $\nu$	0.33	0.1
Thermal conductivity, $K$ [W/m °C]	151	600
Heat capacity, $C$ [N/mm <sup>2</sup> °C]	2.581	2.2028
Melting temperature, $T_m$ [°C]	585	-
Emissivity, $\gamma_c$	0.75	0.02

Table 5.1: Physical and thermal properties of the workpiece and the cutting tool materials [GESA, 2003; Matweb, 1996]

### 5.2.2. *Process Simulation Procedure for Burr Formation in 2D Orthogonal Cutting*

2D plane strain condition was assumed in orthogonal cutting. The chip formation process was simulated as plastic flow and the separation of the chip material at the tool tip was achieved by continuous remeshing. The mesh definitions for the tool and workpiece objects are illustrated in Figure 5.2. A very fine mesh density was assigned near the tool edge radius to avoid accumulation of numerical errors during remeshing.

Process simulation procedures for burr formation can be divided into two steps; (1) steady-state chip formation and (2) burr formation at the exit, as shown in Figure 5.3. Steady-state chip formation employs the routine called “Konti-Cut”, developed by the University of Aachen (RWTH), Germany [Raedt, 2001]. The principle of “Konti-Cut” is briefly described. Each time a remeshing step starts in the simulation; the “Konti-Cut” cuts off an excessive chip material away from the deformation zone and a part of machined workpiece material behind the cutting edge by means of a user-defined fixed “control area”. Meanwhile, new material feeds into the deformation zone from the boundary on the uncut side of the workpiece. By repeating this procedure, the cutting simulation can be run continuously with less computational time due to less numbers of workpiece mesh elements than those consumed in typical Lagrangian cutting simulation.

Following the steady-state chip formation, burr formation simulation was conducted by removing displacement boundary constraints at the exit boundary of the workpiece, as shown in Figure 5.3 (b). Thermal boundary condition at the exit was also changed from constant room temperature to heat convection to the environment. The overall simulation procedures allowed the prediction of the burr shape (i.e. geometries and dimensions) that resulted by chip formation, and the stress fields in the tool and the workpiece.

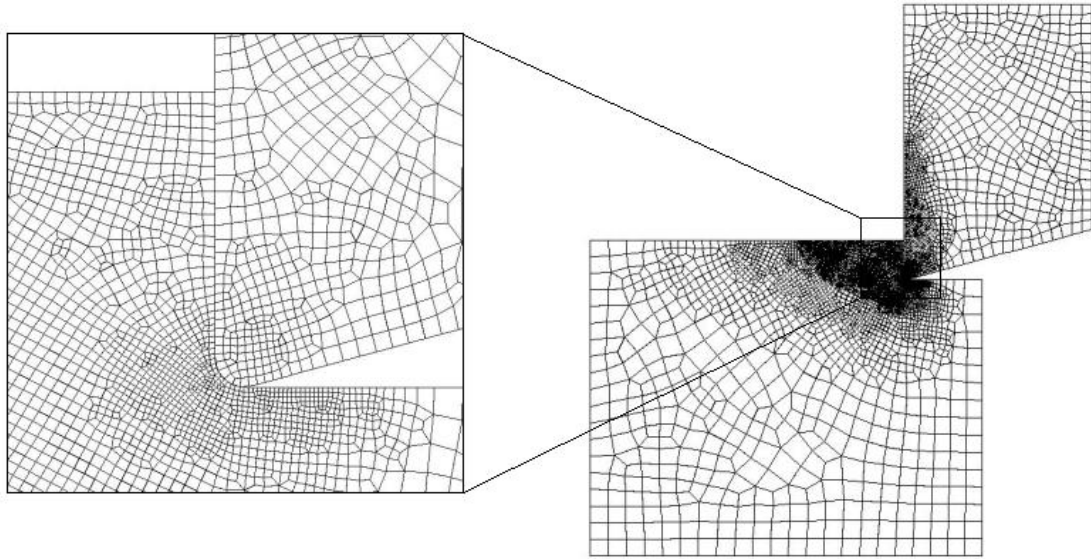


Figure 5.2: Mesh density of tool and workpiece objects in FEM simulation of 2D orthogonal cutting

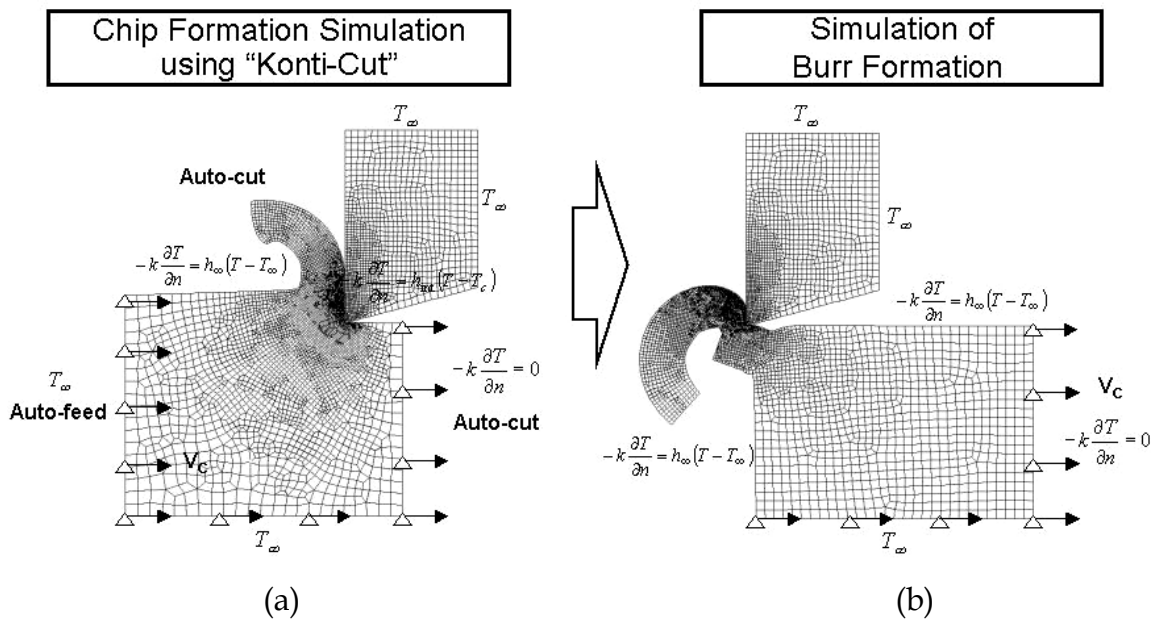


Figure 5.3: Simulation steps for chip formation and following burr formation

### 5.2.3. *The Effect of Tool Rake Angle and Flank Wear*

Two different tool rake geometries, i.e. neutral and hi-shear tools, were simulated at both sharp and worn-out conditions, as shown in Table 5.2. A neutral tool has  $0^\circ$  rake angle while a hi-shear tool has high positive rake angle of  $20^\circ$ . For PCD tools, flank wear typically dominates crater wear and the tool can be considered to be worn-out when the flank wear width reaches 0.4 mm (per suggestion by industrial sponsor). 2D orthogonal cutting simulations can be performed to understand the effects of tool rake angles and flank wear on the predicted burr size. Cutting conditions are set to the values that are actually used in face milling operation, which has the cutting speed ( $V_c$ ) of 1437 m/min, the feed rate ( $f$ ) of 0.254 mm/tooth and the width of cut ( $w$ ) of 2.54 mm.

Simulation Number	Axial Rake Angle (degree)	Flank Wear Width (mm)
1	$0^\circ$ (neutral)	0, sharp
2	$0^\circ$ (neutral)	0.4, worn
3	$+ 20^\circ$ (hi-shear)	0, sharp
4	$+ 20^\circ$ (hi-shear)	0.4, worn

Table 5.2: Simulation matrix for the study on the effects of tool rake angles and flank wear

### 5.2.4. *Performance of Variable Edge Honed Tool*

Conventionally, a tool edge is prepared with a uniform hone radius along the cutting edge and tool corner radius, as shown in Figure 5.4 (a). However, recent edge honing technology can now manufacture a tool insert with variable edge hone radii [Conicity, 1996]. As illustrated in Figure 5.4 (b), the edge hone radius of a variable edge honed tool decreases gradually around the tool corner radius and becomes a sharp edge on the straight trailing edge. This new edge

preparation method was claimed to provide longer tool life than conventional uniform edge honed tool. FEM simulations were conducted to evaluate the tool performance by predicting the burr profiles, tool stresses and tool temperatures.

Practical face milling is 3D cutting in nature. As shown in Figure 5.5, as the tool rotates and cuts the workpiece, the effective feed increases as the tool rotation angle increases and becomes maximum at about the 90th degree of tool rotation angle. In addition, the effective uncut chip thickness is non-uniform along the tool nose. As seen in Figure 5.5 (window), the effective uncut chip thickness along the straight cutting edge is larger than at the tool corner radius.

Burrs are commonly generated along four regions (previously shown in Figure 3.5). Only an exit burr will be the focus of this study since it remains on the machined surface whereas burrs at other locations can be eventually removed by subsequent cutting paths. In this study, tool cutter (an assembly of tool holder and cutting insert) has  $0^\circ$  axial rake and  $0^\circ$  radial rake angles. Procedures to estimate 3D face milling with 2D orthogonal cutting simulations were established to predict the burr profiles, and to obtain tool stress and tool temperature distributions.

#### *5.2.4.1. Analysis of Burr Formation*

To analyze burr formation, a tool section A-A in Figure 5.5 was analyzed. This tool section involves a very small uncut chip thickness and has different edge radius between the uniform and variable edge honed tools. It locates maximum effective uncut chip thickness that is normal to the machined surface and is expected to generate maximum burr thickness at the exit. Two simulations of 2D orthogonal cutting were conducted: using Section A-A with an uncut chip thickness of 0.042 mm and (1) a tool edge radius of 25.4 mm (corresponding to the uniform edge honed tool) and (2) a tool edge radius of 4.2 mm (corresponding to the variable edge honed tool).



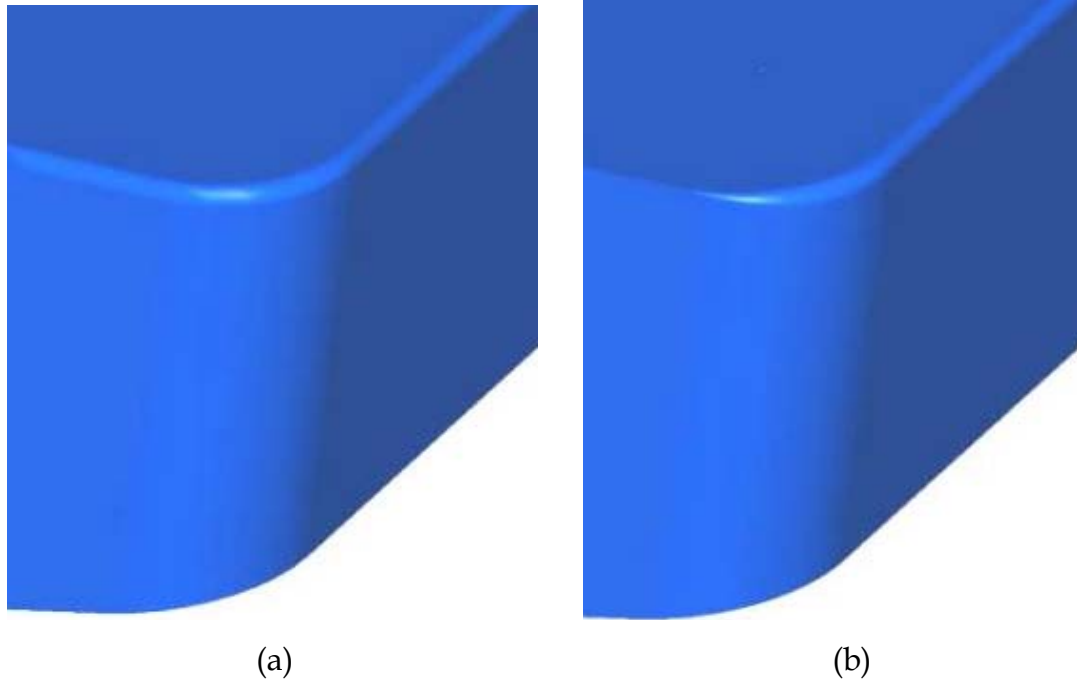


Figure 5.4: (a) Uniform edge honed tool and (b) variable edge honed tool.

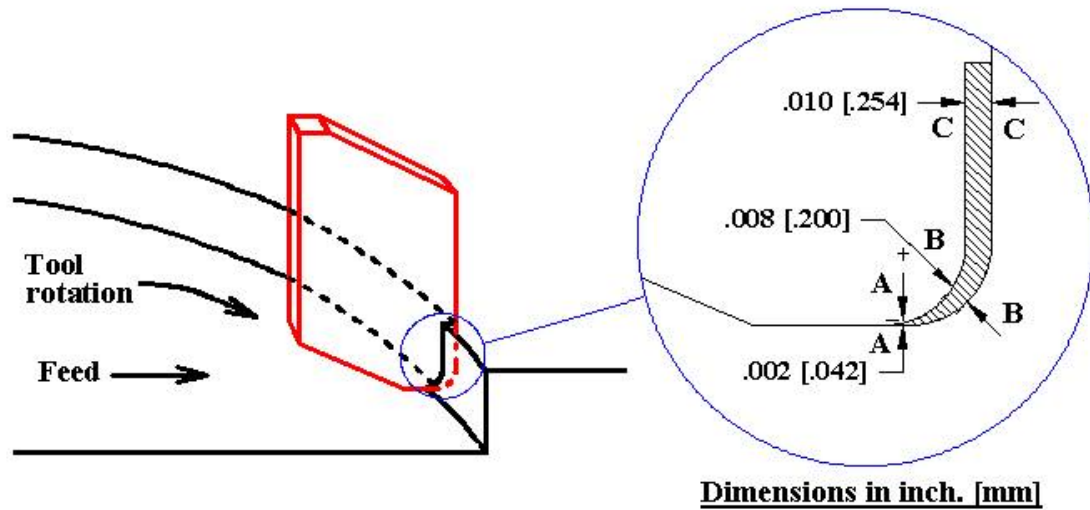


Figure 5.5: Tool-workpiece contact in face milling operation

#### 5.2.4.2. *Analysis of Tool Stress and Tool Temperature*

In order to analyze the tool edge effects upon tool life in practical face milling by using 2D cutting simulations, special tool cross-sections along the plane containing the cutting velocity and chip flow velocity (hereafter, referred to as the orthogonal cutting plane) were considered. Selection for this cross-section was made due to the fact that tool stresses and temperatures are influenced mainly by chip flow, chip formation and interaction along the tool/chip interface. For the purpose of tool stress and temperature analysis, it is practical to estimate 3D milling from 2D cutting at the tool cross-sections in accordance to the direction of the chip flow.

The tool edge geometries for 2D simulations were determined by projecting the round tool edges onto these 2D section planes, which became “waterfall” geometry. Thus, the following steps were used:

- a) Create two 3D solid models of uniform and variable edge honed tools
- b) Estimate the chip flow direction on the tool rake face using Oxley’s approximation theory [Oxley, 1989]. In Oxley’s theory, the chip flow direction is assumed to be along the direction of the resultant friction force on the tool rake face and can be found from the integration of chip load area, which is divided into a series of small elements with infinitesimal width. For the neutral tool and the depth of cut used, the calculated chip flow angle is  $11.7^\circ$  from the normal to the straight cutting edge.
- c) In the solid models of the tool, create section planes at different locations along the cutting edge that are parallel to the orthogonal cutting plane, as indicated by Sections A’-A’, B’-B’ and C’-C’ in Figure 5.6.

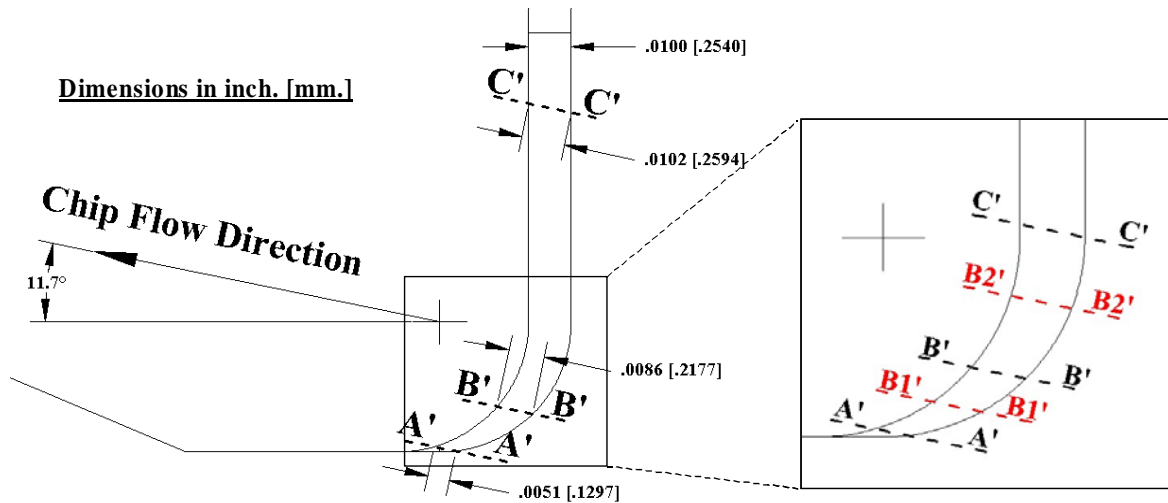


Figure 5.6: Selected section planes along tool corner and the corresponding uncut chip thicknesses

- d) Extract the cross sectional profile of the tool edge from each defined section and save the profile in the 2D drawing format (as a IGS file). This 2D tool profile is imported into DEFORM-2D™ as the geometry of the tool object.
- e) Consider the corresponding effective uncut chip thickness for each section equal to the distance between current and previous tool positions (shifted by the amount of cutting feed) measured along the orthogonal cutting plane. For example, Figure 5.6, the uncut chip thickness values for Sections A'-A', B'-B' and C'-C' are 0.13, 0.218 and 0.259 mm, respectively.
- f) If the tool has non-zero radial and axial rake angles, the normal tool rake angles for each section plane need to be re-determined.

At sections A'-A', B1'-B1', B'-B' and B2'-B2' (see Figure 5.6), the edge radii are different between the uniform edge honed and variable edge honed tools, whereas both tools have the same edge radius at Section C'-C'. Cutting at different tool sections at different edge hone sizes can be simulated to estimate the distributions of maximum tool stresses and maximum tool temperatures along the tool corner radius.

### 5.2.5. 3D Face Milling Simulations

Three-dimensional FEM simulations were conducted using DEFORM-3D™. The purposes of 3D simulations were to validate the capability of 3D FEM model in simulating practical face milling operation and to compare the predicted burrs with (a) the results from 2D simulations and (b) burr measurements from milling experiments. Two 3D face-milling simulations were conducted using the tools for sharp and worn-out conditions. A neutral tool with an axial rake angle of 0°, a radial rake angle of 0°, a lead angle of 0° and edge radius of 0.0254 mm was considered. A cutting condition was set similar to that of previous sections (Section 5.2.3 to 5.2.4).

A 3D solid model of the PCD tool insert was created with the actual tool dimensions provided by tool manufacturer. A solid model of the workpiece was also created in a similar manner, according to the given cutting condition. The workpiece was assumed to be a small section near the exit where the maximum uncut chip thickness located and the geometry cut off from previous milling revolution was included (see Figure 5.7). Both solid models were exported into DEFORM-3D™. Meshes of tool and workpiece objects are shown in Figure 5.7. The numbers of mesh elements were 16,000 for the tool and 70,000 for the workpiece. High mesh density was defined for the regions near the tool corner, along the cutting path of the workpiece and at the milling exit. Minimum

element size was about 50  $\mu\text{m}$ . Material properties of the tool and the workpiece, and friction were the same as those used in 2D simulations. The simulation was conducted under non-isothermal condition, i.e. temperature increases were estimated along with chip flow and tool stresses.

The tool was set to rotate clockwise and contact the workpiece starting from the left side. As the tool rotated further, the chip formation could be observed, and burrs would be generated when the tool exited the workpiece. Burr results from 3D simulations are compared with the results from 2D simulations in the later section.

For simulation of face milling with a worn insert, the flank wear geometries measured from the real worn-out insert (dimensions averaged from seven worn inserts) were included in an original solid model of the tool, as shown in Figure 5.8. Simulation of milling with a worn insert was conducted using the same cutting condition as of the sharp tool. Due to the reduced dimensions by tool flank wear, the initial position of the tool was slightly adjusted for equivalent depth of cut and feed to those used in the simulation of the sharp tool. Burr results from 3D milling simulation of the worn insert are compared with those obtained with the sharp insert and the experimental burr measurements.

Experimental burrs were obtained from face milling tests on a rectangular grate sample with the worn-out tools. Burr geometries were measured using an optical microscope. Details of burr formation experiments were presented in [Sahlan, 2003].

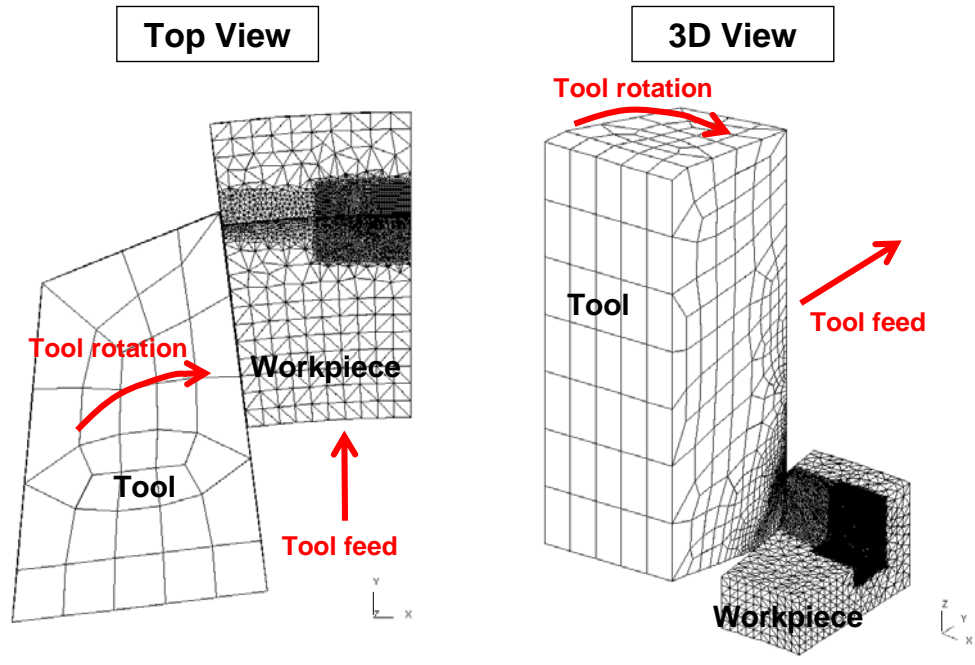


Figure 5.7: Mesh definitions of tool and workpiece objects in 3D face milling simulation

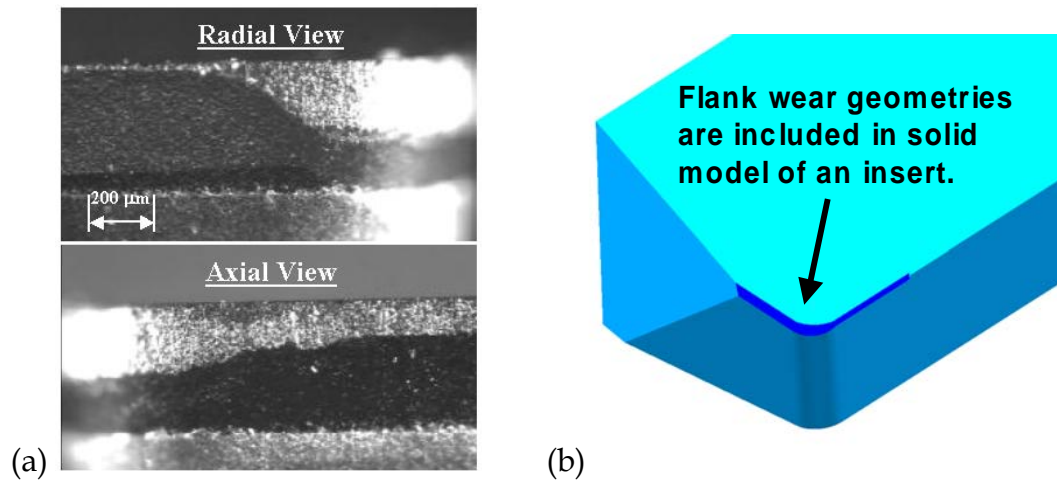


Figure 5.8: (a) Flank wear on the actual tool and (b) a 3D solid model of a worn insert

### 5.3. Simulation Results and Discussions

#### 5.3.1. *The Effects of Rake Angle and Flank Wear*

Figure 5.9 shows the burrs obtained in cutting with sharp and worn tools. Burr height is defined by the profile of the protruded surface at the exit. Burr area can be defined as the area under the burr height curves. Results obtained for the neutral tool, in Figure 5.10, show that the worn insert generates 39% more burr area than the sharp insert. This implies that more force is required to remove burrs generated with worn tool.

Burr areas of both neutral tool ( $0^\circ$  rake angle) and hi-shear tool ( $+20^\circ$  rake angle) are plotted against flank wear width (VB) in Figure 5.11. These results illustrate that the additional positive rake angle is effective for reducing burr at both sharp and worn out conditions. Positive rake angles allow larger amount of deformed material ahead of cutting tool to go with the chip. However, from a viewpoint of tool life, as the rake angle increases, there is a higher possibility of tool tip fracture. As seen in Figure 5.12, a hi-shear tool was subject to higher maximum effective stress than a neutral tool (811 MPa and 516 MPa respectively). Therefore, for tool selection, both burr minimization as well as tool life must be considered. The higher positive rake angle is preferable if the tool life is determined by flank wear rather than the fracture at the tool tip. This would be an important criterion in the selection of tools in roughing versus finishing, due to the increased probability of tool tip fracture in roughing caused by the mechanical impact.

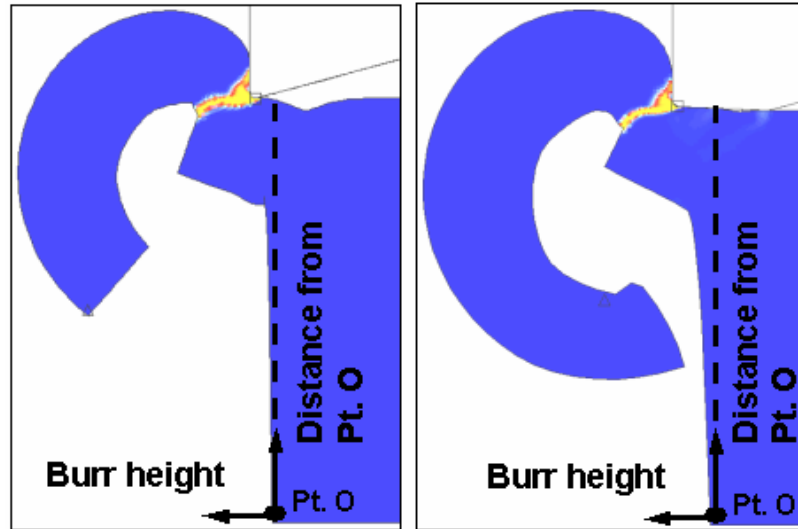


Figure 5.9: Strain rate distribution in exit burrs for neutral tool at sharp (Left) and worn-out conditions (Right).

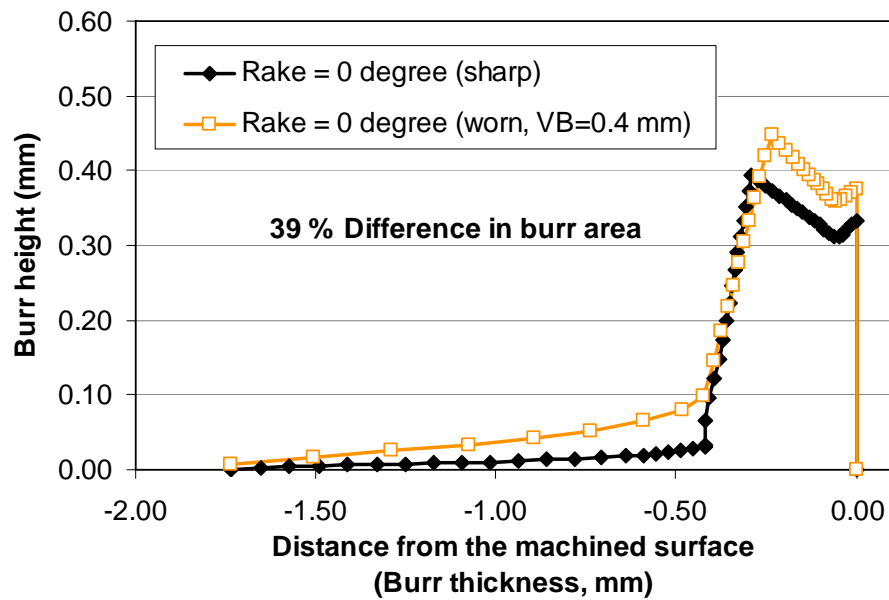


Figure 5.10: Comparison of the burr profiles from cutting with a neutral tool (with 0 degree rake angle) for sharp and worn-out conditions



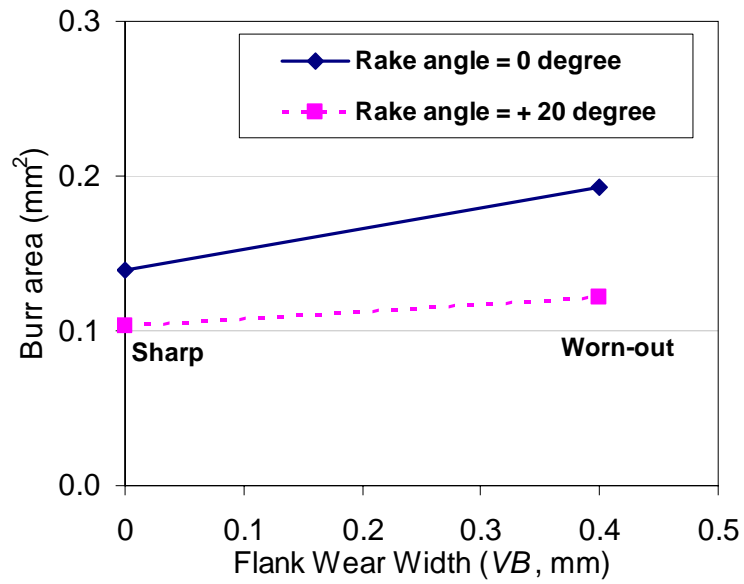


Figure 5.11: Comparisons of burr area in relation to flank wear width (VB) between the tools with 0 degree and +20 degree rake angles.

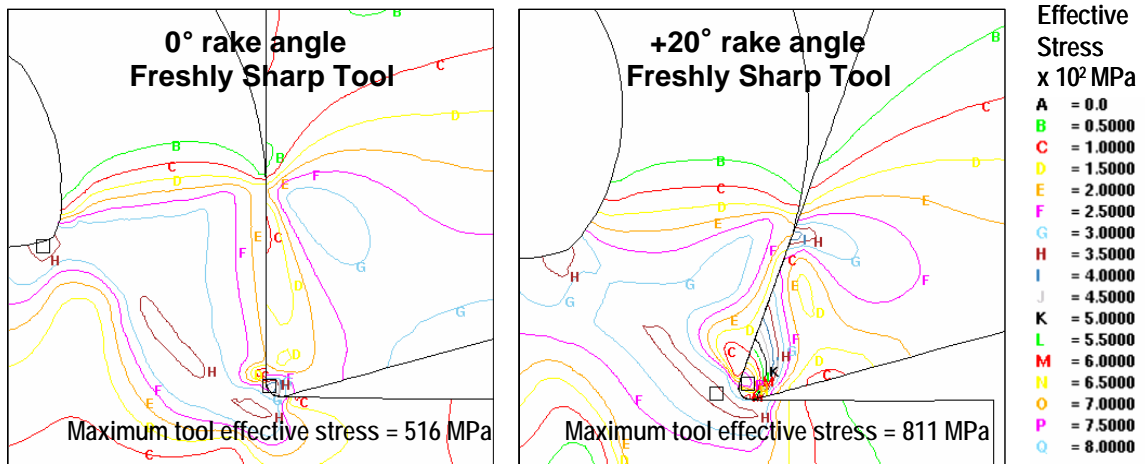


Figure 5.12: Distributions of effective stresses for cutting with neutral (0° rake angle) and hi-shear (+20° rake angle) tools

### 5.3.2. *Performance of Variable Edge Honed Tool*

For an analysis on the burr formation, simulation results of the Section A-A (i.e. the section perpendicular to the machined surface in Figure 5.5) revealed that cutting with a small edge radius (corresponding to a variable edge honed tool) causes a slightly smaller burr area (about 6%) than that obtained with a large edge radius (corresponding to a uniform edge honed tool). This comparison is shown in Figure 5.13. Therefore, in using a new and sharp tool, the size of edge hone radius has insignificant effect on burr reduction for the given cutting condition used in this part of study.

For an analysis of tool stress and tool temperature, simulation results at five orthogonal plane sections along the tool corner (i.e. Sections A'-A' to C'-C' of Figure 5.6) were evaluated. Figure 5.14 shows the effective stress distributions and maximum tool stresses obtained from the simulation in Section A'-A'. The maximum effective stress is lower in the tool with smaller edge radius (522 MPa for the uniform edge honed tool and 465 MPa for the variable edge honed tool). In addition, a higher stress concentration near the tool edge and flank face can be observed in the uniform edge honed tool. Maximum tool stresses of all five sections are plotted and compared in Figure 5.15. At all sections except section C'-C', maximum effective stresses are relatively lower for the variable edged honed tool.

In both uniform edge honed and variable edge honed tools, the overall maximum effective tool stresses are located near the middle of the tool corner radius or at Section B'-B' in Figure 5.6. This infers that maximum tool wear and possible tool fracture are most likely to occur in the middle of tool corner radius. Qualitatively, the results from the FEM simulation agree quite well with the experimental observation, where the locations of maximum flank wear width of the actual worn-out tools are always located in the middle of tool corner radius.

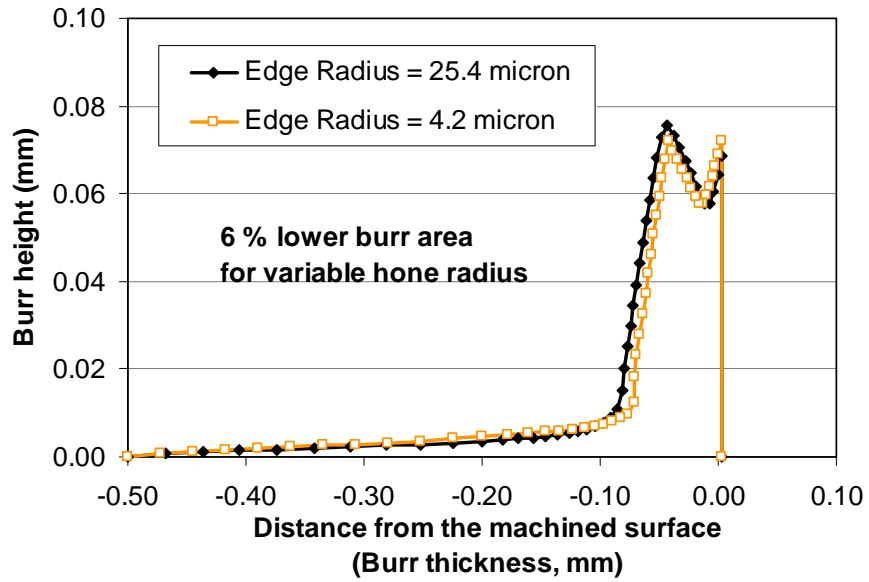


Figure 5.13: Comparison of the burr area when cutting using the tool with the edge radius of 25.4  $\mu\text{m}$  and 4.2  $\mu\text{m}$ .

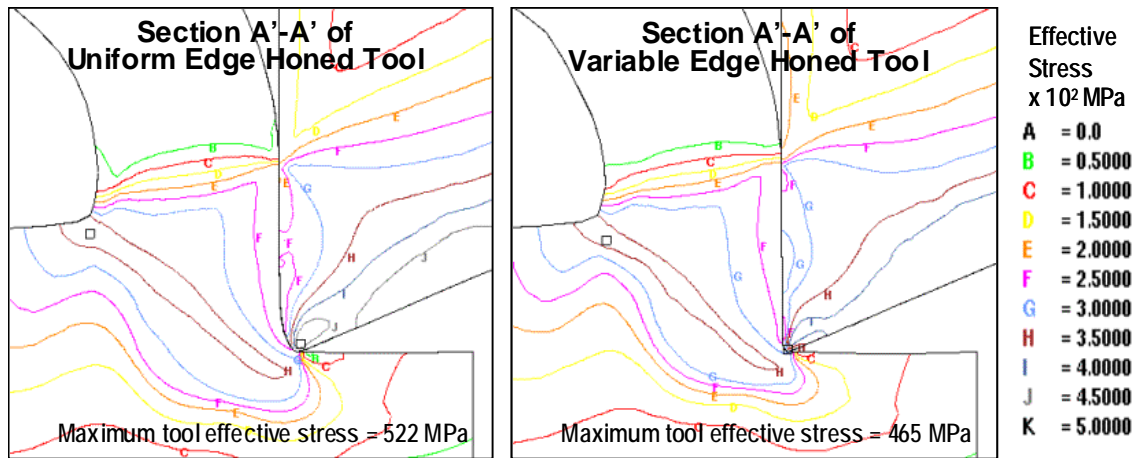


Figure 5.14: Distributions of effective stresses and the maximum tool stress value from the 2D orthogonal cutting simulations of section A'-A', with uniform and variable edge honed tools

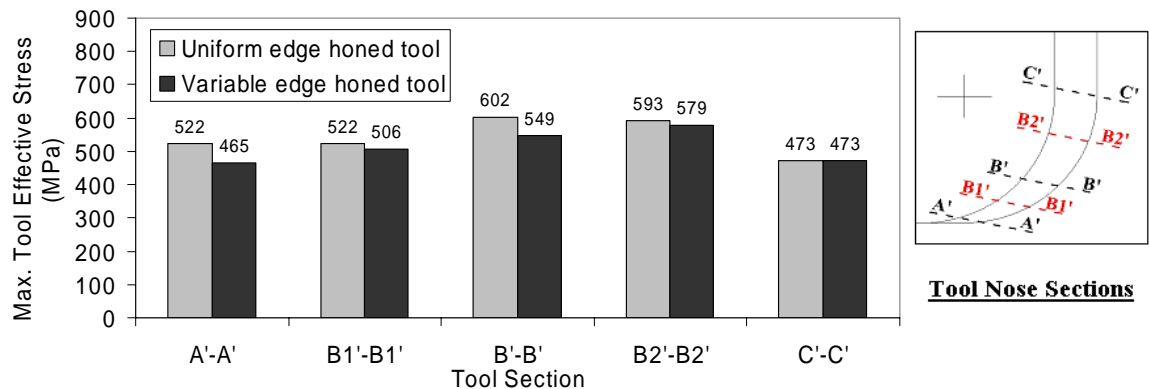


Figure 5.15: Maximum tool effective stresses for different tool orthogonal plane sections

As far as tool temperature is concerned, there is no significant difference in the maximum tool temperature as well as temperature contours between uniform and variable edge honed tools. As seen in Figure 5.16, maximum temperatures for both tools are almost identical at all orthogonal plane sections.

Based on the predicted stress distributions, the variable edge honed tool is expected to have relatively longer tool life than the conventional uniform edge honed tool. Since increased flank wear generates larger burrs, the use of variable edge honed tool can be expected to reduce burr generation rate. Its tool life is longer and the increase in its flank wear is slower. Nevertheless, the additional cost to manufacture a variable edge hone insert should also be considered for cost-effective machining.

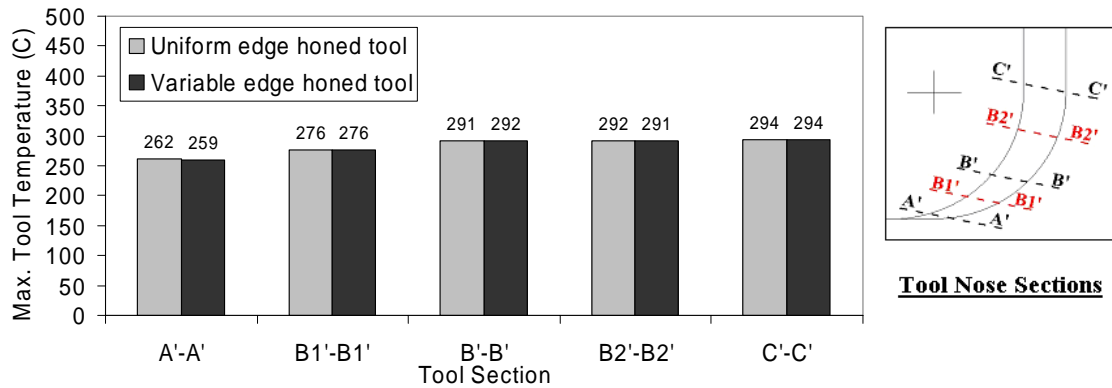


Figure 5.16: Maximum tool temperatures for different tool orthogonal plane sections

### 5.3.3. 3D Simulation of Face Milling

In 3D simulation, burrs could be observed at three different locations, which were indicated as Burr 1, Burr 2 and Burr 3 in Figure 5.17 (a). Only Burr 3, which was the exit burr, was considered in this study. From the FEM simulation, the chip flow angles were approximately  $22^\circ$ , measured at the top, and  $16^\circ$  at the machined surface, as shown in Figure 5.17 (b). Compared with the approximate chip flow angle of  $11.7^\circ$ , determined using Oxley's theory, the difference was noticeable. This difference could be caused by the 3D nature of practical face milling where the uncut chip thickness is non-uniform in the radial direction and along the tool corner radius. In the calculation of chip flow angle, Oxley assumed uniform uncut chip thickness and estimated solution based on turning operation. In addition, since the current 3D simulation was established without considering element separation/deletion by fracture, there was a potential of error due to stress/strain calculated for the elements in the highly stretched region. In 3D simulation, the element stretching with very high strain was located near the exit

burr, as shown in Figure 5.18. In real face milling, this high stretching region may already be broken as the chip separates from the workpiece.

To extract and quantify the burrs from 3D face milling simulations, two section planes were defined: 1) a horizontal plane on the machined surface and 2) a vertical plane normal to the machined surface (as shown in Figure 5.19). The side view of the burr extracted from the vertical plane was comparable to the burr results from a 2D simulation at the section A-A of Figure 5.5. In Figure 5.20, the burr profile from 3D simulation with sharp tool was plotted together with the burr predicted by 2D simulation. Results of burr profiles from both 2D and 3D simulations were in good agreement.

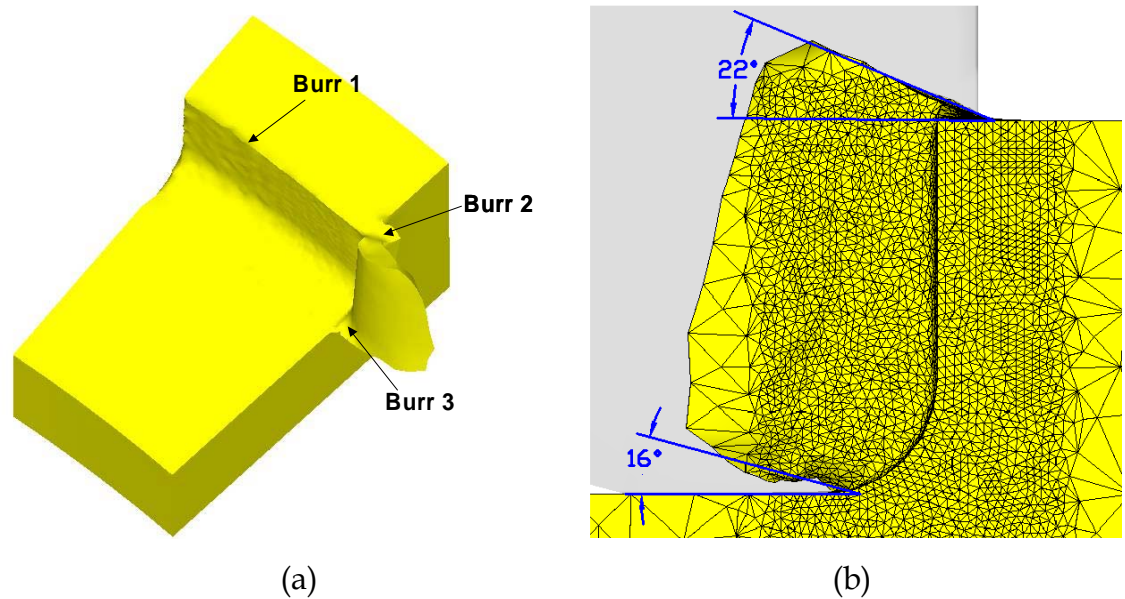


Figure 5.17: (a) Burr locations observed from 3D milling simulation and (b) chip flow angle prediction

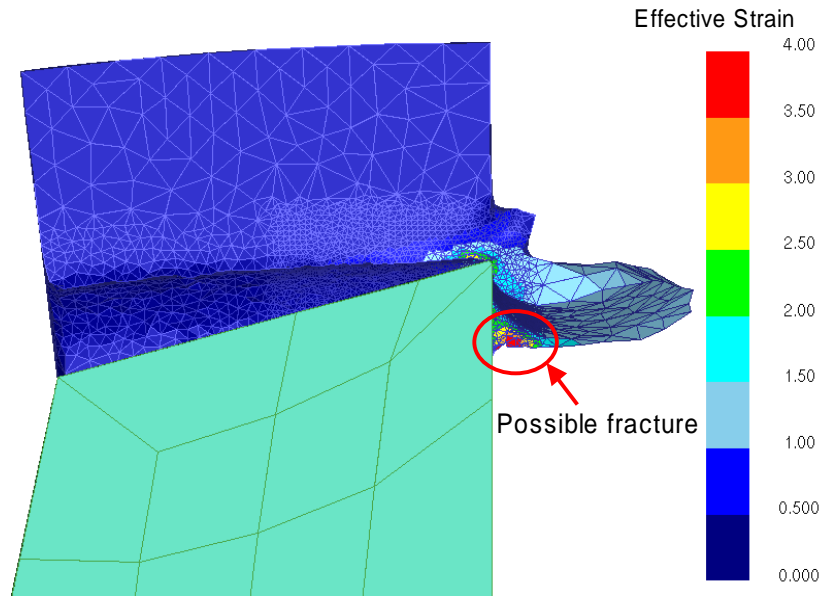


Figure 5.18: Strain distribution of the machined workpiece and possible fracture region

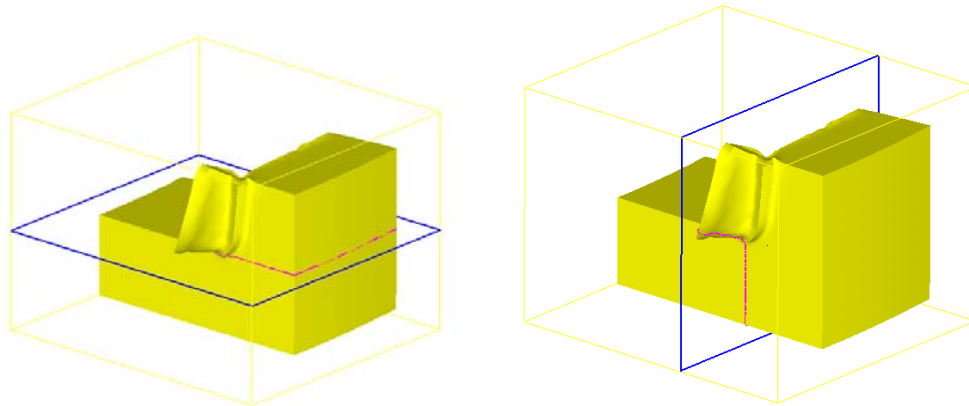


Figure 5.19: Section planes defined for burr investigation: a horizontal plane on the machined surface (Left) and a vertical plane normal to the machined surface (Right)

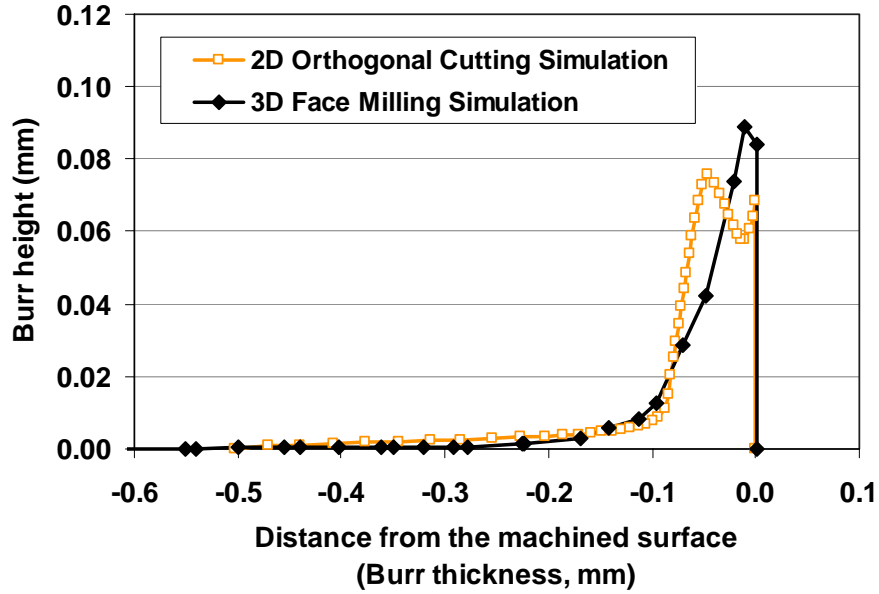


Figure 5.20: Comparison of the burr profiles from 2D simulation at section A-A and the size view of the vertical plane section from 3D face milling simulation

Figure 5.21 and Figure 5.22 show the burr profiles from the top view and the side view respectively. Comparisons were made for the different burr profiles: from (1) a simulation with the sharp tool, (2) a simulation with the worn tool and (3) face milling experiments. Burr results of 3D simulations at the top and the size views showed that milling with worn tool generates larger burrs than milling with sharp tool, which corresponds to the results from 2D simulations and actual milling operation. 3D simulations also indicated that large exit burr was mainly caused by the flank wear along the wiper edge. Flank wear on the wiper edge caused high pressure on the machined surface that was in contact with the tool and thus contributed to increasing bending stress at the boundary surface. As a result, at the exit of cut, the burrs were enlarged.



Reduction of the wiper length in tool insert design can significantly decrease burr generation without major change in machined surface finish.

Compared to experimental burrs, the predicted burrs from the simulations are much smaller than those obtained from experiments. Differences can be explained by several factors. First, the burrs generated during the experiment were non-uniform and resulted from a combination of rollover burr and burr fracture. The locations of relatively large rollover burrs were arbitrarily selected for the measurements. Example of a rollover burr, collected for measurement, is shown in Figure 5.23. These collected burrs could have been accumulated by subsequent cutting passes, rather than one pass that was assumed in 3D simulation. To illustrate the effects of subsequent cutting passes, 2D cutting simulation of the second cutting pass was conducted for the case of a neutral tool ( $0^\circ$  rake angle) with the flank wear width of 0.4 mm. Figure 5.24 shows that burr generated during the second cutting pass is 62% larger in burr area than the burr obtained during the first cutting pass. Unless the burr fractures, the more number of subsequent cutting passes, the larger is the size of the exit burrs.

#### **5.4. Conclusions**

The presented results focus on the effects of the tool edge geometries and the flank wear upon burr formation in face milling. Tool edge geometries considered in this study include the tool rake angle, flank wear on the tool and variable edge honed geometries. The following conclusions can be drawn for the study, discussed in this chapter.

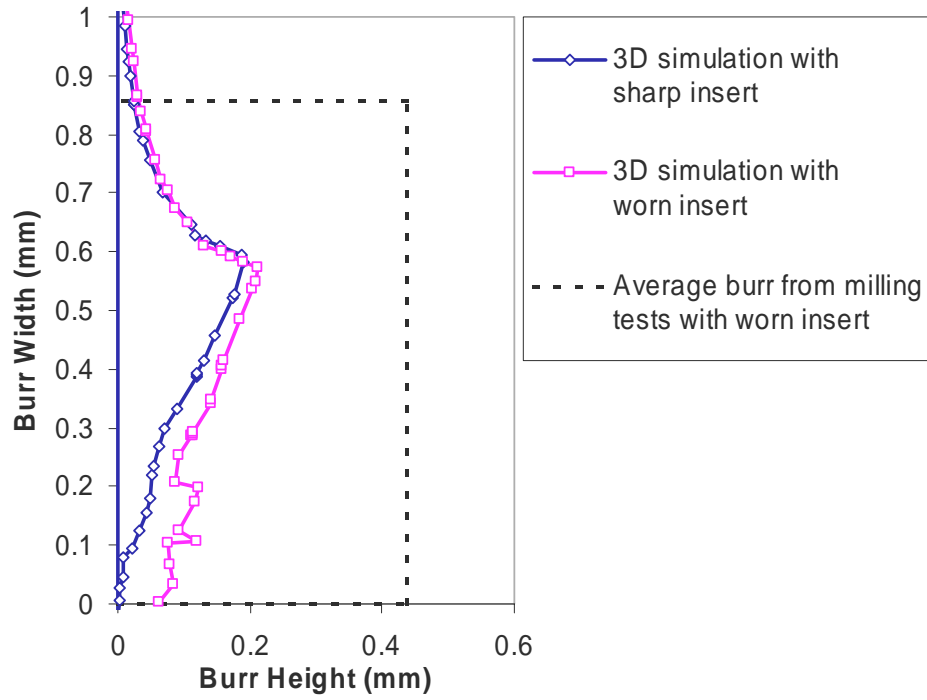


Figure 5.21: Comparison of burr geometries from the top view from (1) simulation with the sharp tool, (2) simulation of the worn tool and (3) milling experiments

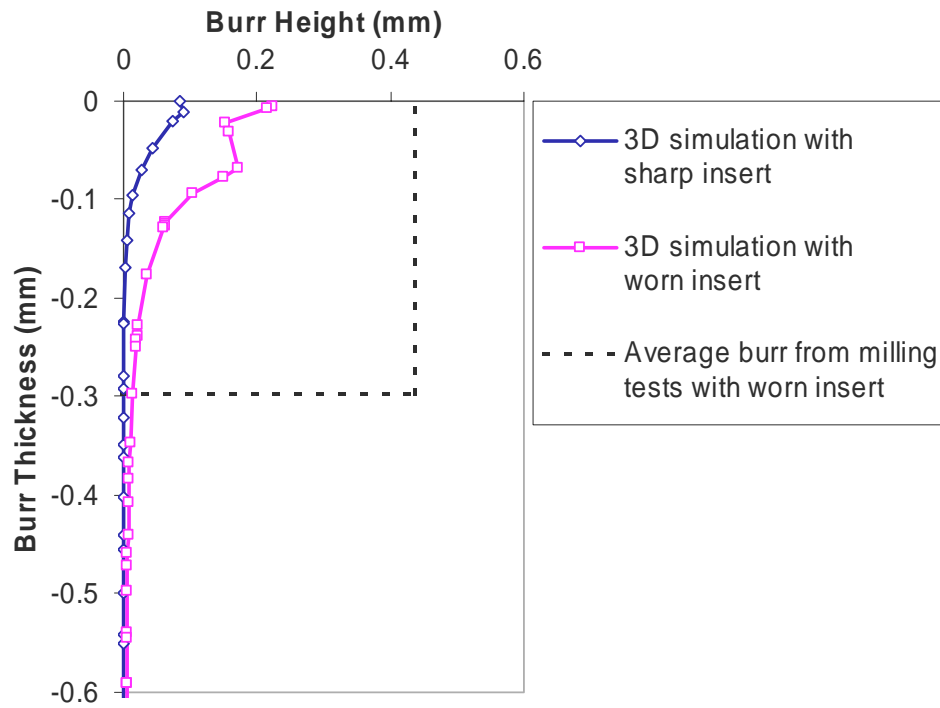


Figure 5.22: Comparison of burr geometries from the side view, from (1) simulation with the sharp tool, (2) simulation with the worn tool and (3) milling experiments

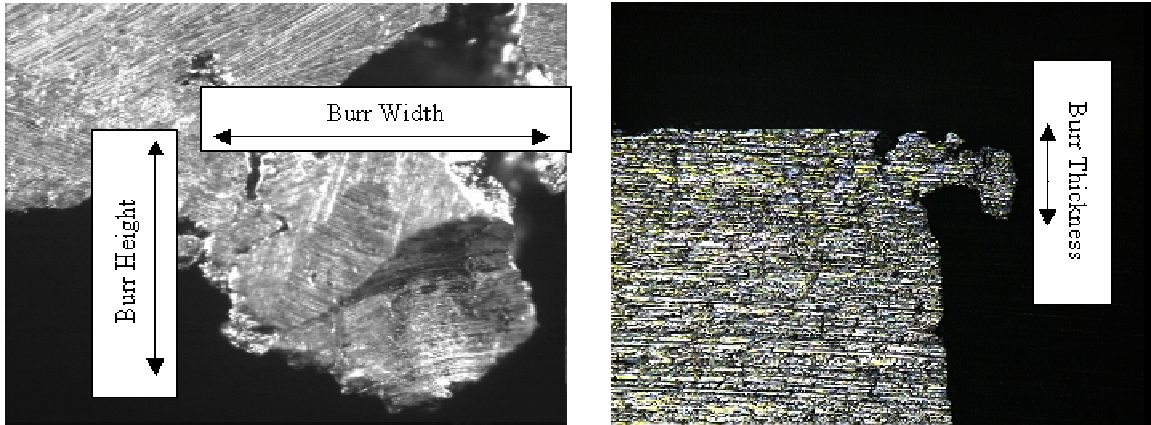


Figure 5.23: Burr obtained from face milling experiment and the definition of burr geometries

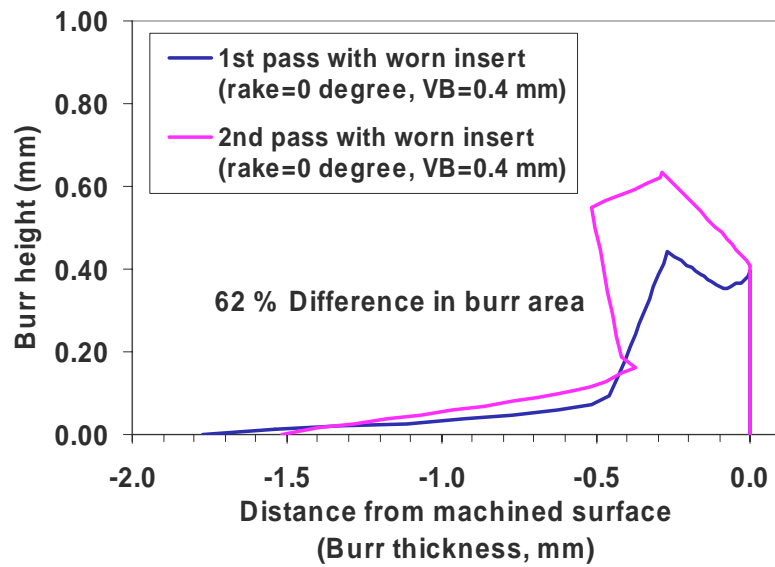


Figure 5.24: Comparison of the burr profiles from the 2D simulations in cutting with a neutral tool at worn-out condition between the first cutting pass and the second cutting pass

- The 2D and 3D simulations show that tool insert with larger flank wear width generates more burrs. Larger positive rake angle (within limits) is desirable for burr reduction if the tool life is determined by flank wear rather than tool fracture.
- Concerning the performance of variable edge hone tool, simulation results show no significant difference in burr formation between cutting with a uniform and variable edge honed tool. However, variable edge honed tool indicates potential increase in tool life and slowing down of burr generation rate.
- The results of 3D face milling simulations show that reduction of the wiper length of the tool insert can contribute to burr reduction.
- The comparison of 3D simulation results and experiments shows that the predicted burrs are much smaller than the burrs seen in experiments. The difference can be explained by the fact that the actual burrs are non-uniform and that the locations of relatively large burrs were arbitrarily selected in the experiments. In addition, several subsequent cutting passes can increase the size of burrs. Unless burrs fracture, the larger number of repetitive cutting passes can result in larger burrs.

## CHAPTER 6

### FLOW STRESS PROPERTIES FOR FEM SIMULATION OF ROLLER BURNISHING

To accurately simulate roller burnishing, the flow stress properties of the material surface layer must be known. Such surface layer could undergo severe plastic deformation and possible phase transformation by prior cutting and/or other prior manufacturing processes. The difference in material's flow behavior between at the surface and the bulk material properties can be highly significant when modeling FEM simulation of surface finishing processes such as roller burnishing. Conventional testing methods such as tensile and compression tests may not be applicable since they can provide only averaged properties of the bulk materials.

The concept is to model the surface layer as a new homogenous material distinct from the substrate (bulk) material. Instrumented indentation test (IIT) is well appropriate for this purpose since it allows acquiring the load-deformation responses locally at the surface (where the maximum penetration depth of the indentation can be up to 0.1 mm away from the surface). These required load and deformation data of the material surface can be used to determine the flow stress property of the surface layer.

In this chapter, two main studies were conducted: 1) evaluation of indenter geometries and 2) FEM based inverse analysis to determine the surface

property. For evaluation of the indenter geometries, a sensitivity analysis of indenter shapes, conical vs. spherical indenters, on the flow stress determination was conducted using FEM simulations. The associated uncertainties and limitations involved in IIT when using two different indenters were compared and discussed. Based on the results of the indenter shape evaluation, the procedure to determine the surface property through FEM inverse analysis and IIT was developed and utilized to determine the flow stress data of the hard-turned surface of an AISI 52100 cylindrical sample. The obtained flow stress will be used in FEM modeling of roller burnishing in the next chapter.

## **6.1. Finite Element Modeling of Indentation**

### **6.1.1. Material Model**

Material model used for all indentation simulations in this study is illustrated in Figure 6.1. For elastic deformation, material property is defined by Young's modulus and Hook's law, while during plastic deformation a power law is employed. The flow stress behavior of an elasto-plastic material may be expressed as Equation 6.1. Assuming continuous transition of the true stress at the yielding, the flow stress equation for plastic behavior, Equation 6.2, is obtained and used in FEM indentation simulations. Young's modulus is assumed as constant throughout this study and is given by [ASM, 1990; ASM, 1991; Matweb, 1996]. Only two parameters of Equation 6.2 need to be determined from the inverse analysis. This equation was also employed in analysis by Dao [Dao, 2001].

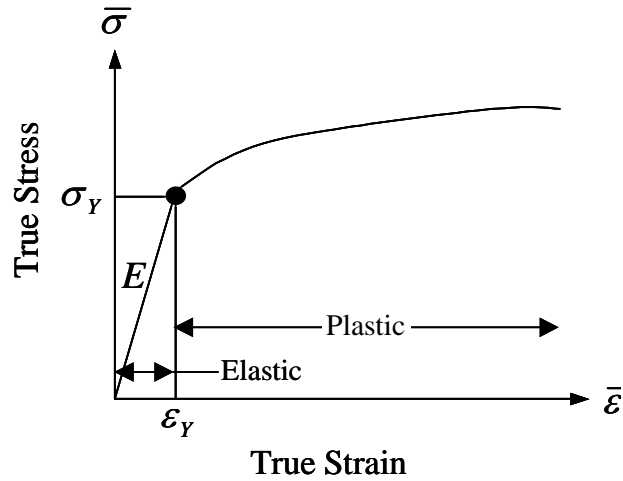


Figure 6.1: True stress-true strain behavior of hardening material

$$\sigma = \begin{cases} E\varepsilon & \text{for } \varepsilon \leq \varepsilon_y \\ K\varepsilon^n & \text{for } \varepsilon \geq \varepsilon_y \end{cases} \quad \text{for overall deformation} \quad \text{Equation 6.1}$$

$$\sigma = \sigma_y \left( 1 + \frac{E}{\sigma_y} \varepsilon_p \right)^n, \quad \text{for plastic deformation} \quad \text{Equation 6.2}$$

where  $\sigma$  = True stress

$\varepsilon$  = True total strain

$E$  = Young's modulus

$\varepsilon_y$  = Yield strain

$K$  = Strength coefficient

$n$  = Strain hardening exponent

$\sigma_y$  = Yield stress

$\varepsilon_p$  = Plastic strain



### 6.1.2. *Finite Element Model*

All FEM simulations were conducted using commercial FEM software, DEFORM-2D™. Axisymmetric condition is considered in this study for both conical and spherical indentation. Figure 6.2 shows mesh definition in FEM simulation of the indentation. The ball indenter diameter is 1.5 mm. The indenter was modeled as a rigid object while the workpiece was assumed as an elasto-plastic object. Total number of workpiece meshes was around 2000 elements. Small elements were assigned near the indenter/workpiece contact, where a very high deformation was expected. The geometry of the specimen was modeled sufficiently large such that the simulation results were not affected by the displacement boundary conditions. The size of the workpiece object in FEM simulations were 2 mm in the axial direction and 4 mm in the radial direction.

For validation, the established FEM simulation was conducted using the material properties and experimental data available in [Dao, 2001]. From Dao's experimental study, a sharp conical indenter with a half-angle of 70.3 degrees was used to test on a flat AA 6061-T6511 sample. Flow stress of the sample was obtained from compression tests [Dao, 2002]. As can be seen in Figure 6.3, two load-depth curves from the simulation and the experiment are almost identical, which demonstrates that the results of the established FEM simulation of indentation are valid and can be used for sensitivity and inverse analysis.

## 6.2. **Evaluation of Indentation with a Conical Indenter**

Typically, the indenter geometry and material are chosen by the type of workpiece material and the load capacity of an indentation machine. A conical indenter is commonly used for hard material since it can penetrate into the workpiece surface with relatively small loads.

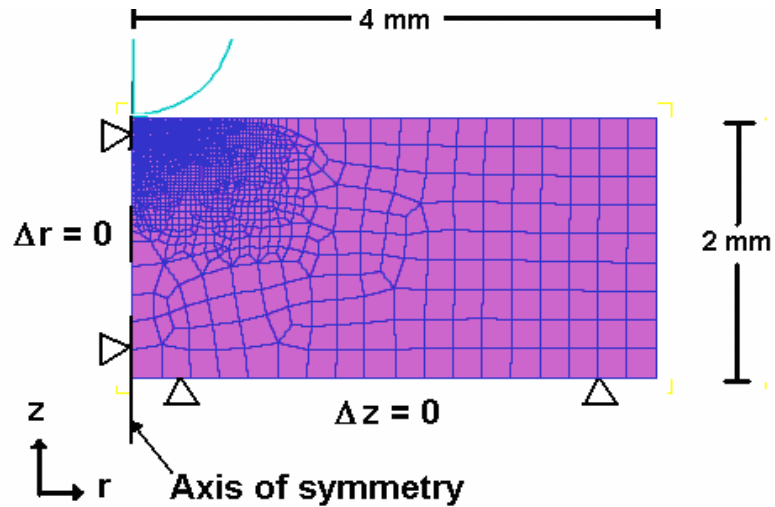


Figure 6.2: Finite element model for ball indentation and boundary conditions in DEFORM-2D.

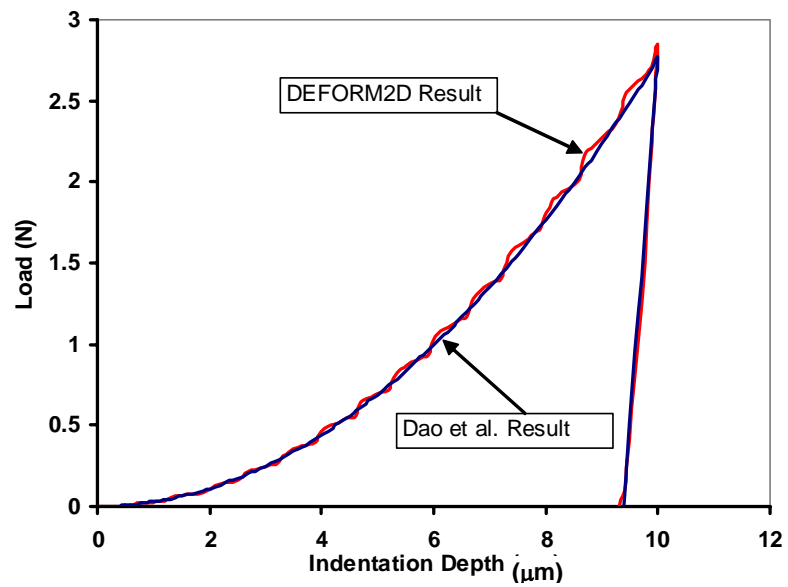


Figure 6.3: Comparison of simulation results with the results provided in [Dao, 2001], for conical indentation ( $70.3^\circ$ ) on an aluminum sample. Flow stress parameters are  $\sigma_y = 278.5$  MPa and  $n = 0.088$ .

For example, the Rockwell Brale indenter is a conical indenter, made of diamond, with a half-angle of 60 degrees and a tip radius of 0.2 mm. This indenter is commonly used to determine the hardness in HRC scale for hard materials, such as hardened and tool steels. Figure 6.4 shows a schematic of indentation using a conical indenter.

Most conical indenters are manufactured to have a small tip radius. This tip radius can be highly significant in modeling of indentation. Although most early mechanistic models by Dao et al. [Dao, 22001; Chollacoop. 2003] assumed perfectly sharp indenter, the tip radius now can be simply included in FEM simulations.

Previous study in [Dao, 2001] derives Equation 6.3 to describe the load-depth response for a perfectly sharp conical indenter using their developed FEM model. However, there is still need to understand the effect of the tip radius. A series of FEM indentation simulation using conical indenters with different tip radii (0, 0.1, 0.2 mm) were performed in order to compare their predicted load-depth curves. Figure 6.5 shows the normalized curves from conical indentation simulations with different tip radii.

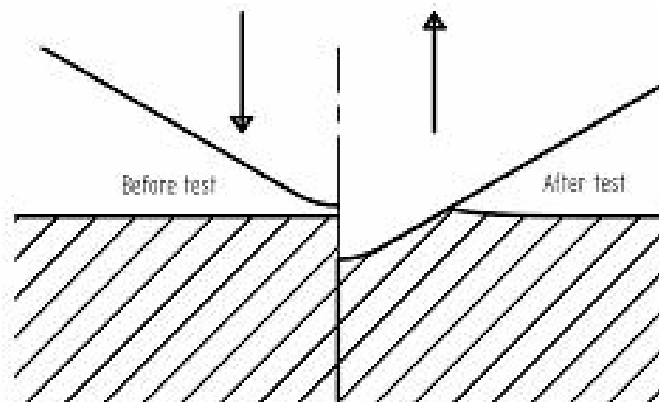


Figure 6.4: Schematic of indentation with a conical indenter

The simulation results clearly show that the tip radius of the conical indenter affects the curvature of the load-depth curves and prove that not all conical indenters produces the load-depth curve following Equation 6.3. From this study, the load-depth curves are better described using Equation 6.4. As the tip radius of the indenter increases, the value of the parameter  $m$  decreases.

$$P = Ch^2 \quad \text{Equation 6.3}$$

$$P = Ch^m \quad \text{Equation 6.4}$$

where  $P$  = load

$h$  = indentation depth

$C$  = a constant, representing load-depth responses

$m$  = a constant, representing load-depth responses and defined by the tip radius.

Effect of tip radius on the P-h curve:  
identified  $C$  and  $m$  values  
in Equation 6.4  
(for  $\sigma_y = 2000$  MPa,  $n = 0.1$ ).

Tip Radius (mm)	$C$	$m$
0.0	71085	2.01
0.1	37123	1.62
0.2	27529	1.38

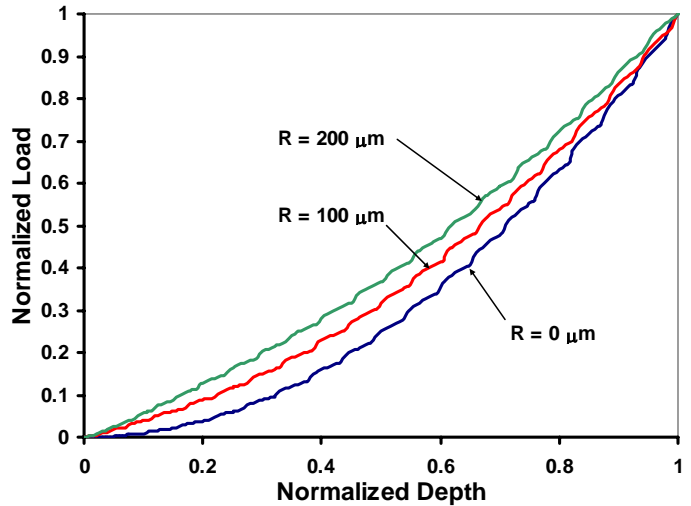


Figure 6.5: Normalized load-depth curve to demonstrate the effect of tip radius on the degree of the curvature (DEFORM 2D simulation results:  $\sigma_y = 2000$  MPa,  $n = 0.1$ ).

### 6.2.1. Representative Strain

As observed in the study by [Dao, 2001], for a single conical indenter, the load-depth curve can be represented by only one constant, which is  $C$  in Equation 6.3. The problem of non-unique solution may be raised in the inverse analysis to determine two parameters of the flow stress equation, which are  $\sigma_y$  and  $n$  in Equation 6.2. This section demonstrates the non-uniqueness problem in conical indentation through a series of FEM simulations and the concept of representative strain.

A series of indentation simulations using different flow stress data sets were conducted. Starting by arbitrarily assuming the strain hardening ( $n$ ) of 0.1 and the yield stress ( $\sigma_y$ ) of 2000, the predicted load-depth curve to be used as a reference curve was obtained. Subsequently, the values of strain-hardening ( $n$ ) were changed to be 0.2 and 0.3 respectively in the indentation simulations, while the yield stresses ( $\sigma_y$ ) were varied at each different strain hardening exponent in order to match the predicted load-depth curve to the reference one. Error criteria to match load data can be expressed using Sum Square Error (SSE), in Equation 6.5. At the minimum SSEs, other two different solutions of the yield stresses for  $n = 0.2$  and  $0.3$  can be found.

$$SSE = \sum_{i=1}^N \left( \frac{P_{0.1,i} - P_{n,i}}{P_{0.1,i}} \right)^2; \quad n = 0.2, 0.3 \quad \text{Equation 6.5}$$

where  $P_{0.1,i}$  = the baseline simulation ( $n = 0.1$ ) load at depth interval  $i$

$P_{n,i}$  = the load at the depth interval  $i$  for the simulation, using  $n = 0.2$  and  $0.3$

$N$  = the total number of steps used

Figure 6.6 shows the predicted load-depth curves from three different flow stress solutions, for  $n = 0.1, 0.2$  and  $0.3$ . The overlap of the predicted load-depth curves indicates that inverse analysis using a conical indentation cannot provide a unique flow stress solution.

Three flow stress solutions are plotted in Figure 6.7. All obtained flow stress curves intersect at the strain of  $0.033$ . The strain at which different flow stress solutions exhibit the same true stress and result in the same predicted load-depth curve is called “representative strain”. This representative strain is determined by the geometry of the indenter and is reported to be  $0.033$  for a sharp, Berkovich indenter (with a half angle of  $70.3$  degrees), as previously illustrated in Figure 3.8 [Dao, 2001]. The estimated representative strain of  $0.033$  from this study matches exactly with the value determined by Dao.

### 6.2.2. *Effect of Friction*

The effect of friction on the load-depth curve is investigated. Constant shear friction ( $\tau = m_f k$ ; where  $\tau$ ,  $m_f$  and  $k$  are shear frictional stress, friction factor and shear flow stress of the workpiece, respectively) was assumed at the interface between the indenter and the workpiece in FEM simulations.

Multiple FEM simulations were conducted using different friction factors. The resulting load-depth curves are shown in Figure 6.8. It is clearly shown that friction has insignificant effect on the load-depth curve. This statement indicates that the established indentation tests and inverse analysis are highly dependent on the material flow stress properties while the effect of friction can be neglected.

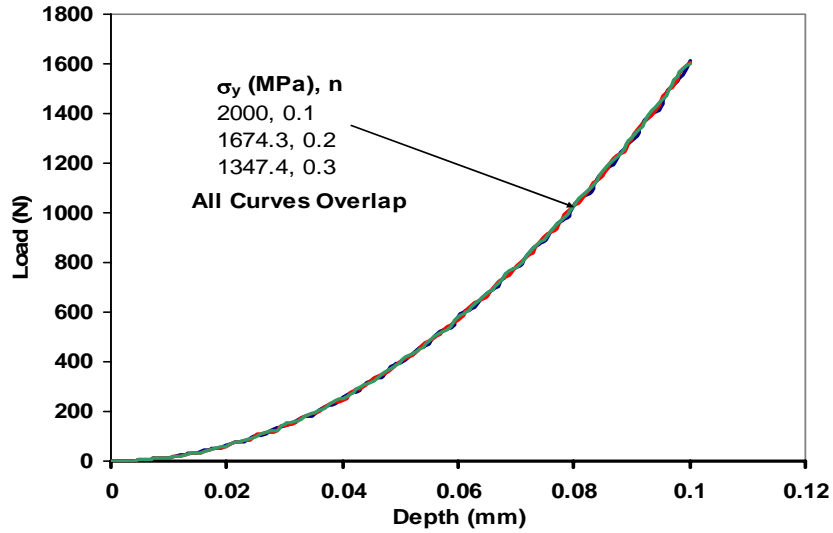


Figure 6.6: The predicted load-depth curves from a conical indenter with a half-angle of  $70.3^\circ$  (Berkovich indenter), using three flow stress equations with a representative strain of 0.033.

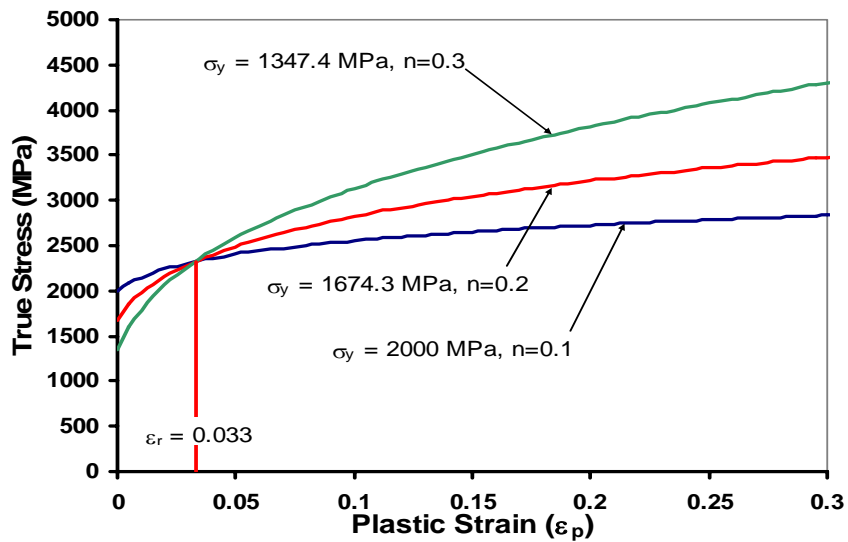


Figure 6.7: The flow stresses used in the simulations in Figure 6.6 showing the representative strain of 0.033.

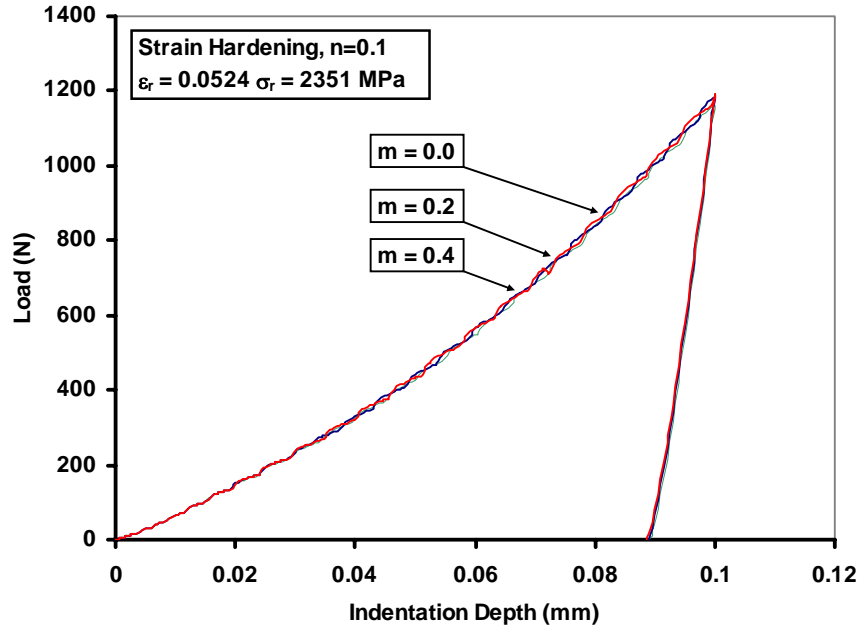


Figure 6.8: The effect of friction on the load-depth curve in simulation of a conical indentation is negligible.

### 6.3. Evaluation of Indentation with a Spherical Indenter

Spherical indentation was explored for the use of inverse analysis to determine the flow stress property of surface layer. These will cover (a) an analysis on the effect of strain-hardening (to evaluate whether unique solution could be obtained through spherical indentation), (b) an analysis on the effect of indentation depth and (c) an analysis on the effect of indenter diameter.

#### 6.3.1. Effect of Strain-Hardening Exponent

A sensitivity analysis was performed to determine how the load-depth curve from FEM simulation was affected by the changes in yield stress ( $\sigma_y$ ) and strain-hardening exponent ( $n$ ) of Equation 6.2. Similar to conical indentation,



simulation results show that the magnitudes of the predicted loads directly depend on the yield stress. This can be explained by the fact that an increase in yield stress indicates that a larger load is required for an indenter to penetrate into the workpiece surface.

For analysis on the effect of strain-hardening, simulations were conducted using a 1.5 mm ball indenter with an arbitrarily assumed yield stress of 300 MPa and varying strain-hardening exponents. The simulation results are shown in Figure 6.9. For better presenting the effect of the strain-hardening, load-depth curves were normalized respect to their maximum indentation depths (0.25 mm) and maximum loads, as shown in Figure 6.10. This figure clearly illustrates the relationship between the curvature of load-depth curve and the strain-hardening exponent. The curvature changes from concave down at low strain-hardening exponent of 0.0 to concave up at high strain-hardening exponent of 0.4.

### **6.3.2. *Effect of Indentation Depth***

Maximum indentation depth used in indentation tests may affect the consistency of the inverse analysis procedure and the obtained flow stress data. An analysis on the effect of indentation depth could be useful to select an appropriate maximum penetration depth for use in actual indentation test.

All normalized load-depth curves of Figure 6.10 had the same maximum depth ( $h_{max}$ ) of 0.25 mm and used a 1.5 mm ball indenter. This gave a value of  $h_{max}/D$  equal to 0.167.

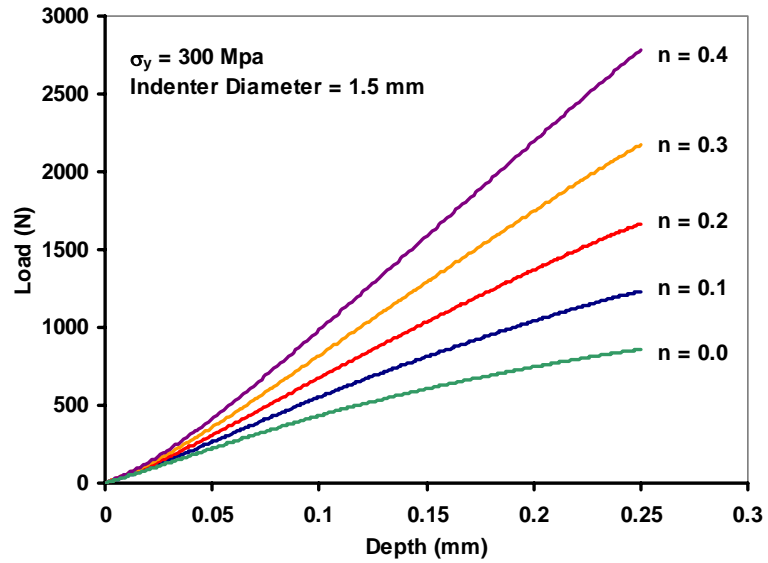


Figure 6.9: Sensitivity analysis results for spherical indentation at different strain-hardening exponents.

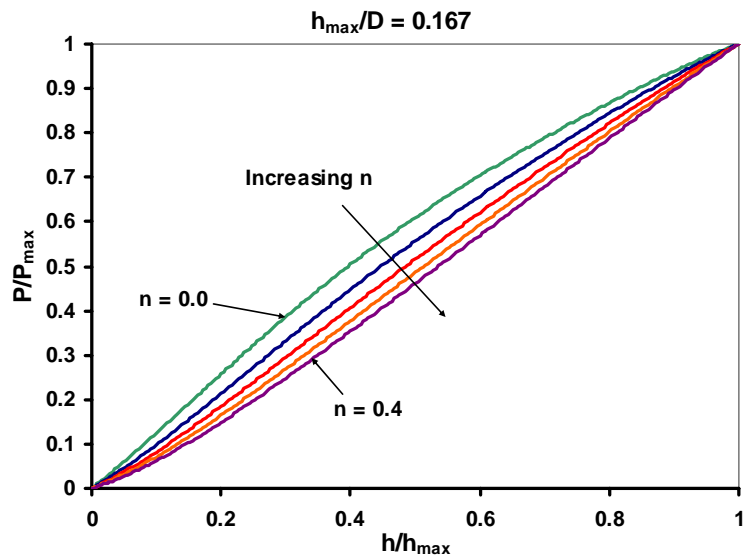


Figure 6.10: Normalized curves from the sensitivity analysis of spherical indentation ( $h_{max}/D=0.167$ ,  $\sigma_y = 300 \text{ MPa}$ ).

Additional simulations were conducted using the same ball indenter size but smaller maximum indentation depths, i.e.  $h_{max} = 0.15$  and  $0.05$  mm, giving  $h_{max}/D = 0.1$  and  $0.033$ . With decreasing values of  $h_{max}/D$  ratios, the sensitivity of the load-depth curve due to the changes in strain-hardening exponent decreased (see Figure 6.10, Figure 6.11 and Figure 6.12). The effect of strain-hardening on the curvature of load-depth curves was more apparent when a maximum indentation ( $h_{max}$ ) of  $0.25$  mm was used, while it was less noticeable when using a maximum indentation depth of  $0.05$  mm.

Therefore, it is important to select a sufficient maximum depth to ensure that the sensitivity of strain-hardening exponent on the load-depth curve can be noticeable. However, in practice, the maximum depth could be limited by the load capacity of the indentation testing machine. If the load capacity of the machine allows it, the higher  $h_{max}/D$  values (those are greater than  $0.167$ , which is the maximum value used in this study) should be evaluated to assure optimum maximum indentation depth. In addition, maximum indentation depth needs to be small enough to ensure homogeneity or slight variation for the surface property in the depth direction.

### **6.3.3. Effect of Indentation Diameter**

Additional simulations were conducted with an indenter diameter of  $1.0$  mm. The load was normalized with the maximum overall loads and the depth was normalized with respect to the indenter diameter. The results for the indenter diameters of  $1.5$  mm and  $1.0$  mm are plotted in Figure 6.13. These two graphs are identical, indicating that the normalized load-depth data are independent to the size of the spherical indenter. Therefore, the inverse analysis through spherical indentation is applicable to any size of the spherical indenter.

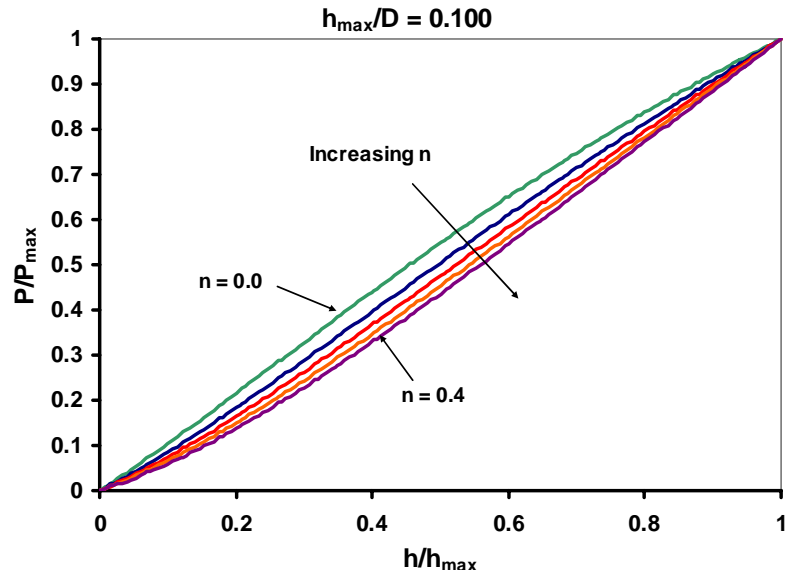


Figure 6.11: Normalized curves from the sensitivity analysis of spherical indentation, for  $h_{\max}/D = 0.1$  ( $h_{\max} = 0.15$  mm,  $D = 1.5$  mm)

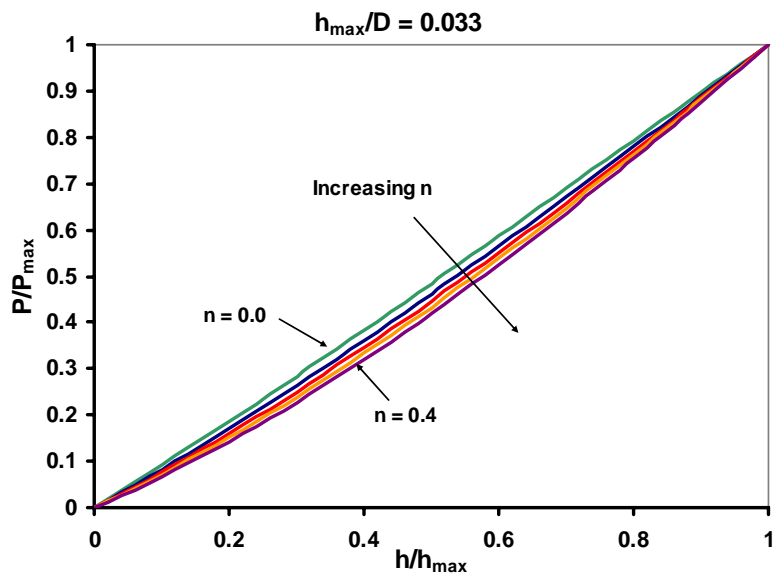


Figure 6.12: Normalized curves from the sensitivity analysis of spherical indentation, for  $h_{\max}/D = 0.033$  ( $h_{\max} = 0.05$  mm,  $D = 1.5$  mm)

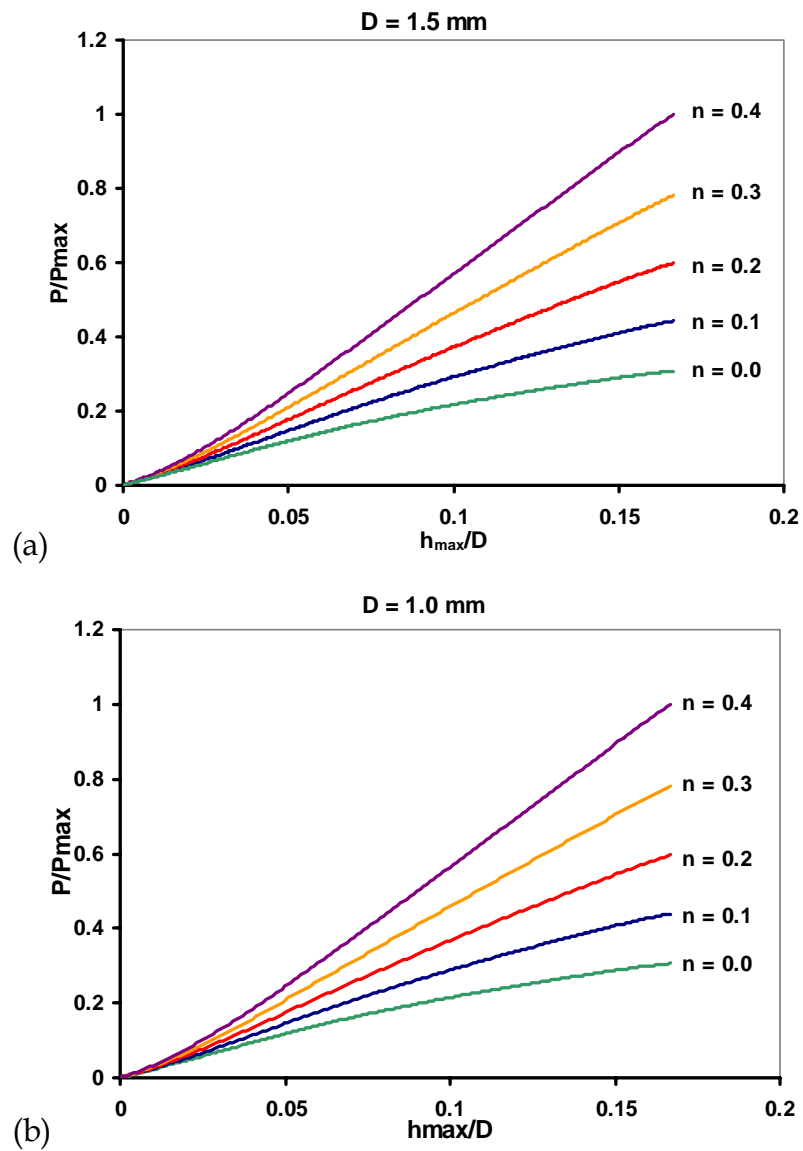


Figure 6.13: Comparison of the normalized load-depth curves from two different sized spherical indenters, for (a) Dia. = 1.5 mm and (b) Dia. = 1.0 mm.

#### **6.4. Comparison of Spherical and Conical Indenters**

Different results between spherical and conical indenters can be explained by the different amount and variation of the deformation over increasing indentation depths. This can be examined through the strain contours beneath the indenter in FEM simulations. Figure 6.14 shows the yield strain contours from FEM simulation of conical indentation at four different indentation depths. Each contour is normalized with respect to the contact radius as defined as " $r_c$ " in Figure 6.14 (left). In Figure 6.14 (right), the depth of the indentation does not affect this normalized yield strain contour, indicating that a conical indenter does not provide sufficient variations of deformation (strain) at different depths. This phenomenon may explain solution non-uniqueness problem that exists in an inverse calculation using a conical indenter.

On the contrary, when the same analysis was performed using a spherical indenter, the yield strain contours are obviously changed with increasing indentation depths, as shown in Figure 6.15. The difference in yield strain contours at different indentation depth indicates more variations in strains and stresses. In addition, the rate of strain that changes over incremental depth can be observed. This information helps to obtain a unique flow stress solution.

#### **6.5. Development of Inverse Analysis to Determine the Flow Stress Property of Surface Layer**

The objective of this study was to develop a robust inverse analysis methodology to determine the properties of materials at the surface. The earlier study provided understanding of the benefits of spherical indentation. Thus, only spherical indentation was used.

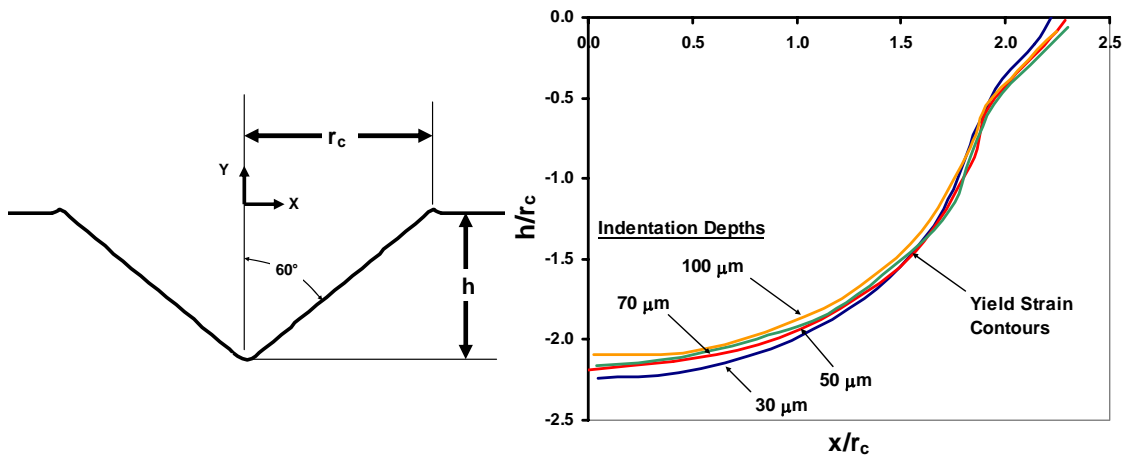


Figure 6.14: Yield strain contours from conical indentation at four different indentation depths, normalized with respect to the contact radius ( $r_c$ )

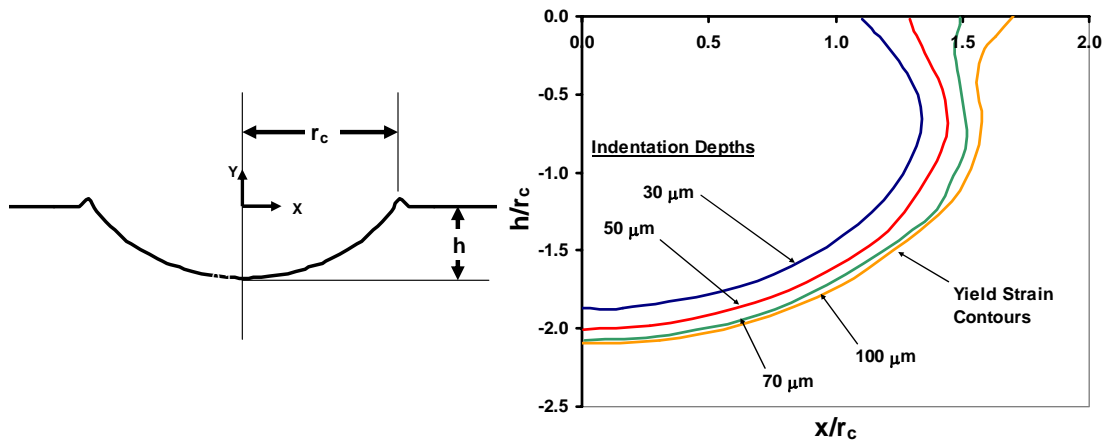


Figure 6.15: Yield strain contours from spherical indentation (with an indenter diameter of 1.5 mm) at four different indentation depths, normalized with respect to the contact radius ( $r_c$ )

Concept of the inverse analysis is to minimize the difference between experimental and simulated load-depth curves by adjusting the material parameters in FEM simulation. When the minimum error is reached, the material parameters of the flow stress equation are identified. The proposed methodology has been applied to identify the flow stress parameters of the hard-turned surface, made of AISI 52100 bearing steel. Validations of the developed inverse analysis was made by (a) comparing load-depth curves between FEM simulation and experiment and (b) comparing the flow stress data obtained from the developed inverse analysis with those determined from compression test.

#### **6.5.1. Proposed Inverse Analysis Methodology**

The procedure to determine the flow stress is a process of matching the predicted load-depth curve from FEM simulation to experiment by systematically changing the values of yield stress and strain-hardening exponent of the flow stress equation. The flow stress equation used in the FEM simulations is given by Equation 6.2. Young's modulus is assumed as constant throughout this study and is given by the standard value [ASM, 1990].

Overall inverse analysis procedure is illustrated in Figure 6.16. First, an FEM simulation is run with a strain-hardening exponent of zero ( $n = 0$ ) and an initial value for yield stress. The simulated load-depth curve is compared with the experimental data at several different points using the sum-squared error (SSE), as shown in Equation 6.6 and Figure 6.17(a). The SSE is minimized by changing the yield stress while keeping the strain-hardening exponent fixed at zero. The procedure is repeated by using different constant strain-hardening exponents of 0.1, 0.2, 0.3, etc. The values of yield stress are again varied to obtain minimum SSE for the given strain-hardening exponent.



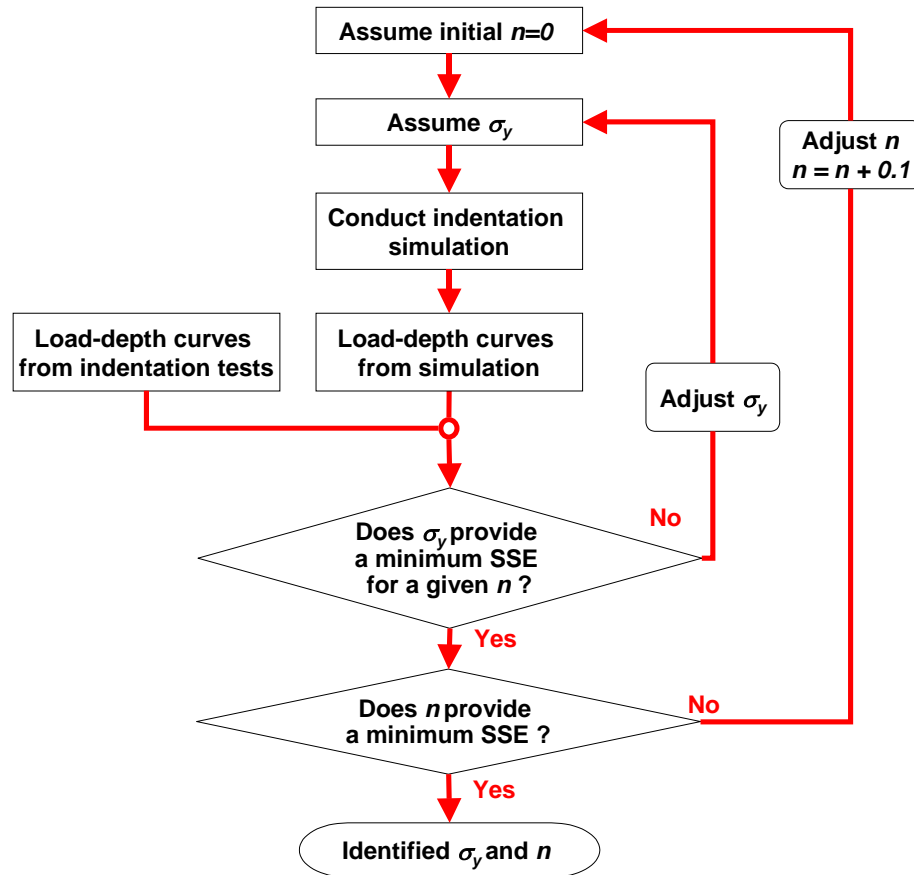


Figure 6.16: Flow chart of the developed inverse analysis procedure to determine the flow stress properties of the material surface layer from spherical indentation test.

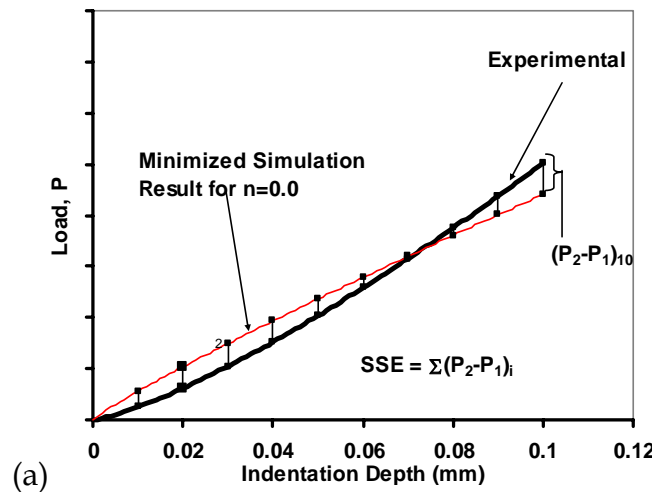
$$SSE = \sum_{i=1}^N (P_{exp,i} - P_{sim,i})^2$$

Equation 6.6

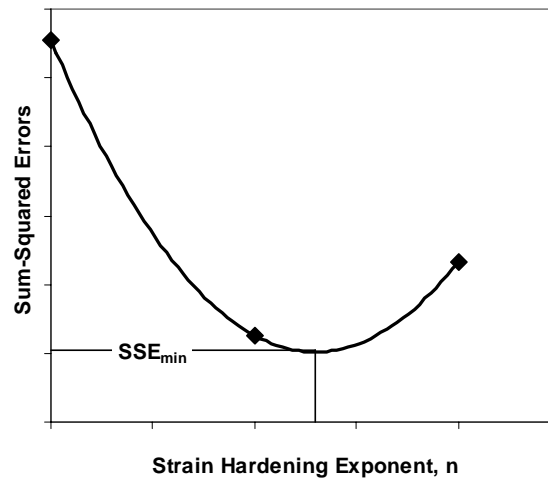
where  $P_{exp,i}$  is the experimental load at depth interval  $i$

$P_{sim,i}$  is the simulation load at depth interval  $i$

$N$  is the total number of load-depth data used



(a)



(b)

Figure 6.17: (a) Minimization of the sum-squared errors of the load-depth curve, assuming  $n = 0$ , and (b) a plot of local minimum SSEs over different strain-hardening exponents.

Next, the minimum *SSEs* for different strain hardening exponents are plotted to find the best strain-hardening value that provide an overall minimum of *SSE*, as shown in Figure 6.17(b). At this overall minimum, the strain-hardening exponent and the yield stress can be considered as the flow stress parameters, representing the material property of the surface layer.

#### **6.5.2. *Determination of the Flow Stress Property for Hard Turned Surface of AISI 52100 (60 HRC)***

The AISI 52100 sample was a cylindrical bar with 50 mm diameter bar. It was hardened to the hardness of 60 HRC and subsequently turned and roller burnished. Figure 6.18 shows a schematic of the AISI 52100 sample and the locations of indentation. Three different surface locations prepared for indentation tests are a) hard turned surface (hardening and then turning), b) roller burnished surface and c) cross section surface. Detailed information of hard turning and roller burnishing experiment will be provided in Section 7.1.

Figure 6.19 shows an Automated Ball Indentation (ABI) machine, manufactured by and located at Advanced Technology Corp., Oak Ridge, TN. Indentations on the AISI 52100 (60 HRC) were conducted using a ball indenter with the diameter of 0.762 mm. Four tests were conducted on each of three different surfaces, giving a total of twelve tests. These were denoted as “A1-A4” for hard turned surface, “B1-B4” for burnished surface, and “C1-C4” for cross-section surface. The experimental load-depth data from indentation tests on AISI 52100 samples are shown in Figure 6.20.

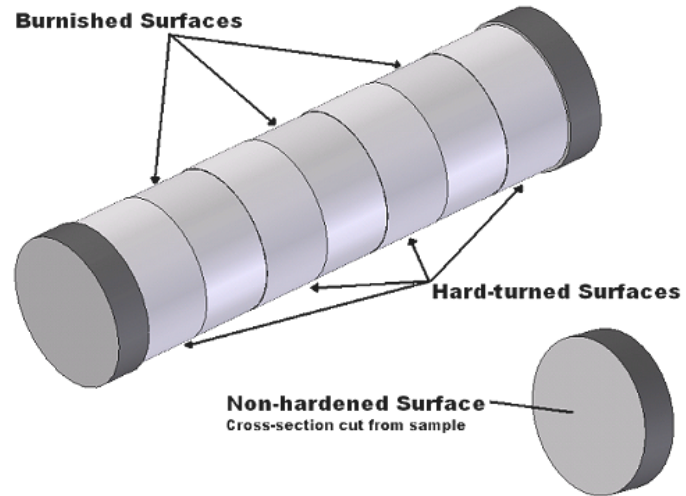


Figure 6.18: Schematic of a cylindrical AISI 52100 sample

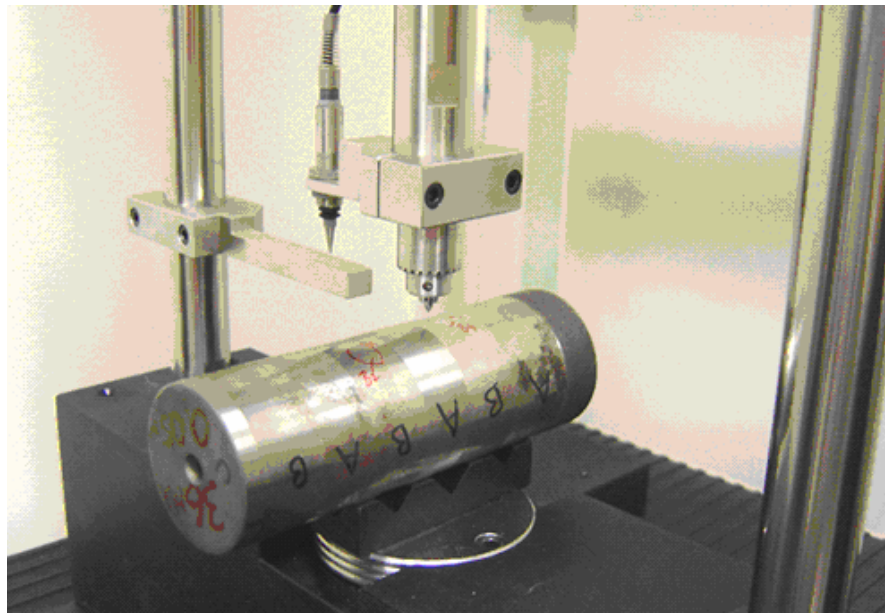


Figure 6.19: Automated Ball Indentation (ABI) machine, at Advanced Technology Corp., Oak Ridge, TN, used in indentation test on an AISI 52100 (60 HRC) sample.

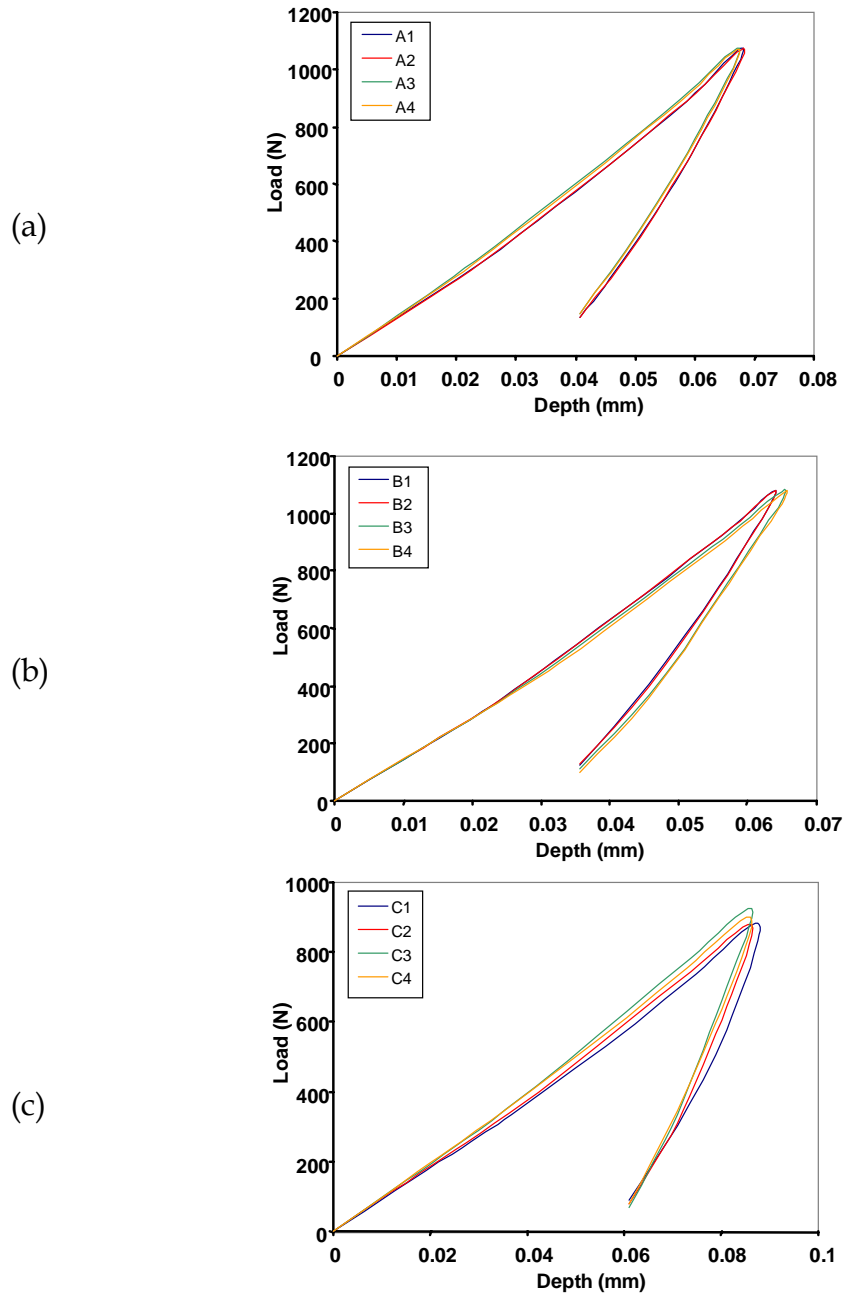


Figure 6.20: Experimental load-depth curves obtained from indentation tests on (a) hard turned surfaces, (b) roller burnished surfaces and (c) cross-section surfaces of an AISI 52100 cylindrical sample, as defined in Figure 6.18, using a 0.762 mm ball indenter (measurements conducted by Advanced Technology Corp., Oak Ridge, TN)

FEM simulations were conducted using a commercial code, DEFORM-2D™. An axisymmetric two-dimensional FEM model was constructed to simulate the indentation response of AISI 52100 steel (60 HRC). Information of mesh definition and other setup for the FEM model was previously presented in Section 6.1.2 and illustrated in Figure 6.2. The spherical indenter was modeled as a rigid object while the workpiece material was assumed homogeneous and elasto-plastic.

Since the sample used in indentation test was cylindrical shape while the indenter was spherical shape, 3D FEM model could provide more realistic contact but could increase computational time considerably. Thus, the effect of the roundness of the workpiece surface was studied by conducting two 2D simulations: (a) an indentation on a flat workpiece surface and (b) an indentation on a hemi-spherical workpiece surface, using the actual workpiece diameter of 50 mm. The simulation results showed no difference in the predicted load-depth curves for both flat and round surfaces. Therefore, it was reasonable to assume flat surface for all simulations conducted in this study.

For an inverse analysis of indentation test, main focus was on the hard-turned surfaces of a cylindrical sample since the flow stress data of this surface will be used for FEM modeling of roller burnishing. With the experimental load-depth curves in Figure 6.20(a) and the established inverse analysis procedures, the flow stress parameters of four hard-turned surfaces can be found, as shown in Table 6.1. In Figure 6.21, the average flow stress of AISI 52100 is plotted and compared with the flow stress that was analytically determined using Haggag's approach [Haggag, 1993]. The obtained flow stress matches well with the analytical results.

For a comparison with the flow stress data from compression tests, the flow stress data obtained from spherical indentation test reasonably agree with

the data from compression (see Figure 6.22). The obtained flow stress data have the slightly lower yield stress but the same strain hardening behavior, comparing to Caccialupi's flow stress data [Caccialupi, 2003].

Flow Stress Parameter	A1	A2	A3	A4	Average	St. Dev.
$\sigma_y$ (MPa)	1667	1665	1860	1869	1765	115
$n$	0.179	0.178	0.128	0.144	0.157	0.025

Table 6.1: The flow stress parameters of the hard-turned surface of AISI 52100 (60 HRC), obtained from the FEM inverse analysis and spherical indentation tests

Load-depth curves from instrumented indentation tests on other two different surfaces, previously shown in Figure 6.20(b) and Figure 6.20(c) (i.e. burnished and cross-section surfaces) are used for determining for the flow stress data for comparison. The flow stress solutions of three surfaces are shown in Figure 6.23. It obviously shows that machining, surface finishing and heat treatment processes can significantly affect the change in the flow stress properties of the engineering surfaces. In addition, it indicates that the procedures to determine the surface property is necessary, especially when modeling surface forming operations such as roller burnishing. The established inverse analysis with spherical indentation test is advantageous since it is cost-effective and simple to be implemented in an industry environment.

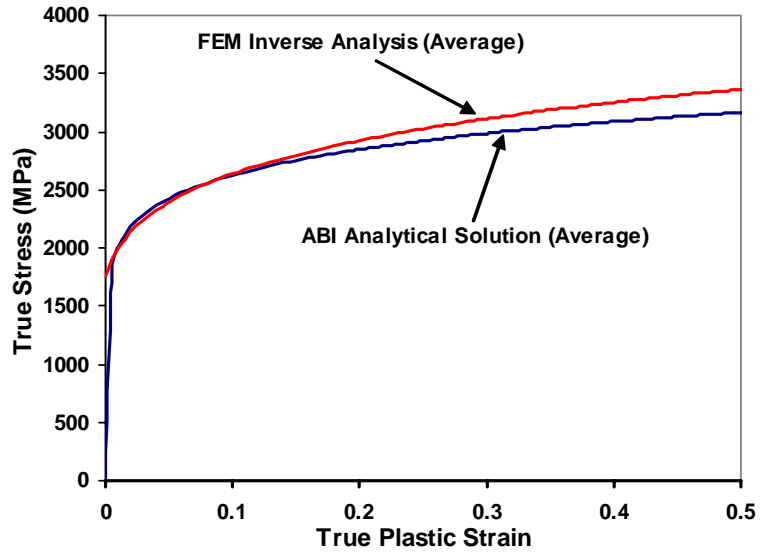


Figure 6.21: Comparison of the flow stress data of the hard-turned AISI 52100 surfaces obtained from FEM inverse analysis and analytical solution derived by [Haggag, 1993]

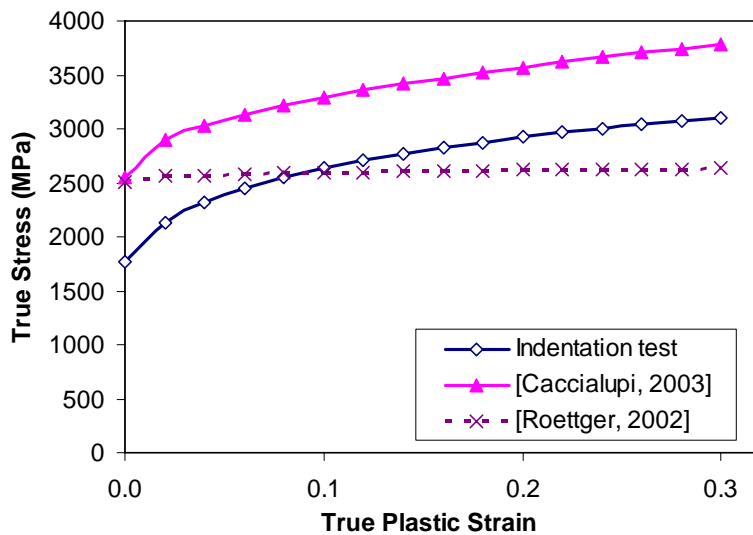


Figure 6.22: Comparison of the flow stress data for AISI 52100 (60 HRC), obtained from indentation test and compression test



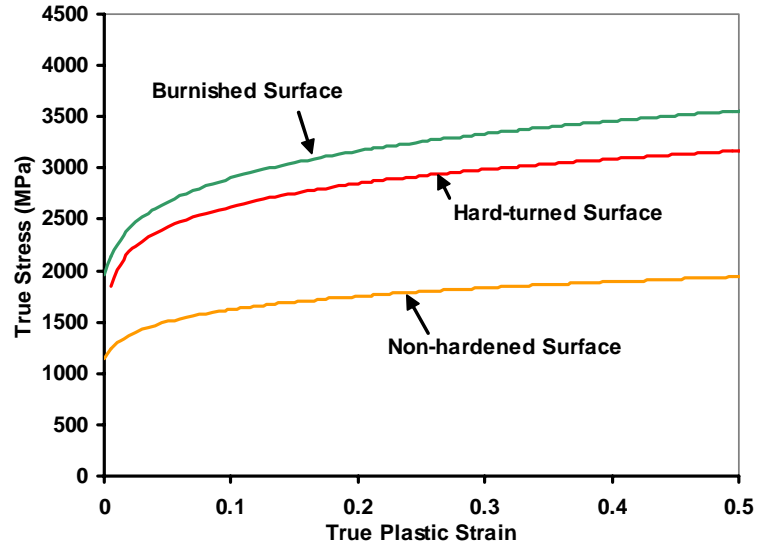


Figure 6.23: Comparison of the flow stress results for the three different surfaces of an AISI 52100 steel sample (as shown in Figure 6.20).

## 6.6. Conclusions

The surface layer of the component before burnishing could undergo severe plastic deformation and possible phase transformation from previous machining operations. The basic concept is to model the surface layer as a homogenous material distinct from the substrate (bulk) material. Instrumented indentation test in conjunction with an inverse analysis has been developed to determine the material properties of the surface layer.

This chapter consists of two main issues: a) evaluation of conical and spherical indenters and b) FEM inverse analysis to determine the flow stress of surface layer. Conclusions of the findings are listed as follows:

- A sensitivity analysis using a series of FEM simulation shows that conical indentation exhibits non-uniqueness when determining the flow stress data from the measured load-depth curve.
- Spherical indenter is shown to provide unique flow stress data, when indentation test is carries out to a sufficient penetration depth. Thus, it is used for inverse analysis to determine the flow stress of surface layer.
- With the experimental load-depth curves, given in Figure 6.20(a) and the established inverse analysis procedures, the flow stress equation of the hard-turned surfaces of an AISI 52100 sample can be found and it is given in Equation 6.7. The obtained flow stress data will be used for the FEM simulations of hard roller burnishing, as discussed in CHAPTER 7.

$$\sigma = 1765(1 + 119\varepsilon_p)^{0.157} \quad \text{Equation 6.7}$$

where  $\sigma$  = True stress  
 $\varepsilon_p$  = Plastic strain

## CHAPTER 7

### ANALYSIS OF SURFACE PROPERTIES FROM ROLLER BURNISHING SIMULATIONS AND COMPARISON WITH EXPERIMENTS

The objectives of this study are to 1) establish an FEM model for roller burnishing to study the effects of roller burnishing parameters (i.e. burnishing pressure and feed rate) on surface roughness and residual stresses and 2) validate the simulation results with results obtained from roller burnishing experiments. In this study, 2D and 3D FEM models of roller burnishing were further developed from previous work presented in [Yen, 2004]. Additional modifications include 1) determination of flow stress of the workpiece surface using instrumented ball indentation tests in conjunction with FEM inverse analysis, 2) calibration of burnishing force by considering pressure loss during FEM simulations, 3) consideration of initial surface roughness and residual stresses from hard turning experiments and 4) validation of FEM simulations with hard roller burnishing experiments.

In this study, 2D and 3D FEM models for hard roller burnishing were established. The developed 2D FEM model was used to study the effects of process parameters (i.e. burnishing pressure, feed rate) upon surface finish and residual stresses. The simulation results were evaluated and compared with the experimental data.

## 7.1. Hard Turning and Hard Roller Burnishing Experiments

Hard turning and consequent roller burnishing experiments were conducted in order to understand the process setup, to evaluate the surface improvement and to understand the influence of process parameters (i.e. burnishing pressure, burnishing feed and burnishing speed). In addition, experiments can provide useful results to assist and validate FEM model. Hard turning and hard roller burnishing experiments were conducted at Hardinge Inc. Measurements of surface roughness and hardness were performed at the Ohio State University, whereas the measurements of residual stresses on machined and burnished surfaces were conducted by The Timken Company.

### 7.1.1. *Specifications of Machine and Tools for Hard Turning and Hard Roller Burnishing Experiments*

A Hardinge CNC lathe “Quest Model” was used for both hard turning and hard roller burnishing experiments. Technical information of CNC machine and tools used in hard turning experiments are shown in Table 7.1. These machine/tools have been used regularly for hard turning of bearing steels.

Hard roller burnishing tools, consisting of a hydraulic unit and a ceramic ball tool, were provided by Ecoroll Company and borrowed through Prof. Marinescu at University of Toledo. A hydraulic unit consists of a hydraulic pump (from Ecoroll), connecting together with an electric panel and a tank. Specifications of the hydraulic pump, the burnishing tools and the hydraulic fluid for burnishing experiments are presented in Table 7.2. Figure 7.1 and Figure 7.2 show a hydraulic unit and a hydrostatic roller burnishing tool, respectively.

<b>Machine Tool</b>		CNC Hardinge Lathe, "Quest" Model (with hydrostatic linear guideway and maximum spindle speed of 15,000 rpm)CNC Hardinge lathe
<b>Cutting Tool</b>	<b>Tool Holder:</b>	Kennametal (AISI MDJNL124B), with the following tool geometries <ul style="list-style-type: none"> <li>- Side Rake Angle = <math>-5^{\circ}</math></li> <li>- Back Rake Angles = <math>-5^{\circ}</math></li> <li>- Lead Angle = <math>-32^{\circ}</math></li> <li>- Included Angle = <math>55^{\circ}</math></li> </ul>
	<b>Cutting Insert:</b>	Kennametal (DNGA432T0820, Grade: K090), <ul style="list-style-type: none"> <li>- A Composite (Black) Ceramic, composed of Alumina and 30% TiC</li> <li>- Included Angle = <math>55^{\circ}</math></li> <li>- Tool Corner Radius = 0.79 mm</li> </ul>

Table 7.1: Specifications of the machine and the cutting tools for hard turning experiments

<b>Hydraulic Pump</b>	Ecoroll, Model "HGP 4.3", with <ul style="list-style-type: none"> <li>- Maximum pressure = 400 bar (or 40 MPa)</li> <li>- Electricity requirement = 50 Hz, 400 Volt</li> </ul>
<b>Hard Roller Burnishing Tools</b>	Ecoroll, Model "HG 6", consisting of <ul style="list-style-type: none"> <li>- Ceramic spherical ball with 6 mm diameter</li> <li>- Tool holder with <math>15^{\circ}</math> contact angle</li> </ul>
<b>Hydraulic Fluid</b>	Trim VHP from Master Chemical

Table 7.2: Specifications of hydraulic pump, tools and coolant used in hard roller burnishing experiments.

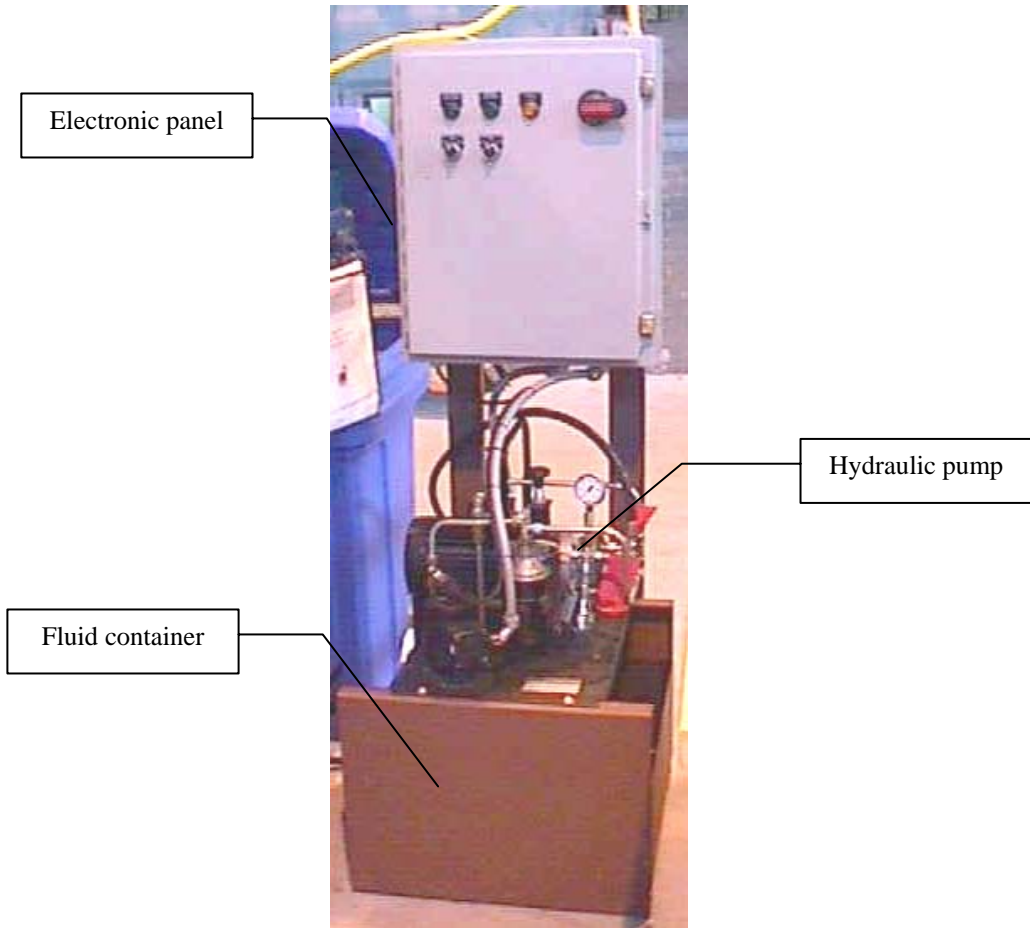


Figure 7.1: Hydraulic unit consists of pump, tank and electric control panel



Figure 7.2: Hydrostatic roller burnishing tool, Ecoroll-HG6

### 7.1.2. *Experimental Procedures and Process Conditions*

Workpiece samples used for hard turning and burnishing experiments were 16 cylindrical bars (50 mm diameter x 150 mm length), made of AISI 52100 bearing steel. Samples were through-hardened to obtain a surface hardness of 58-60 HRC prior to hard turning.

Experimental procedures can be listed as follows.

- 1) A cutting tool and a workpiece sample were mounted on the CNC turning lathe.
- 2) All 16 samples were machined to obtain hard turned surfaces for 130 mm in length, as can be seen in Step 1 of Figure 7.3. Direction of the cutting feed was toward the left.
- 3) Before burnishing operation, burnishing tool was assembled with hydraulic hose and pump. The coolant was mixed with the water and filled into the tank (in a hydraulic unit). Pump was operated and maintained at a certain burnishing pressure.
- 4) A hydrostatic burnishing tool that has a fixed contact angle of +15 degree (see Figure 7.4) was used. In addition, burnishing tool was pressurized and loaded on the workpiece surface before workpiece (or spindle) was rotated.
- 5) Burnishing tests was performed on the machined surface of each sample. Each sample was burnished on three different locations, as shown in Step 2 of Figure 7.3. Similar to turning feed, burnishing feed direction was toward the left, Figure 7.4.
- 6) Each tested sample would contain a non-machined surface, a turned surface and three burnished surfaces.

- 7) Measurements of surface roughness and hardness were performed on machined and burnished surfaces of all tested samples while the residual stresses were measured at the selected surfaces.

Hard turning tests were conducted using one cutting condition so that the test can generate reasonably equivalent machined surface roughness. A cutting condition was selected for finishing of the hardened steel (as shown in Table 7.3). This condition is also corresponding to the conditions used for the same workpiece material in the literature, [Dahlman, 2004; Poulachon, 2004; Thiele, 1999 and Roettger, 2002]. Hard roller burnishing tests used 48 different conditions (from combinations of different burnishing pressures, burnishing feeds and burnishing speeds). Burnishing conditions were selected within operating ranges recommended by Ecoroll Company. These are indicated in Table 7.3.

	<b>Process Parameter (Unit)</b>	<b>Magnitudes</b>
<b>Hard Turning</b>	Cutting Speed (m/min)	122
	Cutting Feed Rate (mm/rev)	0.1
	Depth of cut (mm)	0.127
<b>Hard Roller Burnishing</b>	Burnishing Pressure (MPa)	28, 32, 36, 40
	Burnishing Feed (mm/rev)	0.02, 0.05, 0.08, 0.11
	Burnishing Speed (m/min)	150, 300, 450

Table 7.3: Process conditions for hard turning and hard roller burnishing tests



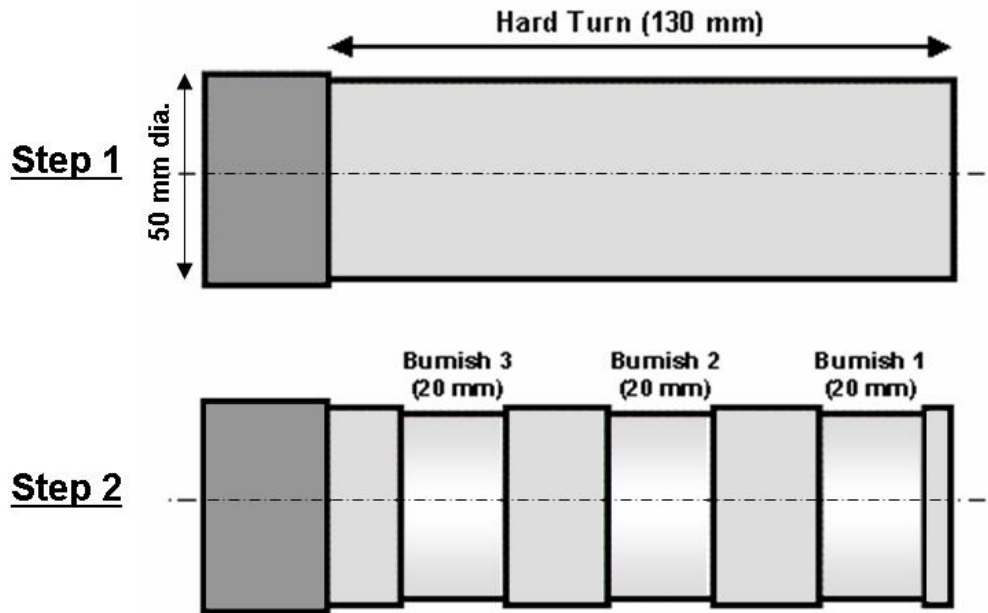


Figure 7.3: Sequences of hard turning and hard roller burnishing experiments

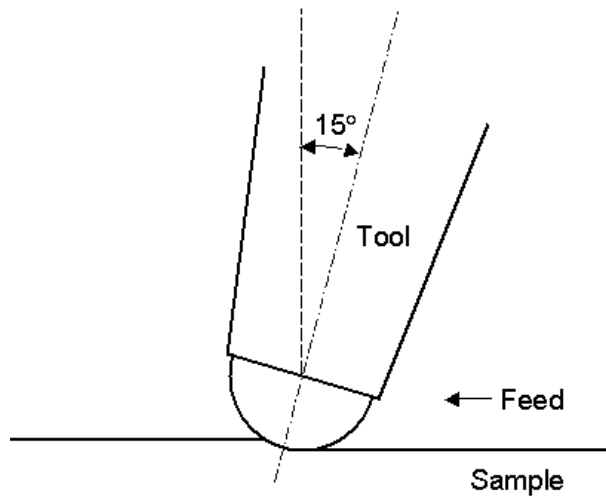


Figure 7.4: Contact angle between a burnishing tool and a workpiece sample.

### 7.1.3. *Experimental Measurements*

Roughness parameters, namely roughness depth ( $R_z$ ) and mean roughness ( $R_a$ ) were measured with a “Stylus” mechanical surface analyzer manufactured by Federal Company. Vertical resolution of the surface analyzer ranges from 0.002 to 0.010  $\mu\text{m}$  (based on assigned length of measurement). Several measuring lengths (1-3 mm) have been tried out in order to obtain consistent surface roughness data. The measured roughness parameters were also compared with other experimental data by Röttger [Röttger, 2002] and Luca [Luca, 2002]. Comparison shows that these roughness data are in the same range. Surface roughness measurements were performed on all hard turned and burnished surfaces of the samples.

Residual stresses were measured in axial ( $\sigma_{r,a}$ ) and tangential ( $\sigma_{r,t}$ ) directions of the cylindrical workpiece, using the X-ray diffraction technique, at the Timken Company. The conditions used for X-ray diffraction measurements are listed in Table 2. Briefly, an X-ray tube generator operated at 52.5 kW to produce Cr  $K\alpha$  radiation. The {2 1 1} reflection from the ferritic peak was used to measure elastic strains. Triaxial stress analysis was conducted for the selected surfaces using specimen tilt angles of  $0^\circ$ ,  $18.4^\circ$ ,  $26.6^\circ$ ,  $33.2^\circ$ ,  $39.2^\circ$  and  $45^\circ$ . Residual stress measurements were conducted for the depths of 0, 0.05, 0.1, 0.2, 0.3 and 0.4 mm from the workpiece surface. Only four surfaces were selected for measurements; including 1) hard turned surface, 2) burnished surface with  $P_b = 40$  MPa,  $f_b = 0.05$  mm/rev., 3) burnished surface with  $P_b = 32$  MPa,  $f_b = 0.05$  mm/rev. and 4) burnished surface with  $P_b = 40$  MPa,  $f_b = 0.02$  mm/rev. Maximum residual stress resolution is within  $\pm 84.9$  MPa. Experimental surface roughness and residual stress data were used for comparisons with the results obtained from FEM simulations.

---

### X-ray diffraction conditions

---

Characteristic X-ray	Cr $K\alpha$
Power	52.5 W; 35 kV, 1.5 mA
Diffraction Plane	{2 1 1}
Collimator diameter	3 mm
Specimen tilt angles	0°, 18.4°, 26.6°, 33.2°, 39.2° and 45°
Stress Constant	Carbon steel stress
X-ray line width (FWHM)	3.98 to 5.35 degree
Resolution	+/- 9.4 MPa to +/- 84.9 MPa

---

Table 7.4: Conditions used in the X-ray measurement of residual stresses

## 7.2. FEM Modeling of Roller Burnishing

Although roller burnishing is a three-dimensional process, the use of 3D FEM model to analyze the effect of various process parameters upon surface properties is limited, due to extremely large computational time required to run the simulation. Thus, the 2D FEM model is more practical and has yet the capability to study the effects of major burnishing parameters (i.e. burnishing pressure and burnishing feed) upon surface finish and residual stresses.

In this study, FEM commercial software DEFORM<sup>TM</sup>-2D is used. The procedure for modeling roller burnishing as a simplified 2D process is illustrated in Figure 7.5 [Yen, 2004].

Figure 7.5a shows roller burnishing on a hard turned surface. Since the diameter of the workpiece sample is considerably larger than the diameter of the ball tool, the workpiece object is assumed to be flat. Plane (W) is assumed to pass through the center of the ball along one roughness ridge. Figure 7.5b shows the

tool motion viewed on the section plane ( $W$ ), which is assumed to pass through the ball's center aligned with one roughness ridge. Consider a material element located in front of the ball at the top of the roughness peak ( $A_0$ ; subscript represents different times) in Figure 7.5b. As both the ball and workpiece rotate, this material element  $A_0$  is rolled over by the ball and moves down vertically to the lowest position  $A_1$  ( $A_0$  to  $A_1$ : loading). As the workpiece advances, this element then rises slightly due to elastic recovery of the surface and loses contact with the ball at the point  $A_2$  ( $A_1$  to  $A_2$ : unloading). The vertical displacements of this element are projected onto a plane at the right window of Figure 7.5b. The symbol ' $D$ ' represents the maximum penetration depth (or interface) of the ball between  $A_0$  and  $A_1$ .

To simulate the deformation process for the material element moving from  $A_0$  to  $A_2$ , the 3D rolling motion of the ball may be virtually transformed into a translational motion in  $Z$  direction in the proposed 2D model representing the projecting plane (small window in Figure 7.5b). In this plane, the surface roughness profile, generated by hard turning, and the effect of burnishing feed rate can be implemented in the 2D FEM model. Steps of 2D simulation are described below and in Figure 7.6.

- Step-1: The ball moves down at a constant velocity to press on the workpiece.
- Step-2: The ball stops at a certain maximum penetration depth ( $D$ ).
- Step-3: The ball unloads from the workpiece and return to its original position and shifts in the right direction about the distance of burnishing feed
- Step-4: The processes of loading/unloading/shift are repeated for 11 cycles.

Burnishing force ( $F_b$ ) can be estimated analytically from the fluid pressure ( $P_b$ ) that applies to the ball tool and the ball diameter ( $d_b$ ), and is given by

$$F_b = \frac{\pi}{4} d_b^2 P_b \quad \text{Equation 7.1}$$

For the same roller burnishing conditions and workpiece material, Röttger measured the burnishing forces by using a dynamometer on the tool holder fixture [Röttger, 2002]. These experimental burnishing forces were compared with the theoretical forces calculated using Equation 7.1. The comparison showed that the experimental forces are approximately 11% lower than the calculated forces. The differences are due to small fluid pressure loss along the circumferential gap between the ball and its socket. This percentage of force reduction due to pressure loss was taken into account in our 2D FEM model. As the experimental setup had a  $15^\circ$  contact angle (or the angle between the ball tool and the normal to workpiece surface), the burnishing force to be used in 2D roller burnishing simulations can be given by

$$F_b = 0.89 \frac{\pi}{4} d_b^2 P_b \cos(15^\circ) \quad \text{Equation 7.2}$$

In FEM model, the ball was considered as a rigid object and the workpiece was considered as an elastic-plastic object. Because pressurized fluid acts as coolant and lubricant in the process, isothermal condition and zero friction ( $m_f = 0$ ) were assumed. The displacement boundary constraints that were applied on the left, right and bottom boundaries of the workpiece are shown in Figure 7.7.

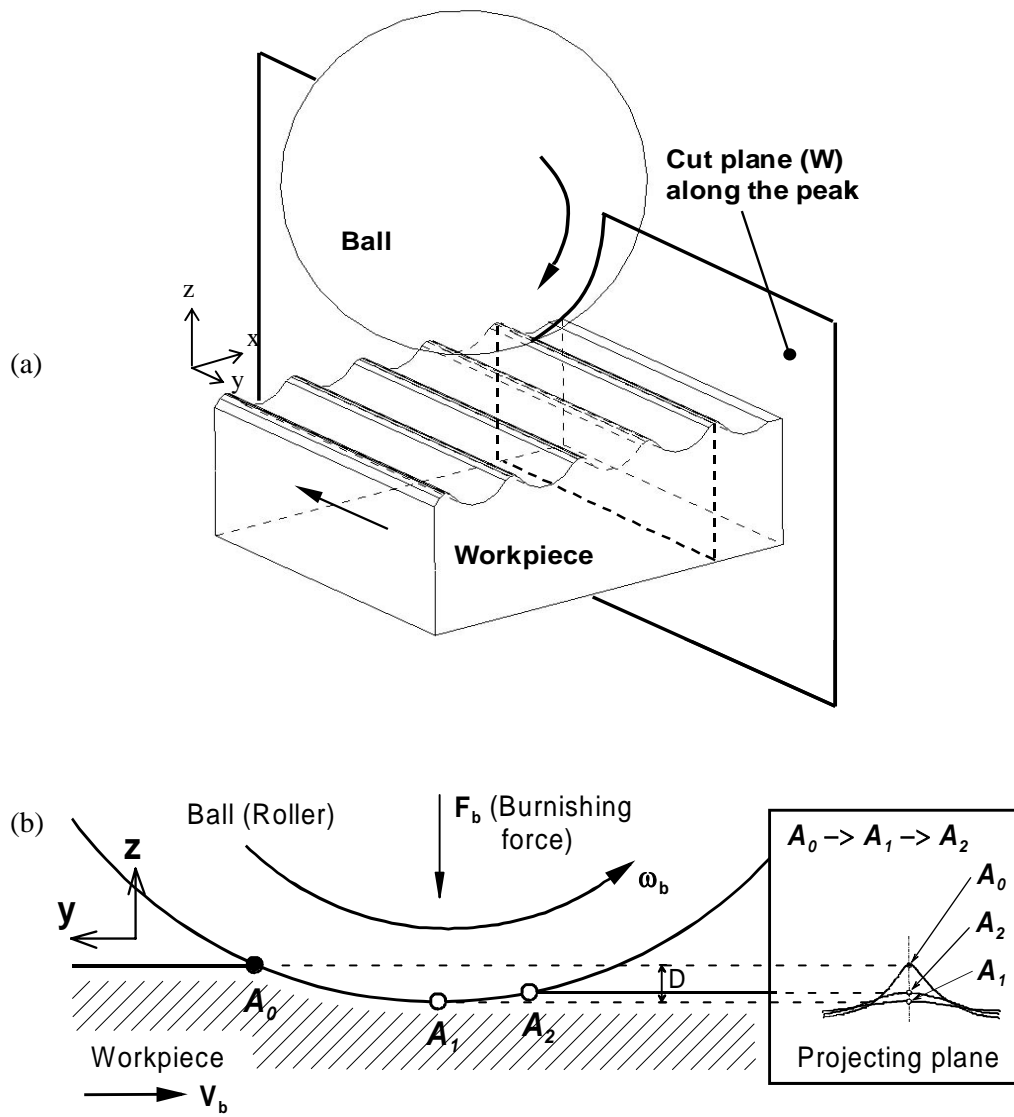


Figure 7.5: (a) Roller burnishing process; (b) schematics of burnishing motion on the plane W [Yen, 2004]

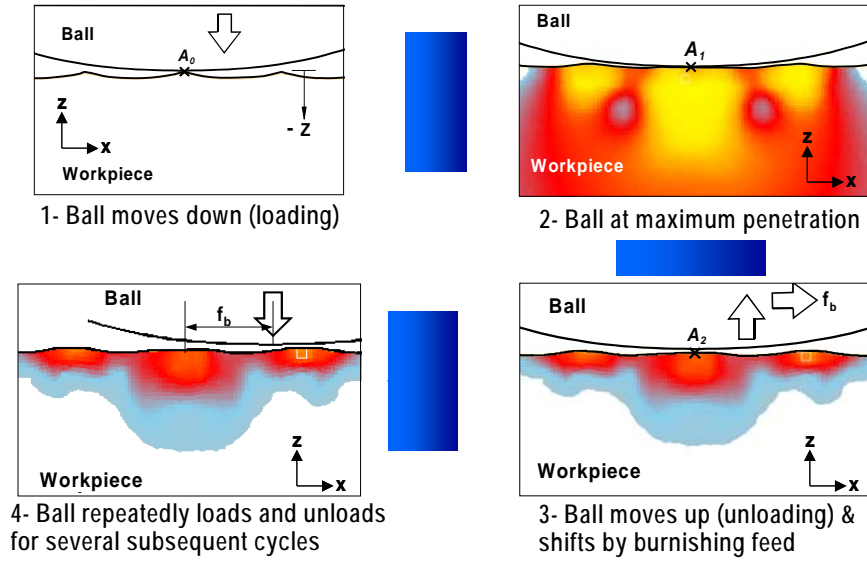


Figure 7.6: Simulation sequence for 2-D FEM modeling of roller burnishing

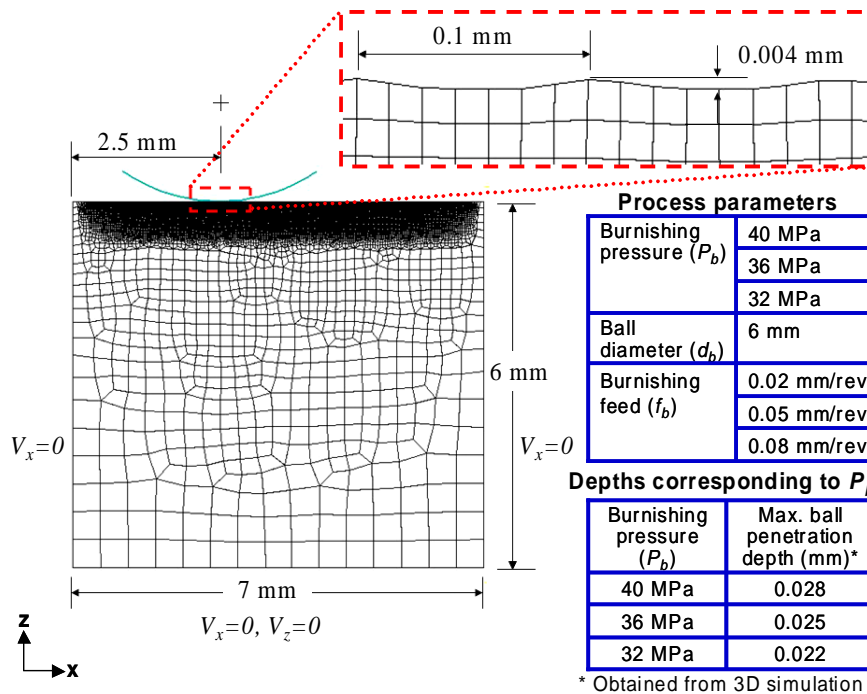


Figure 7.7: Setups of the 2D roller burnishing simulation

The size of workpiece object in 2D FEM simulations was determined by conducting a sensitivity analysis for the effect of workpiece size upon residual stresses and surface roughness. Preliminary 2D roller burnishing simulations were performed for only one indentation cycle (no feed effect) using different workpiece dimensions, i.e. 3x2 mm, 5x3.5 mm, 5x4.5 mm and 7x6 mm. Analysis showed that the size of the workpiece strongly influenced the predicted results for both residual stress and surface roughness. However, the results did not change dramatically when the workpiece size was larger than 5x4.5 mm. Since the burnishing feed rate will need to be considered later in 2D roller burnishing simulations, the workpiece size was assumed to have larger dimensions, i.e. 7x6 mm.

In the established 2D model, the ball movement was controlled by displacement. For every indentation cycle, the ball moved toward the workpiece until reaching the same maximum penetration depth and then unloaded from the workpiece (see Figure 7.6). This maximum ball penetration was established from the results of 3D roller burnishing simulations of a single rolling path with DEFORM<sup>TM</sup>-3D. Mesh density of the workpiece and the ball in 3D FEM model is shown in Figure 7.8. Workpiece object has 190,000 tetrahedral elements with minimum element size of 25  $\mu\text{m}$  at the surface. In the 3D model, the ball tool moves along Y-direction and rotates around its X-axis. Other settings and assumptions used for this 3D model are shown in Table 7.5.

The maximum penetration depth was obtained by conducting three 3D simulations at three different penetration depths to construct the predicted load vs. ball penetration depth curve, as shown in Figure 7.9. For the given burnishing pressure and Equation 7.2, the burnishing force can be calculated. The corresponding maximum ball penetration depth can be found from Figure 7.9.



Maximum ball penetration depths for the given burnishing pressure of 40 MPa and 32 MPa are 0.028 and 0.022 mm, respectively.

Although zero friction was assumed by the fact that pressurized fluid acts as coolant and lubricant, a series of 3D burnishing simulation were conducted to understand the effect of friction condition in the estimation of maximum ball penetration depth. Figure 7.10 shows the predicted force from the 3D FEM simulations using the same interference depth of 0.028 mm but different shear friction factors ( $m_f$  from " $\tau = m_f k$ ", where  $\tau$  is shear friction and  $k$  is shear flow stress of the workpiece material). The results show that friction factor has no effect on the normal force (or the burnishing force), which indicates that assumed friction condition does not affect the estimation of maximum penetration depth for the 2D model.

<b>Object type:</b>	Elastic-plastic workpiece
	Rigid tool
<b>Workpiece size:</b>	2 x 2 x 3 mm
<b>Friction:</b>	$\mu = 0$ (rolling + lubricant)
<b>Thermal condition:</b>	Isothermal (coolant)
<b>Initial roughness:</b>	Mean roughness depth, Rz, measured from stylus profiler
<b>Tool Movement:</b>	Tool moves toward the workpiece + rotates at the same tangential speed.
<b>Burnishing force (<math>F_b</math>):</b>	Controlled by the fluid pressure and calculated by Equation 7.2

Table 7.5: Setup in the 3D FEM roller burnishing model

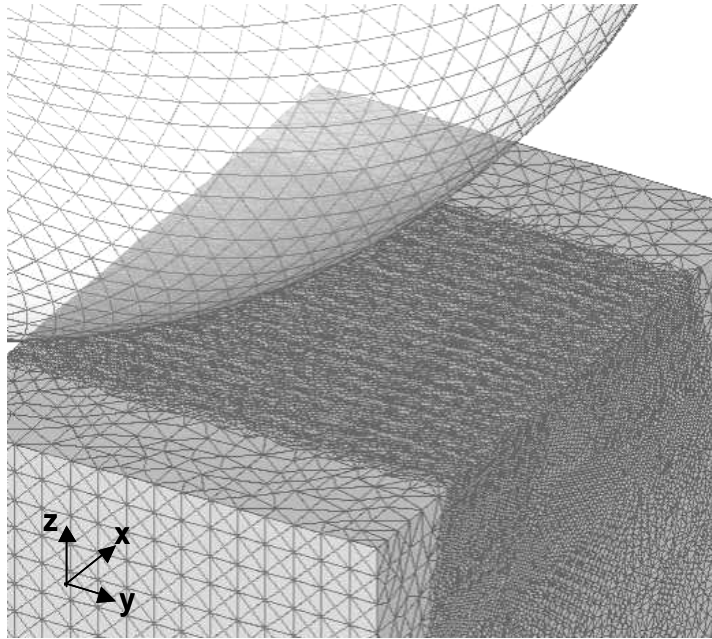


Figure 7.8: Meshes of the ball tool and the workpiece in the 3D roller burnishing simulation

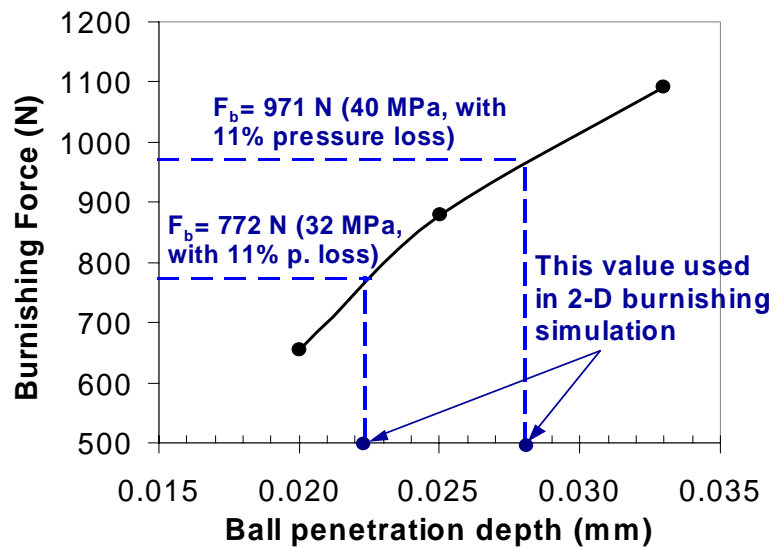


Figure 7.9: Burnishing force vs. depth curve, obtained from 3D roller burnishing simulations

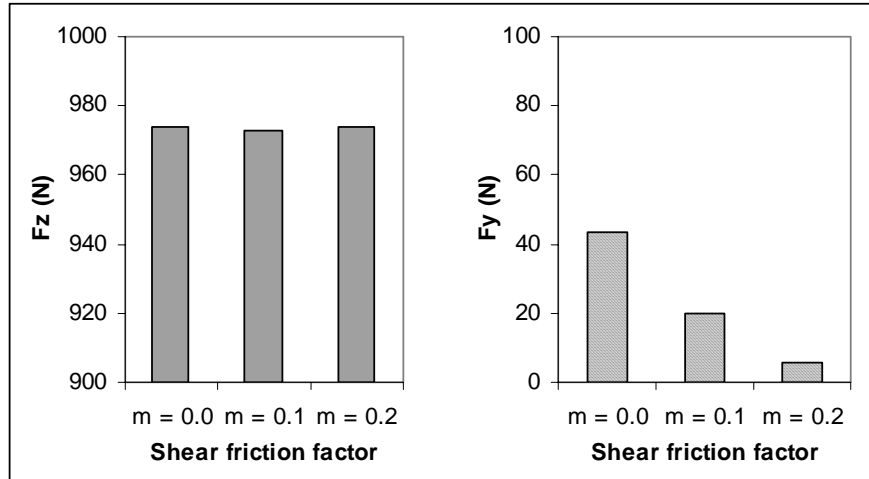


Figure 7.10: Effect of friction factor on normal and rolling forces (in Z and Y directions)

The movement of the ball in the simulation can be controlled by using two different ball movement controls, i.e. displacement control and force control. In the displacement control, the ball moves down and presses on the workpiece surface until reaching a maximum penetration depth for every indentation cycle. In the force control, the ball presses on the workpiece until reaching the maximum applied load for every indentation cycle. The limitation of the force control method used by Röttger [Röttger, 2002] is that the final penetration depth of the ball under the plane strain condition (i.e. line contact) is actually smaller than it should be under the realistic 3D condition with the same applied force. Thus, it is more reasonable to use displacement control method in the 2D FEM model.

In conducting the simulation, the following burnishing conditions were used:

- Burnishing ball diameter ( $d_b$ ) = 6 mm

- Burnishing pressure ( $p_b$ ) = 32, 36, 40 MPa
- Burnishing speed ( $V_b$ ) = 150 m/min
- Burnishing feed rate ( $f_b$ ) = 0.02, 0.05, 0.08 mm/rev.

The initial machined surface roughness for the workpiece model was obtained from experimental measurement instead of theoretical calculation that was determined from nose radius and turning feed by Yen [Yen, 2004] and Röttger [Röttger, 2002]. As shown in Figure 7.7, the distance between two roughness peaks is 0.1 mm (equivalent to the turning feed) and the measured roughness depth ( $R_z$ ) or peak-to-valley roughness is 0.004 mm. Figure 7.7 also displays the displacement constraints that were applied on the left, right, and bottom boundaries of the workpiece. In Röttger [Röttger, 2002], only 4 simulation cycles were used. However, the proposed model uses 11 simulation cycles in order to take into account the full deformation history of a single surface asperity during burnishing when the burnishing feed rate of 0.05 mm/rev is used. The total distance of the deformation zone in the simulation is 0.5 mm. For the burnishing feed rates of 0.02 and 0.08 mm/rev, the numbers of simulation cycles were 26 and 7, respectively in order to produce the equivalent deformation distance of 0.5 mm.

### 7.3. Simulation Results and Discussions

#### 7.3.1. *Data Extraction from FEM Roller Burnishing Simulation*

After the simulation was completed, the geometry of the workpiece object was exported as a tabulated set of ( $x, z$ ) coordinates of the boundary nodes. The node coordinates where the surface was indented by the ball tool were magnified and plotted in Figure 7.11. Typical standard parameters used to describe the

surface topography are the mean roughness ( $R_a$ ) and the roughness depth ( $R_z$ ). A MAPLE code was created in order to read node coordinate data and calculate these surface parameters. First, a mean line was estimated by drawing a line that divides areas beneath the surface profile equally between positive and negative regions (see Figure 7.11). Mean roughness and roughness depth can be calculated using Equation 7.3 and Equation 7.4, respectively. Roughness depth ( $R_z$ ) was calculated by taking an average of " $Z_i = \max(z_i) - \min(z_i)$ " for every interval of 0.1 mm of the burnished surface profile.

$$R_a = \frac{1}{l} \int_0^l |z(x)| dx \quad \text{Equation 7.3}$$

$$R_z = \frac{1}{N} (Z_1 + Z_2 + Z_3 + \dots + Z_N) \quad \text{Equation 7.4}$$

- where
- :  $l$  = Sampling or evaluation length (= 0.5 mm in this study)
  - :  $z$  = z-coordinate of the surface nodes
  - :  $N$  = Number of interval
  - :  $Z$  = Vertical distance of the highest to the lowest profile point

The effective stress contour, in Figure 7.12, shows that high effective residual stresses predicted by 2D FEM simulations are mostly located in the local areas beneath the roughness peaks. This means there is a large variation of the stress from peak to valley positions of the surface profile. In addition, residual stress measurements with X-ray diffraction were conducted at the surfaces of an unknown position (i.e. peak, valley or between them).

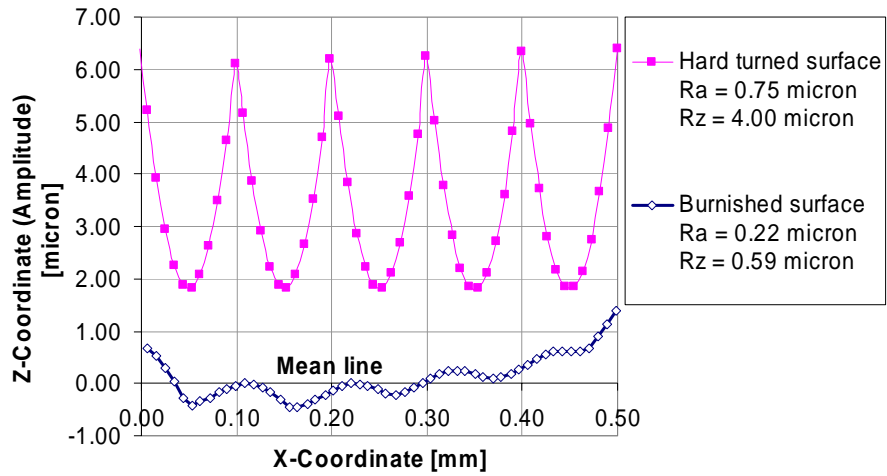


Figure 7.11: Surface nodes of initial hard turned and burnished surfaces obtained from a 2D simulation (a burnishing condition uses  $P_b = 40$  MPa and  $f_b = 0.05$  mm/rev)

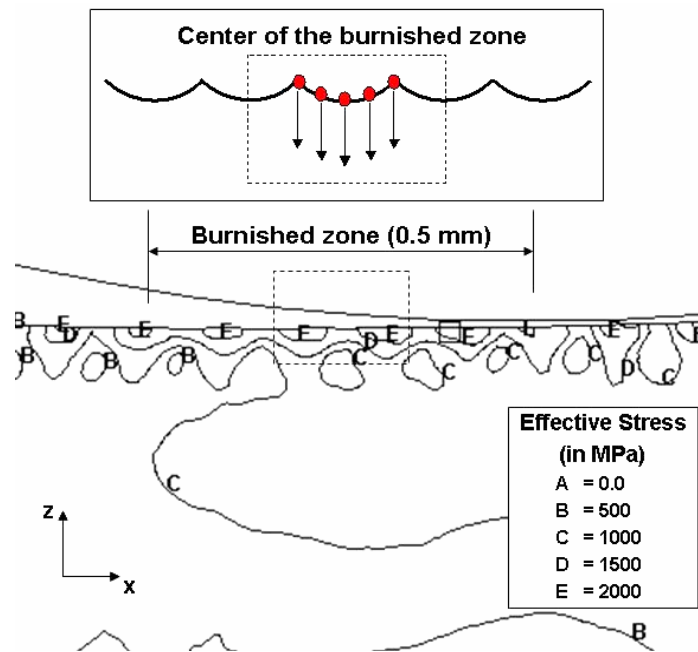


Figure 7.12: Surface nodal points for extraction of residual stress data from 2D simulation ( $P_b = 40$  MPa and  $f_b = 0.05$  mm/rev.)

In order to obtain reasonable representative residual stress distributions from 2D simulations, the residual stress distributions over the depths along 5 points at the middle of the burnished zone were extracted and the average residual stresses were taken. Stresses in x-direction represent axial stress while stresses in y-direction represent tangential stress. Residual stresses in the radial direction (z-direction) are small and negligible. For instance, the averaged residual stress distributions (i.e. tangential and axial stresses) from 2D simulations were plotted and compared with those of X-Ray measurements in Figure 7.13, (for  $P_b = 40$  MPa and  $f_b = 0.05$  mm/rev). In the same figure, both FEM simulation and experiment showed that roller burnishing induces compressive residual stress into the workpiece surface.

### 7.3.2. *Effects of Burnishing Feed Rate*

Figure 7.14 shows the effects of burnishing feed rate on surface roughness parameters  $R_a$  and  $R_z$ , at the same burnishing pressure ( $P_b = 40$  MPa). In the same figure, the results predicted by 2D FEM simulations and those obtained from experiments are shown. It should be noted in this figure that as burnishing feed increases, mean roughness ( $R_a$ ) also increases. This is due to the fact that the distance between successive burnishing ball traces increases with the burnishing feed and thus, there is less chance for the ball to smooth out all the edges of the irregularities.

To obtain a smoother surface by burnishing, the burnishing feed should be smaller than the turning feed. This is due to the fact that if the same or higher burnishing feed is used, the tool's rolling motion may be parallel to the feed grooves of the turned surface. Hence, burnishing ball will rather push surface valleys lower and increase surface roughness instead of smoothen the surface ridges.

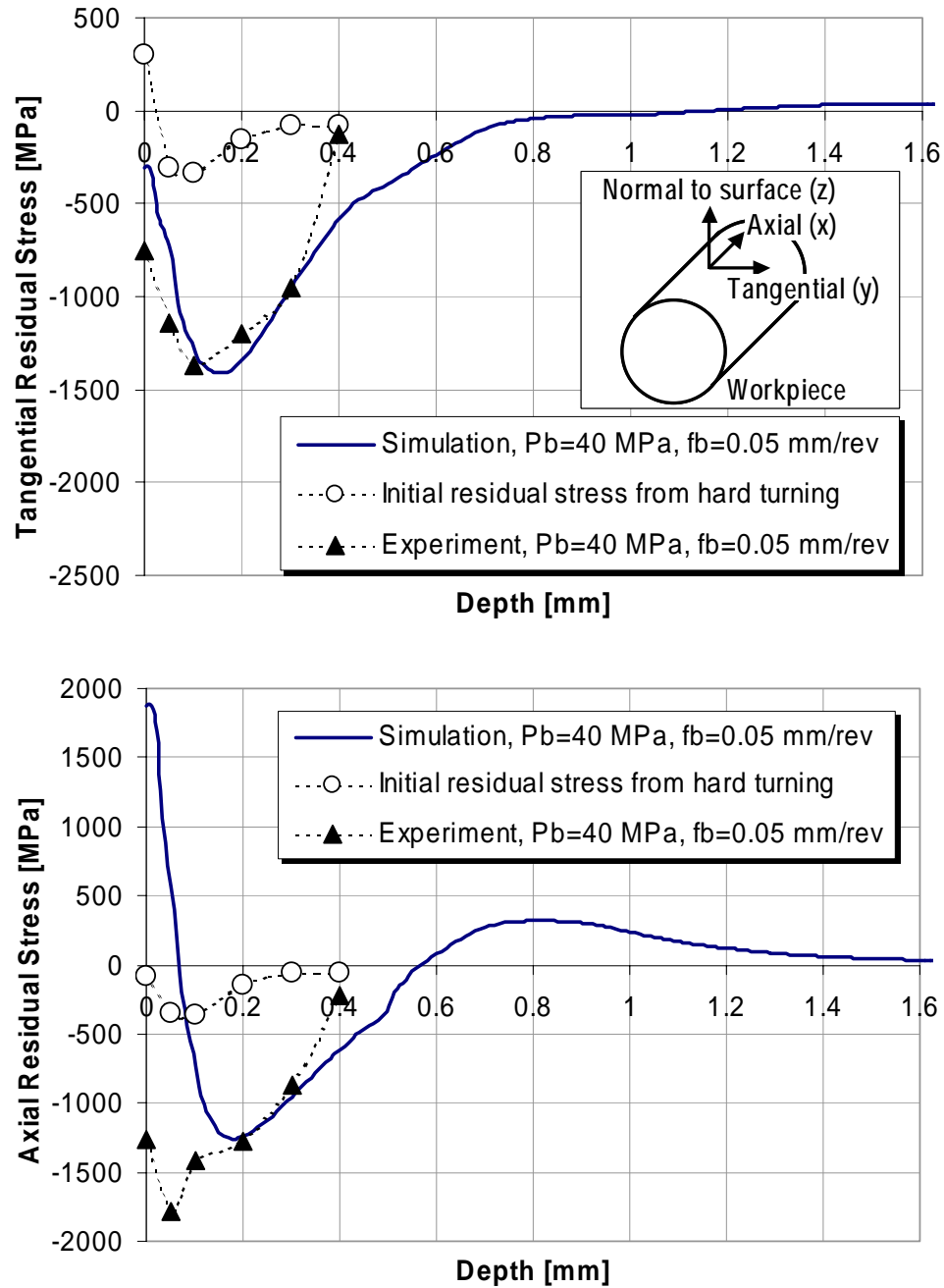


Figure 7.13: Tangential and axial residual stress distributions of the hard turned and the burnished surfaces (from simulation and experiment), for  $P_b = 40$  MPa and  $f_b = 0.05$  mm/rev.



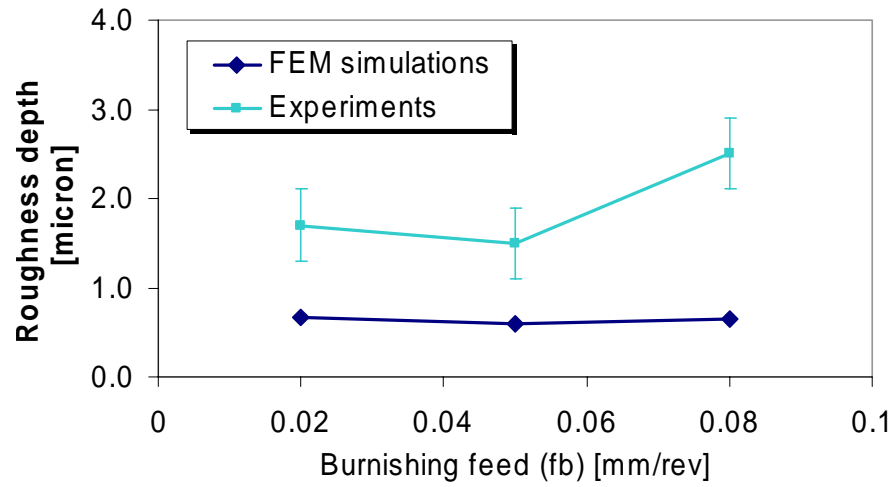
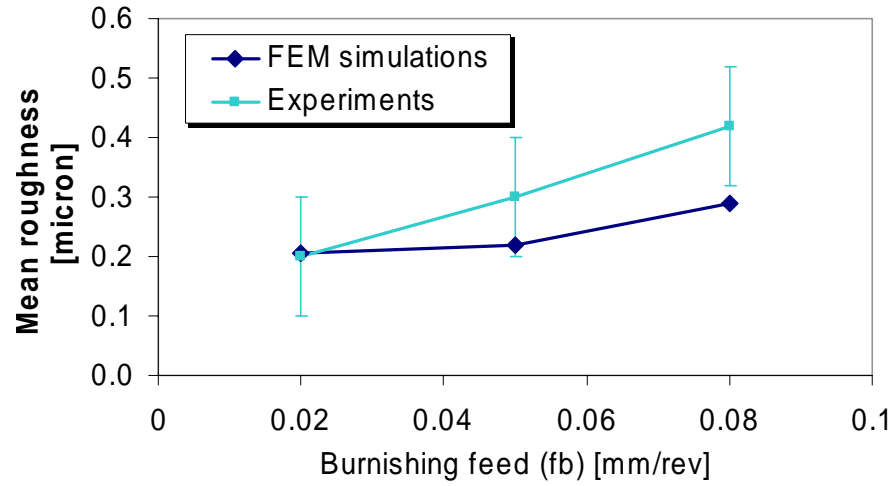


Figure 7.14: Effects of burnishing feed rate (for the same burnishing pressure of 40 MPa) on mean roughness and roughness depth

On the other hand, if a very small burnishing feed is used, the tool has more chances to flatten the surface peaks and produce a greater amount of plastic deformation on the workpiece surface due to overlapping of successive ball traces.

Compared to hard turned surface that has  $R_a = 0.75 \mu\text{m}$  and  $R_z = 4 \mu\text{m}$ , roller burnished surface has less roughness for all different burnishing feed rates used in this study (in Figure 7.14). This surface roughness improvement is shown in FEM simulations as well as in the experiments.

The variation of surface roughness parameters ( $R_a$  and  $R_z$ ) over different feed rates from 2D FEM simulations showed the same trend as experimental results, Figure 7.14. However, simulations show reasonable agreement only for the mean roughness ( $R_a$ ) and significant difference for the roughness depth ( $R_z$ ). This difference may be due to the combination of several factors, i.e. 1) the numerical error produced during FEM calculations, 2) the plane strain assumption (whereas roller burnishing process is a 3-D process in nature) and 3) the fact that FEM model cannot consider the influence of stiffness and dynamics of the machine tool and workpiece-setup.

In fact, roughness produced from manufacturing process is influenced by two main factors; i.e. contact mechanics and dynamics of the machine tools. The present FEM model can consider only the contact mechanics, and not dynamics of the machine tools. Even if the same burnishing condition is used, different models of CNC lathes (with different stiffness and precision) can produce different surface roughness.

With the present computational capability, 2D FEM simulations provided only qualitative results in predicting the surface roughness parameters, especially in the case of the mean roughness.

Figure 7.15 shows that 2D simulations predict the tangential residual stress distributions in good agreement with experimental results. Maximum compressive residual stress values are matched, within 4% difference. The effective depths that contain compressive residual stress predicted by the simulations are slightly larger than the results from experiments. However, FEM simulation cannot predict compressive residual stresses in axial direction, at and near the burnished surface (from the depth of 0 to 0.1 mm). Tensile residual stresses predicted from the simulation are due to the plane strain assumption used in the 2D model since the tool is presented as a cylindrical object rather than a spherical object. Line contact is presumed in the 2D FEM simulation rather than point contact that is typically generated by spherical tool. In the 2D model, the tool geometry, which is assumed to be larger in axial direction, pushes more material to flow aside and generates more tensile stresses in axial direction than what is expected from a spherical tool. Nevertheless, the axial residual stresses beyond 0.2 mm depth match well with the experiments.

According to FEM simulation results in Figure 7.15, a decrease in burnishing feed slightly raises the magnitude of the compressive residual stresses in both axial and tangential directions. This can be explained by the fact that a small feed indicates shorter distance between ball traces. As a result, the workpiece surface was subjected to greater amount of plastic deformation and residual stresses due to more repetitive compression by the ball tool. Simulations showed greater influence of burnishing feed rate on tangential residual stresses (i.e. more variation of residual stresses in tangential direction due to change in burnishing feed). The effects of feed rate on residual stresses are consistent with experimental observations.

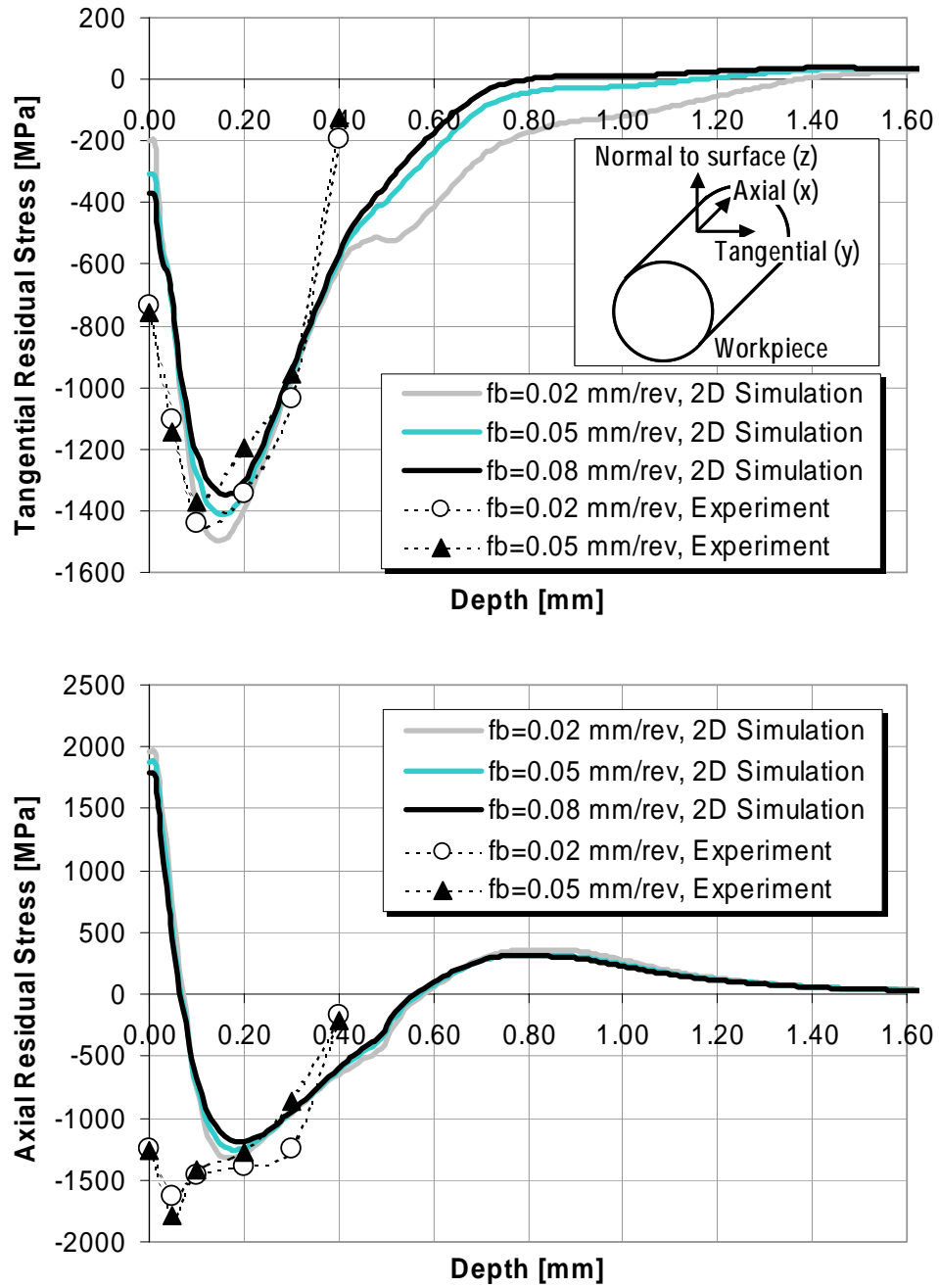


Figure 7.15: Effects of burnishing feed rate (for the same burnishing pressure of 40 MPa) on tangential and axial residual stress distributions along the depth (distance from surface)

### 7.3.3. *Effects of Burnishing Pressure*

The effects of burnishing pressure on surface roughness are shown in Figure 7.16. The values of mean roughness ( $R_a$ ) predicted by FEM simulations reasonably agree with the experimental results. FEM simulations showed that the mean roughness decreased when higher burnishing pressure was used. However, unlike the experimental observations, FEM simulations did not show the trend that there was almost no improvement of surface finish when using burnishing pressure higher than 36 MPa.

The value of roughness depth ( $R_z$ ) predicted by FEM simulation also decreased as the burnishing pressure increased from 32 to 36 MPa. However, further increase in the burnishing pressure up to 40 MPa causes higher roughness depth, which means that for the given material and hardness there is an optimum burnishing pressure for the best surface finish between 32 and 40 MPa. Surface finish predictions by FEM simulations have the same trend as those of experiments, but show considerable difference in the roughness depths. Only qualitative results of surface roughness can be provided through FEM simulations.

Similar to previous section, the quantitative differences may be explained by 1) the numerical error produced during FEM calculations, 2) the 2D plane strain assumption and 3) the influence of stiffness and dynamics of machine tool and workpiece-setup.

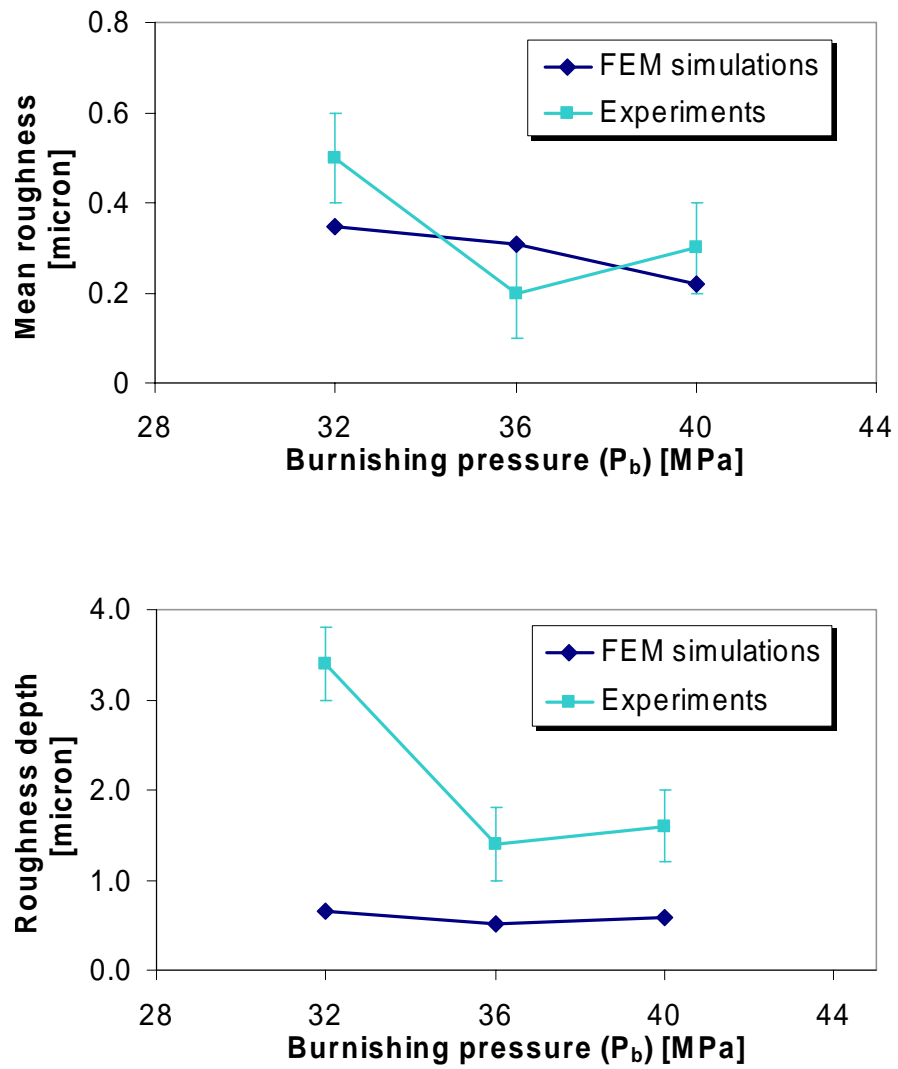


Figure 7.16: Effects of burnishing pressure (for the same burnishing feed rate of 0.05 mm/rev) on mean roughness and roughness depth

Figure 7.17 shows the distributions of the residual stresses when using different burnishing pressures and the same burnishing feed rate. In the same figure, 2D simulations predict the tangential residual stresses in good agreement with the experimental results. Maximum compressive residual stress values are matched, within 11%. The effective depths that contain compressive residual stress from the simulations are slightly larger than the experiments (when comparing 0.55 mm from the simulation and 0.4 mm from experiments).

Similar to previous section, 2D simulations cannot predict compressive residual stresses in axial direction and at the burnished surface (from the depth of 0 to 0.1 mm). Nevertheless, the trends in residual stresses in function of burnishing pressure qualitatively agree with the experiments, where higher burnishing pressures generate more compressive residual stress near the surface and produce a deeper effective compressive stress layer. In addition, the location of maximum compressive residual stresses moves deeper into the surface with increasing burnishing pressure, (at about 0.15 mm for  $P_b = 32$  MPa and at 0.2 mm for  $P_b = 36$  MPa in Figure 7.17).

The increase of burnishing pressure (or applied burnishing force) leads to an increase in the amount of plastic deformation as more roughness valleys are “filled” during the process. This leads to an increase in the compressive stresses applied to the surface, which in turn increase the surface hardness and compressive residual stresses as observed in this study and the study by Klocke et al. [Klocke, 1998].

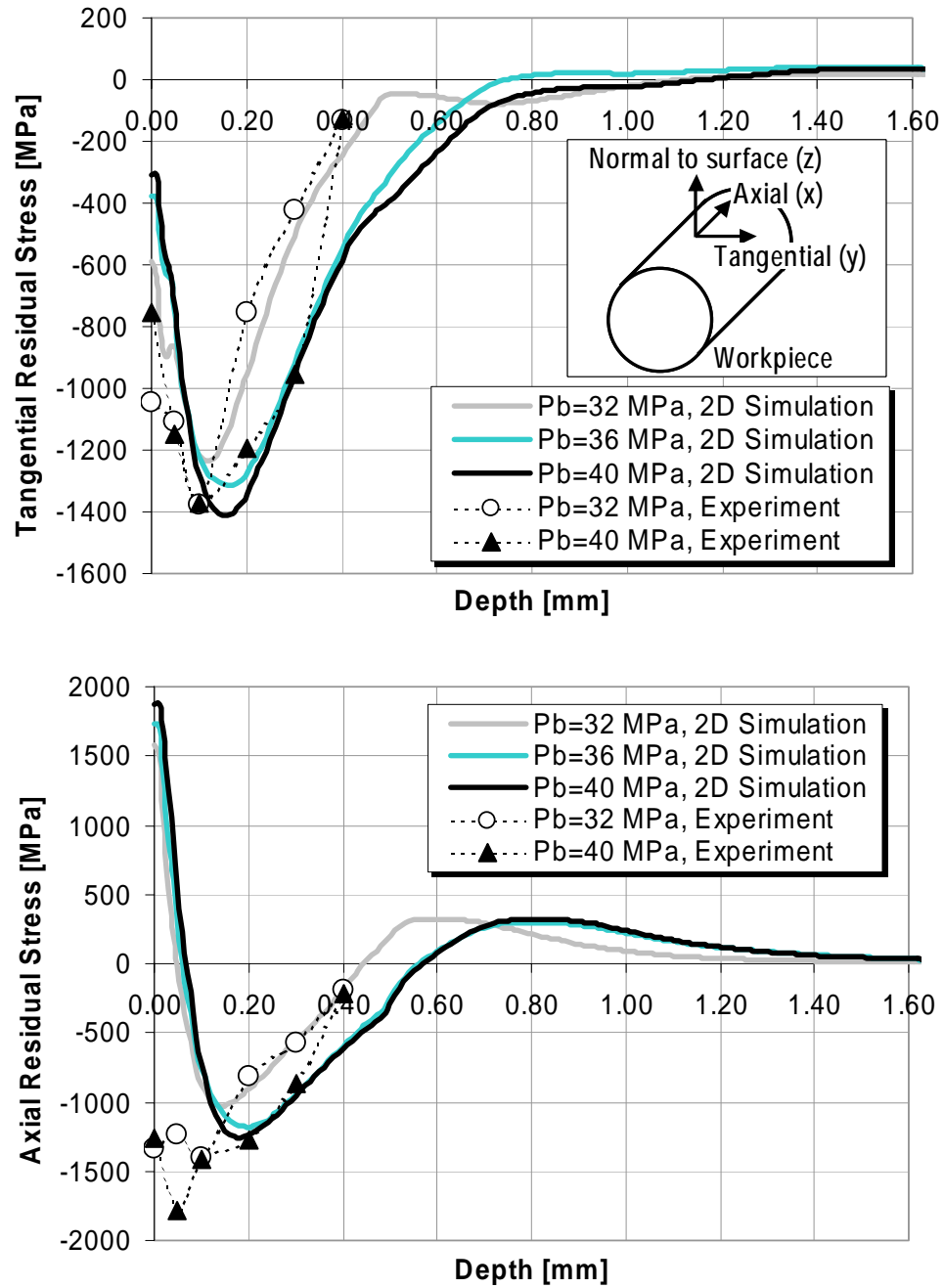


Figure 7.17: Effects of burnishing pressure (for the same burnishing feed rate of 0.05 mm/rev) on tangential and axial residual stress distributions along the depth (distance from surface)



### 7.3.4. *Effects of Ball Diameter*

The effects of ball diameter are studied by conducting a series of 2D burnishing simulations with different ball diameters (i.e. 3, 6 and 12 mm), using the same burnishing pressure and feed rate. For the burnishing pressure of 40 MPa, the burnishing forces can be calculated using Equation 7.2 to be 485.5 N, 971 N and 1942 N for the ball diameters of 3, 6 and 12 mm, respectively. Maximum penetration depths were determined from a series of 3-D roller burnishing simulations for a single ball-rolling path, similar to the approach previously described in Figure 7.9 for the ball diameter of 6 mm. Burnishing force vs. ball penetration depth curves for roller burnishing with 3 and 12 mm ball tools are shown in Figure 7.18. Maximum ball penetration depth respecting to the given burnishing force are calculated to be 0.025 and 0.031 mm for the ball diameters of 3 and 12 mm, respectively.

The effects of ball diameter on surface roughness parameters are shown in Figure 7.19. FEM simulations show that the roughness depth increases when using a larger ball tool. However, increasing ball diameter decreases the mean roughness. Element nodes of the workpiece object after burnishing from FEM simulations are plotted in Figure 7.20 to evaluate the effects of ball diameters on the entire surface roughness profiles. As shown in Figure 7.20, the surface roughness is higher when using larger ball diameter. However, the surface waviness increases when using a smaller ball diameter.

A larger ball tool provides more contact area, where the ball rolls over many roughness ridges in one rolling path. More material is pressed down rather than flows to the side of the ball. As the burnishing feed approaches further, the ball repeatedly press the surface down. In other word, any roughness ridge contacts with the ball more often than burnishing with a smaller ball diameter.

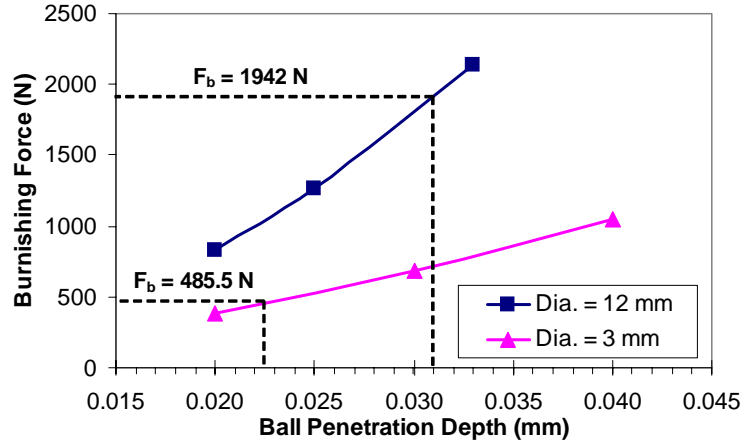


Figure 7.18: Burnishing force vs. penetration depth curves, obtained from 3D FEM burnishing simulation for 3 mm and 12 mm ball tools.

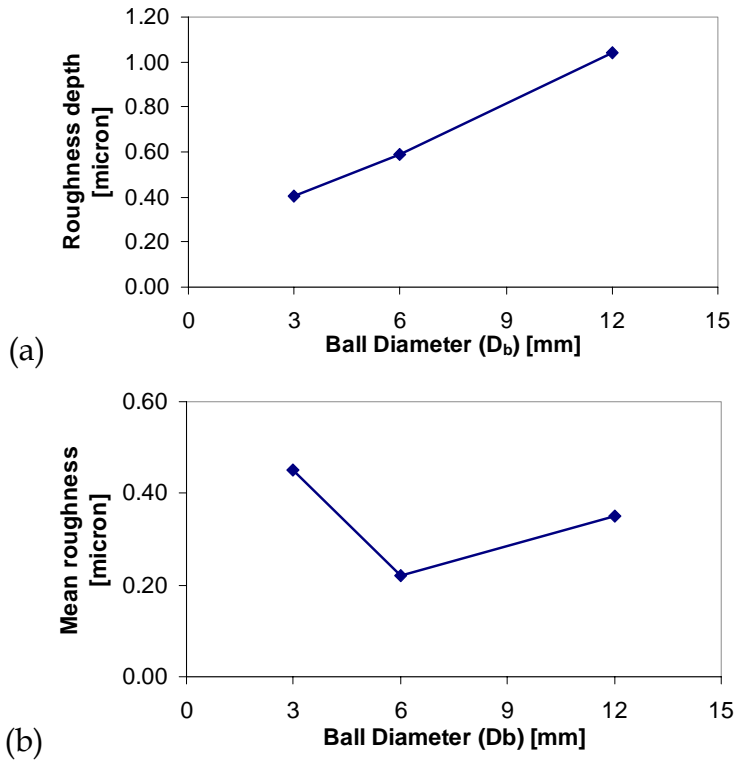


Figure 7.19: The effects of ball diameter on (a) roughness depth ( $R_z$ ) and (b) mean roughness ( $R_a$ ) from FEM simulations

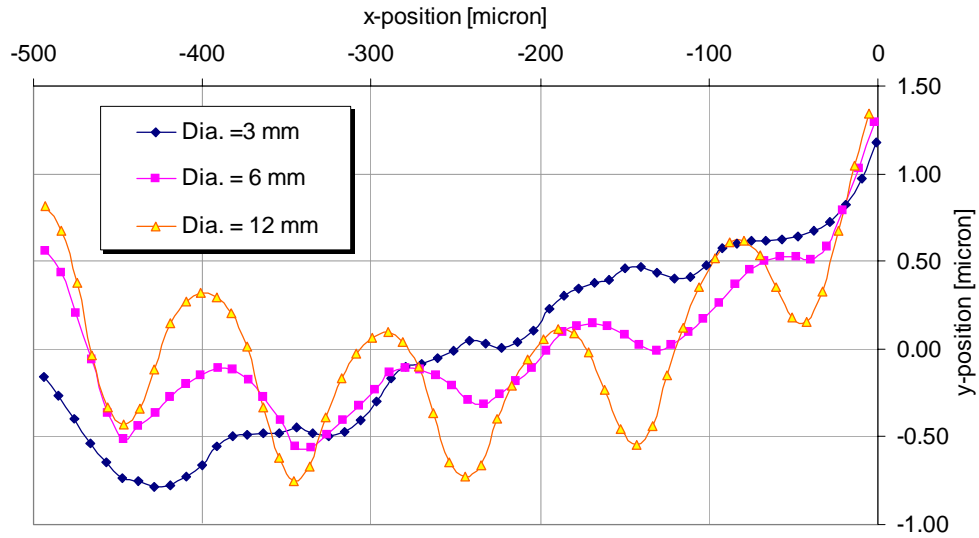


Figure 7.20: The effects of ball diameter on the roughness profiles from FEM simulations

Large elastic deformation was observed at the surface for the case of a larger ball, resulting higher surface roughness (high roughness depth). On the contrary, a contact area is less when using a smaller ball tool. In addition, the smaller ball tool pushes surface material to flow aside the ball rather than presses it down. More local plastic deformation is observed in the simulations. As the feed approaches further, materials formed ahead of the ball in feed direction get accumulated and raise the surface waviness.

The effects of ball diameter on residual stresses are shown in Figure 7.21. As the ball diameter increases, the maximum compressive residual stresses in both tangential and axial directions decreases. However, the layer of compressive residual stresses becomes thicker when using a larger ball tool, i.e. 0.5 mm for 3 mm ball diameter and 0.9 mm for 6 mm ball diameter. This is due to the fact that a larger ball presses the material near the surface down more repeatedly and uniformly, comparing to burnishing with a smaller ball.

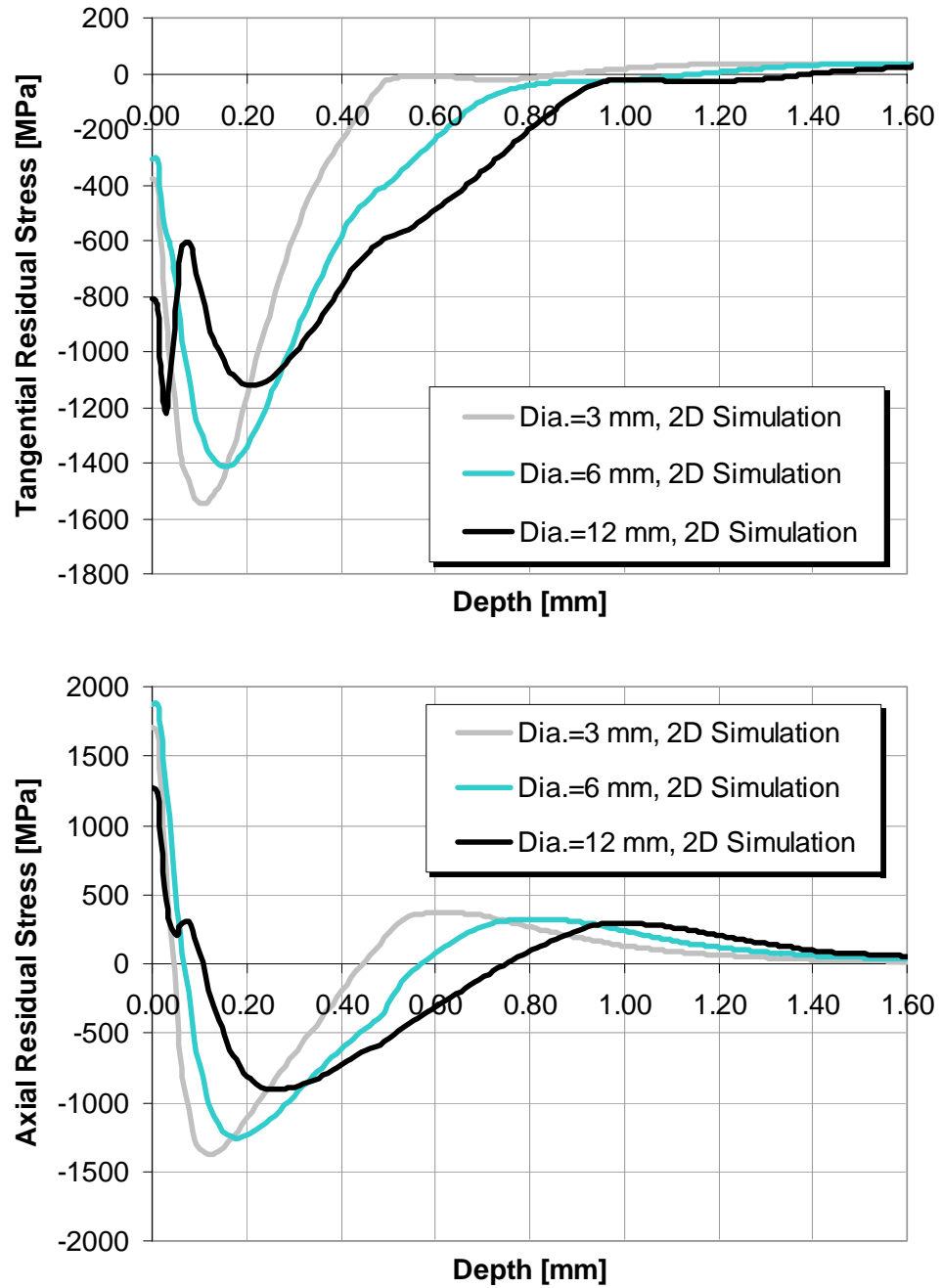


Figure 7.21: The effects of ball diameter of surface residual stress after burnishing in (a) tangential and (b) axial directions.

### 7.3.5. *Effect of Initial Residual Stresses Generated by Hard Turning*

In the actual experiment, hard turning was performed prior to roller burnishing. Residual stresses produced by hard turning may or may not influence the residual stress state after burnishing. This can be studied using 2D FEM model by incorporating the measured residual stresses of the hard turned surface (as shown in Figure 7.13).

A number of MATLAB codes were written to read the tabulated data of residual stress measurements (i.e. residual stress at different depths) and convert them into the stress component data for each mesh element of the workpiece object in the FEM model. This was done by calculating the center coordinate ( $X_{center}$ ,  $Z_{center}$ ) of each quadratic mesh element from the shape function for the bilinear four node square element using Equation 7.5 and Equation 7.6. The stress components of each element were estimated from the given  $Z_{center}$  coordinate and the measured residual stresses from Figure 7.13, using spline-line interpolation.

$$\{x\} = \sum_{a=1}^4 N_a(\xi, \eta) \{x_a\}^e \quad \text{Equation 7.5}$$

$$N_a = \frac{1}{4} (1 + \xi_a \xi) (1 + \eta_a \eta) \quad \text{Equation 7.6}$$

Where :  $x_a$  = Node coordinates in real space

:  $N_a$  = Shape functions for bilinear four node element

:  $\xi_a, \eta_a$  = Node coordinates in the natural space

Initial residual stresses of the workpiece object, in tangential and axial directions, after hard turning and prior to 2D burnishing simulation, are illustrated in Figure 7.22. A 2D roller burnishing simulation with initial stress data was conducted at  $P_b = 32$  MPa and  $f_b = 0.05$  mm/rev. Residual stress results from this simulation were compared with other simulations that were modeled without initial stress as well as the experimental measurements, as shown in Figure 7.23.

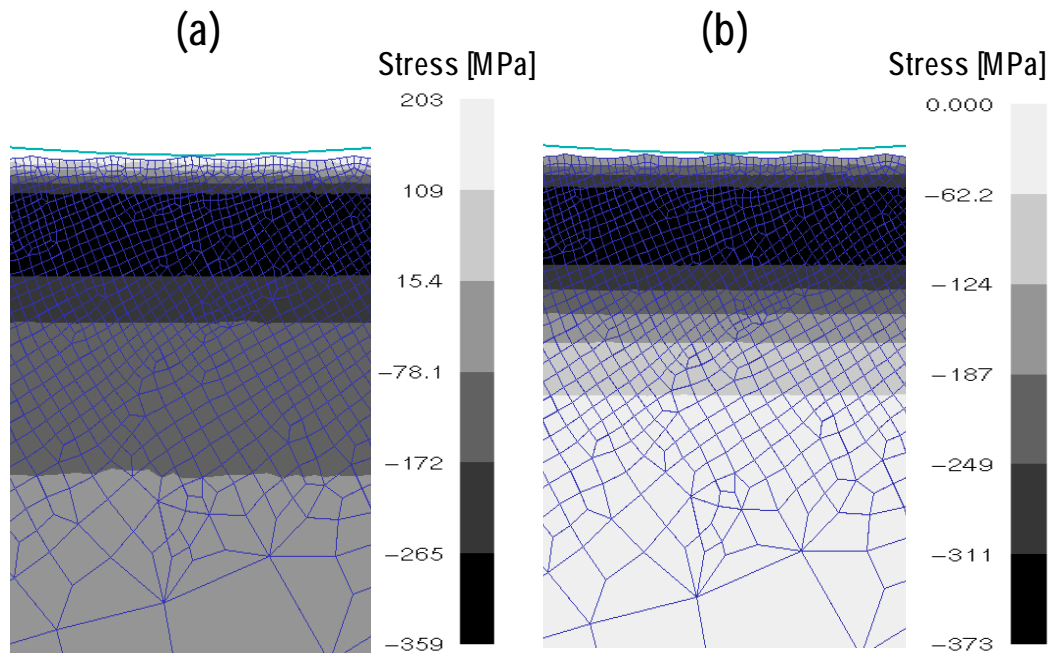


Figure 7.22: Residual stress of hard turned surface, assigned in the workpiece mesh model of 2D roller burnishing simulation: a) tangential residual stress and b) axial residual stress.

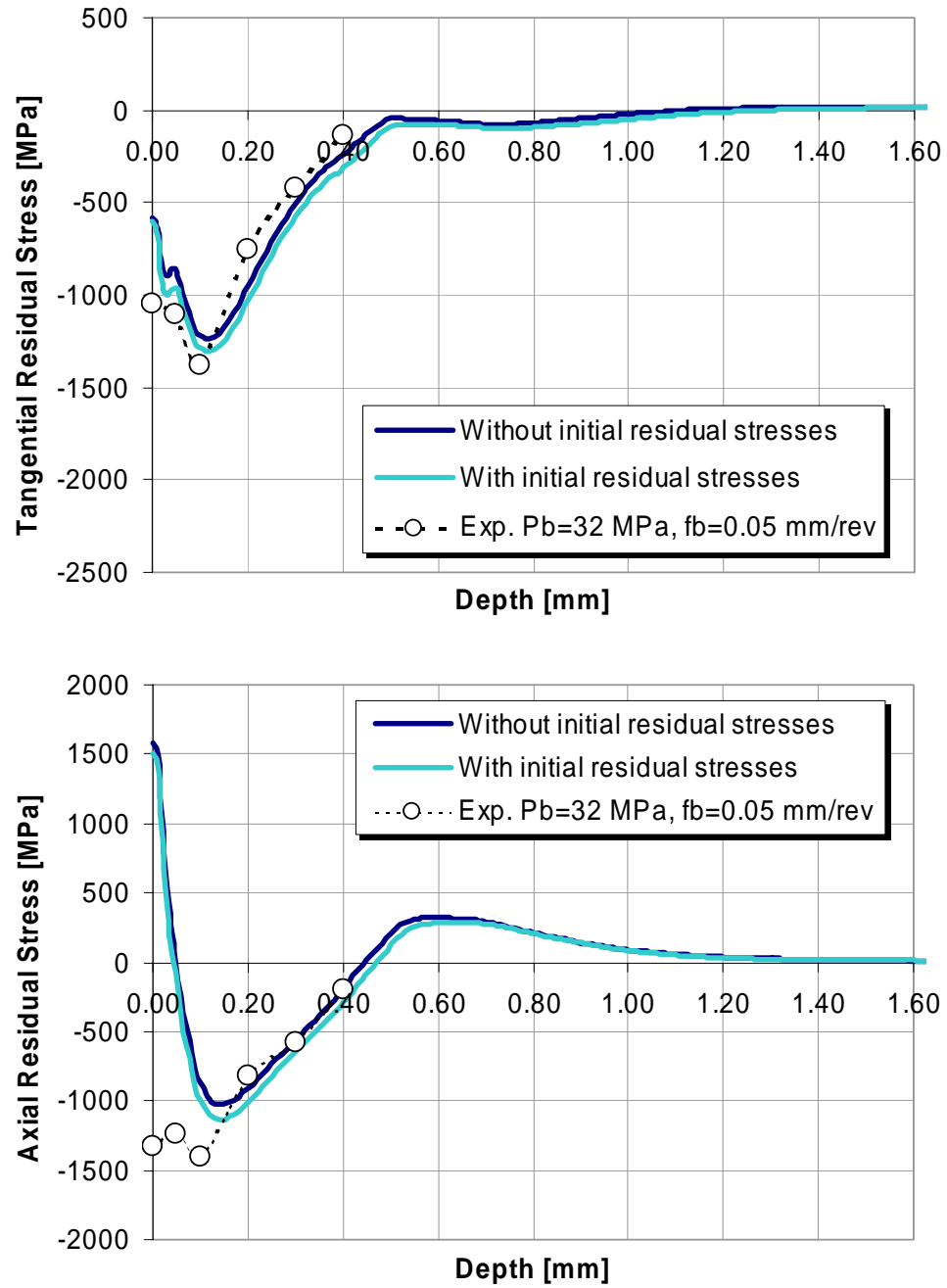


Figure 7.23: Effects of initial residual stresses from hard turning in the predicted residual stresses in 2D roller burnishing simulation, for  $P_b = 32$  MPa,  $f_b = 0.05$  mm/rev

The results show that the initial residual stresses from hard turning have insignificant effect on the residual stresses obtained after roller burnishing for the range of burnishing pressures used in this study. This could be explained by the fact that the minimum burnishing pressure used in this study (32 MPa) had sufficient force to press the surface into a certain depth and could suppress all the residual stresses previously generated by hard turning. According to experimental study in [Röttger, 2002], although high tensile residual stresses were produced by turning with a worn tool, the residual stress after burnishing were still compressive and not different to those obtained from turning with a sharp tool.

#### **7.3.6. Evaluation of 3D Roller Burnishing Simulation**

Mesh elements of the ball tool and the workpiece in the 3D FEM model are shown in Figure 7.8. Ball tool moves in y-direction, while rotating around its x-axis. After movement over the workpiece, the tool was shifted in the distance of burnishing feed in x-direction for the subsequent rolling paths. 3D simulations were conducted for 5 consecutive burnishing passes. The maximum penetration depth of the first rolling path was obtained from Figure 7.9. For the second to fifth rolling paths, maximum penetration depths were found by conducting trial simulations with different depths until the predicted loads were approximately equal to those obtained from the first rolling path and Equation 7.2. Overall computational time for one 3D simulation was approximately two weeks, on a HP workstation ZX-6000 with dual 900MHz Intel Itanium-II processors.

To obtain the residual stresses from 3D simulation, tracking points are assigned in the middle of the workpiece along the depth direction to obtain residual stress data. Figure 7.24 shows a half section of the workpiece after burnishing and a series of tracking points. Residual stresses (i.e. effective,



tangential and axial stresses) over the depth from 3D simulation are plotted and compared with 2D simulation and experiment. However, since residual stress measurements can provide the data only in tangential and axial directions, the experimental effective stresses are calculated using Equation 7.7.

$$\begin{aligned} & (\sigma_x - \sigma_y)^2 + (\sigma_y - \sigma_z)^2 + \dots \\ & + (\sigma_z - \sigma_x)^2 + 6(\tau_{xy} + \tau_{yz} + \tau_{zx})^2 = 2\bar{\sigma}^2 \end{aligned} \quad \text{Equation 7.7}$$

where  $\bar{\sigma}$  = effective stress

$\sigma_x = \sigma_{r,a}$  = axial residual stress

$\sigma_y = \sigma_{r,t}$  = tangential residual stress

: Assuming that  $\sigma_z = \tau_{xy} = \tau_{yz} = \tau_{zx} = 0$

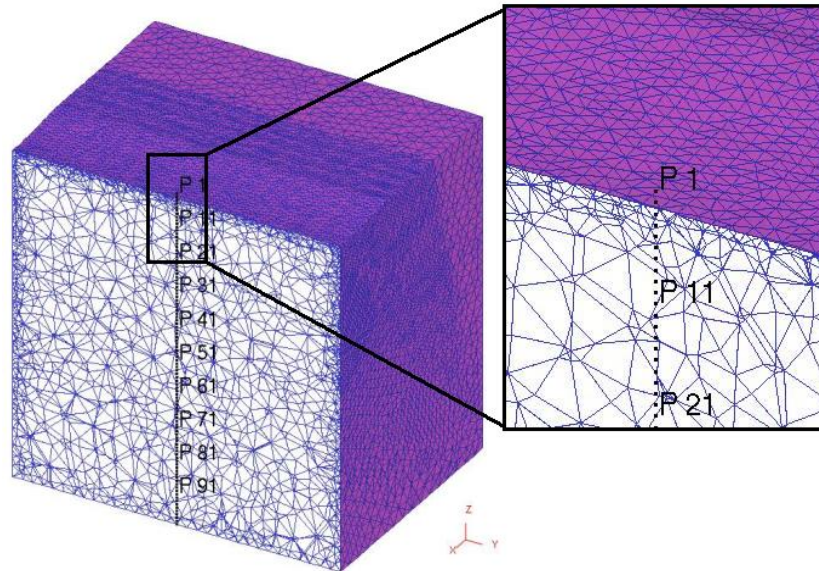


Figure 7.24: Points (point P1 to P100 along the depth) tracked for residual stress data from 3D simulation and comparison of the mesh size between surface and solid body

Comparisons of the residual stresses are shown in Figure 7.25. Overall, the results show that 2D simulations predict the residual stress better than 3D simulations. 3D simulation underestimates the maximum effective residual stress, about 22% less than those of the experiment. It also shows compressive residual stresses at the burnished surface (at the depth = 0 mm) in both tangential and axial directions, unlike 2D simulation that predicts tensile residual stress in axial direction. However, there is a significant difference (more than 100%) in residual stress values in tangential and axial directions between 3D simulation and the experiment.

Figure 7.26 shows the developing residual stress distributions after the 1st, 3rd and 5th rolling paths. After the 1st rolling path, residual stress approaching zero could be observed at about the depth of 1.6 mm. However, after subsequent rolling paths (for the 3rd and 5th rolling paths), the stresses were developed through out the depth of the workpiece object. As the number of rolling paths increased, stresses were more compressive at the greater depth. This indicates that the size of the workpiece model used in this simulation is too small since the applied burnishing force could form the entire workpiece object instead of forming only the material near the surface.

In nature, the residual stresses caused by manufacturing processes are present only in the vicinity of the surface and become zero at a certain distance from the surface. In this study, only 2D simulation could show this residual stress trend. 3D simulation could not predict where the residual stress approached zero. As shown in Figure 7.25, in 3D simulation, the stress existed for entire workpiece, including at the maximum depth of 1.6 mm. This prediction is entirely not correct.

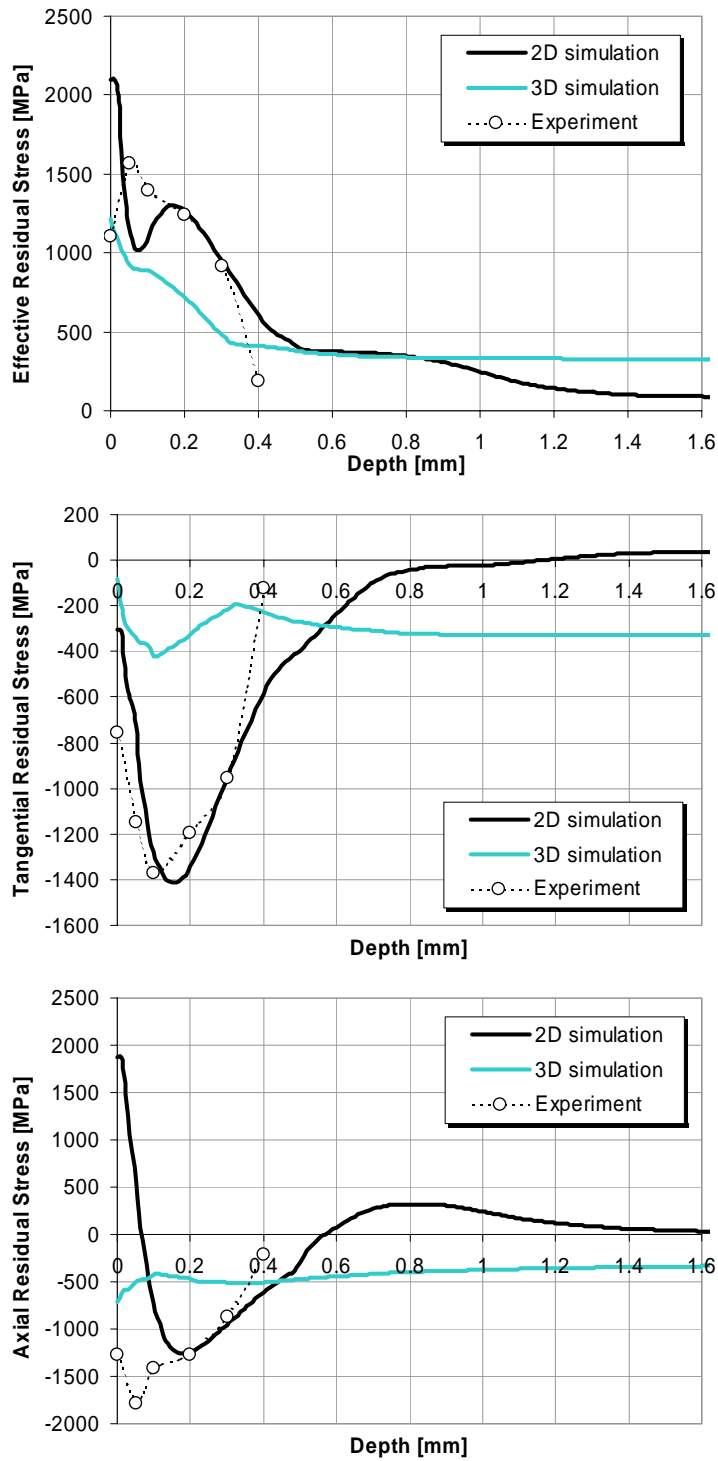


Figure 7.25: Comparison of surface residual stresses from 2D simulation, 3D simulation and the experiment, for  $P_b = 40$  MPa,  $f_b = 0.05$  mm/rev

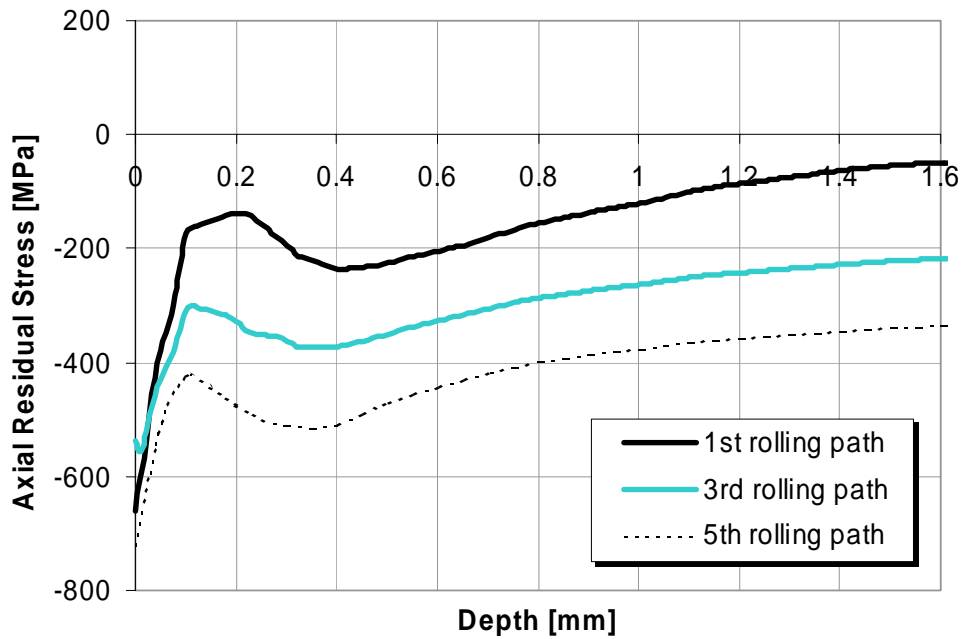
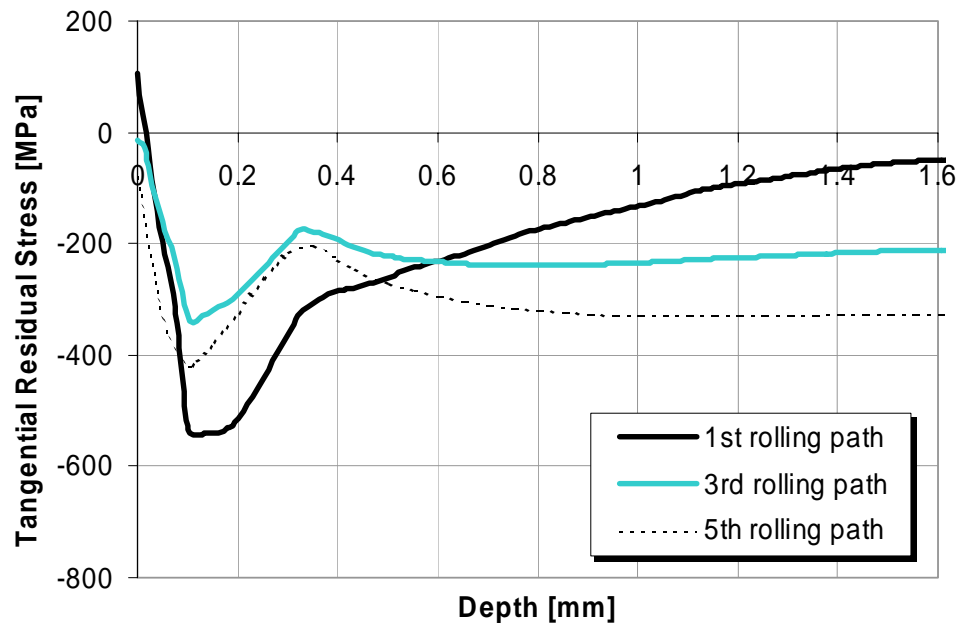


Figure 7.26: Residual stress distributions from 3D roller burnishing simulation, after the 1st, 3rd and 5th rolling paths

It should also be noted that the current FEM software capability could allow the maximum number of 200,000 elements for modeling a workpiece object. To provide reliable results two issues must be resolved: 1) the element size near the surface needs to be sufficiently small to represent surface roughness profile and 2) the workpiece size needs to be sufficiently large to provide reliable residual stress results. Results of this study indicate that further improvements of the 3D model are needed.

Other improvements needed in the 3D model include; 1) different mesh size between surface meshes and solid meshes (see the window of Figure 7.24) and 2) the tetrahedral mesh used here tends to predict very high shear stresses in rolling.

#### **7.4. Summary and Conclusions**

In this part of study, two main tasks were conducted; 1) improvements of FEM roller burnishing model [Yen, 2004] and 2) FEM simulations to analyze the effects of roller burnishing parameters by using the conditions selected for the experiments.

For the modifications of the existing FEM model in [Yen, 2004], the flow stress model from ball indentation tests, the influence of pressure loss during roller burnishing operation, and the actual roughness of the hard turned surface were considered. A workpiece size of 7 x 6 mm was used in the 2D FEM model since the predicted surface roughness and residual stresses were not affected by the displacement boundary constraints. 3D roller burnishing model was conducted to calculate the maximum ball penetration depth for use in 2D FEM model. This allowed having more reliable surface predictions and more realistic tool/workpiece contact.

The effects of roller burnishing parameters can be summarized as follows:

- As burnishing feed rate ( $f_b$ ) increases, surface roughness increases. If a very high feed value is used, the tool has less chance to flatten the roughness peaks.
- FEM simulations can predict only mean roughness ( $R_a$ ) but not roughness depth ( $R_z$ ). Overall, they can provide only a qualitative trend of surface roughness for different process conditions
- Burnishing pressure has the most important effect on surface roughness. Both FEM and experiments show that higher burnishing pressure (40 MPa) produces better surface finish.
- The surface roughness is higher when using a larger ball tool. However, the surface waviness tends to increase when using a smaller ball diameter.
- Predictions of residual stress distributions beneath the burnished surface, with the 2D FEM model are in good agreement with the experimental measurements obtained using X-Ray diffractions.
- Residual stresses are influenced slightly by the burnishing feed rate. Both FEM simulation and experiment show that increasing burnishing feed rate causes a slight decrease in residual stresses.
- Burnishing pressure has a major influence on residual stresses. The amount of plastic deformation in the workpiece increases with pressure and hence the magnitude of compressive residual stresses increase with increasing burnishing pressure.
- As the ball diameter increases, the maximum compressive residual stresses in both tangential and axial directions decrease. However, the

layer of compressive residual stresses becomes thicker when using a larger ball tool

- Initial residual stress produced by hard turning has insignificant effect upon the residual stress predicted in roller burnishing simulation.
- The 3D FEM model needs further improvements for better prediction of surface finish and residual stresses.

## CHAPTER 8

### OVERALL CONCLUSIONS AND FUTURE WORK

This research work was intended to develop the procedure to determine the flow stress properties of the workpiece materials for the finishing processes considered, i.e. machining and roller burnishing, and to be able to employ the developed procedure for FEM modeling of practical applications. Overall conclusions and suggested future work of this study are provided in the following paragraphs.

#### 8.1. Overall Conclusions

For modeling machining with FEM, the flow stress properties at high ranges of plastic strains, strain rates and temperatures need to be considered. In this research work, four main tasks contributing to the flow stress properties for machining were conducted. These include: a) the development of the procedures to determine flow stress through slot milling experiments, b) a sensitivity analysis on the effect of flow stress parameters in FEM simulation of orthogonal cutting, c) the establishment of MAterial DAtabase for Machining Simulations (MADAMS) and d) the utilization of the obtained flow stress to study burr formation problem in face milling. Accomplishments of this study can be summarized as follows:



- The computer program OXCUT that is based on Oxley's machining theory was developed and applied to determine the flow stress data for selected materials; namely AISI 1045, P20 and H13. For each workpiece material, forces and plastic zone thickness ratios were obtained from slot milling experiments and used as input data for OXCUT calculation.
- The flow stress data of AISI 1045 steel obtained from OXCUT are in a good agreement with the data obtained from high speed compression tests. The developed methodology has been applied to determine the flow stress properties for several materials, for both ferrous and non-ferrous types.
- A sensitivity analysis on the effect of flow stress parameters in FEM simulation of orthogonal cutting showed that flow stress parameters influenced mainly the chip thickness, the cutting force and the thrust force. More details on the results of this sensitivity study are presented in Section 4.2.3.
- MADAMS or (MAterial DAtabase for Machining Simulation) program is established to collect the material flow stress properties for FEM machining simulation in an on-line database. General information and the current status of MADAMS can be found at its web site, at <http://nsm.eng.ohio-state.edu/madams/index.html>
- The developed inverse analysis procedure and slot milling test were used for determining the flow stress of AA 356-T6 aluminum alloy. A series of 2D and 3D FEM simulations were conducted using the obtained flow stress data in order to study the effects of the tool edge geometries and the flank wear upon burr formation in face milling.

According to simulation results, recommendations for tool edge design were given as follows: a) larger positive rake angle (within limits) is desirable for burr reduction if the tool life is determined by flank wear rather than tool fracture, b) a variable edge honed tool indicates potential increase in tool life and may slow down burr generation rate and c) reduction of the wiper length of the tool insert can contribute to burr reduction.

For modeling roller burnishing with FEM, the flow stress properties at the surface layer that could undergo severe plastic deformation from previous machining operations need to be determined. In this research work, four main tasks, contributing to the flow stress properties for roller burnishing, were conducted. These include: a) evaluation of conical and spherical indentation, b) an FEM-based inverse analysis to determine the flow stress of the surface layer, c) improvements of the FEM roller burnishing model by Yen [Yen, 2004] and d) an analysis on the effect of burnishing process parameter on surface finish and residual stresses using FEM. Accomplishments of this study can be summarized as follows:

- A sensitivity analysis using a series of FEM simulation showed that conical indentation exhibited non-uniqueness when determining the flow stress data from the measured load-depth curve. However, spherical indentation was shown to provide unique flow stress data. Thus, it was decided to use spherical indentation to determine the flow stress of the surface layer.
- With the experimental load-depth curves from indentation test and the established inverse analysis procedures, the flow stress equation of the hard-turned surfaces of an AISI 52100 sample could be determined, as shown in Equation 6.7.

- For the modifications of the existing FEM model in [Yen, 2004], the flow stress model from ball indentation tests, the influence of pressure loss during roller burnishing operation, and the actual roughness of the hard turned surface were considered. Predictions of residual stress distributions beneath the burnished surface, with the 2D FEM model are in good agreement with the experimental measurements obtained using X-Ray diffractions.
- The effects of roller burnishing parameters using FEM can be summarized as follows: a) as burnishing feed rate increases, surface roughness increase and residual stresses slightly increase; b) burnishing pressure has the most important effect, where higher burnishing pressure produces better surface finish and more compressive residual stresses; c) a larger ball tool produces higher surface roughness and thicker layer of compressive residual stresses, but lower value of the maximum compressive residual stress.

The following research contributions result from this dissertation work:

- An efficient and cost-effective method is developed to determine the flow stress properties for FEM simulation of machining and roller burnishing.
- A material database (MADAMS) that can be useful for those who implement FEM for machining is established and has been maintained.
- Part of this research demonstrates to industry (a) how the FEM process modeling can be utilized efficiently to analyze burr formation in machining process and (b) what are the effects of burnishing parameters upon surface finish and residual stresses.

- Fundamental understanding of the effect of process parameters in roller burnishing upon the surface finish and state of residual stresses is provided.

## 8.2. Future Work

Parts of the findings of this study suggest that the following research topic may need to be considered in the future:

- Incorporating the flow stress at different testing ranges and different testing methods. For example, the flow stress data for a wide testing range can be obtained from conventional compression tests for low strain rates, SHPB tests for “mid” strain rates and machining test for high strain rates. Flow stress data that are applicable for a wide testing range may provide more reliable results in FEM simulation of machining.
- Implementing inverse analysis with FEM cutting simulation. This may reduce the errors that are caused by a number of assumptions used in the analytical approach.
- In this study, the predicted thrust forces at the reference cutting condition are always lower than experimental force by approximately 30% to 45%. Disagreement of the thrust forces may be due to the difference between the FEM model and actual turning operation. Force measurement in orthogonal turning considers not only the thrust force from chip formation but also the force that presses the tool upon the workpiece in feed direction. Most 2D FEM cutting

models, however, simulate a “shaving operation” and disregard this force. This issue needs to be addressed in future research.

- FEM Modeling of burr formation may consider burr fracture when machining brittle materials.
- Further research on FEM inverse analysis with indentation tests may cover the following issues: a) determination of Young’s modulus from unloading curve of indentation and b) indentation to determine surface property at elevated temperature and c) indentation to determine surface property at high speed or impact loading
- FEM roller burnishing simulations can predict only the mean roughness ( $R_a$ ) but not roughness depth ( $R_z$ ). Overall, FEM can provide only a qualitative trend of surface roughness for different process conditions. A statistical approach may be used for modeling surface roughness as function of process parameters.
- The 3D FEM model of roller burnishing needs further improvements for better prediction of surface finish and residual stresses.

## REFERENCES

- [Arrazola, 2003] Arrazola, P. J., Meslin, F. and Marya, S., "Numerical Cutting Modeling Sensitivity Analysis", *CIRP Workshop on FE simulation STC "C" (Cutting) and "F" (Forming)*, Paris, France, January 28, 2003.
- [ASM, 1990] *ASM Handbook Volume 1: Properties and Selection: Irons, Steels, and High-Performance Alloys*, ASM International, 1990.
- [ASM, 1991] *ASM Handbook Volume 2: Properties and Selection: Nonferrous Alloys and Special-Purpose Materials*, ASM International, 1991
- [Astakhov, 1997] Astakhov, V.P., Shvets, S.V., Osman, M.O.M., 1997, "Chip Structure Classification based on Mechanics of its Formation", *Journal of Materials Processing Technology*, Vol. 71, pp. 247 - 257
- [ATP, 2002] Advanced Technology Program (ATP-NIST), "Enabling Technologies for lean manufacturing of critical hardened steel applications," *ATP quarterly R&D performance report*, January 2002
- [Becze, 2001] Becze, C. E., Worswick, M. J., Elbestawi, M. A., 2001, "High Strain Rate Shear Evaluation and Characterization of AISI D2 Tool Steel in Its Hardened State", *Machining Science and Technology*, Vol. 5, No. 1, pp. 131-149.
- [Bil, 2004] Bil, H., Kilic, S. E. and Tekkaya, A. E., 2004, "A Comparison of Orthogonal Cutting Data from Experiments with Three Different Finite Element Models", *International Journal of Machine Tools & Manufacture*, Vol. 44, pp. 933-944.
- [Bouزيد, 2004] Bouزيد, W., Tsoumarev, O., Sai, K., 2004, "An Investigation of Surface Roughness of Burnished AISI 1042 Steel", *International Journal of Advanced Manufacturing Technology*, Vol. 24 , pp. 120-125.
- [Ceretti, 1996] Ceretti, J. E., Fallbehmer, P., Wu, W. T. and Altan, T., 1996, "Application of 2D FEM on Chip Formation in Orthogonal Cutting", *Journal of Material Processing and Technology*, Vol. 59, pp. 169-181.

- [Chandrasekeran, 1965] Chandrasekeran, H. and Kapoor, D.V., 1965, "Photoelastic Analysis of Tool-Chip Interface Stress", *Journal of Engineering for Industry*, Transactions of the ASME, Vol. 87B, pp. 495-502
- [Chen, 1997] Chen, S.R. and Gray III, G.T., 1997, "Influence of Twinning on the Constitutive Responses of Zr: Experiment and Modeling", *Journal De Physique*, Colloque, Vol. 3, No. 8, pp. 741-746.
- [Childs, 1989] Childs, T.H.C. and Mahdi, M.I., 1989, "On the Stress Distribution Between the Chip and Tool During Metal Turning", *Annals of CIRP*, Vol. 38, pp. 55-58.
- [Childs, 1990] Childs, T.H.C. and Maekawa, K., 1990, "Computer Aided Simulation and Experimental Studies of Chip Flow and Tool Wear in Turning Low Alloy Steels by Cemented Carbide Tools", *Wear*, Vol. 139, pp. 235-250.
- [Childs, 1997] Childs, T.H.C., Dirikolu, M.H., Sammons, M.D., Maekawa, K. Kitagawa, T., 1997, "Experiment on and Finite Element Modeling of Turning Free-Cutting Steels at a Cutting Speeds up to 250 m/min", *The 1st French and German Conference on High Speed Machining*, June 1997, pp. 325-331.
- [Childs, 2000] Childs, T. H., Maekawa, K. and Obikawa, T., *Metal Machining: Theory and Application*, Arnold Press, London, 2000
- [Childs, 2003] Childs, T.H.C., 2003, "Numerical Experiments on the Influence of Material Properties on Orthogonal Chip Formation", *Proceedings of 6th CIRP International Workshop on Modeling of Machining Operations*, Ontario, Canada, May 20, 2003.
- [Chollacoop, 2003] Chollacoop, N., Dao, M., and Suresh, S., 2003, "Depth-sensing Instrumented Indentation with Dual Sharp Indenters", *Acta Materialia*, no. 51, pp. 3713-3729.
- [Conicity, 1999] Conicity Technologies Company, with the web site at [www.conicity.com](http://www.conicity.com)
- [Dahlman, 2004;] Dahlman, P., Gunnberg, F. and Jacobson, M., 2004, "The Influence of Rake Angle, Cutting Feed and Cutting Depth on Residual Stresses, in Hard Turning", *Journal of Materials Processing Technology*, Vol. 147, pp. 181-184.
- [Dao, 2001] Dao, M., Chollacoop, N., Van Vliet, K., Venkatesh, T., and Suresh, S., 2001, "Computational Modeling of the Forward and Reverse Problems in Instrumented Sharp Indentation", *Acta Materialia*, no. 49, pp. 3899-3918.

- [Dautzenberg, 1981] Dautzenberg, J. H., Veenstra, P. C. and Van der Wolf, A.C.H, 1981, "The Minimum Energy Principle for the Cutting Process in Theory and Experiment", *Annals of the CIRP*, Vol. 30, pp. 1-4.
- [Deform.com] Internet web site of the commercial FEM package, at [www.deform.com](http://www.deform.com)
- [Dornfeld, 1999] Dornfeld, D.A., Min, S., Kim, J., Hewson, J., Chu, C.H., Tyler, P., Ffield, P., and Askari, A., 1999, "Burr Prevention and Minimization for the Aerospace Industry", *SAE Aerospace Manufacturing Technology Conference*, pp. 1-6.
- [Dornfeld, 2002] Dornfeld, D., 2002, "Analysis of Burr Formation", presented at the *First International Workshop on High Performance Cutting*, Dublin, Ireland
- [Ecoroll, 2001] ECOROLL AG Werkzeugtechnik, 2001, Application Description: Hard Roller Burnishing Status of Research and Application, *ECOROLL AG Werkzeugtechnik Research Report*, B13, No. 5593E, pp.1-11.
- [El-Axir, 2000] El-Axir, M.H., 2000, "An Investigation into Roller Burnishing", *International Journal of Machine Tools & Manufacture*, Vol. 40, pp. 1603-1617.
- [El-Axir, 2003] El-Axir, M.H. and El-Khabeery, M.M., 2003, "Influence of Orthogonal Burnishing Parameters on Surface Characteristics for Various Materials", *Journal of Materials Processing Technology*, Vol. 132, pp. 82-89.
- [Eleiche, 1983] Eleiche, A. M. and El-Kady, M. M, 1983, "Modified Torsional Split Hopkinson Bar for the Cyclic Loading of Materials at Dynamic Strain Rates", in *Novel Techniques in Metal Deformation Testing*, Metallurgical Society of AIME, Warrendale, PA
- [El-Khabeery, 2001] El-Khabeery, M.M. and El-Axir, M.H., 2001, "Experimental Techniques for Studying the Effects of Milling Ball-burnishing Parameters on Surface Integrity", *International Journal of Machine Tools & Manufacture*, Vol. 41, pp. 1705-1719.
- [El-Magd, 1999] El-Magd, E. and Treppmann, C., 1999, "Simulation of Chip Root Formation at High Cutting Rates by Means of Split-Hopkinson Bar Test", *Materialpruefung (German Journal: Materials Testing)*, Vol. 41, No. 11, pp. 457-460.



- [Emmer, 1992] Emmer, T. and Popke, H., 1992, "Hartglattwalzen - eine Verfahrensalternative zum Rundschleifen", *Wissenschaft-liche Zeitschrift der technischen Universität Magdeburg*, Vol. 36, Heft 2/3
- [Ernst, 1941] Ernst, H. and Merchant, M.E., 1941, "Chip Formation, Friction and High Quality Machined Surfaces", *Surface Treatment of Metals*, American Society of Metals, New York, Vol. 29, pp.299.
- [GESA, 2003] General Electric Super Abrasives (currently is Diamond Innovation), 2003, *Private communication*
- [Gilat, 1994] Gilat, A. and Wu, X., 1994, "Elevated temperature testing with the torsional split Hopkinson bar", *Experimental Mechanics*, Vol. 34, No. 2, pp. 166-170.
- [Gilat, 1994a] Gilat, A., Wu, X., Zhang, X. T. and Batra, R. C., 1994, "Dynamic hot forging of a steel connecting rod", *Journal De Physique*, Vol. 4, No. 8, pp. 533-537.
- [Gray, 1997] Gray, G.T. III, 1997, "Influence of strain rate and temperature on the structure on the structure. Property behavior of high-purity Titanium", *Journal De Physique IV*, Vol. 7, pp. 423-428.
- [Guo, 2002] Guo, Y. B. and Liu, C. R., 2002, "Mechanical properties of hardened AISI 52100 steel in hard machining processes" *Journal of Manufacturing Science and Engineering*, Vol. 124, No. 1, pp. 1-9
- [Haggag, 1993] Haggag, F., 1993, "In-situ measurements of mechanical properties using novel automated ball indentation system", Small specimen test techniques applied to nuclear reactor vessel thermal annealing and plant life extension, *ASTM STP*, Vol. 1204, pp. 27-44, 1993.
- [Hamann, 2002] Hamann, J.C., Meslin, F. and Sartkulvanich, J., 2002, "Criteria for the quality assessment of constitutive equations dedicated to cutting models", *Machining Science and Technology*, Vol. 6, No. 3, pp. 331-351.
- [Hashimura, 1999] Hashimura, M., Hassamontr, J. and Dornfeld, D., 1999, "Effects of In-plane Exit Angle and Rake Angle on Burr Height and Thickness in Face Milling Operation", *Journal of Manufacturing Science and Engineering*, Vol. 121, pp. 13-19.
- [Hassan, 1996] Hassan, A.M. and Al-Bsharat, A.S., 1996, "Influence of burnishing process on surface roughness, hardness, and microstructure of some non-ferrous metals", *Wear*, Vol. 199, pp.1-8.

- [Hassan, 1998] Hassan, A.M., Al-Jalil, H.F. and Ebied, A.A., 1998, "Burnishing force and number of ball passes for the optimum surface finish of brass components", *Journal of Materials Technology*, Vol. 83, pp. 176-179.
- [Hassan, 1999] Hassan, A.M. and Al Dhifi, S.Z.S., 1998, "Improvement in the wear resistance of brass components by the ball burnishing process", *Journal of Materials Processing Technology*, Vol. 96, pp. 73
- [Hassan, 2000] Hassan, A.M. and Maqableh, A. M., 2000, "The effects of initial burnishing parameters on non-ferrous components", *Journal of Materials Processing Technology*, Vol. 102, pp. 115-121.
- [Herbert, 2001] Herbert, E., Pharr, G., Oliver, W., Lucas, B. and Hay, J., 2001, "On the measurement of stress-strain curves by spherical indentation", *Thin Solid Films*, no. 398-399. pp. 331-335, 2001.
- [hks.com] Internet web site of the commercial FEM package, at "[www.hks.com](http://www.hks.com)"
- [Hopkinson, 1905] Hopkinson, B., 1905, "The effects of momentary stresses in metals", *Proceedings of Royal Society of London*, Vol. A.74, pp. 498-506.
- [Huang, 2002] Huang, Y., 2002, "Predictive Modeling of Tool Wear Rate with Applications to CBN Hard Turning", *PhD Dissertation*, Georgia Institute of Technology, Georgia.
- [Ivester, 2000] Ivester, R.W., Kennedy, M., Davies, M., Stevenson, R., Thiele, J., Furness, R., and Athavale, S., 2000, "Assessment of Machining Models: Progress Report", *Machining Science and Technology*, Vol. 4, no. 3, pp. 511-538.
- [Iwata, 1984] Iwata, K., Osakada, A. and Terasaka, Y., 1984, "Process Modeling of Orthogonal Cutting by Rigid-Plastic Finite Element Method", *Journal of Engineering Materials and Technology*, Vol. 106, pp. 132-138.
- [Jain, 2001] Jain, A., Yen, Y.-C., and Altan, T., 2001, "Investigation of the effect of tool edge preparation in orthogonal cutting using FEM simulation", *ERC/NSM Report No. HPM/ERC/NSM-01-R-12*, The Ohio State University
- [Jawahir, 1993] Jawahir, I.S. and Van Luttervelt, C.A., 1993, "Recent Developments in Chip Control Research and Applications", *Annals of CIRP*, Vol. 42, No. 2., pp. 659-693.

- [Johnson, 1983] Johnson, G.R. and Cook, W.H., 1983, "A constitutive model and data for metals subjected to large strains, high strain rates and high temperature", *Proceedings of the 7th International Symposium on Ballistics*, The Hague, Netherlands, April 1983, pp. 541-547.
- [Johnson, 1985] Johnson, G. R. and Cook, W. H., 1985, "Fracture Characteristics of Three Metals Subjected to Various Strains, Strain Rates, Temperatures and Pressures", *Engineering Fracture Mechanics*, Vol. 21, No. 1, pp. 31-48.
- [Joyot, 1998] Joyot, P., Rakotomalala, R., Pantale, O., Touratier, M. and Hakem, N., 1998, "Numerical Simulation of Steady State Metal Cutting", *Proceedings of the Institution of Mechanical Engineers, Part C: Journal of Mechanical Engineering Science*, Vol. 212, No. 5, pp. 331-341.
- [Kalhori, 2000] Kalhori, V., Lundblad, M., 2000, "Finite element Modeling of Orthogonal Metal Cutting", included in *Doctoral Thesis of Kalhori on Modeling and Simulation of Mechanical Cutting*, Lulea University of Technology, Sweden.
- [Kececioglu, 1960] Kececioglu, D., 1960, "Shear Zone Size, Compressive Stress, and Shear Strain in Metal Cutting and their Effects on Mean Shear Flow Stress", *Journal of Engineering for Industry*, Transactions of the ASME, Vol. 82, pp. 79 - 86.
- [Klocke, 1998] Klocke, F. and Liermann, J., 1998, "Roller Burnishing of Hard Turned Surfaces", *International Journal of Machine Tools and Manufacture*, Vol. 38, No. 5-6, pp. 419-423.
- [Ko, 1996] Ko, S. L. and Dornfeld, D. A., 1996, "Analysis of fracture in burr formation at the exit stage of metal cutting", *Journal of Material Processing Technology*, Vol. 58, pp. 189-200.
- [Ko, 1996a] Ko, S. L. and Dornfeld, D. A., 1996, "Burr formation and fracture in oblique cutting", *Journal of Material Processing Technology*, Vol. 62, pp. 24-36.
- [Kolsky, 1949] Kolsky, H., 1949, "An investigation of the mechanical properties of materials at very high rates of loading", *Proceedings of the Physical Society, Section B*, Vol. 62, pp. 676-700.
- [Komanduri, 1981] Klopp, R. W., Clifton, R. J. and Shawki, T. G., 1981, "Pressure-Shear Impact and The Dynamic Viscoplastic Response of Metals", *Mechanics of Materials*, Vol. 4, No. 3-4, pp. 375-385.
- [König, 1996] König, W. and Klocke, F., 1997, *Frtigungsverfahren: Drehen*, Springer Verlag Berlin Heidelberg.

- [Kopac, 2001] Kopac, J., Korosec, M. and Kuzman, K., 2001, "Determination of flow stress properties of machinable materials with help of simple compression and orthogonal machining test", *International Journal of Machine Tools and Manufacture*, Vol. 41, No. 9, pp. 1275-1282.
- [Kristyanto, 2002] Kristyanto, B., Mathew, P., Arsecularatne, J. A., 2002, "Development of a variable flow stress machining theory for aluminium alloys", *Machining Science and Technology*, Vol. 6, No. 3, pp. 365-378.
- [Kumar, 1997] Kumar, S., Fallböhmer, P. and Altan, T., 1997, "Computer Simulation of Orthogonal Metal Cutting Process: Determination of Material Properties and Effects of Tool Geometry on Chip Flow", *Proceedings of NAMRC 1997*, Lincoln, NE, May 20-23, 1997, SME Paper MR97-1.
- [Lee, 1951] Lee, E.H. and Shaffer, B. W., 1951, "The theory of plasticity applied to a problem of machining", *Journal of Applied Mechanics*, Transactions of the ASME, Vol. 18, pp. 405-413
- [Lee, 1998] Lee, W.S. and Lin, C.F., 1998, "Plastic deformation and fracture behaviour of Ti-6Al-4V alloy loaded with high strain rate under various temperatures", *Materials Science and Engineering*, Vol. A241, pp. 48-59.
- [Lee, 1998a;] Lee, W.S., Xiea, G.L. and Lin, C.F., 1998, "The strain rate and temperature dependence of the dynamic impact response of tungsten composite", *Materials Science and Engineering*, Vol. A257, pp. 256-267.
- [Lee, 2000] Lee, W.S., Sue, W.C., Lin, C.F. and Wu C. J., 2000, "The strain rate and temperature dependence of the dynamic impact properties of 7075 aluminum alloy", *Journal of Material Processing Technology*, Vol. 100, pp. 116-122.
- [Lei, 1999] Lei, S., Shin, Y.C. and Incropera, F.P., 1999, "Material constitutive modeling under high strain rates and temperatures through orthogonal machining tests", *Journal of Manufacturing Science and Engineering*, Vol. 121, pp. 577-585.
- [Liu, 2000] Liu, R. and Guo, Y., 2000, "Finite Element Analysis of the effect of Sequential Cuts and Tool-Chip Friction on Residual Stresses in a Machined Layer", *International Journal of Mechanical Science*, Vol. 42, pp. 1069-1086.
- [Luca, 2002] Luca, L., 2002, "Investigation into the Use of Ball Burnishing of Hardened Steel Components as a Finishing Process", *PhD Dissertation*, University of Toledo, Toledo, Ohio

- [Luca, 2005] Luca, L., Neagu-Ventzel, S., Marinescu, I., 2005, "Effects of working parameters on surface finish in ball-burnishing of hardened steels", *Precision Engineering*, Vol. 29, pp. 253-256.
- [Madams, 2005] An internet web site, "[http://nsm.eng.ohio-state.edu/madams/madams\\_home.html](http://nsm.eng.ohio-state.edu/madams/madams_home.html)"
- [Maekawa, 1983] Maekawa, K., Shirakashi, T., and Usui, E., 1983, "Flow Stress of Low Carbon Steel at High Temperature and Strain Rate (Part 2)", *B113*, Vol. 17, No. 3, pp.167-172
- [Maekawa, 1991] Maekawa, K., Kitagawa, T. and Childs, T.H.C., 1991, "The effects of flow stress and friction characteristics on the machinability of free cutting steel", *Proceeding of the 2nd International Conference on Behaviour of Materials in Machining - Inst. Metals London Book 1991*, 543, 132-145.
- [Maekawa, 1993] Maekawa, K., Kitagawa, T., Shirakashi, T., Childs, T.H.C., 1993, "Finite Element Simulations of Three-Dimensional Continuous Chip Formation Processes", *Proceeding of the 8th ASPE Annual Meeting*, pp. 519-522.
- [Maekawa, 1996] Maekawa, K., Ohhata, H., Kitagawa, T. and Childs, T.H.C., 1996, "Simulation analysis of machinability of leaded Cr-Mo and Mn-B structural steels", *Journal of Materials Processing Technology*, Vol. 62, pp. 363-369.
- [Marusich, 1995] Marusich, T. D. and Ortiz, M., 1995, "Modelling and Simulation of High-Speed Machining", *International Journal for Numerical Methods in Engineering*, Vol. 38, No. 21, pp. 3675-3694
- [Mathew, 1993;] Mathew, P. and Arya, N.S., 1993, "Material properties from machining", *the 1st Conference on Dynamic Loading in Manufacturing and Service*, Melbourne, Austraria, February 09-11, 1993, pp. 33-39.
- [Matweb, 1996] Material database web site "[www.matweb.com](http://www.matweb.com)"
- [Meyer, 1984] Meyer, L. W., 1984, "Strength and Ductility of a Titanium-Alloy TiAl6V4 in Tensile and Compressive Loading under Low, Medium and High Rates of Strain", *Proceedings of the 5th International Conference On Titanium*, Munich, Germany, September 10-14, 1984, pp. 1851-1850
- [Meyer, 2000] Meyer, W. and Abdel-Malek, S., 2000, "Strain rate dependence of strength-differential effect in two steels", *Journal De Physique IV*, Proceedings 2000, Vol. 10, pp. 63-68.

- [Morris, 2005] Morris, E., Cho, H., Sartkulvanich, P., and Altan, T., 2005, "Determining the Flow Stress at the Surface of Materials using Indentation Testing with Conical or Spherical Indenters", *ERC Thesis Report No. HPM/ERC/NSM-05-R-25*, The Ohio State University, Columbus, Ohio.
- [Movahhedy, 2000] Movahhedy, M.R., Gadala, M.S. and Altintas, Y., 2000, "Simulation of Chip Formation in Orthogonal Metal Cutting Process: An ALE Finite Element Approach", *Machining Science and Technology*, Vol. 4, No. 1, pp.15-42.
- [Müller, 2004] Müller, B., Renz, U., Hoppe, S. and Klocke, F., 2004, "Radiation Thermometry at a High-Speed Turning Process", *Journal of Manufacturing Science and Engineering*, Transactions of the ASME, Vol. 126, p. 488-495
- [Nakayama, 1987] Nakayama, K. and Arai, M., 1987, "Burr Formation in Metal Cutting", *Annals of the CIRP*, Vol. 36, pp. 33-36.
- [Némat, 2000] Némat, M., Lyons, A.C., 2000, "An investigation of the surface topography of ball burnished mild steel and aluminum", *The International Journal of Advanced Manufacturing Technology*, Vol. 16, pp. 469-473.
- [Nemat-Nasser, 1997] Nemat-Nasser, S. and Isaacs, J.B., 1997, "Direct measurement of isothermal flow stress of metals at elevated temperatures and high strain rates with application to Ta and Ta-W alloys", *Acta Materialia*, Vol. 45, No. 3, pp. 907-919.
- [Ng, 2002] Ng, E.-G. and Aspinwall, D., 2002 "Modeling of Hard Part Machining", *Journal of Materials Processing Technology*, Vol. 127, pp. 222-229.
- [Obikawa, 1995] Obikawa, T., Shinozuka, J. and Shirakashi, T., 1995, "Analytical prediction of cutting performances of grooved rake face tools", *Journal of the Japan Society for Precision Engineering*, Vol. 61, No. 9, pp. 1295-1299.
- [Okushima, 1961] Okushima, K. and Hitomi, K., 1961, "An analysis of mechanism of orthogonal cutting and its application to discontinuous chip formation", *Journal of Engineering for Industry*, Transactions of the ASME, Vol. 83, pp. 545-556
- [Olvera, 1996] Olvera, O. and Barrow, G., 1996, "An Experimental Study of Burr Formation in Square Shoulder Face Milling", *International Journal of Machine Tools and Manufacture*, Vol. 36, No. 9, pp. 1005-1020.
- [Oxley, 1989] Oxley, P.L.B., *Mechanics of Machining: An Analytical Approach to Assessing Machinability*, Halsted Press, New York, 1989

- [Oyane, 1967] Oyane, M., Takashima, F., Osakada, K. and Tanaka, H., 1967, "The behaviour of some steels under dynamic compression", *Proceedings of the 10th Japan Congress on Testing Materials*, pp. 72-76.
- [Özel, 2000] Özel, T. and Altan, T., 2000, "Determination of workpiece flow stress and friction at the chip-tool contact for high-speed cutting", *International Journal of Machine Tools and Manufacture*, Vol. 40, No. 1, pp. 133-152.
- [Park, 2000] Park, I. and Dornfeld, D., 2000, "A Study of Burr Formation Processes Using the Finite Element Method: Part I", *Journal of Engineering Materials and Technology*, Vol. 122, pp. 221-228.
- [Park, 2000a] Park, I. and Dornfeld, D., 2000, "A Study of Burr Formation Processes Using the Finite Element Method: Part II-The Influence of Exit Angle, Rake Angle, and Backup Material on Burr Formation Processes", *Journal of Engineering Materials and Technology*, Vol. 122, pp. 229-237.
- [Poulachon, 2001] Poulachon, G., Moisan, A., Jawahir, I.S., 2001, "On Modelling the Influence of Thermo-Mechanical Behavior in Chip Formation During Hard Turning of 100Cr6 Bearing Steel", *Annals of the CIRP*, Vol. 50, No. 1, pp. 31-36.
- [Poulachon, 2004] Poulachon, G., Bandyopadhyay, B. P., Jawahir, I. S., Pheulpin, S. and Seguin, E., 2004, "Wear Behavior of CBS Tools while Turning Various Hardened Steels", *Wear*, Vol. 256, pp. 302-310.
- [Press, 1992] W.H. Press, S.A. Teukolsky, W.T. Vetterling and B.P. Flannery, *Numerical Recipes in C- The Art of Scientific Computing 2nd edition*, Cambridge University Press, New York, 1992.
- [Prevéy, 2000] Prévéy, P. S., 2000, "The Effect of Cold Work on the Thermal Stability of Residual Compression in Surface Enhanced IN718", *Proceedings of 20th ASM Materials Solutions Conference & Exposition*, St. Louis, Missouri, October 10-12, 2000, pp. 1-9.
- [Prevéy, 2000a] Prévéy, P. S., Cammett, J., 2000, "Low Cost Corrosion Damage Mitigation and Improved Fatigue Performance of Low Plasticity Burnished 7075-T6", *Proceedings of 4th International Aircraft Corrosion Workshop*, Solomons, MD, Aug.22-25, 2000, pp.1-9.
- [Prevéy, 2000b] Prévéy, P. S., Telesman, J., Gabb, T. and Kantzos, P., 2000, "FOD Resistance and Fatigue Crack Arrest in Low Plasticity Burnished IN718", *Proceedings of 5th National Engine High Cycle Fatigue Conference*, Chandler, AZ, March 7-9, 2000, pp. 1-12.

- [Prevéy, 2001]                   Prevéy, P. S., Shepard, M. J. and Smith. P. R., 2001, "The Effect of Low Plasticity Burnishing (LPB) on the HCF Performance and FOD Resistance of Ti-6Al-4V", *Proceedings of 6th National Turbine Engine High Cycle Fatigue (HCF) Conference*, March 5-8, 2001, Jacksonville, FL, pp. 1-10.
- [Prevéy, 2003]                   Prevéy, P.S., Ravindranath, R.A., Shepard, and M., Gabb, T., 2003, "Case Studies of Fatigue Life Improvement Using Low Plasticity Burnishing in Gas Turbine Engine Applications", *Proceedings of ASME Turbo Expo*, June 16-19, 2003, Atlanta, Georgia
- [Raedt, 2001]                   Raedt, H.-W., Hoppe, S. and Klocke, F., 2001, "2D-FEM simulation of the orthogonal high speed cutting process", *Proceedings of the Fourth CIRP International Workshop on Modeling of Machining Operations*, Delft, The Netherlands, August 17-18, 2001, pp. 117-124.
- [Ramesh, 2002]                   Ramesh, A., 2002, "Prediction of Process-Induced Microstructural Changes and Residual Stresses in Orthogonal Hard Machining," *Ph.D. Dissertation*, School of Mechanical Engineering, Georgia Institute of Technology.
- [Rosenberg, 1986]               Rosenberg, Z., Dawicke, D. and Bless, S., 1986, "A new technique for heating specimens in split hopkinson-bar experiments using induction coil heaters", *Experimental Mechanics*, Vol. 26, No. 3, pp. 275-278.
- [Röttger, 2002]               Röttger, K., 2002, "Walzen Hartgedrehter Oberflaechen", *Ph.D. Dissertation*, WZL, RWTH-Aachen, Germany.
- [Sahlan, 2003]               Sahlan, H., Moradi, C., Sartkulvanich, P. and Altan, T., 2003, "Tool wear and burr formation in milling of Aluminum alloy A356.0-T6, prepared for General Motors Powertrain (GMPT)", *ERC/NSM Report No. HPM/ERC/NSM-02-R-25*, The Ohio State University, Columbus, Ohio.
- [Sartkulvanich, 2001]       Sartkulvanich, P., Lilly, B. and Altan, T., 2001, "Flow Stress Determination in Metal Cutting: Review of the Literature and Flow Stress Database", *ERC/NSM Report No. HPM/ERC/NSM-01-R-23*, The Ohio State University, Columbus, Ohio.
- [Sartkulvanich, 2001a]       Sartkulvanich, P., Soehner, J. and Altan, T., 2001, "Material Database for Manufacturing Simulation (MADAMS): Summary of the Activities and Flow Stress Database", *ERC/NSM Report No. HPM/ERC/NSM-01-R-76*, The Ohio State University, Columbus, Ohio.



- [Sartkulvanich, 2004] Sartkulvanich, P., Koppka, F. and Altan, T., 2004, "Determination of Flow Stress for Metal Cutting Simulation – A Progress Report", *Journal of Materials Processing Technology*, Vol. 146, No. 1, pp. 61-71.
- [Schulze, 2000] Schulze, V. and Vöhringer, O., 2000, "Influence of Alloying Elements on the Strain Rate and Temperature Dependence of the Flow Stress of Steels", *Metallurgical and Materials Transactions A*, Vol. 31A, pp. 825-830.
- [Sekhon, 1993] Sekhon, G. S. and Chenot, J. L., 1993, "Numerical Simulation of Continuous Chip Formation During Non-Steady Orthogonal Cutting", *Engineering Computations*, Vol. 10, pp. 31-48.
- [Shatla, 1999] Shatla, M., 1999, "Prediction of Forces, Stresses, Temperatures and Tool Wear in Metal Cutting", *Ph.D. Dissertation*, The Ohio State University, Columbus, Ohio.
- [Shatla, 2001] Shatla, M., Kerk, C. and Altan, T., 2001, "Process modeling in machining. Part I: Determination of flow stress data", *International Journal of Machine Tools and Manufacture*, Vol. 41, No. 10, pp. 1511-1534.
- [Shirakashi, 1983] Shirakashi, T., Maekawa, K. and Usui, E., 1983, "Flow stress of low carbon steel at high temperature and strain Rate (Part 1) – Propriety of incremental strain method in impact compression test with rapid heating and cooling systems", *Bulletin of the Japan Society of Precision Engineering*, Vol. 17, No. 3, pp. 161-166.
- [Sizek, 1993] Sizek, H. W. and Gray, G. T. III, 1993, "Deformation of polycrystalline Ni3Al at high strain rates and elevated temperatures", *Acta Metallurgica et Materialia*, Vol. 41, No. 6, pp. 1855-1860.
- [Stevenson, 1997] Stevenson, R., 1997, "Study on the correlation of workpiece mechanical properties from compression and cutting tests", *Journal of Machining Science and Technology*, Vol. 1 (1), 67-79.
- [Strenkowski, 1985] Strenkowski, J. S. and Carroll, J. T., 1985, "A Finite Element Model of Orthogonal Metal Cutting", *Journal of Engineering for Industry*, Transactions of the ASME, Vol. 107, pp. 347-354.
- [Sutter, 1997] Sutter, G., Faure, L., Moulinari, A., Delime, A. and Dudzinski, D., 1997, "Experimental Analysis of Cutting Process and Chip Formation at High Speed Machining", *Journal de Physique IV*, Vol. 7, No. C3, pp. 33-38.

- [Thiele, 1999] Thiele, J. D., Melkote, S. N., 1999, "Effect of Cutting Edge Geometry and Workpiece Hardness on Surface Generation in the Finish Hard Turning of AISI 52100 Steel", *Journal of Material Processing Technology*, Vol. 94, pp. 216-226.
- [thirdwavesys.com] Internet web site of the commercial FEM package, at "[www.thirdwavesys.com](http://www.thirdwavesys.com)"
- [Timme, 1880] Timme, I. I., *On the Resistance of Metal and Wood to Cutting*, Dermacov, St. Petersburg, 1880 (in Russia)
- [Toenshoff, 1999] Toenshoff, H. K. and Hollmann, F., 1999, "Cutting of Metallic Materials at High Velocities (in German)", *Workshop on the Special Research Project of the German Research Foundation (DFG)*, Nov. 18, 1999, Bonn, Germany
- [Treppman, 2001] Treppman, C., 2001, "Fließverhalten Metallischer Werkstoffe bei Hochgeschwindigkeits beanspruchung", *Dr.-Ing. Dissertation*, RWTH Aachen, Germany
- [Usui, 1982] Usui, E., Shirakashi, T., 1982, "Mechanics of Machining from Descriptive to Predictive Theory", *On The Art of Cutting Metals – 75 Years Later - ASME-PED*, Vol. 7, pp. 13-15.
- [Usui, 1984] Usui, E., Obikawa, T. and Shirakashi, S., 1984, "Study on chip segmentation in machining titanium alloy", *Proceedings of the Fifth International Conference on Production Engineering*, Tokyo, Japan, July, 9-11, 1984, pp. 233-239.
- [Vyas, 1999] Vyas, A. and Shaw, M. C., 1999, "Mechanics of saw-tooth chip Formation in Metal Cutting", *Journal of Manufacturing Science and Engineering*, Vol. 121, pp. 163 - 172.
- [Xu, 2001] Xu, Y.B., Zhong, W.L., Chen, Y.J., Shen, L.T., Liu, Q., Bai, Y.L. and Meyers, M.A., 2001, "Shear localization and recrystallization in dynamic deformation of 8090 Al-Li alloy", *Materials Science and Engineering A: Structural Materials: Properties, Microstructure and Processing*, Vol. 299, No. 1-2, pp. 287-295.
- [Yen, 2000] Y.C Yen and M. Shatla, 2000, "Determination of Flow Stress in Machining, Comparison of Data from Orthogonal Turning and Orthogonal Milling", *ERC/NSM Report No. HPM/ERC/NSM-00-R-01*, The Ohio State University, Columbus, Ohio.
- [Yen, 2002] Yen, Y.C., Soehner, J., Lilly, B., and Altan, T., 2002, "Estimation of Tool Wear in Orthogonal Cutting using FE Analysis", *Journal of Materials Processing Technology*, Volume 146, No. 1 , pp. 82-91.

- [Yen, 2003] Yen, Y.C., Jain, A., Chigurupati, P., Wu, W.T. and Altan, T., 2003, "Computer Simulation of Orthogonal Cutting Using a Tool with Multiple Coatings", *the 6th CIRP Workshop on Modeling of Machining*, Hamilton, Ontario, Canada, May 19-20, 2003.
- [Yen, 2004] Yen, Y. C., 2004, "Modeling of Metal Cutting and Ball Burnishing - Prediction of Tool Wear and Surface Properties-", *Ph. D Dissertation*, The Ohio State University, Columbus, Ohio.
- [Zerilli, 1987] Zerilli, F.J. and Armstrong, R.W., 1987, "Dislocation-mechanics-based constitutive relations for material dynamics calculations", *Journal of Applied Physics*, Vol. 61, No. 5, pp. 1816-1825.
- [Zorev, 1966] Zorev, N. N., *Metal Cutting Mechanics*, Pergamon Press, Oxford, 1966

## APPENDIX A - DOWNHILL SIMPLEX METHOD

The downhill simplex algorithm uses an entirely self-contained strategy to find the minimum of a function with more than one independent variable. Details of this algorithm can be found in [Press, 1992].

A “simplex” is the geometrical figure consisting, in  $N$  dimensions, of  $N + 1$  points (or vertices) and all their interconnecting line segments, polygonal faces, etc. In two dimensions, a simplex is a triangle. In three dimensions it is a tetrahedron. If any point of a nondegenerate simplex (that enclose a finite inner  $N$ -dimensional volume) is taken as the origin, then the  $N$  other points define vector directions that span the  $N$ -dimensional vector space. For multidimensional minimization the algorithm require an initial guess, that is, an  $N$ -vector of independent variables as the first point to try. The algorithm is then supposed to make its own way downhill through the unimaginable complexity of an  $N$ -dimensional topography, until it encounters a (local, at least) minimum.

The downhill simplex method must be started not just with a single point, but with  $N + 1$  points, defining an initial simplex. If one of these points is defined as initial starting point  $P_o$ , then the other  $N$  points are

$$P_i = P_o + \lambda e_i \qquad \text{Equation A.1}$$

where the  $e_i$ 's are  $N$  unit vectors, and where  $\lambda$  is a constant which is a guess of the problem's characteristic length scale.

The downhill simplex method takes a series of steps, most steps just moving the point of the simplex where the function is largest (“highest point”)

through the opposite face of the simplex to a lower point. These steps are called reflections, and they are constructed to conserve the volume of the simplex (hence maintain its nondegeneracy). When it can do so, the method expands the simplex in one or another direction to take larger steps. When it reaches a “valley floor,” the method contracts itself in the transverse direction and tries to ooze down the valley. If there is a situation where the simplex is trying to “pass through the eye of a needle,” it contracts itself in all directions, pulling itself in around its lowest (best) point. These basic moves are summarized in Figure A.1.

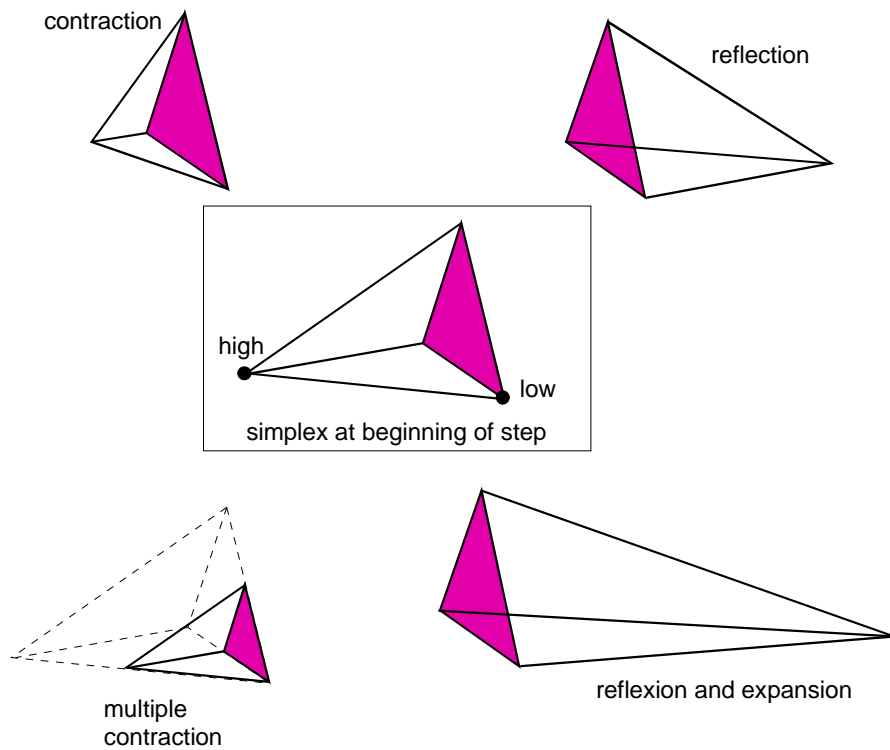


Figure A.1: Schematic of downhill simplex minimization

## APPENDIX B - UNIVERSAL HARDNESS

The Universal hardness (DIN 50359), HU, is defined as the maximum applied load ( $F_{max}$ ) divided by the real (or 'developed') contact area ( $A_r$ ) at that load and is defined for Vickers and Berkovich indenter geometries but not for spherical or Knoop indenters. For a Vickers indenter and a standard Berkovich indenter, the Universal hardness is given by

$$HU = \frac{F_{max}}{A_r(h)} \approx \frac{F_{max}}{26.43h^2} \quad \text{Equation B.1}$$

where  $A_r(h) = \frac{P \cdot \tan(\alpha/2)}{\cos(\alpha/2)} \cdot h^2$ ,  $P=4$  and  $\alpha=136^\circ$  for Vickers indenters and  $P=3\sqrt{3}$  and  $\alpha=130.06^\circ$  for Berkovich indenters,  $h$  is the maximum penetration depth measured during the indentation, and  $\alpha$  is the angle between the two opposing faces of the pyramidal tip.

If the projected contact area  $A_p(h)$  is used in Eq. (B.1) rather than  $A_r(h)$ , the hardness definition becomes the Indentation Hardness, which is based on the mean contact pressure. A summary of the four most commonly used pyramidal indenter geometries is given in Table B.1.

	Vickers	Berkovich	Modified Berkovich	Cube Corner
$\alpha_t$	136°	141.9°	142.3°	90°
$\alpha$	136°	130.06°	130.54°	70.528°
$A_r/h^2$	$4 \cdot \frac{\tan(\alpha/2)}{\cos(\alpha/2)} \approx 26.43$	$3\sqrt{3} \cdot \frac{\tan(\alpha/2)}{\cos(\alpha/2)} \approx 26.43$	$3\sqrt{3} \cdot \frac{\tan(\alpha/2)}{\cos(\alpha/2)} \approx 26.97$	4.5
$A_p/h^2$	$4 \cdot \tan^2 \alpha \approx 24.504$	$3\sqrt{3} \cdot \tan^2 \alpha \approx 23.96$	$3\sqrt{3} \cdot \tan^2 \alpha \approx 24.494$	$3\sqrt{3}/2 \approx 2.598$
$A_r/A_p$	$1/\sin \alpha = 1.0785$	$1/\sin \alpha = 1.1031$	$1/\sin \alpha = 1.1010$	$1/\sin \alpha = 1.7320$

Table B.1: Summary of angle and area data for the four most commonly used indenter geometries, where  $\alpha_t$  is the total included angle,  $\alpha$  is the angle between the two opposing faces of the pyramid,  $A_r$  is the real (or 'developed') contact area and  $A_p$  is the project contact area